

# **For Reference**


---

**NOT TO BE TAKEN FROM THIS ROOM**



EX LIBRIS  
UNIVERSITATIS  
ALBERTAENSIS





Digitized by the Internet Archive  
in 2023 with funding from  
University of Alberta Library

<https://archive.org/details/Syrett1976>











THE UNIVERSITY OF ALBERTA

RELEASE FORM

NAME OF AUTHOR                      Barry Albert Syrett

TITLE OF THESIS                      Feedforward Linearization of a  
   Stable IMPATT Amplifier

DEGREE FOR WHICH THESIS WAS PRESENTED      Doctor of Philosophy

YEAR THIS DEGREE GRANTED      1976

Permission is hereby granted to THE UNIVERSITY OF ALBERTA LIBRARY to reproduce single copies of this thesis and to lend or sell such copies for private, scholarly or scientific research purposes only.

The author reserves other publication rights, and neither the thesis nor extensive extracts from it may be printed or otherwise reproduced without the author's written permission.





THE UNIVERSITY OF ALBERTA

FEEDFORWARD LINEARIZATION  
OF A STABLE IMPATT AMPLIFIER

by



BARRY ALBERT SYRETT

A THESIS

SUBMITTED TO THE FACULTY OF GRADUATE STUDIES AND RESEARCH IN  
PARTIAL FULFILMENT OF THE REQUIREMENTS FOR THE DEGREE OF  
DOCTOR OF PHILOSOPHY

DEPARTMENT OF ELECTRICAL ENGINEERING

EDMONTON, ALBERTA

FALL, 1976





THE UNIVERSITY OF ALBERTA  
FACULTY OF GRADUATE STUDIES AND RESEARCH

The undersigned certify that they have read, and recommend to the Faculty of Graduate Studies and Research, for acceptance, a thesis entitled Feedforward Linearization of a Stable IMPATT Amplifier submitted by Barry Albert Syrett in partial fulfilment of the requirements for the degree of Doctor of Philosophy in Electrical Engineering.





To my wife Kathy  
and my Parents

Who encouraged me to study ..... in lieu of time I would  
otherwise have spent with them.





## ABSTRACT

The use of feedforward correction to reduce nonlinear distortion in a stable IMPATT amplifier is investigated theoretically and experimentally. The motivation for this investigation is that, when such a linearized amplifier is used in a microwave telecommunications system, SSB-AM modulation becomes a viable alternative to the FM modulation now in use; SSB-AM makes more efficient use of the frequency spectrum than FM.

Intermodulation (IM) distortion in an IMPATT amplifier is analysed by two different methods. The first method uses the Volterra series approach. An IMPATT amplifier model which incorporates the nonlinearities of the diode and its linear embedding circuitry is described. The Volterra transfer functions up to and including fifth-order are derived for this model. Expressions are derived for IM distortion products, and intercept points for a low-level two-tone input. These expressions demonstrate the dependence of distortion on amplifier centre-frequency, the equivalent load conductance, and the nonlinear diode parameters. In the second method, the IMPATT amplifier model comprises admittance operators which represent the nonlinear active diode and the linear passive embedding circuitry. These admittance operators are defined analytically in terms of the RF-voltage amplitude and frequency, and approximated by cubic-spline fitting of experimental data. The nonlinear differential equation for the model is solved numerically using quasistationary analysis; the steady-state solution gives the IM distortion, up to seventh-order, of the IMPATT amplifier.

An expression is derived using Volterra series analysis for the reduction of IM products in the feedforward-corrected IMPATT amplifier,



in terms of the feedforward network parameters. It is shown that:

1) imbalance in the error-correction loop mainly determines the distortion suppression in the feedforward system; 2) imbalance in the error-detection loop dictates the required power capability of the error amplifier. Further, the gain sensitivity of the feedforward amplifier as a function of gain- and phase imbalance is obtained.

A technique for the measurement of the IMPATT-diode large-signal electronic admittance is developed. The technique features: 1) measurement with the diode *in situ*; 2) flexibility through use of an automatic network analyser; 3) accuracy enhancement by computer-aided data reduction. The electronic admittance of an IMPATT diode (HP 5082-0431) was measured within an estimated error of 20% at 25-mA dc bias, in the range 5.7 to 6.5 GHz, for RF voltage amplitudes up to 20 V.

The IM distortion of an experimental 17-dB gain, 5.905-GHz IMPATT amplifier was measured for an equal-level two-tone input in the 64-MHz passband. The experimental third-order IM products were approximately 20 dB below the carrier for 0-dBm output power, and compared favourably with the predicted distortion. An experimental feedforward amplifier was realized in waveguide using the experimental IMPATT amplifier as the main amplifier and a low-noise TWT as the error amplifier. The observed IM products were reduced by ~20 dB over a 6-MHz bandwidth, and by 30 dB at the centre frequency. The improvement attained agrees with the improvement expected from theoretical analysis.





## ACKNOWLEDGMENT

The author expresses his sincere appreciation for the interest, advice, and encouragement provided by his supervisor, Dr. P.A. Goud, during all phases of this work. The author also wishes to thank Dr. A. Javed for his invaluable assistance in developing the Volterra series model, and Mr. J.E. Fearn, of the Microwave Electronics Laboratory for his help in performing the experimental measurements.

The author is grateful to Dr. J. Nigrin and Dr. C.G. Englefield, for many fruitful discussions during the period Dr. Goud was on sabbatical leave.

The financial support provided by the following organizations is greatly appreciated: The National Research Council of Canada for several postgraduate scholarships; Alberta Government Telephones for a Centennial Fellowship; and the Department of Electrical Engineering for part-time teaching assistantships. The research reported in this thesis was supported in part by the National Research Council of Canada under Grant NRC A-3725.

Lastly, the author must thank his wife, Kathy, and his parents for their unwavering patience and inspiration to completion of this thesis.



# TABLE OF CONTENTS

Chapter		Page
1	INTRODUCTION .....	1
	1.1 General Considerations .....	1
	1.2 Thesis Objectives and Approach .....	3
	1.3 Thesis Organization.....	6
2	IMPATT AMPLIFIER DISTORTION AND FEEDFORWARD CORRECTION ...	8
	2.1 Synopsis .....	8
	2.2 Types of Distortion Produced by Amplifier Nonlinearities .....	8
	2.3 Evaluation of Amplifier Nonlinearities .....	11
	2.3.1 Intermodulation (IM) Distortion Product .....	11
	2.3.2 Intercept Points.....	13
	2.4 Some Properties of IMPATT Diodes and of Stable IMPATT Amplifiers .....	13
	2.4.1 Small-Signal IMPATT-Diode Characteristics .....	13
	2.4.2 Large-Signal IMPATT-Diode Characteristics .....	16
	2.4.3 Stable IMPATT-Diode Reflection Amplifier .....	16
	2.4.4 Nonlinear Characteristics of Stable IMPATT Amplifiers.....	18
	2.5 Survey of Amplifier Linearization Techniques .....	21
	2.6 Principles of Feedforward Correction .....	27
	2.7 Summary .....	34
3	COMPUTER-AIDED LARGE-SIGNAL MEASUREMENT OF IMPATT-DIODE ELECTRONIC ADMITTANCE .....	36
	3.1 Introduction .....	36
	3.2 Theoretical Details of the Electronic-Admittance Measurement Technique .....	42
	3.2.1 The Circuit Model .....	42
	3.2.2 Calibration of the Measurement System .....	45
	3.2.3 Determination of the Coaxial System Transmission Parameters .....	49
	3.2.4 Determination of IMPATT Electronic Admittance .	52
	3.3 Experimental Details of the Electronic-Admittance Measurement Technique .....	55
	3.3.1 Experimental Electronic-Admittance Measurement Set-Up .....	55
	3.3.2 The Experimental Procedure .....	58
	3.4 Computational Details of the Electronic-Admittance Measurement Technique .....	59
	3.5 Measured IMPATT-Diode Electronic Admittance and Error Analysis .....	59
	3.6 Summary .....	71





Chapter		Page
4	DISTORTION ANALYSIS OF A FEEDFORWARD-CORRECTED IMPATT AMPLIFIER USING VOLTERRA SERIES REPRESENTATION.....	73
4.1	Introduction with Historical Notes.....	73
4.2	Some Preliminary Results for Volterra Series Analysis .....	75
4.3	Distortion Analysis of a Stable IMPATT Amplifier Using Volterra Series Representation .....	80
4.3.1	A Nonlinear Model of a Stable IMPATT Amplifier .....	80
4.3.2	Determination of the IMPATT-Amplifier Volterra Transfer Functions .....	86
4.3.3	Intermodulation Distortion in an IMPATT Amplifier .....	90
4.3.4	Third- and Fifth-Order Intercept Points of an IMPATT Amplifier .....	94
4.3.5	Gain Compression in an IMPATT Amplifier .....	95
4.3.6	Computed IMPATT-Amplifier Distortion .....	96
4.4	Extension of Volterra Series Distortion Analysis to a Microwave Feedforward Amplifier .....	114
4.4.1	Basic Nonlinear Model of a Microwave Feedforward Amplifier .....	114
4.4.2	Determination of the Feedforward Amplifier Volterra Transfer Functions .....	119
4.4.3	Intermodulation Distortion in a Feedforward Amplifier .....	121
4.4.4	Computed Distortion in a Feedforward-Corrected Amplifier .....	126
4.5	Power Considerations in Microwave Feedforward Amplifier Design .....	129
4.6	Gain Sensitivity of a Microwave Feedforward Amplifier .....	132
4.7	Summary .....	133
5	QUASISTATIONARY NONLINEAR DISTORTION STUDY OF A FEEDFORWARD-CORRECTED IMPATT AMPLIFIER .....	135
5.1	Introduction and Overview .....	135
5.2	Derivation of Active and Passive Circuit Non-CW Admittance Operators .....	137
5.2.1	Linear Passive Circuit Non-CW Admittance Operator .....	137
5.2.2	Approximation of the Passive Circuit Linear Admittance Operator by Cubic Spline Interpolation .....	142
5.2.3	Nonlinear Active Circuit Non-CW Admittance Operator .....	146
5.2.4	Approximation of the Active Circuit Nonlinear Admittance Operator by Bicubic Spline Interpolation.....	152
5.3	Numerical Quasistationary Distortion Analysis of an IMPATT Amplifier .....	158
5.3.1	Equivalent Circuit of a Stable IMPATT Amplifier .....	158



5.3.2	Intermodulation Distortion Analysis of an IMPATT Amplifier by Numerical Solution of the Amplifier's Nonlinear Differential Equation ..	165
5.3.3	Computed IMPATT-Amplifier Distortion .....	177
5.4	Reduction of IMPATT-Amplifier Distortion by Feed- forward Correction .....	192
5.5	Summary .....	195
6	EXPERIMENTAL STUDY OF IMPATT-AMPLIFIER DISTORTION AND OF FEEDFORWARD-CORRECTED DISTORTION .....	197
6.1	Scope of the Experimental Study .....	197
6.2	The Experimental Stable IMPATT Amplifier .....	198
6.3	The Experimental Feedforward-Corrected IMPATT Amplifier .....	205
6.4	The Experimental IM Distortion Test Bench and Procedures .....	211
6.5	Experimental IMPATT-Amplifier Distortion Results and Comparison With Theory .....	215
6.6	Experimental Distortion Results for the Feedforward- Corrected IMPATT Amplifier and Comparison with Theory .....	220
7	CONCLUSION .....	228
7.1	Recapitulation of Theoretical and Experimental Results with Concluding Remarks .....	228
7.2	Recommendations for Further Research .....	236
	* * *	
	REFERENCES .....	239
	APPENDIX A INTERMODULATION DISTORTION IN TERMS OF VOLTERRA TRANSFER FUNCTIONS .....	246
	APPENDIX B GAIN COMPRESSION IN TERMS OF VOLTERRA TRANSFER FUNCTIONS .....	250





## LIST OF TABLES

Table	Description	Page
4.1	IMPATT-Amplifier Nonlinear Model Parameters	99



## LIST OF FIGURES

Figure		Page
2.1	Types of amplifier distortion. (a) Nonlinear amplitude (envelope) distortion. (b) Nonlinear phase distortion. (c) Linear amplitude distortion. (d) Linear phase distortion.	10
2.2	IMPATT diode operation. (a) Terminal I-V characteristics of a PN junction. (b) Read diode structure [22]. (c) Electric field profile. (d) Applied RF voltage. (e) Avalanche current or current injected into intrinsic region. (f) Induced external current.	15
2.3	Typical IMPATT-diode large-signal electronic admittance for a given dc bias current [30].	17
2.4	Typical IMPATT-diode reflection amplifier.	17
2.5	Typical stable IMPATT-diode reflection amplifier distortion [12], [31]. (a) Nonlinear amplitude distortion. (b) Nonlinear phase distortion. (c) Linear amplitude distortion. (d) Linear phase distortion.	19
2.6	Amplifier linearization techniques. (a) Backoff of amplifier output power. (b) Equalization of amplifier nonlinearities. (c) Bias-current compensation of IMPATT amplifier [41].	22
2.7	Feedback-linearized amplifiers. (a) Basic feedback amplifier. (b) Microwave feedback amplifier [46]. (c) Siemens Gmbh. 400-MHz feedback amplifier [48].	25
2.8	Feedforward-corrected amplifiers. (a) Black's feedforward amplifier [4], [5]. (b) Seidel's microwave feedforward amplifier [55], [56].	28
3.1	Typical packaged negative-resistance diode.	37
3.2	Packaged diode end-mounted in precision 50- $\Omega$ coaxial line with an impedance transformer.	37
3.3	Equivalent circuit of packaged diode end-mounted in precision 50- $\Omega$ coaxial line according to Getsinger [63].	39
3.4	Transformation of IMPATT electronic admittance $Y_e$ to measurement reference plane M-M' according to Gewartowski and Morris [68].	39
3.5	Block diagram of large-signal electronic admittance measurement set-up.	43





Figure		Page
3.6	Transformation of IMPATT electronic admittance $Y_e$ to calibration reference plane 2-2' and to measurement reference plane 1-1'.	46
3.7	Schematic diagram of large-signal electronic admittance measurement set-up.	56
3.8	Resistance and differential capacitance of the active region of the experimental IMPATT diode below breakdown voltage.	60
3.9	Behaviour of the small-signal electronic conductance of the experimental IMPATT diode.	62
3.10	Behaviour of the small-signal electronic susceptance of the experimental IMPATT diode.	63
3.11	Frequency behaviour of the large-signal electronic conductance of the experimental IMPATT diode.	65
3.12	Frequency behaviour of the large-signal electronic susceptance of the experimental IMPATT diode.	66
3.13	RF voltage behaviour of the large-signal electronic conductance of the experimental IMPATT diode.	67
3.14	RF voltage behaviour of the large-signal electronic susceptance of the experimental IMPATT diode.	68
3.15	Frequency- and RF voltage behaviour of the large-signal electronic admittance of the experimental IMPATT diode.	69
4.1	Volterra-Wiener model of an $n^{\text{th}}$ -order nonlinear system [80].	79
4.2	Equivalent circuit used for Volterra series distortion analysis of a stable IMPATT reflection amplifier.	82
4.3	Comparison of measured IMPATT-amplifier gain with the gain predicted using the IMPATT-diode amplifier model for Volterra series distortion analysis (at 25-mAdc bias current).	97
4.4	Comparison of measured IMPATT-amplifier phase shift with the phase shift predicted using the IMPATT-diode amplifier model for Volterra series distortion analysis (at 25-mAdc bias current).	98



Figure		Page
4.5	Calculated values of small-signal electronic conductance and the nonlinear conductance parameter in the characterization of the IMPATT-diode electronic conductance ( $I_{dc} = 25$ mA) for Volterra series distortion analysis.	100
4.6	Calculated values of small-signal equivalent diode capacitance and the nonlinear diode capacitance parameter in the characterization of the IMPATT-diode electronic susceptance ( $I_{dc} = 25$ mA) for Volterra series distortion analysis.	101
4.7	Computed linear transfer function, at frequency $f_1$ , for the experimental IMPATT amplifier ( $I_{dc} = 25$ mA) with a CW input.	103
4.8	Computed third-order nonlinear (Volterra) transfer function, at frequency $2f_1-f_2$ , for the experimental IMPATT amplifier ( $I_{dc} = 25$ mA) with a two-tone input ( $f_2 = f_1 + 1$ MHz).	104
4.9	Computed fifth-order nonlinear (Volterra) transfer function, at frequency $3f_1-2f_2$ , for the experimental IMPATT amplifier ( $I_{dc} = 25$ mA) with a two-tone input ( $f_2 = f_1 + 1$ MHz).	105
4.10	Predicted frequency-dependence of IM distortion, using Volterra series analysis, for the experimental IMPATT amplifier ( $I_{dc} = 25$ mA) with a two-tone input ( $f_2 = f_1 + 1$ MHz) and constant -10-dBm output power. (a) Predicted third-order IM distortion at $2f_1-f_2$ . (b) Predicted fifth-order IM distortion at $3f_1-2f_2$ .	107
4.11	Comparison of measured and predicted IM distortion, using Volterra series analysis, for the experimental IMPATT amplifier ( $I_{dc} = 25$ mA) with a two-tone input ( $f_1 = 5.905$ GHz, $f_2 = 5.906$ GHz) at the centre frequency.	108
4.12	Comparison of measured and predicted fundamental output power and IM distortion products, using Volterra series analysis, for the experimental IMPATT amplifier ( $I_{dc} = 25$ mA) with a two-tone input ( $f_1 = 5.905$ GHz, $f_2 = 5.906$ GHz) at the centre frequency.	109





Figure		Page
4.13	Comparison of measured and predicted frequency-dependence of third-order IM distortion at $2f_1-f_2$ , using Volterra series analysis, for the experimental IMPATT amplifier ( $I_{dc} = 25$ mA) with a two-tone input ( $f_2 = f_1 + 1$ MHz).	111
4.14	Predicted frequency-dependence of fifth-order IM distortion at $3f_1-2f_2$ , using Volterra series analysis, for the experimental IMPATT amplifier ( $I_{dc} = 25$ mA) with a two-tone input ( $f_2 = f_1 + 1$ MHz).	112
4.15	Predicted gain compression/expansion, using Volterra series analysis, for the experimental IMPATT amplifier at 25-mA <sub>dc</sub> bias current.	113
4.16	Feedforward amplifier representation for the Volterra series analysis of nonlinear distortion. (a) Feedforward amplifier circuit representation. (b) Overall feedforward system representation.	115
4.17	Improvement in third- and fifth-order IM distortion, $IM_3$ and $IM_5$ , for various values of imbalance in the feedforward amplifier error-correction loop.	127
4.18	Contours of constant improvement in third- and fifth-order IM distortion, $IM_3$ and $IM_5$ , for various values of imbalance in the feedforward amplifier error-correction loop.	128
4.19	Relative contribution of the error-amplifier power and main-amplifier power to the feedforward-amplifier power for various values of imbalance in the feedforward amplifier error-detection loop.	131
5.1	(a) IMPATT-diode reflection-type amplifier circuit. (b) Equivalent circuit used for quasistationary distortion analysis of a stable IMPATT amplifier.	159
5.2	Measured circuit admittance presented to the active region of the IMPATT diode in the experimental IMPATT amplifier. The measured small-signal electronic admittance (negative) of the IMPATT diode ( $I_{dc} = 25$ mA) is also shown.	178
5.3	Comparison of measured IMPATT-amplifier small-signal gain with the gain predicted using the measured circuit- and electronic admittance ( $I_{dc} = 25$ mA). The effect of a 4% increase and a 4% decrease in the measured circuit conductance and susceptance, respec-	



tively, on the predicted gain is shown. The calculated insertion loss  $x_2$  of the coupling network K is also plotted.

180

- 5.4 Comparison of measured and predicted IM distortion, using quasistationary distortion analysis, for the experimental IMPATT amplifier ( $I_{dc} = 25$  mA) with a two-tone input ( $f_1 = 5.905$  GHz,  $f_2 = 5.906$  GHz) at the centre frequency. The measured circuit admittance is used in the analysis. 182
- 5.5 Comparison of measured and predicted frequency-dependence of third-order IM distortion at  $2f_1 - f_2$ , using quasistationary distortion analysis, for the experimental IMPATT amplifier ( $I_{dc} = 25$  mA) with a two-tone input ( $f_2 = f_1 + 1$  MHz). The measured circuit admittance is used in the analysis. 183
- 5.6 Comparison of measured IMPATT-amplifier gain with the gain predicted using the IMPATT-diode amplifier tuned-circuit model for quasistationary distortion analysis (at 25-mA dc bias current). 184
- 5.7 Comparison of measured IMPATT-amplifier phase shift with the phase shift predicted using the IMPATT-diode amplifier tuned-circuit model for quasistationary distortion analysis (at 25-mA dc bias current). 185
- 5.8 Comparison of measured and predicted IM distortion, using quasistationary distortion analysis of the amplifier tuned-circuit model, for the experimental IMPATT amplifier ( $I_{dc} = 25$  mA) with a two-tone input ( $f_1 = 5.905$  GHz,  $f_2 = 5.906$  GHz) at the centre frequency. 187
- 5.9 Comparison of measured and predicted fundamental output power and IM distortion products, using quasistationary distortion analysis of the amplifier tuned-circuit model, for the experimental IMPATT amplifier ( $I_{dc} = 25$  mA) with a two-tone input ( $f_1 = 5.905$  GHz,  $f_2 = 5.906$  GHz) at the centre frequency. 188
- 5.10 Comparison of measured and predicted frequency dependence of third-order IM distortion at  $2f_1 - f_2$ , using quasistationary distortion analysis of the amplifier tuned-circuit model, for the experimental IMPATT amplifier ( $I_{dc} = 25$  mA) with a two-tone input ( $f_2 = f_1 + 1$  MHz). 189



Figure		Page
5.11	Comparison of measured and predicted frequency-dependence of fifth-order IM distortion at $3f_1-2f_2$ , using quasistationary distortion analysis of the amplifier tuned-circuit model, for the experimental IMATT amplifier ( $I_{dc} = 25$ mA) with a two-tone input ( $f_2 = f_1 + 1$ MHz).	190
5.12	Predicted gain compression/expansion, using quasistationary distortion analysis of the amplifier tuned-circuit model, for the experimental IMPATT amplifier at 25-mAdc bias current.	191
6.1	Cross section of J-band coaxial double-slug-tuned IMPATT amplifier circuit.	199
6.2	Measured gain behaviour of the experimental IMPATT amplifier at constant 25-mAdc bias current.	201
6.3	Measured saturation characteristics of the experimental IMPATT amplifier at constant 25-mAdc bias current.	203
6.4	Measured gain compression of the experimental IMPATT amplifier at constant 25-mAdc bias current.	204
6.5	The experimental feedforward-corrected IMPATT amplifier.	206
6.6	Photographic view of the experimental feedforward-corrected IMPATT amplifier and two-tone IM distortion test equipment.	208
6.7	Measured variation in the quality of error-detection loop balance and error-correction loop balance in the experimental feedforward-corrected IMPATT amplifier.	210
6.8	The experimental two-tone IM distortion test bench.	212
6.9	Schematic diagram of IF frequency comparator circuit for microwave two-tone generator (modified from [100]).	214
6.10	Comparison of measured third-order IM distortion at $2f_1-f_2$ , for the experimental IMPATT amplifier ( $I_{dc} = 25$ mA) with a two-tone input ( $f_2 = f_1 + 1$ MHz) with the theoretical values calculated using 1) the Volterra series analysis; 2) the quasistationary distortion analysis.	216





Figure		Page
6.11	Comparison of measured fifth-order IM distortion at $3f_1 - 2f_2$ , for the experimental IMPATT amplifier ( $I_{dc} = 25$ mA) with a two-tone input ( $f_2 = f_1 + 1$ MHz) with the theoretical values calculated using 1) the Volterra series analysis; 2) the quasistationary distortion analysis.	218
6.12	Spectrum photographs of the IM products of the experimental feedforward amplifier with an equal-level (-13.8 dBm) two-tone input at the centre frequency ( $f_1 = 5.9045$ GHz, $f_2 = 5.9055$ GHz) [vertical scale 10 dB/cm; horizontal scale 1 MHz/cm]. (a) The output of the feedforward amplifier without feedforward correction. (b) The input to the error amplifier when the error-detection loop is balanced at 5.905 GHz. (c) The output of the feedforward amplifier with feedforward correction applied.	221
6.13	Spectrum photographs of the output of the feedforward amplifier with an equal-level (-13.8 dBm) two-tone input at the centre frequency ( $f_1 = 5.9045$ GHz, $f_2 = 5.9055$ GHz) [vertical scale 10 dB/cm; horizontal scale 1 MHz/cm]. (a) The feedforward-corrected output for 1-dB amplitude imbalance in the error-correction loop. (b) The feedforward-corrected output for $2^\circ$ phase imbalance in the error-correction loop. (c) The feedforward-corrected output for both 1-dB amplitude imbalance and $2^\circ$ phase imbalance in the error-correction loop.	224
6.14	Spectrum photographs of the IM products of the experimental feedforward amplifier with an equal-level (-13.8 dBm) two-tone input at 5.901 GHz ( $f_1 = 5.9005$ GHz, $f_2 = 5.9015$ GHz) [vertical scale 10 dB/cm; horizontal scale 1 MHz/cm]. (a) The output of the feedforward amplifier without feedforward correction. (b) The input to the error amplifier when the error-detection loop is balanced at 5.905 GHz. (c) The output of the feedforward amplifier with feedforward correction applied.	225
6.15	Comparison of measured reduction of IMPATT-amplifier third-order IM distortion by means of feedforward correction with the expected improvement values as a function of frequency.	226
6.16	Comparison of measured feedforward-amplifier gain sensitivity with the predicted gain sensitivity.	226



## CHAPTER 1

### INTRODUCTION

#### 1.1 General Considerations

Great interest has arisen recently in the use of Single-Sideband AM Frequency Division Multiplexing (SSB-AM-FDM) for common carrier microwave communications [1]. This is due to the superiority of SSB-AM over narrowband FM in: 1) signal-to-noise performance at relatively high transmission capacities; 2) its inherent frequency spectrum conservation over the microwave FM links now in use. In AM systems, however, intermodulation (IM) distortion seriously degrades system performance. This IM distortion results primarily from third-order amplitude distortion and third-order AM-to-PM conversion in the transmitter output stage operating near saturation [1], [2]. Such distortion is caused in microwave amplifiers by nonlinear output-amplitude variation with input signal level and nonlinear phase shift variation with input signal level, respectively. As much emphasis must be placed on phase nonlinearities as on amplitude nonlinearities in any amplifier distortion study because reactive or memory effects are very significant at high frequencies. In addition to contributing to IM distortion, phase nonlinearities cause IM distortion to be frequency-dependent. Unfortunately, unless an amplifying device is driven into its nonlinear region of operation, it can neither deliver its full power capability nor can it be efficient [3]. A suitable technique must be used to linearize the transmitter power amplifier and to reduce nonlinear distortion to required SSB-AM system specifications.

Feedforward linearization is an effective distortion reduction technique which predates feedback; both techniques were invented by





H.S. Black [4], [5]. The capabilities of feedforward correction exceed those of feedback, but at low frequencies the extra complexity and cost involved are normally not warranted. At microwave frequencies, where feedback path length becomes an appreciable fraction of a wavelength, stability and bandwidth problems render feedback impractical. On the other hand, feedforward correction is very attractive at high frequencies, since it takes cognizance of time delays directly-- there is no need to reprocess or recirculate a signal once it has passed through the amplifier, thereby assuring stability. The essential principle of feedforward correction is that the distorted output signal of the main amplifier is compared with a delayed sample of the input signal to derive an error signal. The amount of delay is equal to that of the transit time of the amplifier and associated circuitry. The error signal is then amplified and injected into the main signal output with the appropriate time delay needed to cancel the noncoherent noise and distortion previously introduced by the main amplifier.

By using microwave integrated-circuit (MIC) technology as well as low-cost solid-state amplifiers, the cost of feedforward correction can be reduced to a level at which feedforward amplifiers can compete with conventional amplifiers in microwave communications systems. Hsieh and Chan [6], [7] constructed a 1.25-W feedforward-corrected MIC transistor amplifier at 2.2 GHz with all IM distortion products 50 dB below the carrier level. Two-terminal negative-resistance semiconductor diodes are also available for microwave power generation [8]. Specifically, the IMPATT diode (acronym for IMPact ionization Avalanche Transit Time) is now being employed widely as the active device in low-cost, low- to medium-power microwave oscillators and amplifiers. Indications are that



this trend will continue in the foreseeable future [9].

Bowers [10], amongst others, describes the advantages and limitations of using IMPATT reflection amplifiers in microwave systems. As advantages he lists: higher reliability than conventional travelling-wave tube (TWT) amplifiers; higher power at higher frequencies than transistor amplifiers; also reasonable bandwidth (typically 300 MHz) and gain (typically 20 dB). As disadvantages he cites a higher noise figure than for Gunn diodes and transistors, and a prohibitively low gain-bandwidth product for some broadband applications.

A narrowband stable IMPATT-diode reflection amplifier will be used here for the main amplifier in a 6-GHz feedforward correction system. This thesis presents a study of the reduction of IMPATT amplifier distortion through feedforward linearization.

## 1.2 Thesis Objectives and Approach

The theoretical objective of this thesis is to develop a suitable mathematical model for the "feedforward IMPATT amplifier". The model must be able to predict IM distortion of both the IMPATT amplifier itself and of the IMPATT amplifier with feedforward correction applied, since IM distortion is a convenient gauge of amplifier nonlinearity.

The experimental aims of this thesis are 1) to check the developed model and predicted response, and 2) to study the effectiveness of the feedforward circuit for reduction of amplifier distortion. This latter study involves determination of the dominant parameters of the feedforward amplifier, the various tradeoffs amongst them for best linear amplifier response, and the degree of linearization which can be achieved.



Microwave two-terminal negative-resistance devices, such as IMPATT diodes, normally exhibit both nonlinear conductance and nonlinear susceptance at their terminals. The nonlinear susceptance of the active device together with the susceptance of the passive circuit load are responsible for memory effects: the current  $i$  flowing through the active device is not an instantaneous function of the applied voltage  $v$ . An accurate mathematical model should describe both the amplitude- and phase nonlinearities observed in microwave active devices and circuits, and the resulting IM performance.

In the literature, several models for the active device and external circuitry have been developed. Van der Pol [11] represents the nonlinear active device simply as a linear negative conductance  $-\alpha$  and a constant  $\beta$  such that  $i = -\alpha v + \beta v^3$ . Such a memoryless power series representation of the device terminal voltage-current relationship does not suffice at high frequencies where memory effects must be included. Hines [3], Kuno [12] and Berceci [13] amongst others, model the active device as a nonlinear conductance in shunt with a nonlinear susceptance, both described by Van der Pol - type cubic nonlinearities. This approach is fine for small- to medium-signal single-frequency (CW) excitation of the device but the nonlinearities are not characterized adequately for large-signal excitation or multiple-input IM distortion test signals. Heiter [14] extends the conventional amplitude power series expansion to include order-dependent time delays representing phase nonlinearities. Since the parameters of Heiter's model do not relate directly to physical device parameters, such as the admittance of the active region of the device (i.e., the electronic admittance), the measured values of the parameters vary greatly with the measurement procedure. Heiter's model thus precludes





its application to arbitrary signal excitation, but is adequate for a given IM distortion measurement technique. The describing function representation of nonlinear microwave circuits [15] does not readily allow modulated signals to be analysed. In addition, it is laborious to measure the characteristic describing function, and application of the method to most circuits with memory elements is difficult. The mathematical models which are developed in this thesis feature: 1) detailed and accurate representation of device characteristics, including memory; 2) simple measurement of relevant device and circuit parameters; 3) simple analysis of two-tone IM distortion test signals.

It is assumed that the IMPATT-diode reflection-type amplifier is tuned so that it is stable. The word *stable* is taken to mean three things: 1) there are no free oscillations in the network; 2) there are no integral multiple subharmonic responses; 3) there are no bias-circuit oscillations or parametric-type oscillations.

Two approaches for IM distortion analysis of a mildly-driven nonlinear stable IMPATT amplifier are developed. The first approach models the IMPATT amplifier by a tuned RLC circuit in parallel with the nonlinear IMPATT diode electronic admittance. The nonlinear circuit is then analysed using the time-invariant functional series known as the Volterra series [16]. The Volterra series consists of a set of time-domain functions which are termed nonlinear impulse responses or Volterra kernels. In the frequency-domain, the Volterra series is characterized by a set of nonlinear transfer functions which are multidimensional Fourier transforms of the Volterra kernels. The complex nonlinear transfer functions are determined from circuit analysis of the nonlinear equivalent circuit of the amplifier. Frequency-



dependent IM distortion is predicted from a knowledge of these nonlinear transfer functions. The Volterra series model is then extended to represent the feedforward amplifier and to predict the reduction in IM distortion as a function of its dominant parameters.

In the second approach, the IMPATT amplifier is modelled as a parallel connection of passive circuit admittance and nonlinear active diode admittance driven by a current generator. The complex nonlinear differential equation describing this model is solved numerically for steady-state IM distortion using quasistationary analysis. The model is then extended to describe the feedforward amplifier by treating all circuitry external to the IMPATT amplifier as linear and by applying linear circuit analysis techniques.

Each of these approaches relies on an accurate knowledge of the nonlinear IMPATT-diode admittance. A method of accurate measurement of large-signal IMPATT-diode electronic admittance is developed and each of the above models are based on the measured results.

Intermodulation distortion is measured using the two-tone test. This method, although not conclusively diagnostic for determining communications system real distortion performance, is convenient for both analysis and measurement, and is in widespread use [14], [17], [18].

### 1.3 Thesis Organization

Amplifier nonlinearities and their effects are discussed in Chapter 2; a survey of available methods for distortion reduction is presented and the principle of feedforward correction is also explained. Results and details of the large-signal admittance measurements of IMPATT diodes are contained in Chapter 3. The Volterra series approach to modeling the IMPATT- and feedforward amplifier is developed in Chapter 4;



theoretical IM distortion performance, based on the Volterra series, is presented. Chapter 5 is concerned with the second modelling approach; the nonlinear equivalent circuit is developed and the procedure for numerical solution of the nonlinear differential equation is given. Also, the predicted IM distortion is presented for the second model. In Chapter 6, the experimental feedforward IMPATT amplifier and test bench are described. Further, the measured IM distortion is compared with that predicted by each model. Chapter 7 summarizes the work and discusses conclusions drawn from the results of Chapters 4 to 6. Areas of future desirable research are also identified.





## CHAPTER 2

### IMPATT AMPLIFIER DISTORTION AND FEEDFORWARD CORRECTION

#### 2.1 Synopsis

This chapter provides the technical and historical background for general concepts involved in later chapters. By presenting these preliminary results it is hoped that the rationale for the research will become clear.

The effect of nonlinearities in amplifiers is discussed in general terms in Section 2.2. The types of distortion, both linear and nonlinear, which arise in practical amplifiers are explained. The intermodulation (IM) distortion product, and the intercept point are defined in Section 2.3 as convenient criteria for assessing amplifier nonlinearity. Following a brief review of IMPATT diode operation and of IMPATT-diode amplifiers, the distortion produced by a stable IMPATT-diode reflection amplifier is described in Section 2.4. Section 2.5 contains a literature survey of the available methods for the reduction of the effects of nonlinearities in amplifiers. In Section 2.6 a new technique, feedforward correction or linearization, for the reduction of amplifier distortion is described. The last section summarizes the main ideas presented in this chapter.

#### 2.2 Types of Distortion Produced by Amplifier Nonlinearities

The output signal of an ideal amplifier is an enlarged exact replica of the applied input signal translated in time. Physically, such an ideal linear amplifier cannot be realized since nonlinearities and dispersion are inherent to some degree in all amplifier components [19]. At high frequencies, amplifier nonlinearities, in general, have memory



due to the effect of distributed reactances. Various types of distortion, both nonlinear and linear, occur in an amplifier due to its nonideal characteristics.

Nonlinear distortion is caused by a nonlinear output amplitude- and/or phase variation with input signal level. Nonlinear amplitude (envelope) distortion [19] is shown in Fig. 2.1(a). Here, the output power and gain of the amplifier are dependent on the signal input drive. This nonlinearity causes AM compression since the amplifier will change the depth of AM. In addition, when signals of different frequencies and power levels are applied, such amplitude nonlinearities result in harmonic distortion (generation of second-, third-, or higher harmonics of the applied input signals), intermodulation distortion (generation of spurious signals within the frequency band of the applied signals), and amplitude crossmodulation distortion (transfer of AM from one input signal frequency to another) [20].

Nonlinear phase distortion [19], in which the relative phase shift through the amplifier is a function of the input signal drive, is shown in Fig. 2.1(b). This causes AM-to-PM conversion because the amplifier will introduce a spurious PM on an input AM signal with no definite phase relation between the two types of modulation. Phase nonlinearities also produce frequency-dependent harmonic and intermodulation distortion, and phase crossmodulation distortion (transfer of PM to one carrier from AM on another carrier).

An amplifier introduces linear distortion through the dependence of gain and phase shift on frequency. It is called "linear distortion", which may appear a misnomer, because the gain and phase deviations do not produce new frequencies, but do alter the relative amplitude and phase



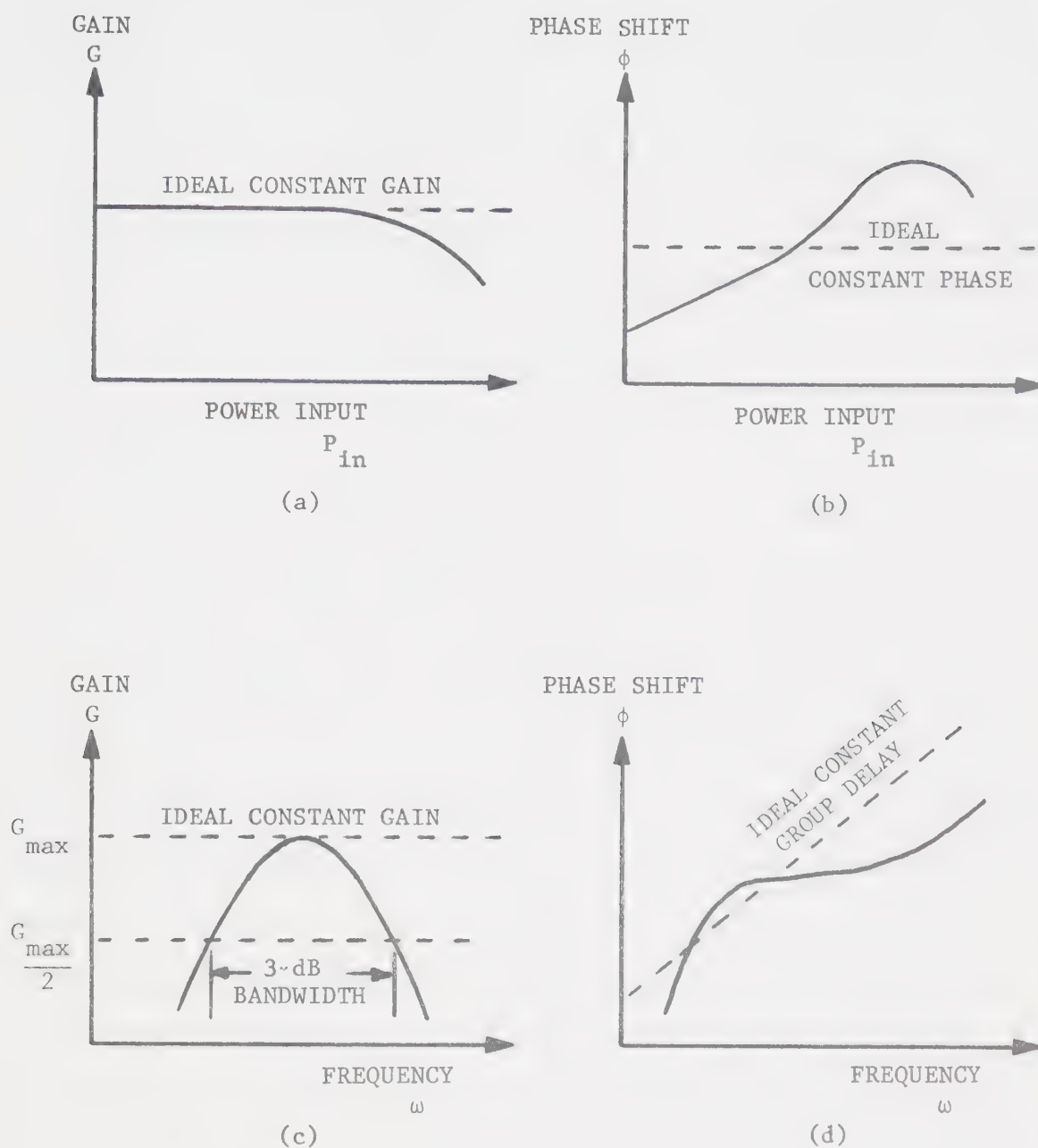


Figure 2.1 Types of amplifier distortion. (a) Nonlinear amplitude (envelope) distortion. (b) Nonlinear phase distortion. (c) Linear amplitude distortion. (d) Linear phase distortion.



shift of the input signals [19]. Linear amplitude distortion and linear phase (or group-delay) distortion are shown in Figs. 2.1(c) and 2.1(d), respectively. Such variations of gain or group delay (defined as  $-d\phi/d\omega$ ) with frequency produce AM-to-PM and PM-to-AM conversion.

All of these effects can be present in an amplifier, to a greater or lesser degree, even with signal levels low enough so that the single-tone behaviour of the amplifier is essentially linear [20].

## 2.3 Evaluation of Amplifier Nonlinearities

### 2.3.1 Intermodulation (IM) Distortion Product

Intermodulation (IM) distortion serves as a convenient measure for specifying the upper limit of dynamic range or the maximum allowable distortion of an amplifier. It also has practical significance in evaluation of amplifiers for multiple carrier systems in which IM performance is important. A recent panel session [17] came to the conclusion that the only truly reliable signal to test for IM distortion in communications systems is the real-life signal. However, for the purpose of device characterization, multiple-tone tests normally suffice [14].

The information gained from a two-tone test is almost as meaningful as from a three- or higher-tone test since the data breaks down in an actual system under real-signal load. Hence for simplicity, balanced two-tone tests will be used for nonlinearity testing [14], [18]. To be more specific, the ratio of IM distortion to the desired output, when two equal magnitude signals are applied in the passband of the amplifier is a measure of its linearity.

The two-tone test signal allows the analysis of amplifier nonlinearities to be treated simply. Consider a test signal consisting of





a pair of equal-level tones, at frequencies  $f_1$  and  $f_2$ , whose frequency difference  $\Delta f$  is small compared with their individual frequencies.

When these two frequencies pass through the nonlinear device, additional frequencies are produced. The output will contain components at adjacent frequencies

$$f_n = |pf_2 \pm qf_1|, \quad p, q = 0, 1, 2, 3, \dots \quad (2.1)$$

where  $n = p+q$  is called the order of the distortion product. The various IM products will have different effects in different systems. For example, even-order products, such as the second-order product ( $f_2-f_1$ ), cannot appear in narrowband systems unless the ratio of the highest frequency ( $f_2$ ) to the lowest frequency ( $f_1$ ) is at least two to one. This case is excluded for  $\Delta f \ll f_1, f_2$ . Odd-order products appear in the passband regardless of the frequency ratio. Consequently, third-, fifth-, and other higher odd-order products present the greatest problem in narrowband amplifiers such as IMPATT-diode amplifiers. The third- and fifth-order products are especially important because they lie nearest the original frequencies and usually dominate the distortion. For  $f_2 > f_1$ , third-order distortion products appear at  $2f_2-f_1$  (upper) and  $2f_1-f_2$  (lower) while fifth-order distortion products appear at  $3f_2-2f_1$  (upper) and  $3f_1-2f_2$  (lower).

Third-order distortion,  $IM_3$ , may be defined [21] as the ratio of the output power at the third-order product ( $2f_2-f_1$ ) or ( $2f_1-f_2$ ), to the output power at one of the fundamental signals  $f_1$  or  $f_2$ :

$$IM_3(\text{dB}) = 10 \log \left| \frac{\text{Amplitude of third-order distortion product in output}}{\text{Amplitude of fundamental signal in output}} \right|^2. \quad (2.2)$$



Similarly, the fifth-order distortion,  $IM_5$ , may be defined as

$$IM_5(dB) = 10 \log \left| \frac{\text{Amplitude of fifth-order distortion product in output}}{\text{Amplitude of fundamental signal in output}} \right|^2. \quad (2.3)$$

The quantities  $IM_3$  and  $IM_5$  will be used as gauges for amplifier non-linearity.

### 2.3.2 Intercept Points

For comparison of amplifier distortion performance, a common figure-of-merit is the  $n^{th}$ -order intercept point,  $P_n$ . In a well-behaved amplifier operating in the small-signal region, the linear output component has unity slope, and each  $n^{th}$ -order output has slope  $n$ , when output power in dB is plotted against input power (for each tone) in dB. The output power at which the tangent to the linear response intercepts the  $n^{th}$ -order response, both drawn in the small-signal region, is called the  $n^{th}$ -order intercept  $P_n$  [14]. The larger the value of  $P_n$ , the less important the  $n^{th}$ -order nonlinear response is for the amplifier, relative to the linear response. Hence the higher the intercept value, the more linear the amplifier.

## 2.4 Some Properties of IMPATT Diodes and of Stable IMPATT Amplifiers

### 2.4.1 Small-Signal IMPATT-Diode Characteristics

An IMPATT diode is a two-terminal device which displays negative resistance in the microwave frequency band. The microwave properties of IMPATT diodes have been discussed extensively in the literature; references [22] to [25], amongst others, give rigorous small-signal analyses of the device; reference [26] provides a simpler treatment along with basic applications. Consideration of the diode proposed by Read [22]



illustrates the processes which lead to negative resistance.

The Read diode, Fig. 2.2(b), consists of a narrow avalanche region at one end of a relatively high resistance region of width  $W_D$  termed the drift space. In normal operation, the diode is reverse-biased at the dc breakdown voltage  $V_B$ , given in Fig. 2.2(a). Application of a small sinusoidal RF voltage  $v_{RF}(t)$ , as in Fig. 2.2(d), causes avalanche multiplication to occur in the avalanche region when the total diode voltage  $|V_B + v_{RF}(t)|$  exceeds  $|V_B|$ . The resulting excess charge builds up slowly at first and peaks sharply when  $v_{RF}(t)$  is zero as in Fig. 2.2(e). The avalanche current,  $i_{inj}(t)$ , injected into the drift region thus lags  $v_{RF}(t)$  by  $\pi/2$  radians. The direction of the electric field  $E(x)$ , Fig. 2.2(c), is such that the injected charge, holes in this case, drifts to the right at saturated velocity,  $v_{sat}$ , in a transit time  $\tau = W_D/v_{sat}$ . The injected charge traversing the drift region in a constant electric field induces a current  $i_{ext}(t)$ , Fig. 2.2(f), in the external circuit. Depending on the frequency  $\omega$ , the combined delay of the avalanche process and the transit angle  $\omega\tau$  across the drift space together cause the external RF current to lag the applied RF voltage by greater than  $\pi/2$  radians. Above the avalanche frequency,  $\omega_A$ , the diode supplies RF energy to the external circuit and the diode displays a negative resistance; below  $\omega_A$ , the combined delay is less than  $\pi/2$  radians and the diode has a positive resistance.

For normal IMPATT operation above  $\omega_A$ , Gilden and Hines [23] found the diode electronic admittance (admittance of the active part of the diode alone),  $Y_e$ , to be

$$Y_e(\omega, I_{dc}) = G_e(\omega, I_{dc}) + jB_e(\omega, I_{dc}) \quad (2.4)$$





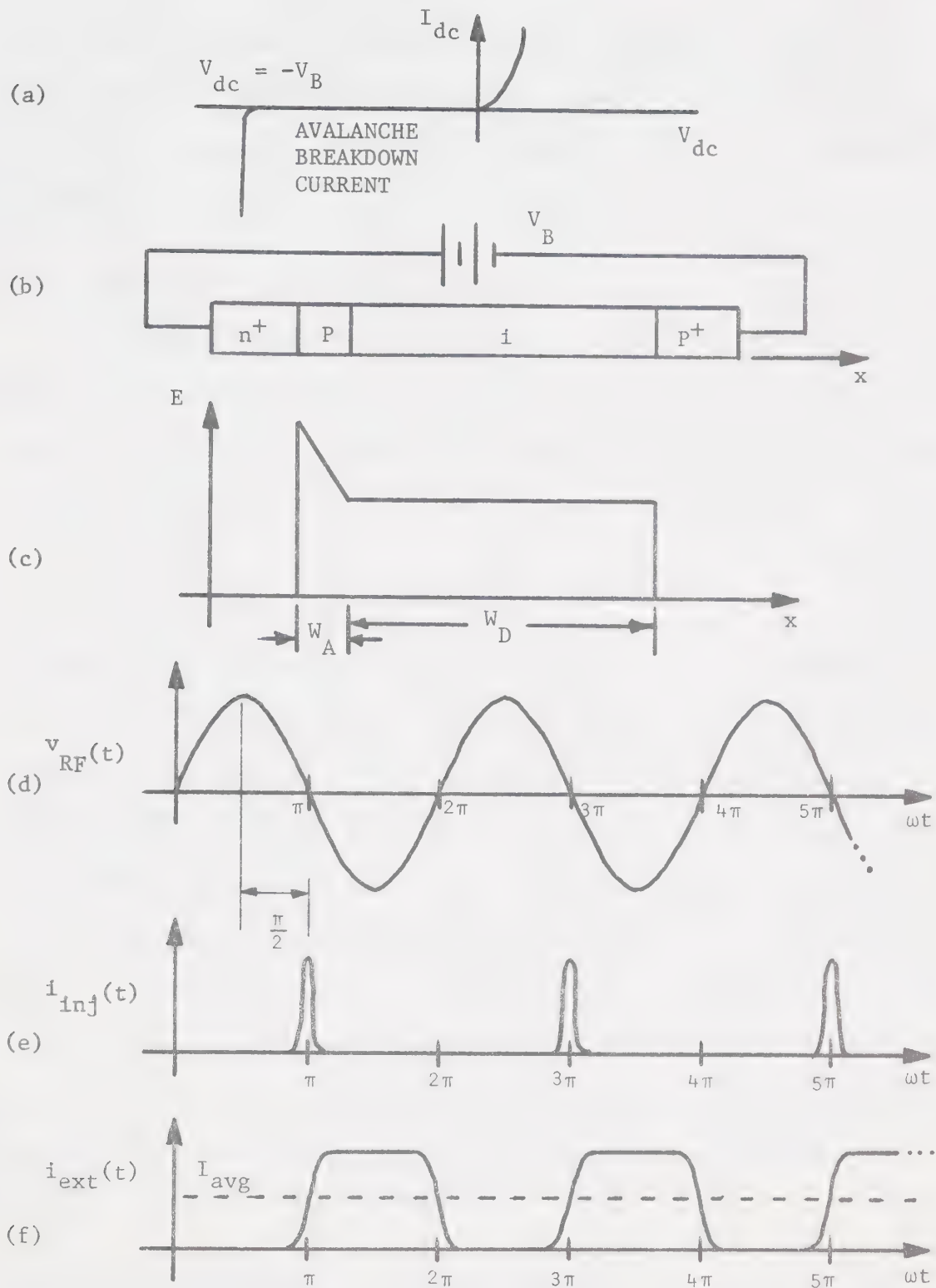


Figure 2.2 IMPATT diode operation. (a) Terminal I-V characteristic of a PN junction. (b) Read diode structure [22]. (c) Electric field profile. (d) Applied RF voltage. (e) Avalanche current or current injected into intrinsic region. (f) Induced external current.



where  $G_e$  is a negative conductance,  $j$  is  $\sqrt{-1}$ , and  $B_e$  is a capacitive susceptance. In the small-signal model,  $G_e$  and  $B_e$  vary with the bias current  $I_{dc}$  (assumed constant) and frequency  $\omega$ , but are not dependent on the RF signal amplitude.

#### 2.4.2 Large-Signal IMPATT-Diode Characteristics

The small-signal Read model cannot explain the nonlinear effects which occur for high RF drive levels. The inherent device nonlinearities cause the electronic admittance to be dependent on the RF voltage magnitude  $V_{RF}$  as well as on frequency and on bias current so that

$$Y_e(\omega, I_{dc}, V_{RF}) = G_e(\omega, I_{dc}, V_{RF}) + jB_e(\omega, I_{dc}, V_{RF}) \quad . \quad (2.5)$$

The large-signal electronic admittance can be predicted by computer solution of the Poisson's and continuity equations for holes and electrons with the appropriate boundary conditions. Typical results of such studies on X-band diodes [27]-[30] are summarized in the curves for  $Y_e(\omega, \text{constant } I_{dc}, V_{RF})$  in Fig. 2.3. It can be seen that for constant  $\omega$ ,  $|-G_e|$  decreases and  $|B_e|$  increases with increasing  $V_{RF}$ . Increasing  $I_{dc}$  tends to shift the curves  $Y_e$  to the left, to the region of larger negative electronic conductance. In Fig. 2.3,  $-Y_c$  is a typical locus of the negative of the circuit admittance at the diode electronic admittance terminals. It will be used in Section 2.4.4 to explain amplifier behaviour.

#### 2.4.3 Stable IMPATT-Diode Reflection Amplifier

IMPATT diodes, because of their broadband negative resistance, can be used as the active device in microwave reflection amplifiers. The configuration of a circulator-coupled, negative-resistance reflection



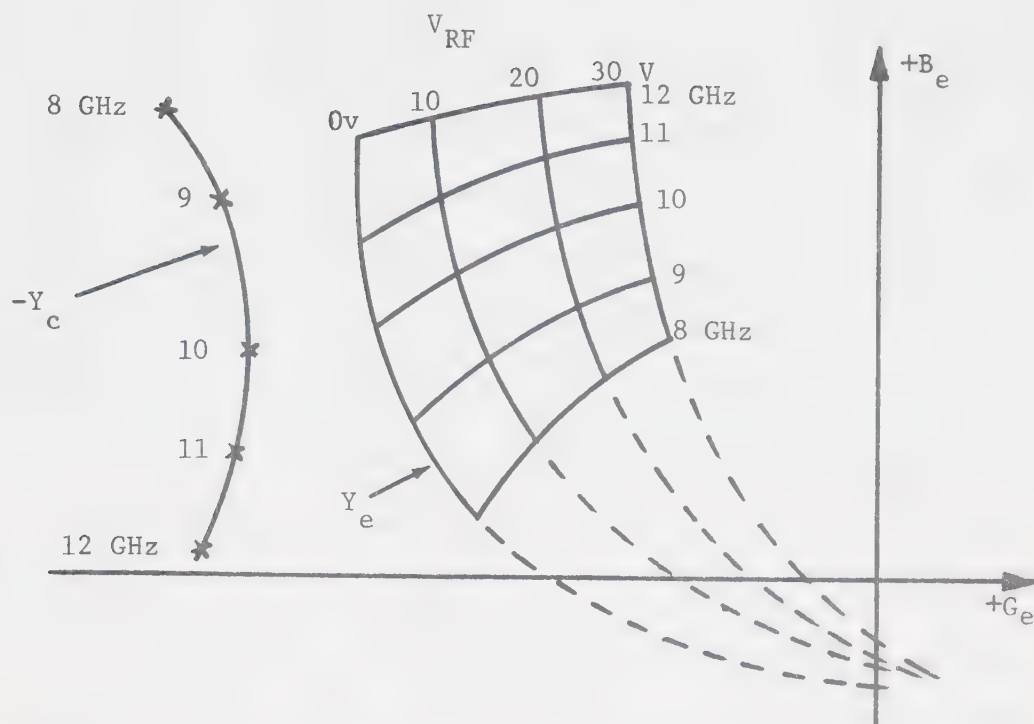


Figure 2.3 Typical IMPATT-diode large-signal electronic admittance for a given dc bias current [30].

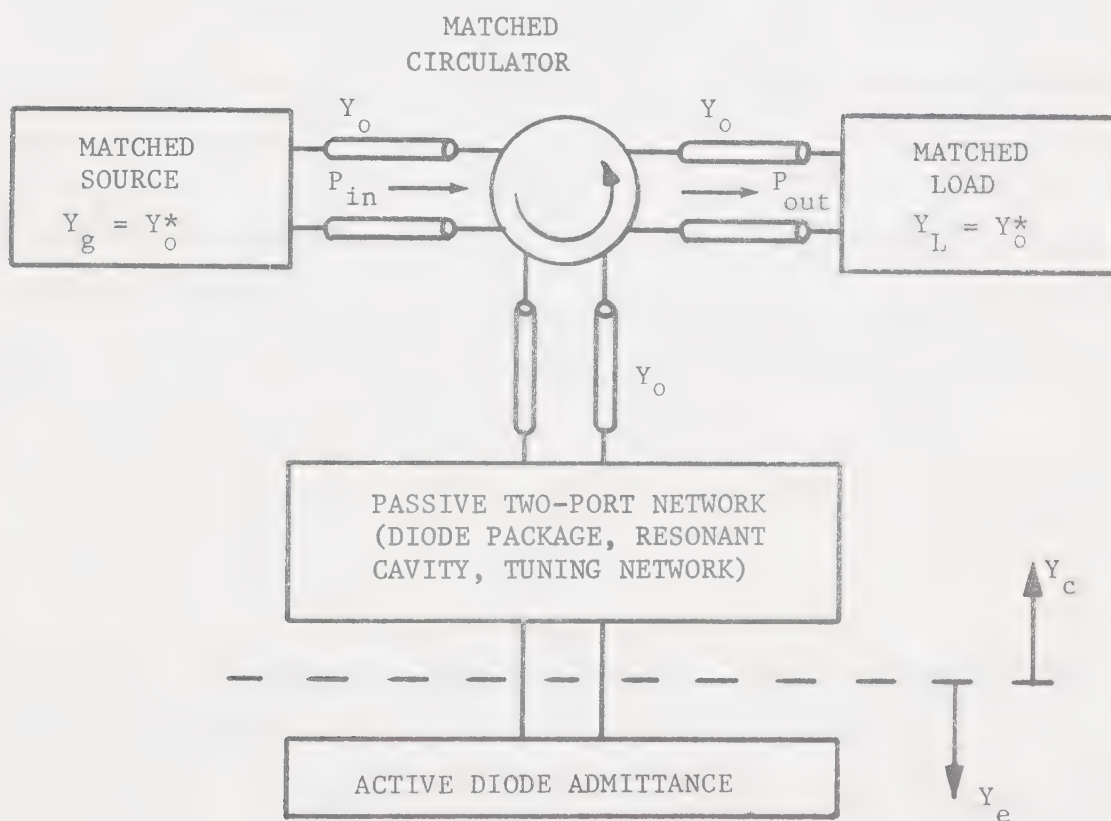


Figure 2.4 Typical IMPATT-diode reflection amplifier.



amplifier is shown in Fig. 2.4. The circulator is required to separate the input signal, incident on the diode, from the amplified signal, reflected from the diode. The passive two-port network in Fig. 2.4 includes the inactive diode admittance, the package parasitics, an inductive resonator to tune out the diode- and package capacitive reactance at the amplifier centre frequency, and an impedance transformer to match the transmission line admittance,  $Y_0$ , to the active diode admittance. To increase the amplifier bandwidth, more resonating sections may be added, having the same centre frequency but different reactance slopes with frequency. Each tuning resonator requires an impedance transformer to match the input impedance of the next resonator. In coaxial systems, the tuning resonators are usually series sections of coaxial 50- $\Omega$  transmission line; the impedance inverters are usually quarter-wavelength transformers of lower characteristic impedance. Hines [3] presents a simple analysis of a single-tuned amplifier together with its single-frequency nonlinear behaviour.

#### 2.4.4 Nonlinear Characteristics of Stable IMPATT Amplifiers

A qualitative explanation of the nonlinear behaviour of IMPATT amplifiers is given by Laton and Haddad [31] based on the device-circuit diagram, Fig. 2.3, and the equation for amplifier power gain:

$$|\Gamma|^2 = \left| \frac{Y_c - Y_e^*}{Y_c + Y_e} \right|^2 = \left| \frac{-(-Y_c) - Y_e^*}{Y_e - (-Y_c)} \right|^2 \quad (2.6)$$

where  $Y_c$  and  $Y_e$  have been previously defined,  $\Gamma$  is the voltage wave reflection coefficient, and  $*$  denotes complex conjugate.

Figure 2.5 presents the phase shift, gain, saturation and bandwidth properties of a typical amplifier. Laton and Haddad [31] relate





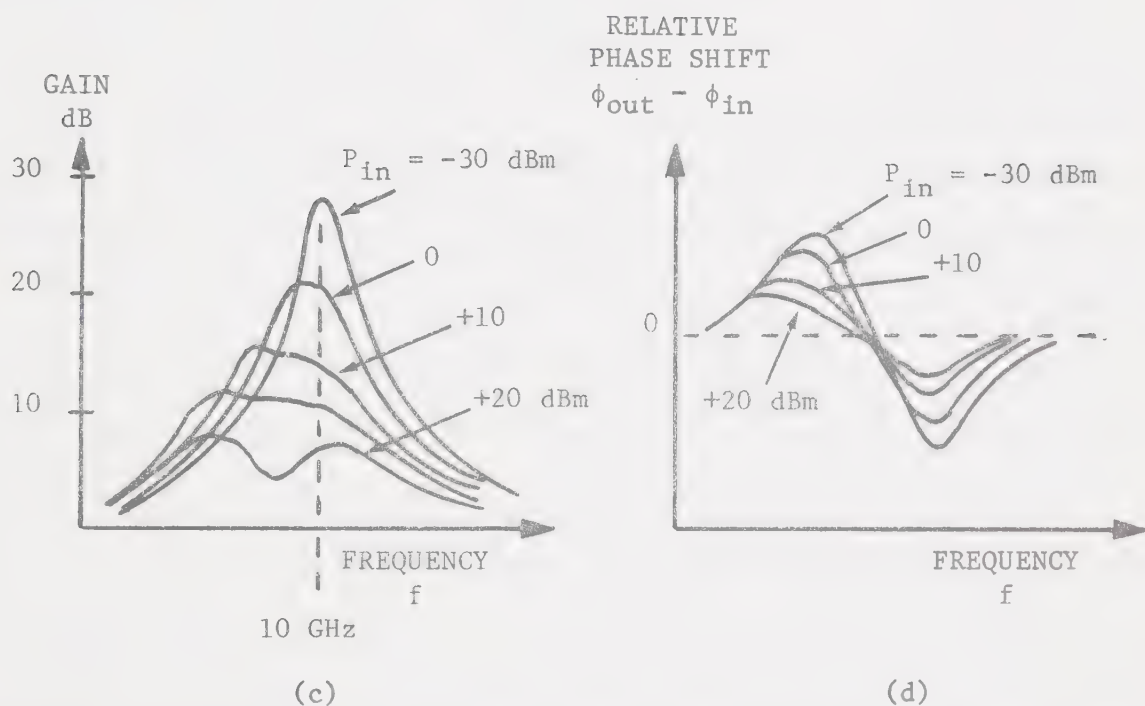
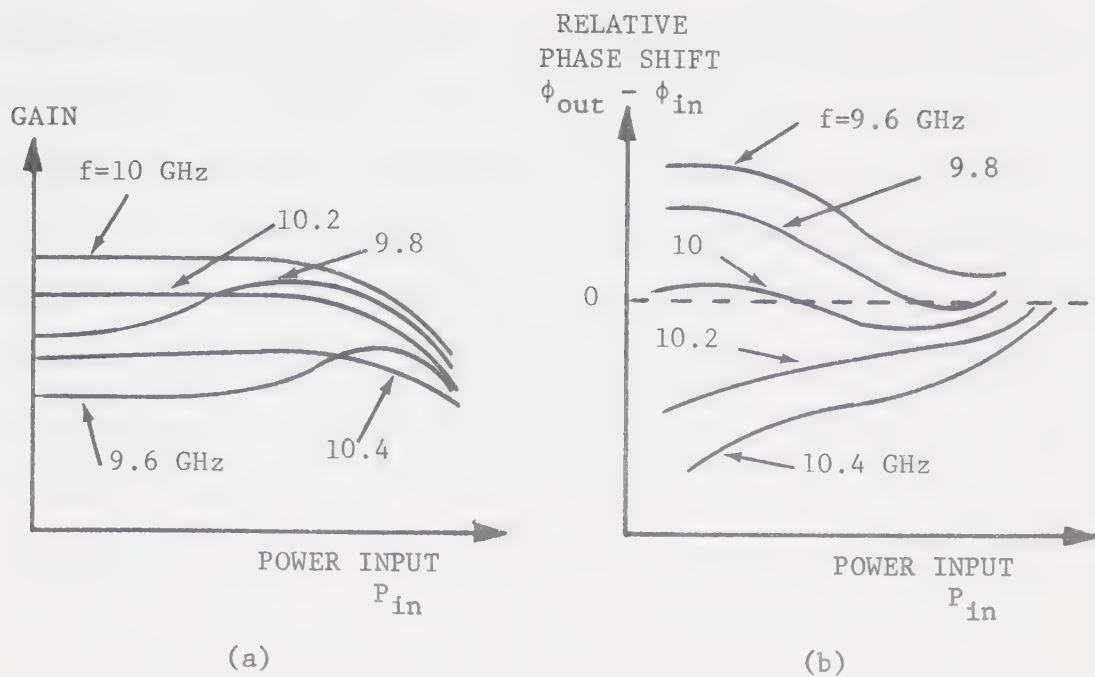


Figure 2.5 Typical stable IMPATT-diode reflection amplifier distortion [12], [31]. (a) Nonlinear amplitude distortion. (b) Nonlinear phase distortion. (c) Linear amplitude distortion. (d) Linear phase distortion.



the variation of gain with frequency and RF drive level to the distance between circuit (negative) and device operating points in Fig. 2.3, according to the inverse relationship given in Eqn. (2.6). Their discussion is lengthy and will not be repeated here. Kuno [12] obtains results similar to Fig. 2.5. In summary, as the input signal level increases, the amplifier gain decreases, the bandwidth increases, and the centre frequency shifts to the lower side of the passband. The downward shift of the centre frequency may result in gain expansion with increasing input drive level at the lower half of the passband for a high-gain, narrowband amplifier.

Trew *et al.* [32] extend the analysis to explain a low-frequency dominance mechanism in which low-frequency signals are amplified more than high-frequency signals depending on their location relative to the amplifier passband. The authors also found that increasing the frequency separation between the fundamental signals resulted in less interaction between them such that there were fewer intermodulation products generated.

Other nonlinear effects occur at high signal levels. For example: stability problems may arise since negative resistance can be induced under large-signal conditions at a subharmonic below the avalanche frequency [33]; pronounced decrease in gain can occur near midband as in Fig. 2.5(c) [34]; or spurious "parametric" oscillations may appear when the signal excitation exceeds a critical value that is often below the power-saturation point [35]. For purposes of analysis, it is assumed in this thesis that amplifier tuning conditions and signal levels are such that these nonlinear effects do not occur.

The nonlinear characteristics of IMPATT-diode microwave amplifiers give rise to the multiple distortion mechanisms outlined at the beginning



of this chapter. Of particular importance for AM communications systems is the level of IM distortion in the transmitter power amplifier. Several authors have reported [32] typical measured third-order IM products in the range 10-20 dB for a stable X-band IMPATT amplifier operating in the large-signal region. Such high IM products do not meet the required specifications for most SSB-AM systems. For instance, a typical requirement in microwave AM systems is to have a transmitter which can deliver 1 W of output power with all the IM distortion products down at least 50 dB from the carrier level [7]. An effective technique must be used to reduce nonlinear distortion produced in an IMPATT amplifier to stringent system specifications.

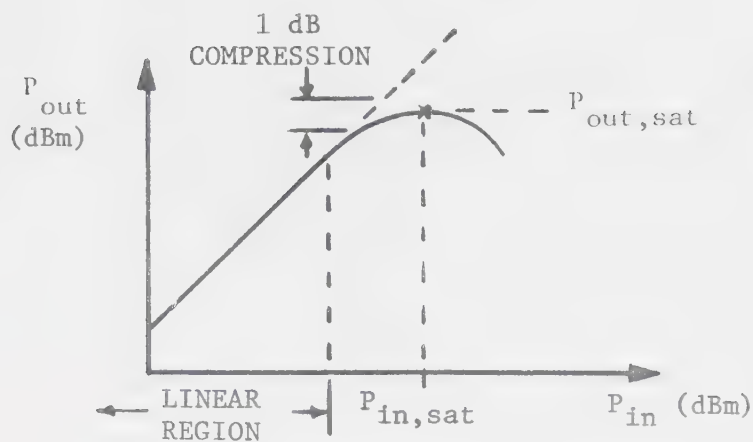
## 2.5 Survey of Amplifier Linearization Techniques

The simplest and most obvious technique, termed "back-off" [20], [36], to reduce nonlinear distortion to a tolerable level is to operate at power levels well below output saturation, as in Fig. 2.6(a). The effects of nonlinearities decrease as the input signal level is reduced. In fact, in a well-behaved amplifier  $n^{\text{th}}$ -order distortion products vary at  $n$  times the rate of the input signals; i.e.,  $n^{\text{th}}$ -order distortion products are lowered by  $n$  dB for every dB of input power reduction [37]. The amount of "back-off" represents a corresponding reduction in amplifier efficiency (dc to RF) since dc operating conditions must be maintained at the original levels. Hence, this scheme is self-defeating.

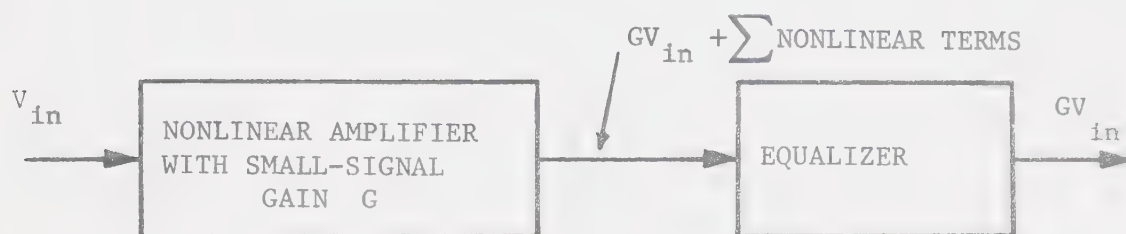
Equalization is another method of reducing nonlinear distortion [38]-[40]. The nonlinear characteristics of the amplifier are compensated by cascading it with another two-port device having the inverse nonlinear transfer function of the amplifier, Fig. 2.6(b). For practical purposes, it is very difficult to construct a device having the desired inverse



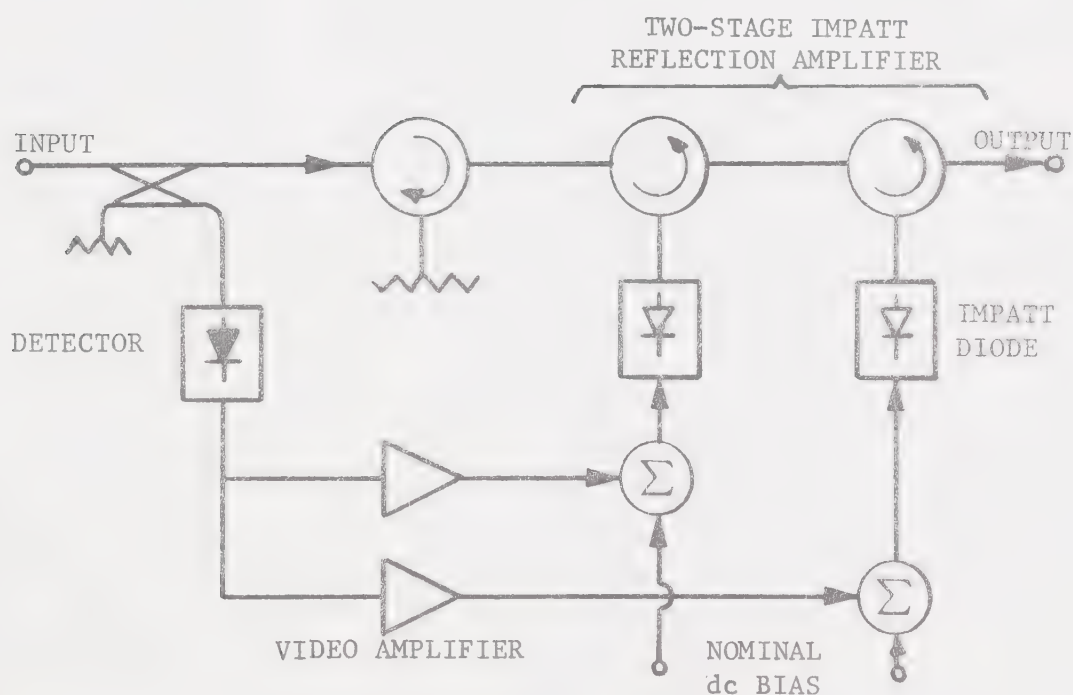




(a)



(b)



(c)

Figure 2.6 Amplifier linearization techniques. (a) Back-off of amplifier output power. (b) Equalization of amplifier nonlinearities. (c) Bias-current compensation of IMPATT amplifier [41].



nonlinear transfer characteristic, at least over the wide dynamic range common to power amplifiers. Furthermore, the device must not change the spectral content of the amplifier input signal. This is usually an impossible constraint.

In 1973 Komizo *et al.* [41] reported on the improvement in nonlinear distortion of an IMPATT amplifier using a diode bias current compensation technique. The diode electronic conductance increases and susceptance decreases with an increase in bias current, with the inverse occurring for an increase in RF signal level. As a result, controlling the bias current according to the RF input level improves the linearity of the IMPATT amplifier. A block diagram of this technique appears in Fig. 2.6(c). The directional coupler samples the input signal and the signal envelope is detected by a diode detector. Video amplifiers amplify the detected waveform to give ac bias currents which are superimposed on the fixed dc bias current. For a 13-GHz, two-stage stable IMPATT amplifier with 21-dBm output level and 11-dB gain, Komizo *et al.* [41] report a 2-dB improvement in input signal level to reach 1-dB compression (see Figure 2.6(a)) and a 10- to 20-dB improvement of the third-order IM product. However, the diodes must operate at a higher dc bias level than normal to allow for ac bias current swings; typically, the diodes must dissipate 1.1 W of power more than if operated at the recommended dc bias point. Also, since IMPATT diodes are current-limited devices, transients in the bias current (although limited by the 20-MHz passband of the video amplifier) may cause diode burnout or a shorter operating life.

The most conventional technique used for amplifier linearization is negative feedback. Negative feedback was analysed in the classic text by Bode [42]. In principle, the application of feedback to an amplifier



with gain  $\mu$  (Fig. 2.7(a)) involves subtracting a portion of the output signal from the input signal through a shaping feedback network with loss  $\beta$ . The overall transfer function of the amplifier is then given by

$$\frac{V_{\text{out}}}{V_{\text{in}}} = \frac{\mu}{1+\mu\beta} \quad (2.7)$$

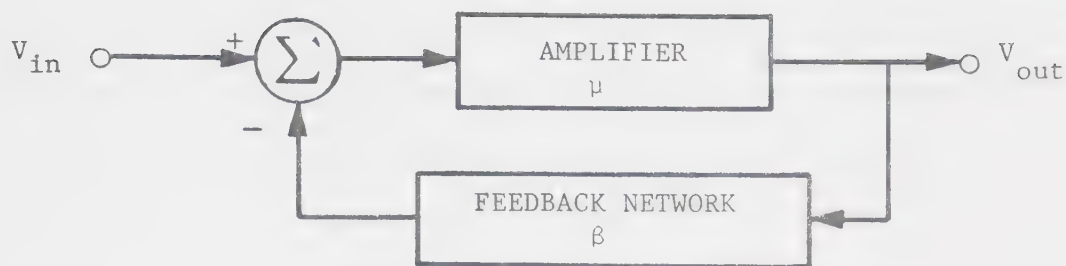
By shaping the feedback network frequency response  $\beta$ , the sensitivity of the closed-loop system to variations in amplifier gain  $\mu$  is decreased, the transient response is controlled, and the steady-state error is reduced [43]. IM distortion performance is also improved. In fact,  $n^{\text{th}}$ -order distortion products introduced by a nonlinear amplifier,  $\mu$ , are reduced by the factor  $(1+\mu_n\beta_n)$ , where  $\mu_n, \beta_n$  are  $\mu$  and  $\beta$ , respectively, evaluated at the frequency of the  $n^{\text{th}}$ -order product [44], [45]. This reduction can be quite significant for amplifiers with large open-loop gain; i.e.,  $|\mu_n\beta_n| > 1$ .

However, there is a price to pay for the advantages feedback linearization has to offer. Primarily these costs are a reduction in gain, and potential instability. The gain of the amplifier is reduced the same amount as the distortion products, by the factor  $(1+\mu\beta)$ . If voltage gain is required, this is a severe disadvantage.<sup>†</sup> Secondly, in a practical amplifier there is a limit to the amount distortion products can be reduced because of gain-limiting [19]. In no case is it possible to obtain loop gains  $(\mu\beta)$  greater than the difference between the total gain  $\mu$  and the insertion gain  $1/\beta$ .

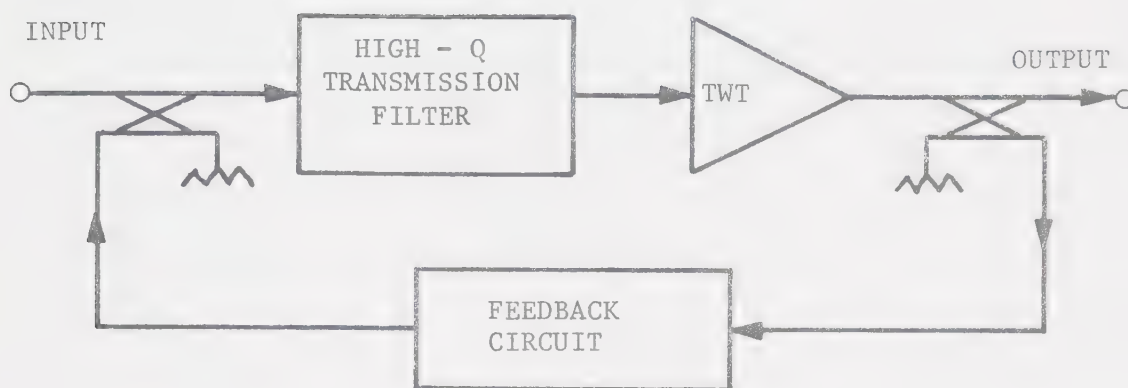
---

<sup>†</sup> It is to be noted that Eqn. (2.7) is the input-output voltage gain. The closed-loop amplifier, in general, has widely different input and output impedance levels and consequently substantial power gain.

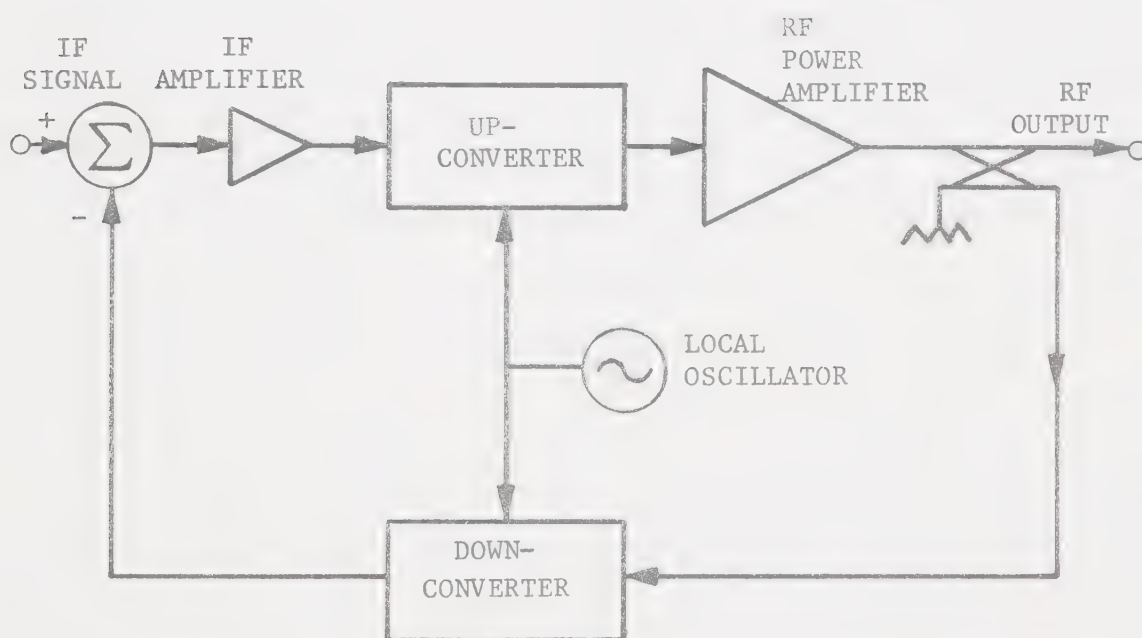




(a)



(b)



(c)

Figure 2.7 Feedback-linearized amplifiers. (a) Basic feedback amplifier. (b) Microwave feedback amplifier [46]. (c) Siemens GmbH. 400-MHz feedback amplifier [48].





Broadband feedback amplifiers are usually stability-limited. Stability considerations dictate that the group delay of the amplifier and feedback path must not introduce a significantly large phase shift at any frequency within the passband of the amplifier. To ensure stability, phase- and gain margins must be specified, thereby limiting the available in-band feedback.

At microwave frequencies, difficulties in implementing feedback linearization arise since underlying assumptions are invalid. The instability problem results from the "time-smearing" process of comparing the delayed amplifier output with the input signal. For the resulting error signal to be meaningful, the two events must be as closely spaced in time as possible. At low frequencies, adequate simultaneity between the input and output is relatively easy to achieve and instability can be avoided. However, at higher frequencies the propagation time around the feedback loop introduces excess phase shift since the path length becomes an appreciable fraction of a wavelength [42]. Thus, at microwave frequencies negative feedback generally cannot be used. Under certain conditions the signal fed back can have the correct phase relationship for negative feedback, but this will work only over a very narrow bandwidth.

Several reports on the use of negative feedback narrowband linearization of TWT amplifiers have appeared in the literature [46]-[48]. Rosen and Owens [46], reduced third-order IM distortion by 13 dB in a narrow 1-MHz bandwidth, 3-GHz TWT feedback amplifier. A block diagram of their system is shown in Fig. 2.7(b). The high-Q transmission



filter can be placed in either the main arm or feedback path. This filter is required to prevent instability due to the large bandwidth of the TWT and the group delay of the feedback loop. In a similar study by Bava *et al.* [47], the TWT amplifier 1-dB gain compression point was extended by about 3 dB; third-order IM products were reduced by 3 dB over a 20-MHz bandwidth at 6 GHz and 15-dB gain.

Siemens Gmbh has developed a 120 channel, 400-MHz system [48] employing negative feedback in a modified form. In this system, the feedback loop surrounds the entire superheterodyning transmitter, not just the power amplifier, as in Fig. 2.7(c). The increase in gain to compensate for the gain reduction due to feedback is provided by the IF amplifier. This low-frequency amplifier can compensate over a broader band than the high-frequency output amplifier. Nevertheless, the system is still relatively narrowband.

It appears then that negative feedback is not a realistic means of linearizing a broadband microwave amplifier. The next section discusses a method which is currently attracting a great deal of attention in this regard.

## 2.6 Principles of Feedforward Correction

Feedforward correction, invented by H.S. Black [4] in 1924, can provide a high degree of amplifier linearization at microwave frequencies, without the instability problems and loss of gain associated with feedback control. References [5], [36], [49]–[51] are introductory papers on feedforward technology.

Figure 2.8(a) is a schematic diagram of Black's patented amplifier [5]. The signal-adding boxes are biconjugate devices (e.g., three-winding



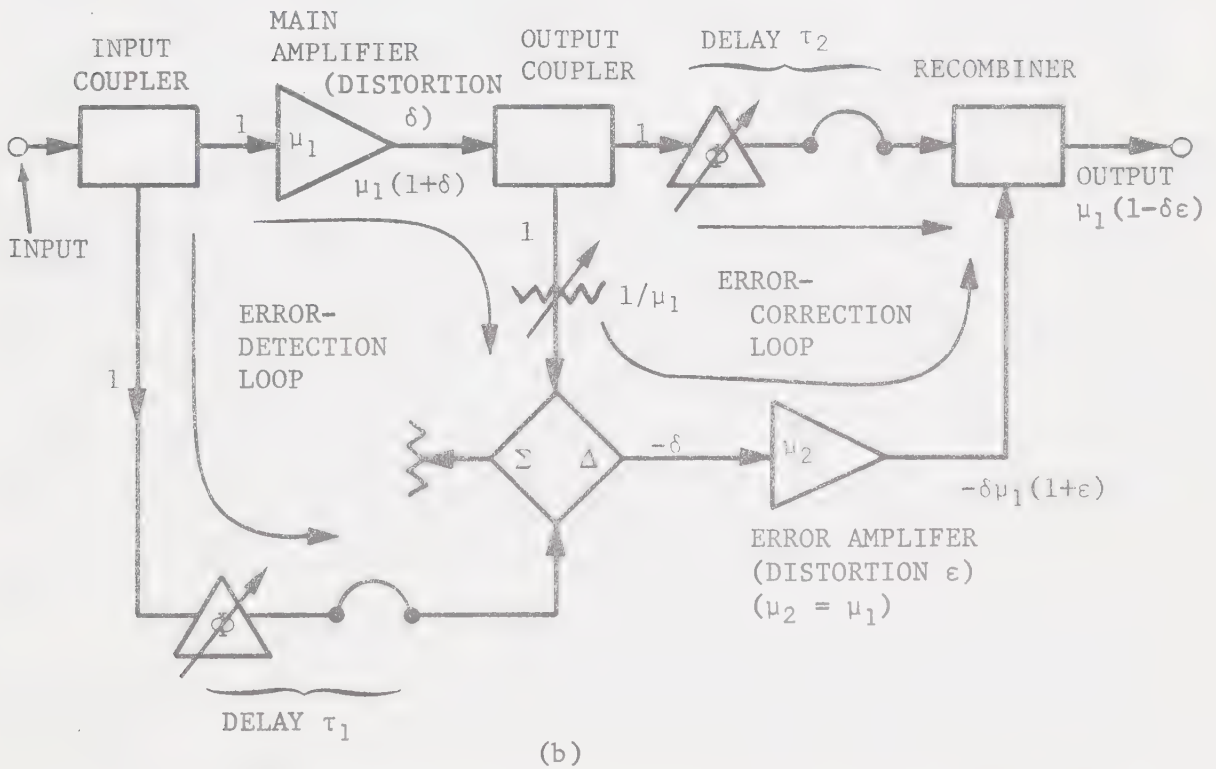
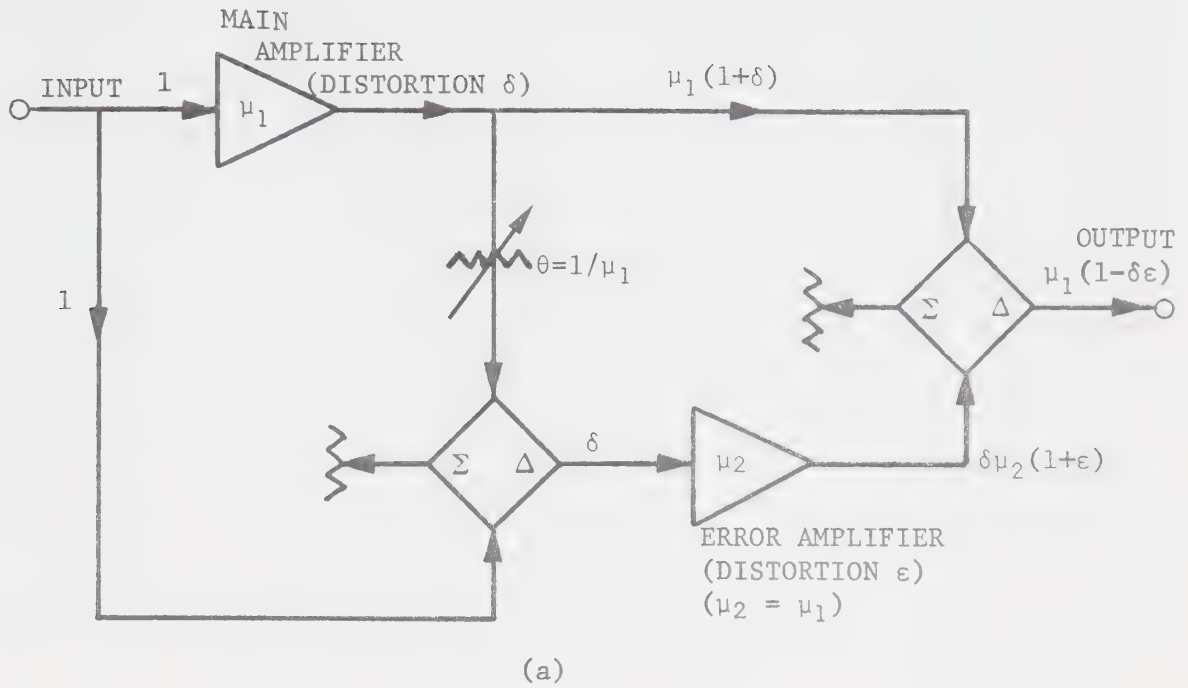


Figure 2.8 Feedforward-corrected amplifiers. (a) Black's feedforward amplifier [4],[5]. (b) Seidel's microwave feedforward amplifier [55],[56].





transformers or magic tees) in which transmission occurs from any input to adjacent outputs but not to the opposite output. The upper amplifier  $\mu_1$  is the main amplifier; i.e., the amplifier to be linearized. The lower amplifier  $\mu_2$  is the error amplifier. Nominally, the gain  $\mu_2$  is equal to the gain  $\mu_1$ . The quantities  $\delta$  and  $\epsilon$  represent first-order deviations from gain linearity of the main amplifier and of the error amplifier, respectively. The amplified signal (containing first-order distortion terms) in the main path is sampled, attenuated by  $\Theta = 1/\mu_1$  to bring it back to the level of the input signal, and balanced against the undistorted input signal to provide an error signal  $\delta$  at the input of the error amplifier. The output of the error amplifier is subtracted from the main amplifier output to produce a signal  $\mu_1 (1 - \delta\epsilon)$  at the output terminal. Hence the output has only second-order deviations from the gain  $\mu_1$  required, and linearity has been improved.

The advantages of this scheme are twofold. First, the error signal at the input of amplifier  $\mu_2$  is much smaller than the signal at the main amplifier input. This allows the error amplifier to operate in its linear region, well below saturation, and to contribute very little distortion itself. Secondly, the two amplifier system provides increased reliability since, if the main amplifier fails, transmission is uninterrupted through the second amplifier (but distortion is not reduced).

Black's amplifier, because of delicate balancing requirements between amplifier gain, adding circuits, and attenuator loss, operated only over a narrow frequency range. Several other investigations of feed-forward control followed that by Black. These were notably van Zelst's [52] study on tube amplifiers and that of Golembeski *et al.* [53] on transistor amplifiers. Neither of these papers significantly advanced



feedforward technology since the authors [52], [53] regarded it as a redundancy technique rather than as an error-reduction scheme.

Recently feedforward correction as a method for amplifier linearization came to the attention of Seidel, Beurrier and Friedman [54] with Seidel subsequently publishing three papers on this subject [51], [55], [56]. Seidel *et al.* [54] recognized the important role that time delay plays in error-reduction schemes as explained in Section 2.5. A block diagram of their basic system is shown in Fig. 2.8(b). The amplifiers  $\mu_1$  and  $\mu_2$  have group delays  $\tau_1$  and  $\tau_2$  associated with them, respectively. Consequently, delay lines having corresponding time delays have been inserted in the main and secondary arms parallel to the amplifiers. The operation of the feedforward amplifier of Fig. 2.8(b) is the same as Black's original amplifier, however the time delay effects, so important at high frequencies, have effectively been accounted for.

The advantages of feedforward correction over feedback control are based on the fact that feedforward linearization recognizes time delay and that error reduction is achieved by time synchronization of the main and error paths. The ensuing advantages are [56], [57] listed.

1) The feedforward amplifier is inherently unconditionally stable, since all signal comparison is done in a forward sequence.

2) The feedforward amplifier has no regenerative (backward) paths so that arbitrarily low distortion can be achieved (in theory) by using multiple feedforward loops;<sup>†</sup> i.e., treating the amplifier of Fig. 2.8(b)

---

<sup>†</sup> The term "feedforward loop" denotes a circuit arrangement of two parallel branches through which signals propagate towards a signal-combining element.



as a main amplifier and providing feedforward correction around it, and so on. In practice, however, the input power must be split between the main and reference path at each stage of the nested amplifier. As a result, the deteriorating signal-to-noise ratio in the reference paths sets a practical upper limit on the number of stages.

3) Amplifier gain is not substantially reduced since the error reduction is an additive process.

4) Gain-bandwidth is conserved within the band of interest since device speed is only that required for the bandwidth of the information signal.

5) Feedforward amplifier gain and distortion reduction are independent quantities.

6) Under normal operation the error amplifier need only handle the small error signals; hence, it can be a low-power, low-noise amplifier. For a well-adjusted feedforward amplifier, the overall noise figure is the noise figure of the error amplifier in dB plus the attenuation in dB of the signal between the input to the input coupler and the input to the error amplifier [56], [57]. Essentially, the feedforward amplifier has the power-handling capability of the main amplifier, and the noise figure (usually low) of the error amplifier. Use of a high-power error amplifier compromises the noise figure but provides a fail-safe redundancy scheme.

There are four main disadvantages of feedforward correction which have to be considered.

1) The feedforward amplifier circuit is complex, requiring a second amplifier and two delay lines. Thus system cost is increased.

2) Drift in device characteristics causes changes in loop balance and error correction capability to occur.



3) For significant distortion reduction, the balance in the error-correction loop must be near the precise value.

4) Some of the main amplifier power is lost in the output coupler and recombiner.

Through feasibility studies in the VHF and 4-GHz common carrier bands, Seidel and his associates have proved that these difficulties can be overcome. Their work on a 30-MHz, 40-W amplifier and a 75-MHz, 10-W amplifier showed that a dynamic range of 104 dB could be obtained by feedforward correction [54]. Seidel obtained a 42-dB improvement in the third-order IM product of an L-4 coaxial system 20-MHz amplifier [55]. Finally, single-stage feedforward correction applied to a 4-GHz TWT resulted in a 38-dB reduction in third-order distortion over a 20-MHz channel [56]. In the latter experiment, balance of the error-correction loop, see Fig. 2.8(b), with time was maintained through the use of auxiliary controls. The precision of balance of the error-detection loop, with respect to the reference signal and the coherent portion of the main amplifier output signal, does not affect the portion of the error signal composed of IM distortion and noncoherent thermal noise. It is the balance of the error-correction loop which is critical in cancelling the distortion from the output. For 40-dB reduction in distortion, the gain imbalance of this loop must be  $\leq 0.08$  dB, or the phase imbalance must be  $\leq 0.6$  degrees, or both may be present to a lesser extent. Adaptive control maintained this precision of balance.

Bennett and Clements [57] discussed the concept of feedforward correction and listed the following set of design criteria based upon the above observations:

1) For the overall noise figure to be close to that of the error amplifier, the input coupler and comparator must not attenuate the reference signal appreciably.





2) Feedforward amplifier gain is reduced by the coupling factor of the input coupler. Gain-reduction will be significant for optimum low-noise performance given by 1). However, output power level, in general, is more important than amplifier gain, so overall gain loss due to the choice of input coupler is less important than loss of power due to both output coupler and recombiner. The output coupler and recombiner coupling ratios should be chosen to attenuate only slightly the main amplifier output signal whilst allowing the error amplifier to operate at small power levels.

3) The performance of the amplifiers and other required components need only be specified over the frequency range of interest.

As a practical example, Bennett and Clements [57] constructed a 9-GHz feedforward amplifier using two TWTs. Intermodulation products were reduced by more than 20 dB over a 100-MHz bandwidth without the use of special adaptive control for loop balance.

In assembling these working systems, Seidel *et al.* [54] and other independent researchers [57] showed that feedforward correction is a feasible technique for reduction of amplifier distortion. Indeed, it was used to linearize a 4-GHz satellite TWT [58] and a 1-MHz operational amplifier [59]. Meyer *et al.* [60] constructed a wideband feedforward amplifier in the frequency range 30-300 MHz in thin-film hybrid form; third-order IM distortion was improved 20 dB at 300 MHz. A great advance in feedforward technology was made by Hsieh and Chan [6], [7]. They fabricated a 2.2-GHz feedforward amplifier system in thin-film hybrid form using microwave transistors; an RF gain of 30 dB with 1.25 W of output power and distortion products 50 dB down from the carrier level over a 100-MHz bandwidth were reported. Feedforward correction holds the greatest



promise in microwave integrated circuit form, because system complexity and added cost are no longer a problem. In addition, the use of similar components, assembly techniques and common heat sink allows component parameters which drift to track one another. Quite precise loop balance can thus be sustained.

## 2.7 Summary

IMPATT-diode amplifiers have great promise for use in future communications systems, for example in 14-GHz satellite ground stations, because of their low cost, medium to high power, and high reliability.

Nonlinearities in IMPATT diodes, and all amplifiers in general, pose serious problems for the communications system designer in the distortion they produce. Such distortion is inevitable, since to utilize the full power capability of amplifiers, as required in the output stage of a transmitter or repeater, amplifiers must be driven into the nonlinear region where efficiency and power output are greatest. Several methods of reducing distortion such as feedback, equalization and back-off are available; however, these require the designer to trade off amplifier characteristics, usually gain, bandwidth or power. A new method of amplifier linearization, feedforward correction, appears to be a viable alternative involving less compromise in other amplifier parameters, and unconditional stability.

There has been some research into the effects of system parameters on feedforward amplifier performance, and determination of the dominant parameters. Working systems have been designed. To date, the feedforward amplifier has not been modelled successfully; neither has anyone (to the author's knowledge) reported on feedforward correction applied to a highly nonlinear stable IMPATT amplifier. In this thesis, these experimental



and theoretical investigations are undertaken so that the advantages of feedforward correction can be fully realized.

Amongst the several methods used to measure nonlinear distortion, the two-tone test has been widely used. It is adopted here to determine third- and fifth-order IM distortion products and their corresponding intercept points. These quantities are suitable criteria for evaluating the effects of amplifier nonlinearities.

The next chapter investigates in detail the nonlinear admittance of IMPATT diodes. Measured data is required for developing the models of the IMPATT- and feedforward IMPATT amplifiers.



## CHAPTER 3

### COMPUTER-AIDED LARGE-SIGNAL MEASUREMENT OF IMPATT-DIODE ELECTRONIC ADMITTANCE

#### 3.1 Introduction

Large-signal characterization of an IMPATT diode is essential to the investigation of nonlinear phenomena occurring in IMPATT-diode amplifiers. Several large-signal theories [27]-[29], [61],[62] have been developed, which are generally adequate for qualitative analyses of nonlinear IMPATT-diode behaviour. However, for studies of the quantitative behaviour of specific diodes in actual applications, the IMPATT diode's large-signal characteristics must be measured, preferably in the circuit in which the diode is to be used.

A fundamental problem in the characterization of IMPATT diodes is de-embedding the active chip electronic admittance,  $Y_e$ , from the passive packaging and mounting network [63]. The parasitic reactances of the package and mount have a great effect on circuit operation. In fact, the resonant frequencies of the package normally lie within the frequency range over which the device is active; i.e., displays negative resistance. The result is a complex, frequency-dependent transformation of the nonlinear, but rather well-behaved chip admittance, into a more frequency-sensitive terminal admittance  $Y_t$ . De-embedding is desirable, since it eliminates the effects of this transformation and allows one to use the electronic admittance  $Y_e$  in theoretical studies.

Consider an IMPATT diode in a typical "pill with one prong" package as shown in Fig. 3.1, end-mounted to a coaxial line, Fig. 3.2. The transformer matches the packaged-diode impedance to the 50- $\Omega$





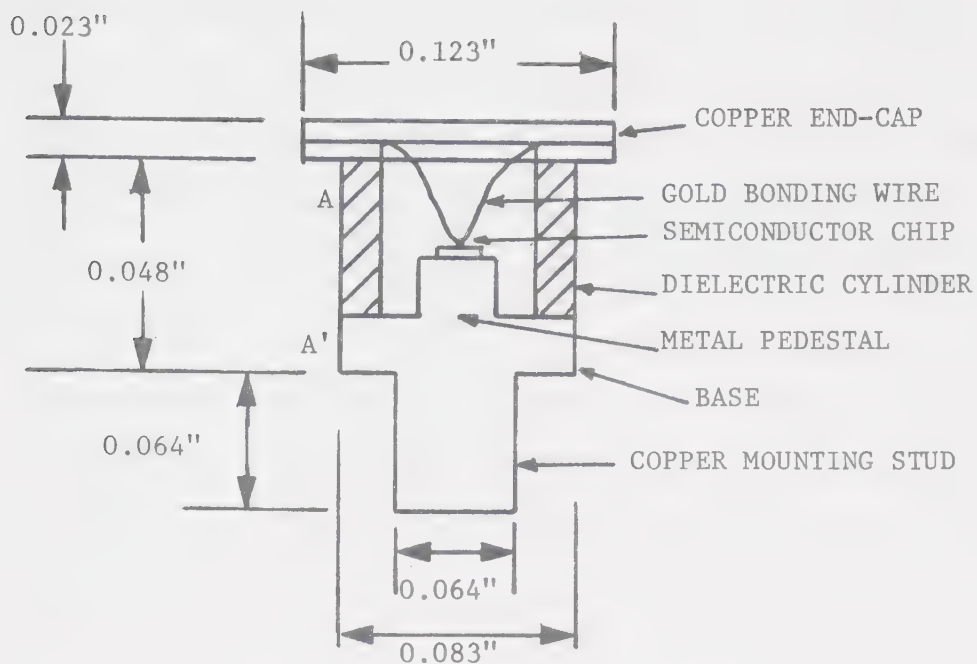


Figure 3.1 Typical packaged negative-resistance diode.

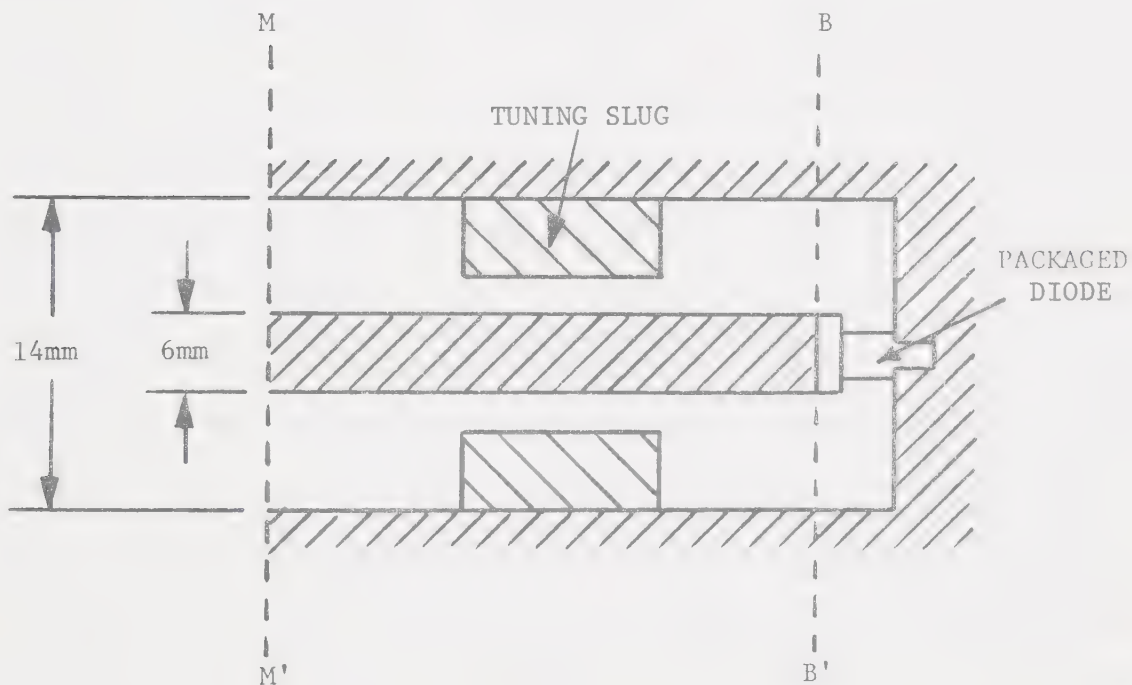


Figure 3.2 Packaged diode end-mounted in precision 50- $\Omega$  coaxial line with an impedance transformer.



characteristic impedance of the measuring equipment. The terminals of the active part of the diode chip are inaccessible, so  $Y_e$  cannot be obtained directly. A number of methods to determine the passive network separating the active semiconductor chip from the measurement reference plane M-M' in the external microwave circuitry have been given in the literature [63]-[71].

Getsinger [63] developed the lumped-element equivalent circuit for the packaged and coaxially-mounted diode shown in Fig. 3.3. Since the package is electrically small at the diode operating frequency, the lumped-element model is valid over a narrow frequency band. The package terminals A-A' are at the outer surface of the dielectric cylinder in Fig. 3.1. The package capacitance,  $C_p$ , includes the geometric capacitance between the base and end cap through the dielectric ring, as well as most of the stray capacitance between the bonding wire and the mounting pedestal. The remaining fringing capacitance,  $C_F$ , across the diode wafer between the bonding wire and the pedestal is very small ( $\sim$  a few hundredths of a pF) and is usually neglected. The inductor,  $L_s$ , represents the inductance of the bonding wire. The resistance of the bonding wire, of the diode ohmic contacts and of the inactive semiconductor regions is represented by  $R_s$ . The element values are found by forward- and reverse-bias measurements on packaged diodes, and by a 1-MHz bridge measurement on an empty package to determine  $C_p$ . Typical values for the Hewlett Packard S-4 package are:  $C_p \approx 0.3$  pF,  $L_s \approx 0.6$  nH, and  $R_s \approx 0.5 \Omega$ . Two-port network number 2 is an LC network representing the conversion of the radial mode, present near the package, to the TEM coaxial mode existing some distance from the diode in the coaxial line. Two-port network number 1 is a lumped-element reactive network transforming the terminal admittance  $Y_t$  to the



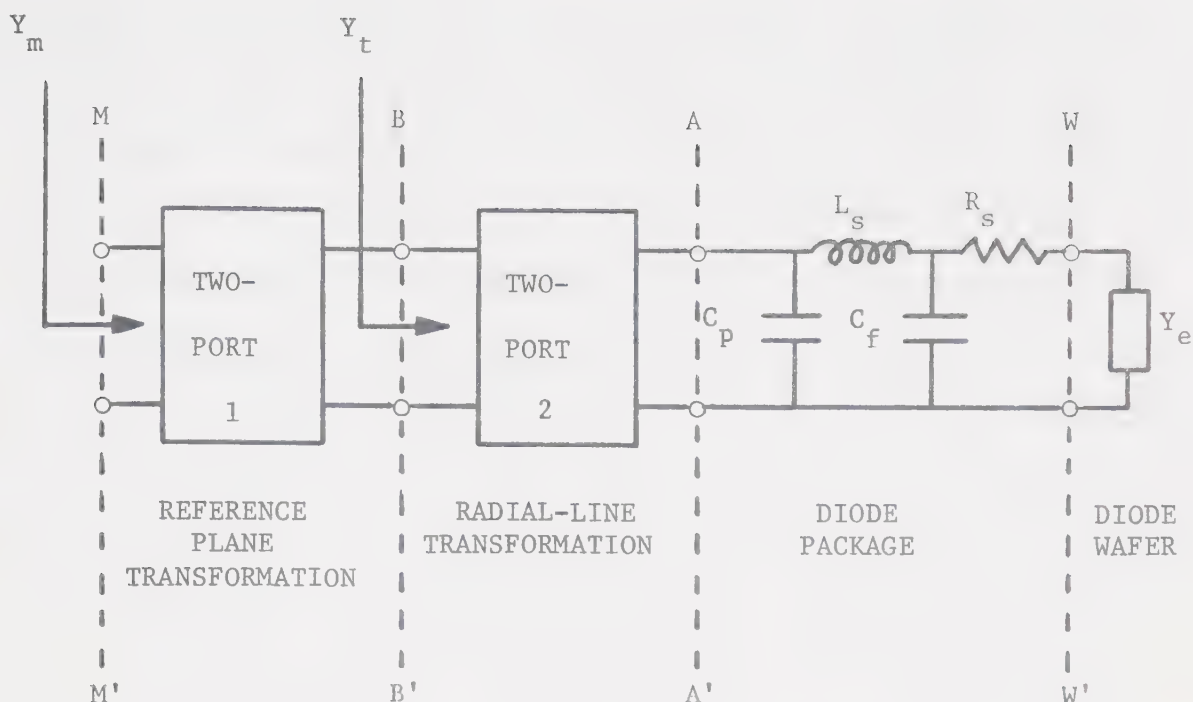


Figure 3.3 Equivalent circuit of packaged diode end-mounted in precision 50-Ω coaxial line according to Getsinger [63].

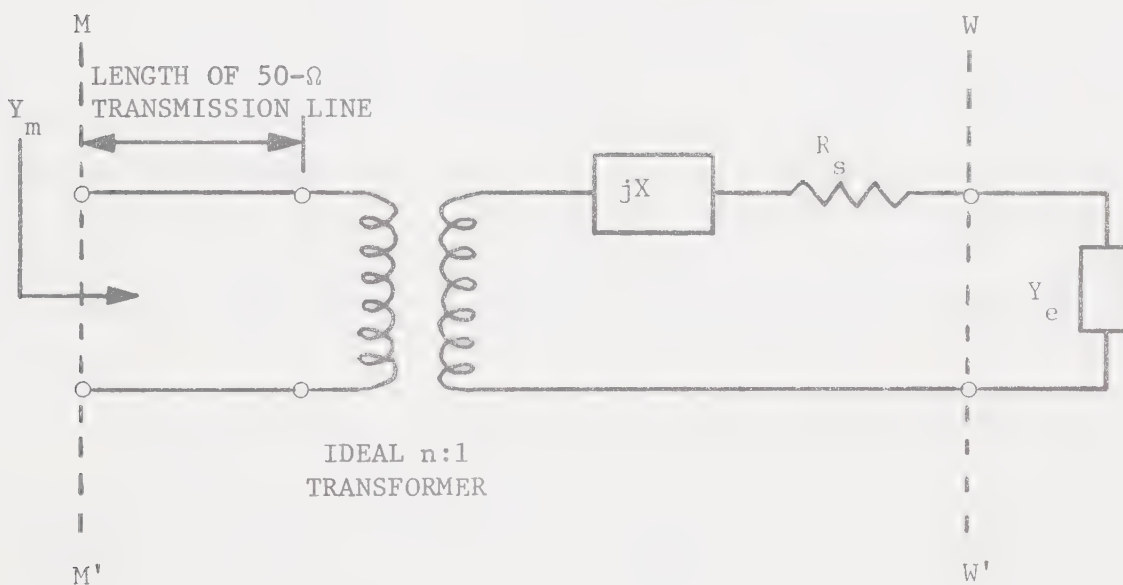


Figure 3.4 Transformation of IMPATT electronic admittance  $Y_e$  to measurement reference plane M-M' according to Gewartowski and Morris [68].



measurement reference plane  $M-M'$ . The values of the reactances in two-port networks number 1 and 2 can be deduced from theory [63].

Van Iperen and Tjassens [64], [65] extended Getsinger's work to develop an equivalent circuit for an IMPATT diode mounted in reduced-height waveguide. They used the package model of Getsinger and developed a tee-network for the transformation from the waveguide impedance to the packaged-diode impedance. The authors [64] measured small- and large-signal impedances of IMPATT diodes at 10 GHz very accurately (2%) using an unusual waveguide bridge circuit. Calibration of this system is very tedious, however, and must be repeated at each frequency, making the method impractical for measuring the frequency dependence of the IMPATT-diode electronic admittance.

There are many problems associated with the equivalent circuits just described. The values for the elements of Getsinger's diode package model should be measured for each mounted device because of tolerances in chip fabrication, and differences in diode encapsulation and mounting. Secondly, theoretically calculated values of the package to radial-line or waveguide transformation may not apply. The alternative, measurement of these values, involves substitution of a solid metal dummy package for the packaged diode. Such a disturbance of the microwave circuit should be avoided.

Dunn and Dalley [66] described a method for measuring small-signal IMPATT-diode electronic admittance using a coaxial circuit and network analyser. Decker, Dunn and Frank [67] adapted the same method to the large-signal case. The combination of computer data reduction with network analyser measurements make this method rapid. However, to determine the





equivalent circuit of the packaged device, Fig. 3.3, it relies on microwave measurements of three different capacitances having the package shape, which were calibrated at 30 MHz. The substitution of these calibration capacitances is difficult to accomplish accurately.

The properties of the package and its mount can also be determined by measuring the transformation from the diode chip to the external reference plane directly. Gewartowski and Morris [68] measured the admittance of IMPATT diodes, mounted as in Fig. 3.2, by means of a slotted-line at 6 GHz. They developed the equivalent circuit of Fig. 3.4. The elements of the coupling network were determined without the use of substituted impedances by fitting impedance data measured at microwave frequencies to capacitance-voltage data measured on a 1-MHz capacitance bridge. The authors [68] assumed the diode capacitance below breakdown at RF frequencies to be the same as at 1 MHz, and calculated the microwave series resistance  $R_s$  from the capacitance. The accuracy of the method was reported at 6%. Isobe and Nakamura [69] followed the same method as Ref. [68] for X-band IMPATT diodes. Unfortunately, slotted-line measurements are very time-consuming, and special attention must be paid to algebraic sign when measuring negative resistance in this manner.

Steinbrecher and Peterson [70] characterized the coupling two-port network in Fig. 3.4 by ABCD transmission parameters. They used the same calibration procedure as Gewartowski and Morris [68], but assumed that the diode has a series resistance which is independent of voltage. Measurements of electronic admittance of IMPATT diodes were made using a network analyser but were confined to the small-signal region.

Ito *et al.* [71] also measured the large-signal electronic admittance of an IMPATT diode mounted in a waveguide reflection amplifier



circuit. The ABCD parameters of the transformation network were determined, within 10% error, by a least-squares approximation of microwave impedance measured below breakdown to chip impedance below breakdown similar to the method in Ref. [68].

For the reasons stated, none of the above methods are suitable for adoption here. An accurate, rapid technique for the measurement of large-signal IMPATT-diode electronic admittance as a function of frequency is developed in this chapter. The method combines and refines several published procedures; viz, the use of a network analyser for rapidity of measurements [66], [67]; direct transformation of electronic admittance to device terminal admittance [71]; determination of the transformation network without physical disturbance of the circuit [68]; and computer reduction of measured data [66], [68]. In Section 3.2, the theoretical details of the measurement technique are developed. In Section 3.3, the experimental test bench and the experimental procedure are described. The measured large-signal IMPATT-diode electronic admittance is presented in Section 3.4. The measurement error is also estimated. The results are summarized in the final section.

## 3.2 Theoretical Details of the Electronic-Admittance Measurement Technique

### 3.2.1 The Circuit Model

The IMPATT diode is end-mounted in a precision 50- $\Omega$  14-mm coaxial cavity with a single, movable-slug 4- $\Omega$   $\lambda/8$  transformer [26] (see Fig. 3.2). The basic block-diagram of the admittance measurement set-up is shown in Fig. 3.5. A bias tee is attached at the input of the coaxial cavity. The entire arrangement is connected via an adapter to a waveguide circulator and operated as a stable reflection amplifier. Waveguide directional



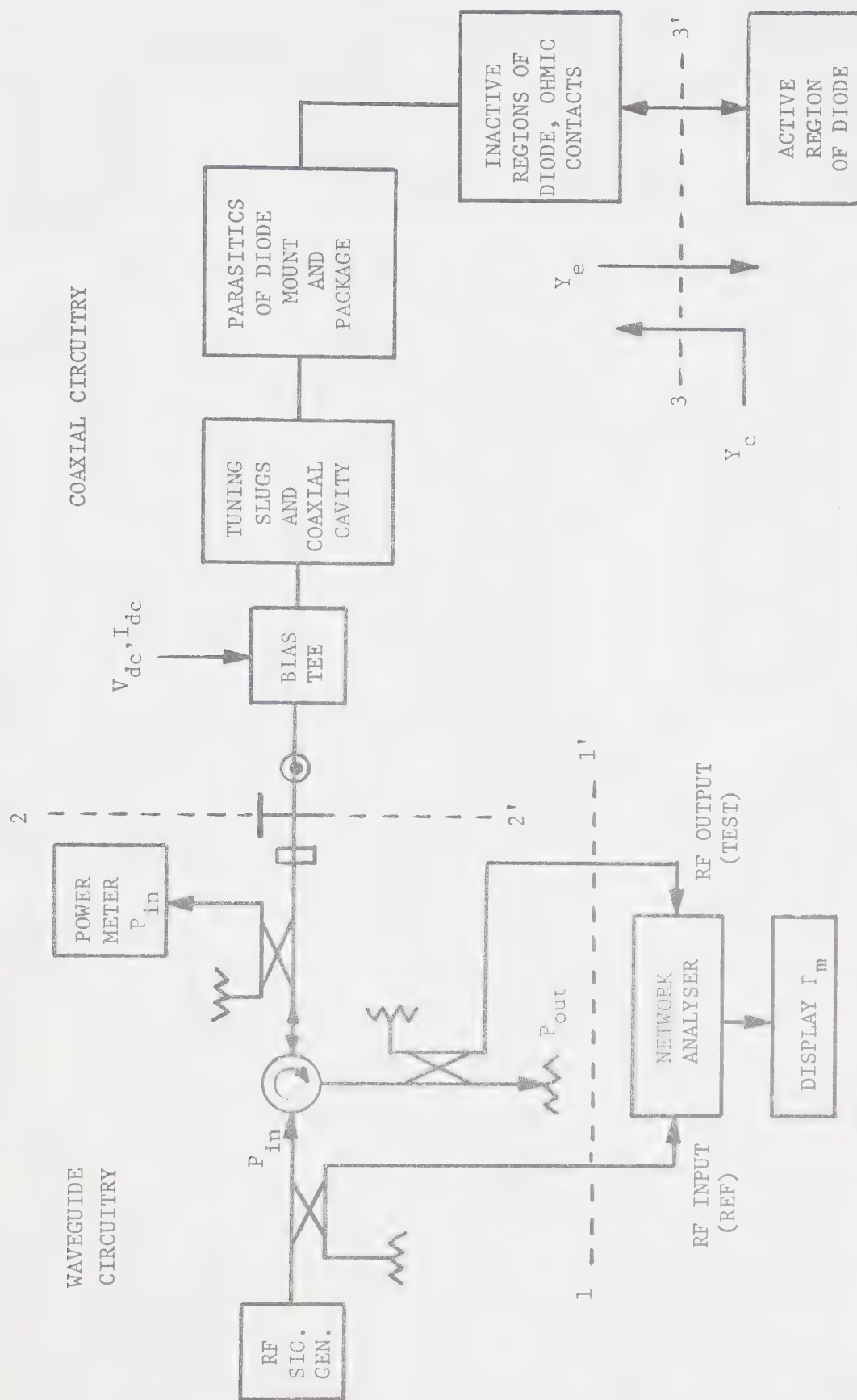


Figure 3.5 Block diagram of large-signal electronic admittance measurement set-up.



couplers sample the RF input signal,  $V_{in}$ , and reflected signal,  $V_{out}$ . The network analyser compares these two signals and displays the measured complex reflection coefficient  $\Gamma_m$  from which the measured impedance  $Z_m$  (admittance  $Y_m$ ) can be calculated. The incident signal power  $P_{in}$  is also measured.

Three reference planes are delineated in Fig. 3.5. Plane 1-1', the reference plane for measurement of  $\Gamma_m$  without calibration, is situated inside the coaxial circuitry of the network analyser. Its exact location cannot be determined. However at microwave frequencies, "impedance" only has meaning with reference to specific transmission-line modes at physically localized terminal planes. Hence it is required to establish the plane 2-2', through which power  $P_{in}$  is flowing towards the IMPATT diode and  $P_{out}$  is reflected from the IMPATT diode, as a well-defined reference plane for impedance measurements. This is accomplished by measuring convenient, known calibration impedances connected at plane 2-2'. Terminal plane 2-2' is physically situated and fixed at the waveguide flange of the waveguide-to-coaxial transition. Since it is desired to isolate the electronic admittance  $Y_e$  from the microwave network in which it is embedded, terminal plane 3-3' must also be well-established by measuring suitable calibration impedances located there.

An equivalent circuit for the measurement set-up and diode is shown in Fig. 3.6. The planes 1-1', 2-2', and 3-3' demarcate the components for RF signal generation and analysis (assumed ideal), the measurement system, the coaxial system, and the active region of the IMPATT diode, respectively. The measurement system represents nonideal operation of the network analyser such as directivity errors, mismatch errors, and tracking errors [72], as well as all the waveguide circuitry between





planes 1-1' and 2-2' in Fig. 3.5; e.g., the circulator and directional couplers. The coaxial system includes the transitions, the bias circuitry, the tuning transformer and the coaxial cavity. It also includes the parasitic dissipative and reactive elements of the diode mount and package, and the series resistance of the inactive regions of the IMPATT diode; viz, the unswept epitaxial region, spreading and contact resistances.

The analysis of the equivalent circuit is based on the use of transfer matrices, or ABCD transmission parameters [73]. Referring to Fig. 3.6, the waveguide and coaxial systems can be represented by passive, lossy, frequency-dependent two-port coupling networks  $K_1[A_1 B_1 C_1 D_1]$  and  $K_2[A_2 B_2 C_2 D_2]$  respectively. The nonlinear electronic admittance  $Y_e$  of the IMPATT diode depends on frequency, RF signal level, and dc bias (Eqn. (2.5)). The admittance  $Y_r$  is the mounted-diode admittance at reference terminals 2-2' looking into the diode. The admittance  $Y_m$  is the measured driving-point admittance at the network analyser internal measurement port 1-1'. At each frequency of interest, the matrices  $K_1$  and  $K_2$ , and the electronic admittance  $Y_e$  are to be determined.

### 3.2.2 Calibration of the Measurement System

The determination of matrix  $K_1$ , mentioned in the previous section, is essentially a calibration process. It accounts for the internal system errors of the network analyser, and the transformation properties of the circuitry between planes 1-1' and 2-2'.

Since reference plane 2-2' occurs in a waveguide medium, a suitable calibration standard that can be employed is a waveguide precision movable short-circuit. Assuming the movable short-circuit to be virtually lossless, its reflection coefficient,  $\Gamma_s$ , is given by:



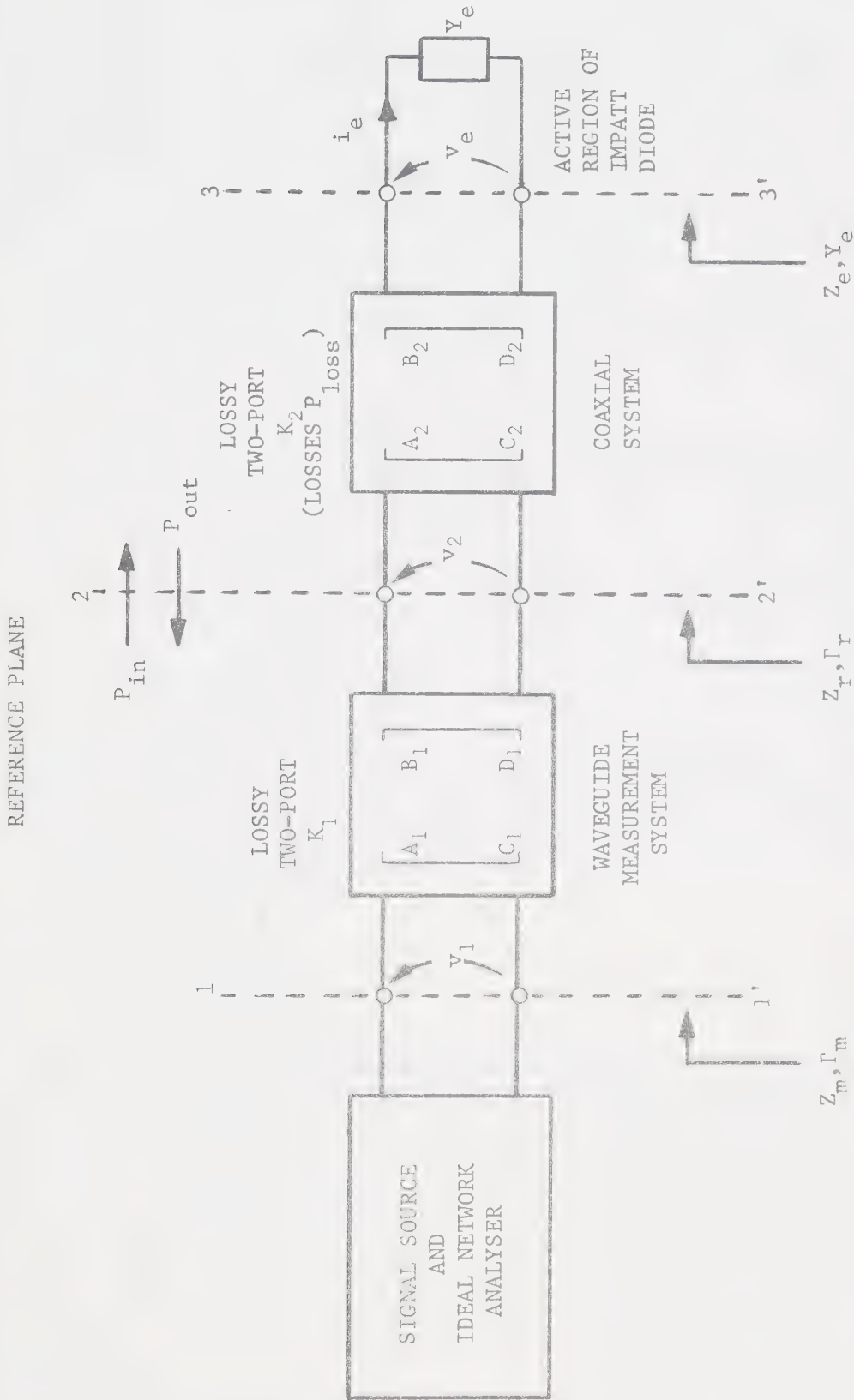


Figure 3.6 Transformation of IMPATT electronic admittance  $Y_e$  to calibration reference plane 2-2' and to measurement reference plane 1-1'.



$$\Gamma_s = -1 \cdot \exp(-j2\beta\ell) \quad (3.1)$$

where

$$\beta = 2\pi/\lambda_g \text{ is the phase constant for the waveguide} \quad (3.2)$$

$$\lambda_g = \lambda_o / \sqrt{1 - (\lambda_o/\lambda_c)^2} \text{ is the guide wavelength} \quad (3.3)$$

$$\lambda_o = c/f \text{ is the free-space wavelength} \quad (3.4)$$

$$\lambda_c = 6.970 \text{ cm (1.732 in) is the cut-off wavelength for}$$

WR-137 waveguide

$$c = 2.998 \times 10^{10} \text{ cm/s}$$

$f$  = the frequency of measurement

$\ell$  = the distance the short is offset from plane 2-2'.

With  $\Gamma_s$  connected at plane 2-2' in Fig. 3.6, the measured reflection coefficient,  $\Gamma_m$ , is given by the bilinear transformation [74]

$$\Gamma_m = \frac{A'_1 \Gamma_s + B'_1}{C'_1 \Gamma_s + D'_1} \quad (3.5)$$

where the  $[A'_1 B'_1 C'_1 D'_1]$  parameters are algebraic functions of the conventional  $[A_1 B_1 C_1 D_1]$  parameters. By normalizing the  $[A'_1 B'_1 C'_1 D'_1]$  parameters to  $D'_1$ , Eqn. (3.5) can be written as

$$\Gamma_m = \frac{a'_1 \Gamma_s + b'_1}{c'_1 \Gamma_s + 1} \quad (3.6)$$

where  $[a'_1 b'_1 c'_1]$  are the normalized parameters. For  $N$  offsets  $\ell_1, \ell_2, \dots, \ell_N$  of the movable short, the measured reflection coefficients are

$$\Gamma_{m_i} = \frac{a'_1 \Gamma_{s_i} + b'_1}{c'_1 \Gamma_{s_i} + 1} ; i = 1, 2, \dots, N \quad (3.7)$$

where

$$\Gamma_{s_i} = -1 \cdot \exp(-j2\beta\ell_i) ; i = 1, 2, \dots, N. \quad (3.8)$$



To determine  $K_1[a'_1 b'_1 c'_1]$  only three measurements of  $\Gamma_m$  corresponding to three different positions of the movable short need be taken ( $N = 3$ ). However, to improve the accuracy of the calibration procedure, more than three measurements should be taken and the "best" values for  $K_1[a'_1 b'_1 c'_1]$  calculated. To find these "best" values, the mean-square error between the measured reflection coefficient  $\Gamma_m$  and the transformed value of  $\Gamma_s$  can be minimized by an optimization routine. The objective function used was

$$U[K_1] = \min \left\{ \frac{1}{N} \sum_{i=1}^N \left| \Gamma_{m_i} - \left( \frac{a'_1 \Gamma_{s_i} + b'_1}{c'_1 \Gamma_{s_i} + 1} \right) \right|^2 \right\} \quad (3.9)$$

This procedure must be repeated at each frequency of interest.

Knowledge of  $K_1[a'_1 b'_1 c'_1]$  at each frequency permits all subsequent measurements on unknown impedances to be corrected and transformed to reference plane 2-2' by the inverse bilinear transformation

$$\Gamma_r = \frac{b'_1 - \Gamma_m}{c'_1 \Gamma_m - a'_1} \quad (3.10)$$

Then,

$$\tilde{Z}_r = \frac{Z_r}{Z_o} = \frac{1 + \Gamma_r}{1 - \Gamma_r} = \frac{1}{\tilde{Y}} \quad (3.11)$$

where  $\tilde{Z}_r$  is the normalized impedance, referred to plane 2-2'. Since plane 2-2' is in a waveguide medium, it is difficult to determine the normalization factor  $Z_o$ , the characteristic impedance of the waveguide, but fortunately it is not required.





### 3.2.3 Determination of the Coaxial System Transmission Parameters

Terminals 3-3' are not accessible for the substitution of usual calibration standards. Furthermore, it is desirable to make all measurements with the diode wafer *in situ*. The electronic impedance  $Z_e$  of the diode below breakdown voltage can be used to determine the matrix  $K_2[A_2B_2C_2D_2]$ .

In reverse bias, below breakdown voltage  $V_B$ , the impedance of the active layer of an IMPATT diode is [71]

$$Z_e(V) = R_s(V) - j[\omega C_d(V)]^{-1} = R_s(V) - jX_d(V) \quad (3.12)$$

where

$V$  = the reverse bias voltage ( $V < V_B$ )

$R_s(V)$  = the series resistance of the unswept region

$\omega = 2\pi f$

$C_d(V)$  = the capacitance of the depletion layer.

Since the active region width (typically 10 microns) is very small compared to wavelength at RF frequencies, the depletion layer capacitance is independent of frequency well into the microwave region. It can be measured as a function of voltage on a conventional 1-MHz capacitance bridge. The series resistance  $R_s(V)$  is calculated from the low-frequency  $C_d$ -V data according to Gewartowski and Morris [68]. There are four steps in this computation:

1) The impurity concentration profile  $N_x$  of the depletion region is calculated as a function of distance from the junction. For the  $i^{\text{th}}$  voltage interval  $\Delta V_i$ , the impurity concentration is

$$N_{x_i} = \frac{-k(C_{\text{avg}_i})^3 \Delta V_i}{d^4 \Delta C_i} \quad (\text{cm}^{-3}) \quad (3.13)$$



where

$$\Delta V_i = V_{i+1} - V_i ; \text{ for } V_i < V_B \quad (V)$$

$$\Delta C_i = C_d(V_{i+1}) - C_d(V_i) \quad (\text{pF})$$

$$C_{\text{avg}_i} = [C_d(V_{i+1}) + C_d(V_i)]/2 \quad (\text{pf})$$

$$d = \text{junction diameter} \quad (\text{mils})$$

$$k = \text{constant} = 2.38 \times 10^{17} \text{ for Silicon.}$$

2) The resistivity of the depletion region is calculated as a function of distance from the junction using the set of concentrations  $N_x$ . The conductivity  $\sigma$  of a semiconductor is given by [75]

$$\sigma = qN_x\mu(N_x) \quad (3.14)$$

where

$q$  = the quantity of electric charge

and  $\mu(N_x)$  = mobility of the minority carriers as a function of doping concentration.

Then resistivity  $\rho$  of the depletion region is

$$\rho = 1/\sigma = [qN_x\mu(N_x)]^{-1} \quad (\Omega\text{-cm}) \quad (3.15)$$

$$\text{or} \quad \ln[\rho] = -\ln[q\mu(N_x)] - \ln[N_x] \quad (3.16)$$

From a graph [75] of  $\ln[\rho]$  versus  $\ln[N_x]$ , Eqn. (3.16) can be expressed in the  $i^{\text{th}}$ - interval by the empirical relation

$$\ln[\rho_i] = 29.686 - 0.82609 \ln[N_{x_i}] \quad (3.17)$$

in the range  $5 \times 10^{15} < N_x < 5 \times 10^{16} \text{ (cm}^{-3}\text{)}$  for n-type Silicon. This range is appropriate for 6-GHz IMPATT diodes.

3) The change in resistance of the unswept region in the  $i^{\text{th}}$ - interval,  $\Delta R_i$ , is calculated from the set of resistivities and capacitances:

$$\Delta R_i = \epsilon \rho_i \left\{ [C_d(V_i)]^{-1} - [C_d(V_{i+1})]^{-1} \right\} \quad (\Omega) \quad (3.18)$$



where

$\epsilon$  = dielectric constant = 1.036 pF/cm for Silicon.

Since  $C_d(V_{i+1}) < C_d(V_i)$ , then  $\Delta R_i$  is negative. As the reverse bias is increased below breakdown, the depletion layer widens, causing  $C_d$  to decrease; the unswept region shrinks to zero causing  $R_s$  to decrease.

4) The absolute series resistances  $R_s(V)$  is calculated. This step is a departure from the procedure in Ref. [68] where the change in impedance with voltage is used rather than the absolute value. Above breakdown all inactive regions of the IMPATT diode are lumped into the coaxial system  $K_2$ ; the active wafer consists solely of the depletion layer. At breakdown voltage,  $V_B$ , the depletion region is fully depleted; i.e., there is no unswept region. Hence,  $R_s$  is assumed to be zero just below breakdown. Integrating for the  $i^{\text{th}}$ - interval we obtain

$$R_s(V_i) = \sum_{n=i}^N (-\Delta R_n) ; \quad i = 1, 2, \dots, N-1 \quad (3.19)$$

where

$$R_s(V_N) = R_s(V_B) = 0 \quad (3.20)$$

and  $N$  = the number of voltage measurements.

Computer reduction of the  $C_d$ - $V$  data utilizing Eqns. (3.12)-(3.20) yields the electronic impedance  $Z_e(V)$  below breakdown. Microwave measurements on the assembled system of Fig. 3.6 at the same reverse bias voltages below breakdown are used to find the coupling two-port matrix  $K_2[A_2 B_2 C_2 D_2]$  as follows:

1) Using the bilinear transformation [74], we can express

$$Z_r(V) = \frac{A_2 Z_e(V) + B_2}{C_2 Z_e(V) + D_2} \quad (3.21)$$



Since  $Z_r$  is measured in waveguide, only the normalized impedance  $\tilde{Z}_r = Z_r/Z_o$ , Eqn. (3.11), is available. Dividing by  $Z_o$  and normalizing  $[A_2 B_2 C_2 D_2]$  to  $D_2$  in Eqn. (3.21) results in

$$\tilde{Z}_r(V) = \frac{a_2 Z_e(V) + b_2}{c_2 Z_e(V) + 1} \quad (3.22)$$

where

$$a_2 = A_2/Z_o D_2 \quad (S) \quad (3.23a)$$

$$b_2 = B_2/Z_o D_2 \quad (\text{dimensionless}) \quad (3.23b)$$

$$\text{and} \quad c_2 = C_2/D_2 \quad (S) \quad (3.23c)$$

Two-port number 2 does not contain ferrite devices or active devices. We can thus write the reciprocity condition:

$$A_2 D_2 - B_2 C_2 = 1 = Z_o^2 D_2^2 (a_2 - b_2 c_2) \quad (3.24)$$

2) As before, the "best"  $K_2[a_2 b_2 c_2]$  is found by minimizing in the least-squares sense the objective function

$$U[K_2] = \min \left\{ \frac{1}{N} \sum_{i=1}^N \left| \tilde{Z}_r(V_i) - \left( \frac{a_2 Z_e(V_i) + b_2}{c_2 Z_e(V_i) + 1} \right) \right|^2 \right\} \quad (3.25)$$

Determination of  $K_1[a_1' b_1' c_1']$  and  $K_2[a_2 b_2 c_2]$  at each frequency completes the de-embedding procedure.

### 3.2.4 Determination of IMPATT Electronic Admittance

With reverse bias above the breakdown voltage  $V_B$ , the diode breaks into avalanche and can operate in the normal IMPATT mode.

$\tilde{Z}_r(V_{RF})$  is calculated from complex reflection coefficient measurements,  $\Gamma_m$ , measured at terminals 1-1' and transformed to terminals 2-2' via  $K_1[a_1' b_1' c_1']$  (Eqns. (3.10) and (3.11)), where  $V_{RF}$  is the RF voltage across the active region of the IMPATT diode. The electronic admittance at





constant dc current and RF frequency is then given by the inverse mapping of Eqn. (3.22), namely:

$$Y_e(V_{RF}) = \frac{1}{Z_e(V_{RF})} = \frac{c_2 \tilde{Z}_r(V_{RF}) - a_2}{b_2 - \tilde{Z}_r(V_{RF})} = G_e(V_{RF}) + jB_e(V_{RF}) \quad (3.26)$$

where  $G_e$  and  $B_e$  are the conductance (negative) and susceptance, respectively, of the diode's active region.

The circuit in Fig. 3.5 can be operated as a reflection amplifier when properly tuned. Referring to the equivalent circuit of Fig. 3.6,

$$P_{out} = P_{in} + P_g - 2P_{loss} \quad (3.27)$$

where

$P_{in}$  = the input power at plane 2-2'

$P_{out}$  = the output power at plane 2-2'

$P_g$  = the RF power converted from dc by  $Y_e$

and  $P_{loss}$  = the insertion loss of coupling network  $K_2$ .

For practical amplifiers,  $P_g > 2P_{loss}$  and the amplifier gain is

$$|\Gamma_r|^2 = P_{out} / P_{in} > 1. \quad (3.28)$$

The voltage  $V_{RF}$  applied to admittance  $Y_e$  can be related to  $P_{in}$  by the transmission parameters of matrix  $K_2$ . The voltage transmission coefficient at reference plane 2-2' in Fig. 3.6 is defined as

$$v_2/v_i = 2Z_r/(Z_r + Z_0) \quad (3.29)$$

where  $v_i$  is the incident voltage wave at plane 2-2', and  $v_2$  is the net voltage across the terminals 2-2'. The transmission matrix  $K_2$  gives

$$v_2 = (A_2 + B_2 Y_e) v_e \quad (3.30)$$



where  $v_e$  is the net voltage across the admittance  $Y_e$ . Substituting Eqns. (3.22), (3.23), (3.26) and (3.30) into (3.29), we obtain

$$v_i = v_e [a_2 + c_2 + (b_2 + 1)Y_e] Z_o D / 2 \quad (3.31)$$

The input power at reference plane 2-2' can be expressed by

$$P_{in} = \text{Re} \left\{ |v_i|^2 / 2Z_o \right\} = |v_i|^2 / 2Z_o \quad (3.32)$$

where  $Z_o$  is the characteristic impedance of the waveguide seen through the circulator. The characteristic impedance,  $Z_o$ , of waveguide is the ratio of the transverse electric field at any point in the waveguide to the transverse magnetic field at the same point, for a specific mode (usually the  $TE_{10}$  mode in rectangular waveguide). The transverse electric field is in phase with the transverse magnetic field (assuming negligible losses in the waveguide) and hence the characteristic impedance  $Z_o$  is a real quantity. Substituting Eqn. (3.31) into (3.32), and then using (3.24), the result is [71]

$$|v_e| = V_{RF} = \frac{(8P_{in} |a_2 - b_2 c_2|)^{1/2}}{|(b_2 + 1)Y_e + a_2 + c_2|} \quad (3.33)$$

The admittance  $Y_e$  is thus completely characterized as a nonlinear function of  $V_{RF}$  and frequency.



### 3.3 Experimental Details of the Electronic-Admittance Measurement Technique

#### 3.3.1 Experimental Electronic-Admittance Measurement Set-Up

A schematic diagram of the circuit for large-signal measurement of IMPATT-diode electronic admittance appears in Fig. 3.7. The salient features of this set-up are listed.

1) A J-band (4-8 GHz) klystron signal generator (Model HP 618C) is used to ensure a noise-free stable reference signal at 0-dBm power (10 dB below its rated output power). This signal is amplified by a 30-dB gain, 1-W TWT amplifier (Model HP 493A). The output ports of both the generator and the TWT are isolated to prevent interference problems.

2) The incident signal level is controlled by a precision attenuator and monitored on a power meter; frequency and stability are observed on a frequency counter.

3) The IMPATT diode (type HP 5082-0431) is end-mounted in a 50- $\Omega$  precision 14-mm coaxial cavity as in Fig. 6.1. Bias is provided from a constant dc current supply via a bias tee.

4) The IMPATT-diode circuit is tuned to operate as a reflection amplifier so that sufficiently large RF voltages can be applied across the diode's active region. Tuning was accomplished with a  $\lambda/8$  4- $\Omega$  impedance transformer. Without tuning, the diode package parasitics and diode-to-coaxial line mismatch reflected most of the incident RF power.

5) A large copper heatsink is used to mount the diode so that, after sufficient time for stabilization, thermal effects can be neglected.

6) The nonlinearities of the IMPATT diode result in harmonics and other spurious signals appearing at large-signal levels. The spectrum analyser is used to check that the input- and output signals are sinusoids



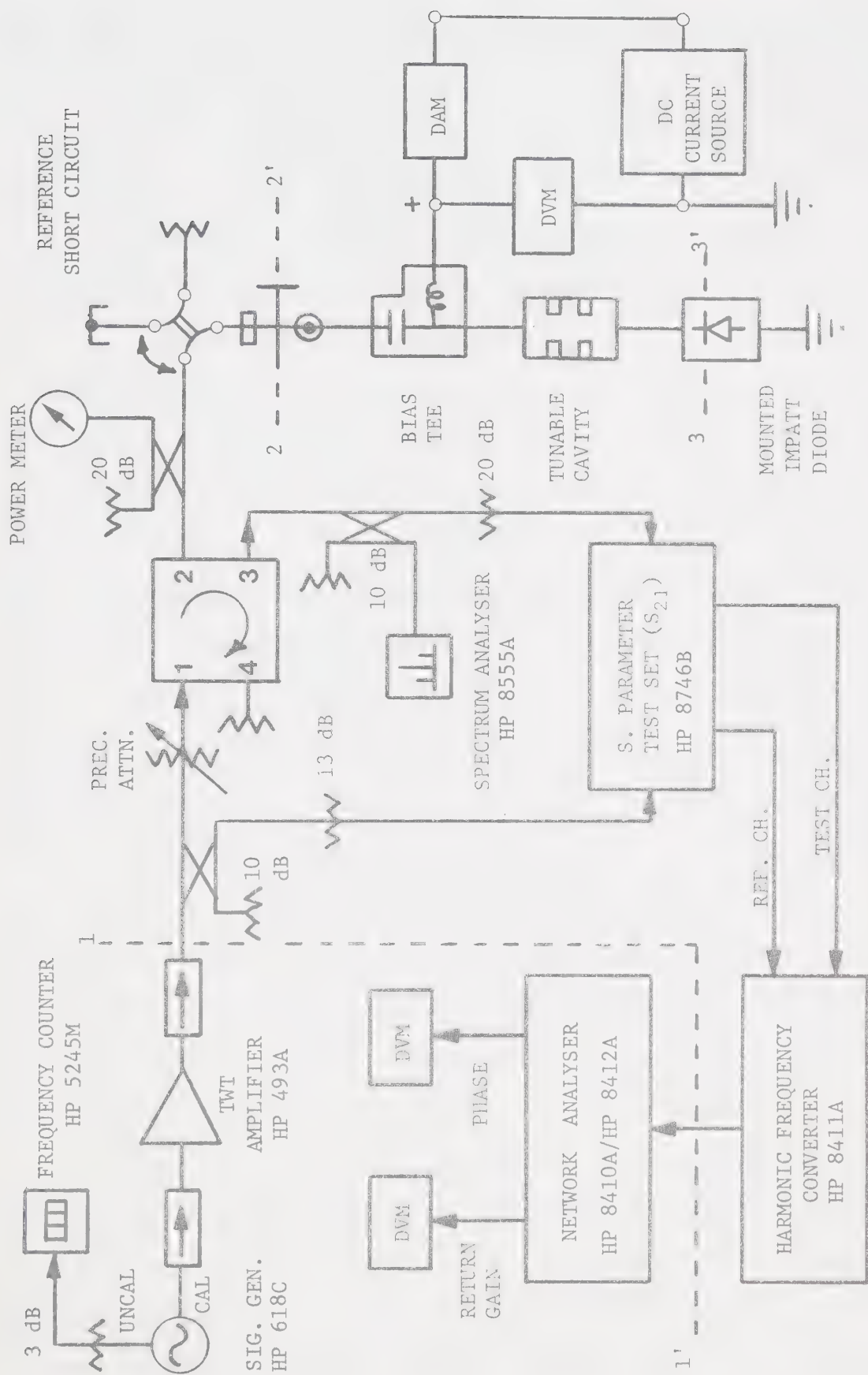


Figure 3.7 Schematic diagram of large-signal electronic admittance measurement set-up.





or, for practical purposes, near-sinusoids. The measured electronic admittance is then the approximate CW admittance; i.e., the complex ratio of the sinusoidal voltage across the diode's active region to the sinusoidal current through the same region.

7) The network analyser [72] was modified to operate in the large-signal region. The power at the RF INPUT of the S-parameter test set [77] must lie in the range -7 dBm to +9 dBm for the network analyser to operate properly. Due to an intrinsic 23-dB loss between the RF INPUT and PORT 1, the maximum power normally incident on the test device is -14 dBm (40  $\mu$ W), and the measured  $S_{11}$  is thus a small-signal measurement. The modified circuit in Fig. 3.7 permits large-signal measurements to be made. The incident signal is sampled by the 10-dB directional coupler, attenuated to lie within operating range, and applied to the RF INPUT of the S-parameter test set. The reflected signal is applied to PORT 2 through a 20-dB attenuator. With switch  $S_{21}$  of the S-parameter test set depressed, the RF INPUT signal arrives at the REF CHANNEL output, while the PORT 2 signal arrives at the TEST CHANNEL output. The measurement is then a reflection-coefficient measurement  $\Gamma_m$ . The measured data from the network analyser consist of two voltages displayed on digital voltmeters: one is proportional (50 mV/dB) to the return gain  $R_G$ ; the other is proportional (10 mV/deg) to  $\arg(\Gamma_m)$ . The return gain, defined as negative return loss in dB, is converted to  $|\Gamma_m| = \log^{-1}(R_G/20)$ .

8) Due to the need for high gain and phase sensitivity, excessive drift of the network analyser posed a difficult problem for sufficient precision to be attained. Also,  $\Gamma_m$  was found to vary greatly with the signal power incident on a constant test load. Adding a waveguide switch to the circuit solved these problems: one path in Fig. 3.7 is the normal



path for diode measurements; the alternate path is terminated by a precision short-circuit. The short-circuit served as a calibration reference for every measurement  $\Gamma_m$ ; i.e., all measurements were referred to the same impedance and could be compared relative to one another regardless of the drift of the network analyser or of any other slow changes in the complete set-up. Mechanical switching between the two paths was reproducible to the required accuracy.

### 3.3.2 The Experimental Procedure

The breakdown voltage of the experimental IMPATT diode (type HP 5082-0431) was about 101 Vdc. Therefore, 13 capacitance measurements were made on the 1-MHz capacitance bridge (Boonton model 71A) at reverse-bias voltages in the range 0 to 100 Vdc. The bridge was initially nulled with an open-circuit package connected in place of the packaged diode. The measured capacitance is thus the depletion layer capacitance since the stray capacitance of the connector and parasitic capacitances of the package have been calibrated for.

The active junction area of a similar diode was measured under a microscope to be  $10^{-4} \text{ cm}^2 \pm 5\%$ .

To extract matrix  $K_1$  at each frequency, 10 reflection measurements were performed with the following impedances connected at plane 2-2': a fixed short-circuit, and 9 positions (0.10 to 0.50 in) of the movable short-circuit.

After the diode was mounted in the cavity, 25-mAdc bias current was applied, and the amplifier was tuned for 5 to 10 dB of gain at the desired measurement frequency over a 1-dB bandwidth of about 50 MHz. Reflection coefficient measurements were then made on the amplifier



assembly with the diode biased below breakdown at the same voltages as for the 1-MHz capacitance measurements. Computer reduction of the measured data yielded the coupling matrix  $K_2$ .

With the diode biased above breakdown, and incident power  $-20$  dBm ( $10 \mu\text{W}$ ), reflection coefficient measurements were used to calculate the small-signal electronic admittance  $Y_e$  at several dc bias currents (2 to 25 mA). For constant dc bias current 25 mA and varying incident RF power ( $-20$  dBm to  $+23$  dBm) reflection coefficient measurements yielded the large-signal admittance. None of the measurements had any discernible distortion. Observable distortion products at the input were more than 40 dB below the fundamental frequency. Spurious signals in the output of the reflection amplifier were more than 25 dB down from the fundamental, verifying the single-frequency admittance measurement.

Each of the above measurements were performed at various frequencies in the range 5.7 to 6.5 GHz.

### 3.4 Computational Details of the Electronic-Admittance Measurement Technique

All calculations were performed in double precision on the IBM 360/370 computer. Optimization of Eqns. (3.9) and (3.25) was achieved by a library routine implementing the Fletcher-Powell algorithm [78]. The calculated electronic admittance data were interpolated in frequency and RF voltage using a cubic-spline interpolation routine to yield  $Y_e$  at convenient values of these parameters [79].

### 3.5 Measured IMPATT-Diode Electronic Admittance and Error Analysis

In Fig. 3.8 the results of the 1-MHz  $C_d$ -V measurements below breakdown are plotted. The junction capacitance  $C_d$  decreases exponentially from 3.8 pF at 0-Vdc to 0.26 pF at 100-Vdc reverse bias, just below breakdown.



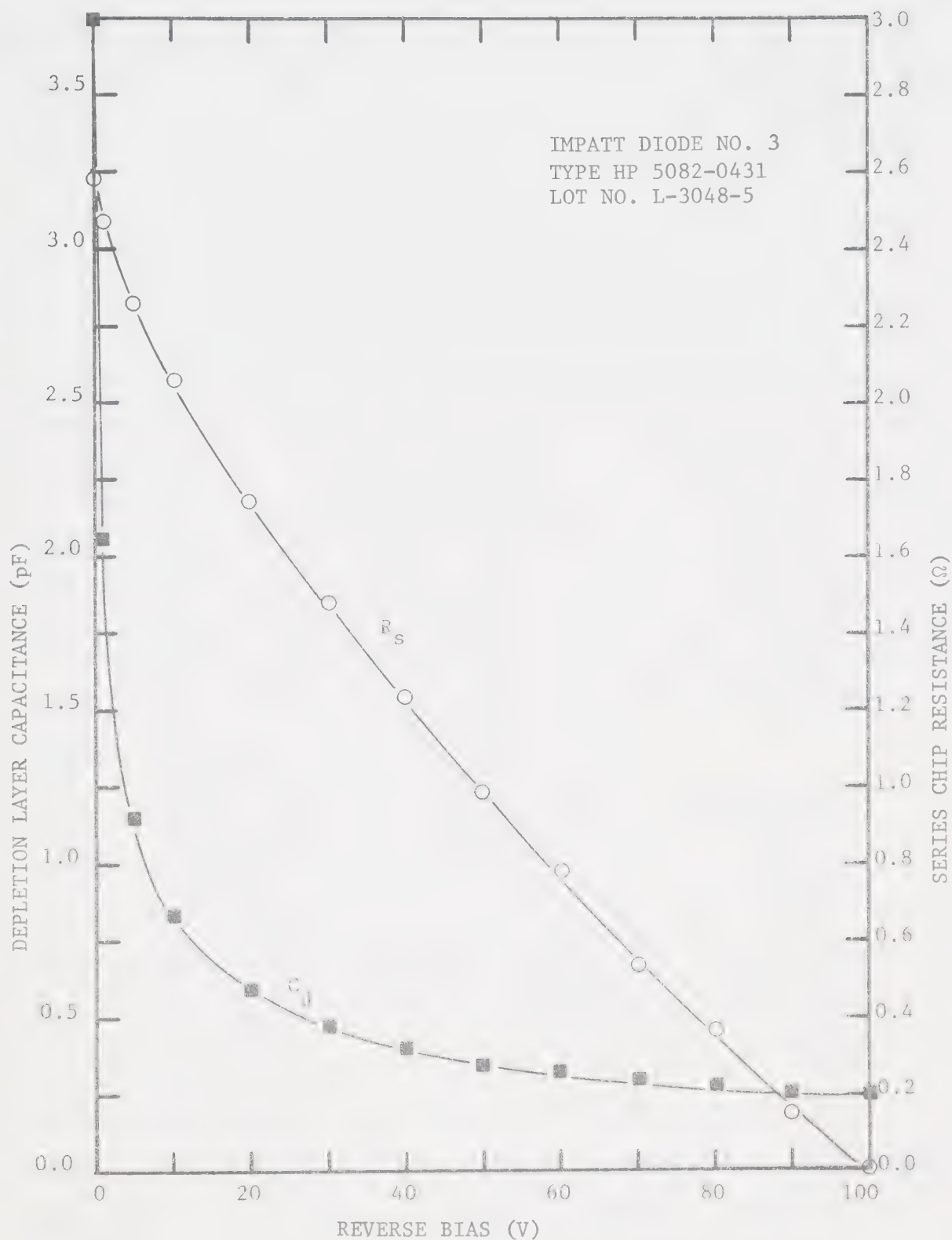


Figure 3.8 Resistance and differential capacitance of the active region of the experimental IMPATT diode below breakdown voltage.





The package capacitance (0.29 pF) has been subtracted so the  $C_d$ -V curve shown is for the depletion layer alone. The error in the measurement of  $C_d$  is  $\pm 0.05$  pF, for  $C_d$  greater than 1 pF, and  $\pm 0.01$  pF for  $C_d$  less than 1 pF.

The second curve in Fig. 3.8 shows the dependence of the series resistance,  $R_s$ , of the diode's active region on reverse bias voltage. As the reverse bias increases, the undepleted region of the wafer becomes more and more narrow until it becomes negligible just below breakdown. A maximum resistance of  $2.6 \Omega$  occurs at 0 V. Since  $R_s$  is small compared to the reactance of  $C_d$ ,  $R_s$  is very difficult to determine accurately. The error in calculation of  $R_s$  is estimated to be about 10%. This error estimate comprises the small error in the measurement of the  $C_d$ -V data ( $\sim 2\%$ ) and error in measurement of junction area ( $\sim 5\%$ ). Also included is a small error introduced in the calculation of impurity concentration profile due to the assumption of a "one-sided" junction in which the depletion layer widens in only one direction [75].

Figures 3.9 and 3.10 show the behaviour of the small-signal electronic conductance and susceptance, respectively, as a function of frequency and dc bias current. The electronic conductance is seen to be relatively independent of frequency in the measured frequency range, indicating operation in the optimum frequency band (6-GHz diodes). On the other hand, the electronic susceptance increases almost linearly with frequency. The susceptance decreases with dc bias, and the negative conductance increases with dc bias as expected from theory. The small-signal conductance lies in the range  $-0.1$  to  $-1.0$  mS and the susceptance lies in the range  $5.0$  to  $9.0$  mS. The susceptance is from 5 to 100 times larger than the electronic conductance.

The measured large-signal electronic admittance is presented in



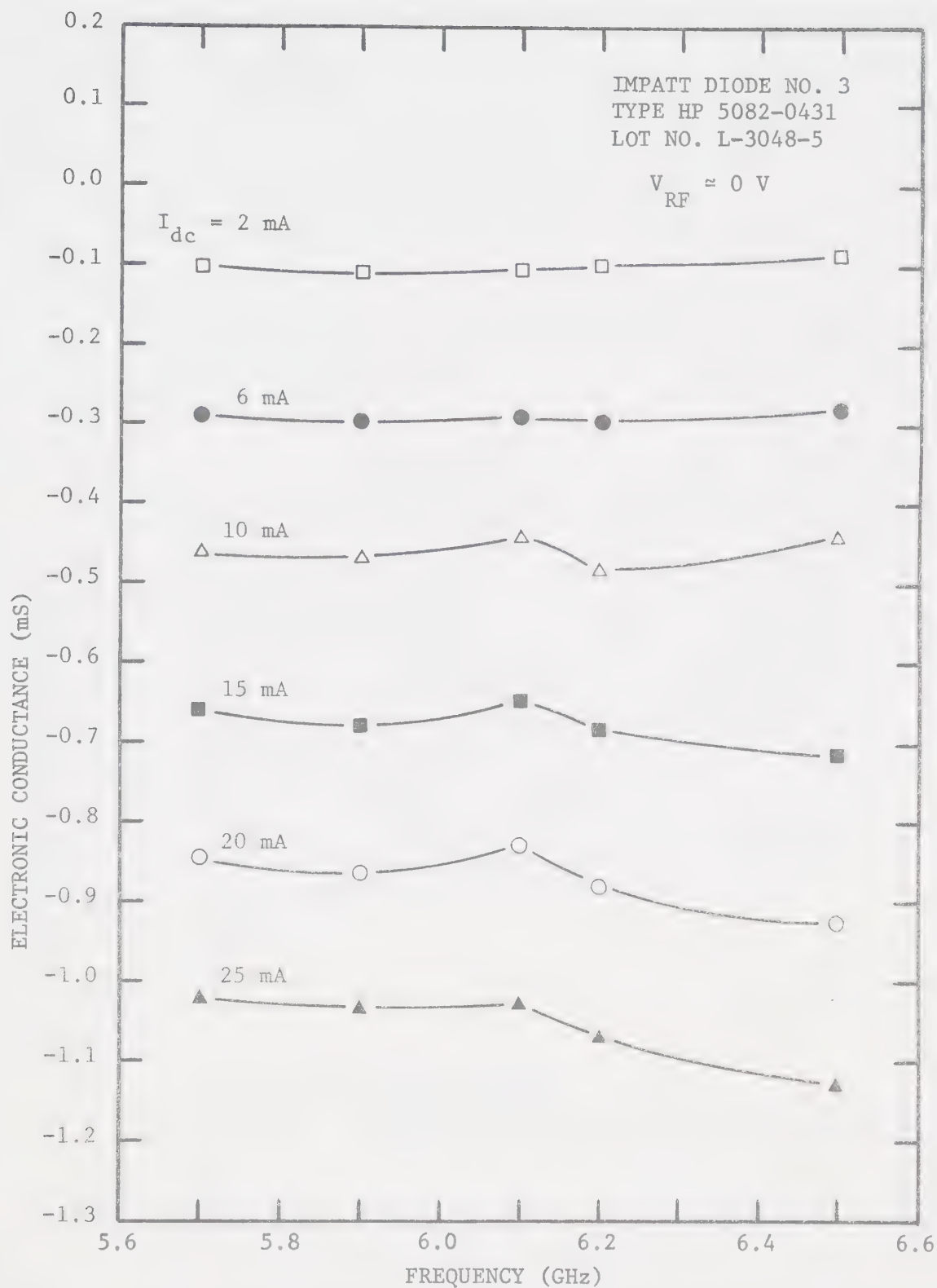


Figure 3.9 Behaviour of the small-signal electronic conductance of the experimental IMPATT diode.



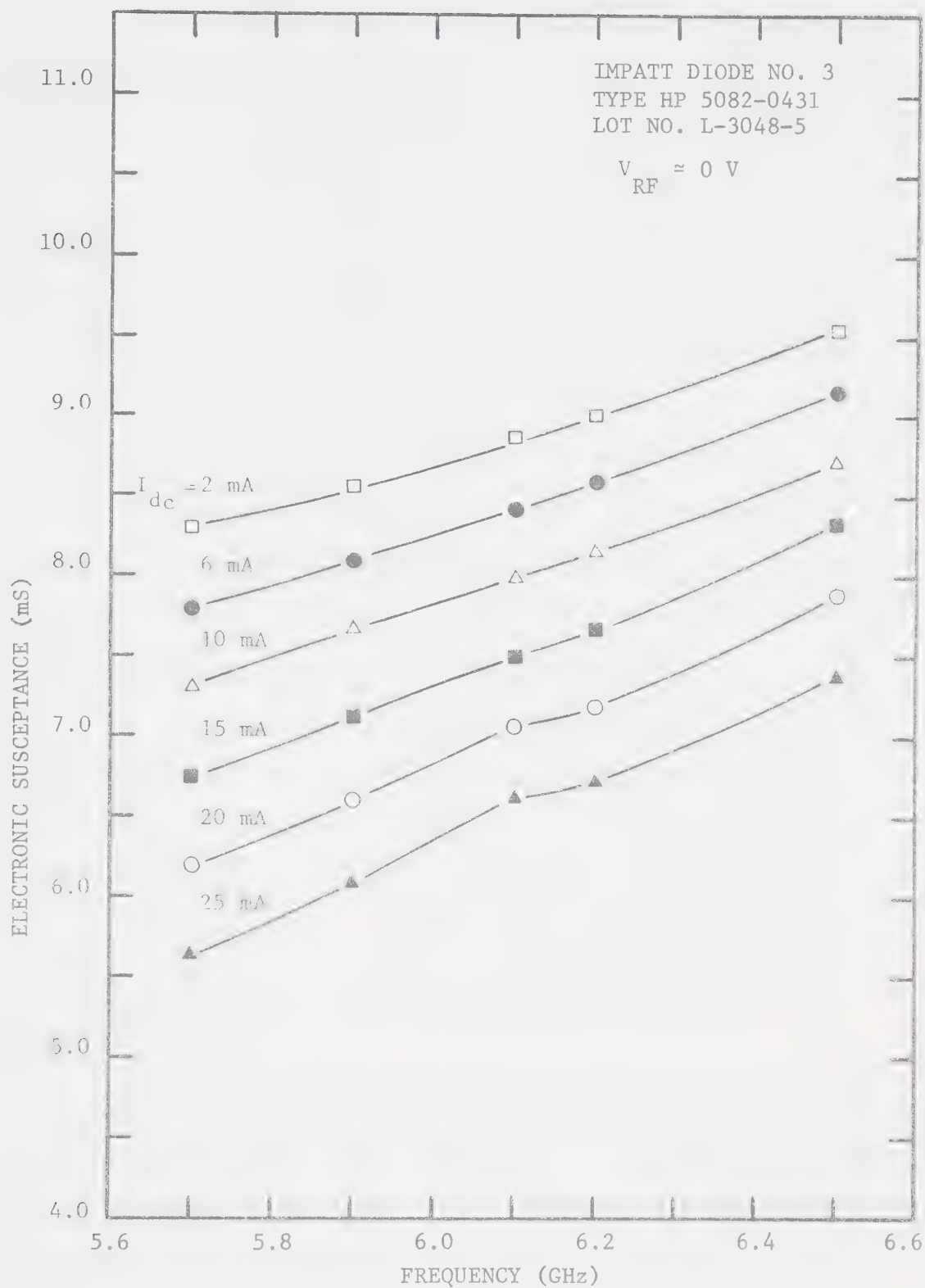


Figure 3.10 Behaviour of the small-signal electronic susceptance of the experimental IMPATT diode.



Figs. 3.11 to 3.15 to show its behaviour as a function of frequency and RF voltage. Since the diode is operating at its designed centre frequency, Fig. 3.11 shows the electronic conductance  $G_e$  to be relatively independent of frequency with increasing signal level, and to follow the small-signal contour. Also  $|G_e|$  decreases with increasing signal level, resulting in a decrease in amplifier gain. Figure 3.12 illustrates the continuous increase of electronic susceptance  $B_e$  with frequency and RF signal level. The decrease of  $|G_e|$  and increase of  $B_e$  with increasing signal level are shown to greater advantage in Figs. 3.13 and 3.14 respectively.

The dependence of large-signal electronic admittance on frequency and on drive signal is illustrated clearly in Fig. 3.15. It should be noted that the curves at frequencies 5.8, 6.0, 6.3 and 6.4 GHz are interpolated from measured results at other frequencies. The warping of the constant voltage contours is a result of experimental error, especially in the 6.5-GHz curve where amplifier gain was considerably less than for measurements at lower frequencies. The admittance was measured at a constant dc current of 25 mA, equivalent to a constant current density of  $250 \text{ A/cm}^2$ . The measured results are in the same range as those predicted theoretically by Scharfetter and Gummel [27] for an ideal Read diode operating at  $200 \text{ A/cm}^2$ .

It is difficult to determine an accurate error estimate for the large-signal admittance. The normal approach to the estimation of measurement error is to separate the measurement system into its critical subsystems, evaluate either theoretically or experimentally the systematic (nonrandom) error in each, and by error propagation analysis determine the effect on the final measurement. In low-frequency measurement systems, those instrument errors which directly affect accuracy are added linearly





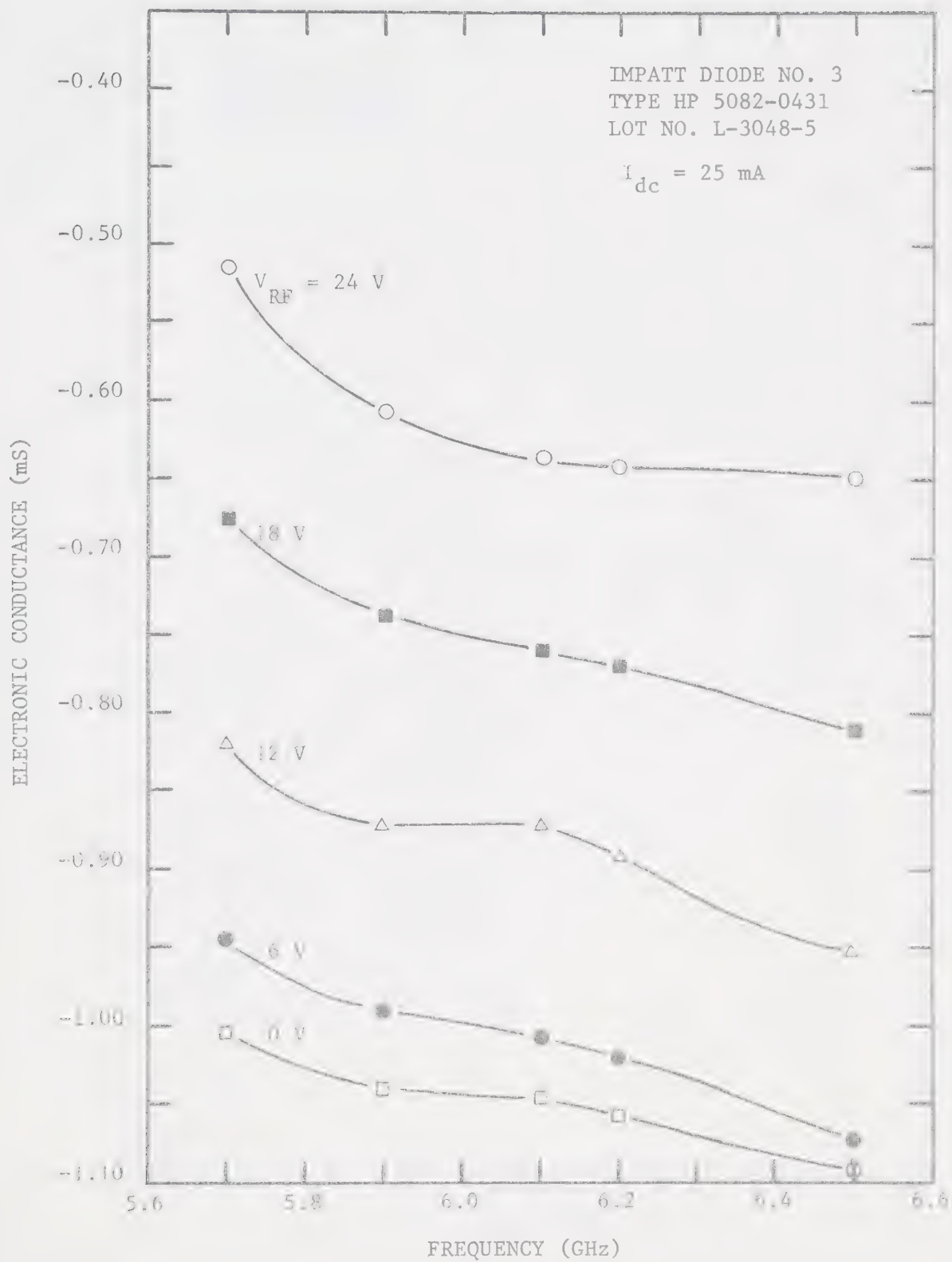


Figure 3.11 Frequency behaviour of the large-signal electronic conductance of the experimental IMPATT diode.



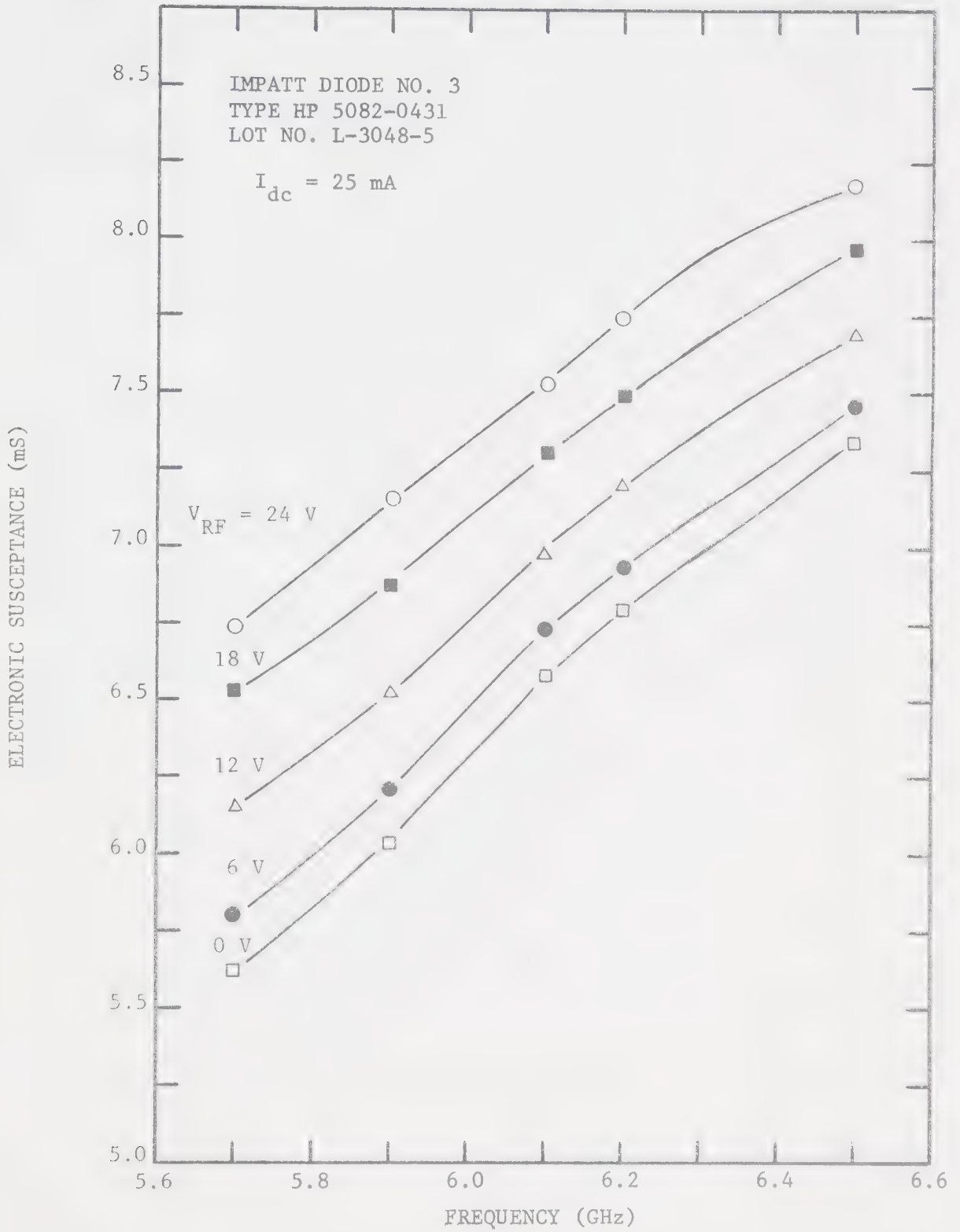


Figure 3.12 Frequency behaviour of the large-signal electronic susceptance of the experimental IMPATT diode.



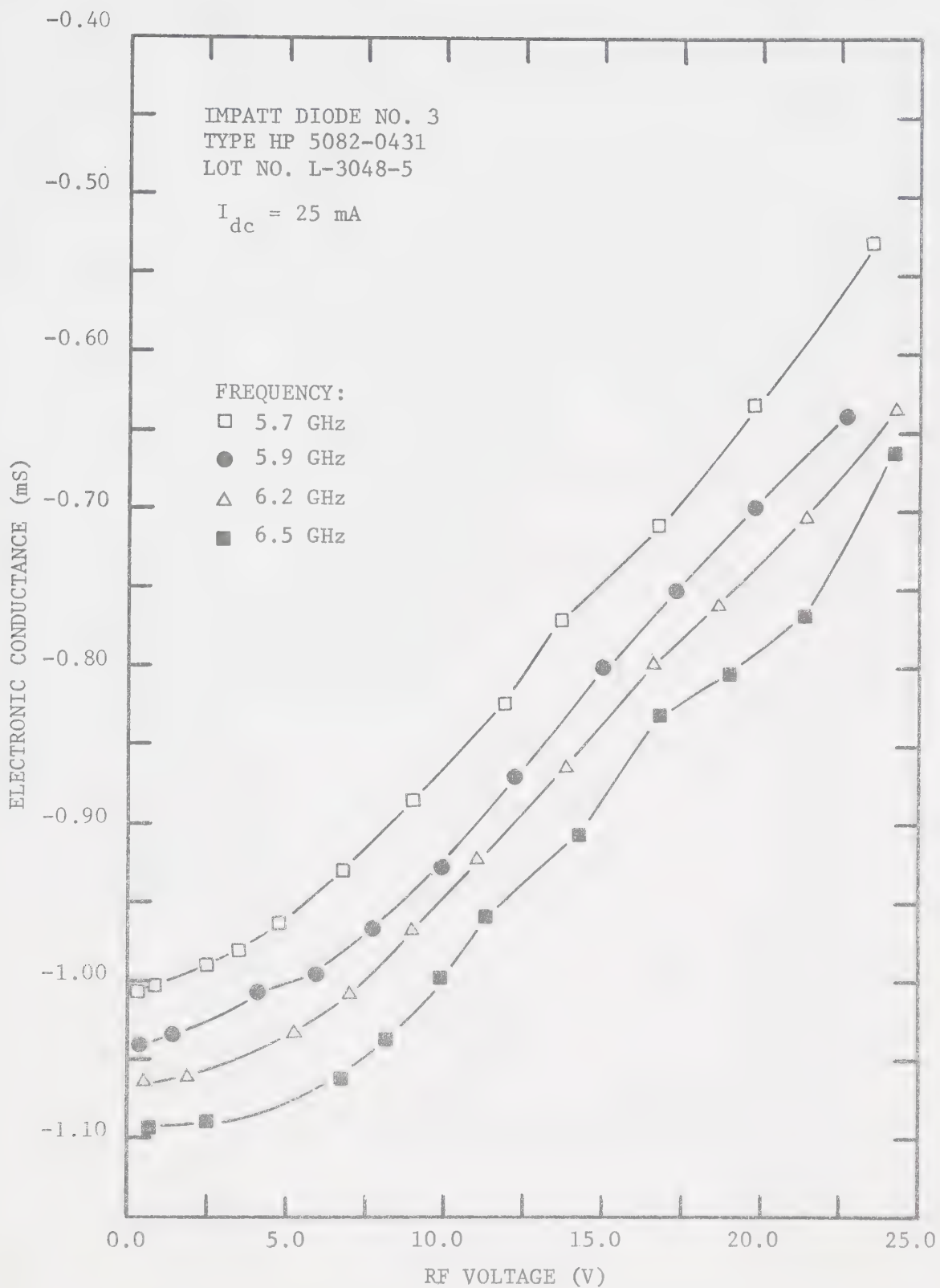


Figure 3.13 RF voltage behaviour of the large-signal electronic conductance of the experimental IMPATT diode.



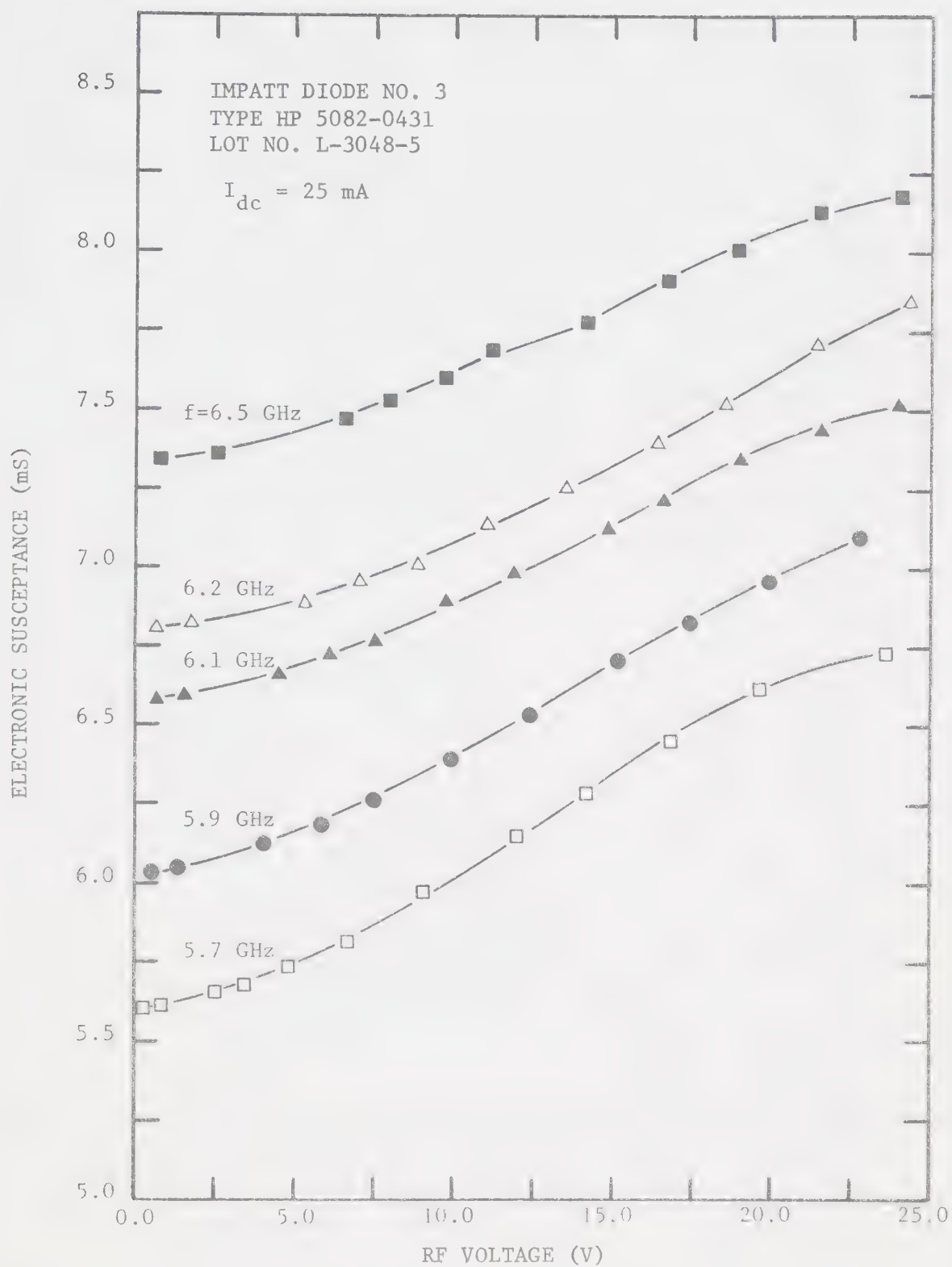


Figure 3.14 RF voltage behaviour of the large-signal electronic susceptance of the experimental IMPATT diode.





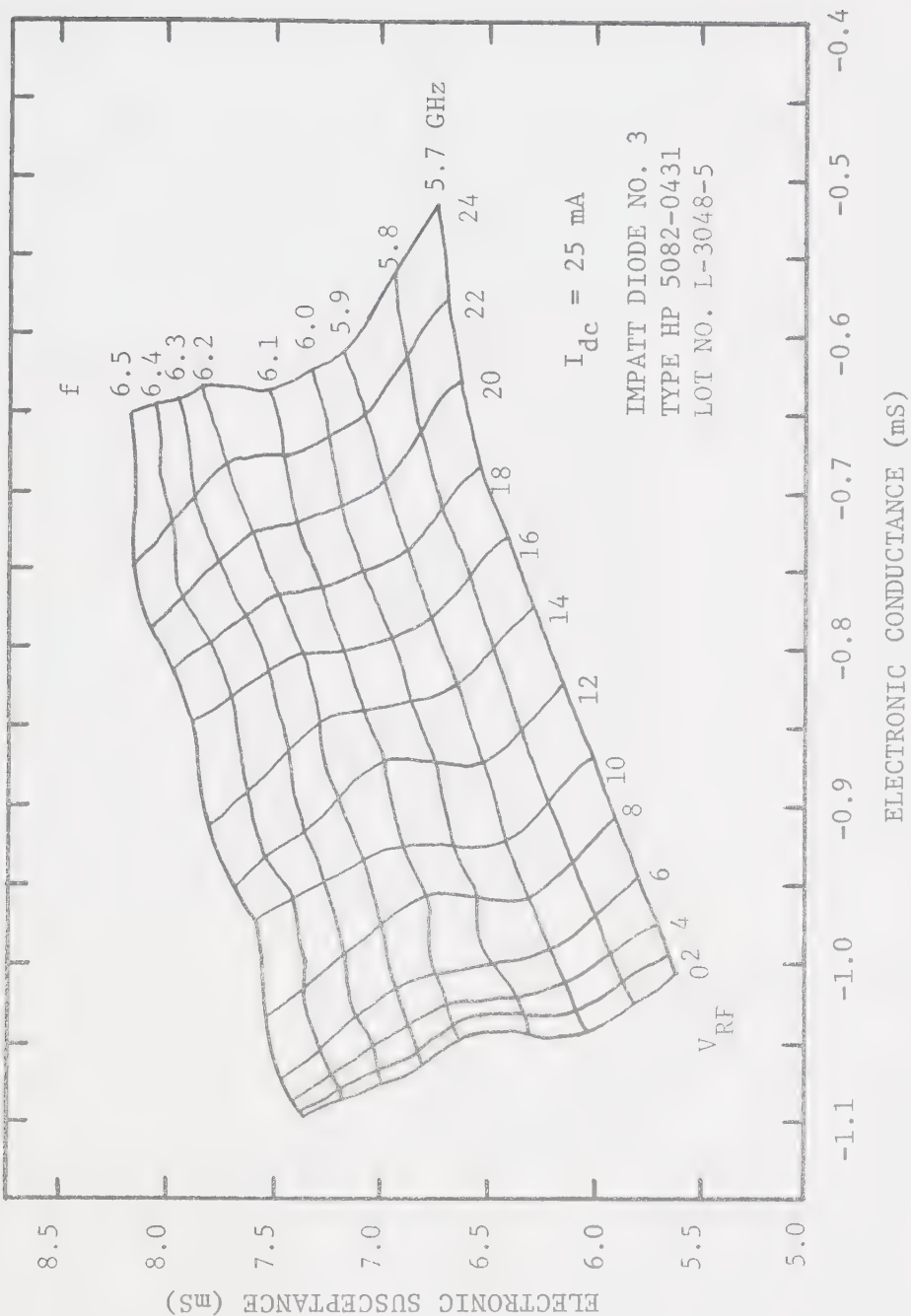


Figure 3.15 Frequency- and RF voltage behaviour of the large-signal electronic admittance of the experimental IMPATT diode.



or, one error predominates and is taken as the total system error. In the microwave measurement system of Fig. 3.7, however, the number of possible sources of error is so much greater that simple linear addition of them results in an error bound which may be much larger than the expected error.

The described calibration procedure improves measurement accuracy significantly. It removes systematic errors of residual VSWR (mismatch), network analyser dc drift, and gain- and tracking errors of the directional couplers internal to the network analyser [72]. From repeated measurements and Hewlett Packard specifications for the network analyser (Model HP 8410A) the error in measured reflection coefficient  $\Gamma_m$  is estimated to be  $\pm 0.1$  dB in magnitude (return loss) and  $\pm 1$  degree in phase.

The second factor influencing the error in the calculation of electronic admittance is the accuracy in determination of the coupling matrices  $K_1$  and  $K_2$ . The results of three separate calibration runs indicate an error of 3% in determination of  $K_1[a'_1 b'_1 c'_1]$ . This good accuracy is obtained because of the use of redundant data and least-squares optimization. For the diode biased below breakdown, a typical figure for the measured reflection coefficient is  $\Gamma_m \approx -1.6$  dB (return loss)  $\angle 100^\circ$ . Using the estimated instrument errors in the measurement of  $\Gamma_m$ , a representative error in  $\Gamma_m$  for the diode biased below breakdown is 7%.  $\Gamma_r$  is calculated from the inverse transformation of  $K_1$  on  $\Gamma_m$  according to Eqn. (3.10), and may be expected to be in error by approximately 10%. Next,  $\Gamma_r$  and the impedance  $Z_e$  of the diode chip extrapolated from 1-MHz data are used to determine network  $K_2$  via Eqn. (3.21). The error in  $Z_e$  is due mainly to 10% error in calculation of  $R_s$  and can also be estimated at 10%. Thus the matrix  $K_2[a_2 b_2 c_2]$  would normally be obtained with 20% error. However, the use of redundant data and least-squares optimization is esti-



mated to reduce the error in  $K_2$  to 10-15%.

The large-signal electronic admittance is measured with the diode biased above breakdown. For this case, a typical figure for the measured reflection coefficient is  $|\Gamma_m| \approx 5.0 \pm 0.1$  dB (return loss)( $\pm 2\%$ ) and  $\arg \Gamma_m = 100^\circ \pm 1^\circ$  ( $\pm 1\%$ ). This typical 3% error in  $\Gamma_m$  is augmented by the error in transformation through networks  $K_1$  (3% error) and  $K_2$  (15% error) to yield an error estimate of about 20% for the large-signal electronic admittance.

### 3.6 Summary

For studies on IMPATT-diode amplifiers, the large-signal behaviour of the diode needs to be known independent of the circuit in which it is embedded. A method is developed here for the accurate measurement of the IMPATT-diode large-signal electronic admittance, using a network analyser and computer-aided data reduction techniques. The method allows measurement of the admittance with the IMPATT diode *in situ*, thereby greatly enhancing measurement accuracy. Secondly, the admittance of the diode's active region is separated from the external circuitry and package parasitic elements by a de-embedding procedure. This extraction of the electronic admittance isolates the diode nonlinearities and simplifies further studies on the effects of such nonlinearities in different circuit configurations. Other advantages of the method are speed and ease of changing measurement frequency. The method is quite accurate; the estimated error in the measurement of electronic admittance is about 20%. The method is not as accurate as the single-frequency method of van Iperen and Tjassens [64], but is thought to be at least as accurate as other published multi-frequency methods.

In the next two chapters, two different models for the feedforward



IMPATT amplifier are discussed. Both models are based on the measured large-signal electronic-admittance data.





## CHAPTER 4

### DISTORTION ANALYSIS OF A FEEDFORWARD-CORRECTED IMPATT AMPLIFIER USING VOLTERRA SERIES REPRESENTATION

#### 4.1 Introduction with Historical Notes

In this chapter, both the IMPATT-diode amplifier and the feedforward-corrected IMPATT amplifier are analysed for distortion using Volterra series representation. Special problems are encountered in modelling nonlinear circuits at microwave frequencies, because reactive or "memory" effects are important and must be accounted for. In the past, nonlinear circuits operating at frequencies where reactive effects are definitely not negligible, have been analysed for distortion using conventional, low-frequency power-series representation of the nonlinearities. Strictly, such analyses apply only to nonlinear zero-memory circuits, for which the output at time  $t$  depends only on the input at the same instant; i.e., infinitely broadband nonlinear resistive circuits. Microwave amplifiers have many parasitic nonlinear energy-storage (memory) elements which produce frequency-dependent distortion. The transfer characteristic of such an amplifier with memory can be represented by a Volterra series. It can be shown that the power-series approach is actually a special case of the Volterra series representation.

The Volterra series method is based on the theory of functionals developed by Volterra [16] in 1930. Wiener [80] was the first to apply this technique to find the response of a nonlinear device to noise in 1942. Following Wiener's pioneering work, there was continued application of the Volterra series to nonlinear system theory. Brilliant [81], George [82], Zames [83], Chesler [84], and Parente [85], reported on nonlinear system analysis, multi-dimensional transforms, nonlinear operators, Gaussian



inputs, and convergence problems respectively. The paper by Bedrosian and Rice [86] is an excellent review of nonlinear systems with memory driven by harmonic and Gaussian inputs.

There was little application of the Volterra series to nonlinear circuit problems, however, until Narayanan [87] used the technique to calculate transistor amplifier distortion in 1967. This delay is due to the following reasons. 1) The solid theoretical framework for use of the Volterra series had to be developed. 2) It cannot conveniently be applied to strong nonlinearities because the high-order terms, which cannot be neglected in this case, are awkward to handle and slow down the rate of convergence of the series. 3) The inverse transformation of the high-order transfer functions to the time domain is difficult. Few practical advantages were seen in using Volterra series analysis, but this approach is well-suited for calculating distortion in mildly nonlinear amplifiers. In such studies, since the response to two or three sinusoidal input signals is of interest, meaningful results are obtainable entirely in the frequency domain. The nonlinear transfer functions representing the nonlinearity account for frequency-dependent distortion and are easily calculated on a computer.

Nonlinear distortion can be computed with the help of the Volterra series for a wide class of practical amplifiers. Narayanan extended his own work to predict distortion in cascaded transistor amplifiers [88] and in feedback amplifiers [89]. Since 1970, H. Poon has used Volterra analysis of the charge control transistor model for third-order distortion studies [90], and Kuo and Witkowski have developed a computer program for calculating the distortion of transistor amplifiers by using Volterra techniques [91]. Crossmodulation and intermodulation in 100-MHz



transistor amplifiers were investigated by Meyer *et al.* [21] using the Volterra series approach. Bussgang *et al.* [92] have employed the Volterra series in modelling communications receivers to account for their nonlinear response to multiple input signals. Volterra analysis has also been used to predict intermodulation (IM) distortion generated in a Schottky barrier mixer diode [93].

Volterra series analysis will be applied here to the problem of predicting IM distortion in a feedforward IMPATT-diode amplifier with a two-tone input. Section 4.2 is an introduction to the Volterra series representation of nonlinear circuits and systems, with pertinent reference to the problem under consideration. The nonlinear model for the IMPATT amplifier is developed in Sec. 4.3. The Volterra series representing this model is used to predict third- and fifth-order IM distortion products and intercept points, as well as gain compression; computed results are presented and commented upon. In Sec. 4.4 the general microwave feedforward amplifier is analysed using Volterra series representation of the amplifier nonlinearities. The improvement in IM distortion by feedforward correction is discussed. Power requirements for the error amplifier with a knowledge of the gain- and phase variations of the main amplifier and its IM distortion are considered in Sec. 4.5. The gain sensitivity of a microwave feedforward amplifier is dealt with in Sec. 4.6. The analysis in Secs. 4.4 to 4.6 are generally applicable; in particular, to the IMPATT amplifier under investigation. The highlights of the chapter are itemized in Sec. 4.6.

## 4.2 Some Preliminary Results for Volterra Series Analysis

A system can be considered to act as an operator, transforming one set of time functions, all possible inputs  $x(t)$ , to another set of



time functions, all possible outputs  $y(t)$ . If for each input function a unique output function results, then this transformation is one-to-one and the system is said to be deterministic. If we fix the time  $t$  at which we observe the system output, the system can be considered to be a functional. Symbolically, this functional is denoted by

$$y(t) = H[x] = H[x(s); -\infty < s \leq t] \quad (4.1)$$

which states that the output time function at time  $t$  depends upon the input time function for all past values of time.

Volterra showed that every functional  $H[x]$ , continuous in the field of continuous functions, can be represented by the expansion [16]

$$H[x] = \sum_{n=0}^{\infty} H_n[x] \quad (4.2)$$

in which  $H_n[x]$  is a regular homogeneous functional, of degree  $n$ , of the form

$$H_n[x] = \int_a^b \dots \int_a^b h_n(\tau_1, \tau_2, \dots, \tau_n) x(\tau_1) \dots x(\tau_n) d\tau_1 \dots d\tau_n \quad (4.3)$$

The series (4.2) resulting from a functional expansion is a Volterra series. A necessary and sufficient condition that a system  $H$  can be represented in some neighbourhood about the zero input by a convergent Volterra series [85] is that the system  $H$  be deterministic, time-invariant and have a functional representation  $H[x]$  which is





analytic<sup>†</sup> about  $x(t)=0$ . In practice, a convergent Volterra series exists if the system is asymptotically stable in the bounded-input bounded-output sense.

Wiener applied the Volterra series to the analysis of nonlinear systems [80] by relating the system input  $x(t)$  to the output  $y(t)$  by means of a functional series

$$y(t) = \sum_{n=1}^{\infty} y_n(t) \quad (4.4)$$

where  $y_1(t) = \int_{-\infty}^{\infty} h_1(\tau)x(t-\tau)d\tau \quad (4.5)$

$$y_2(t) = \iint_{-\infty}^{\infty} h_2(\tau_1, \tau_2)x(t-\tau_1)x(t-\tau_2)d\tau_1d\tau_2 \quad (4.6)$$

and in general,

$$y_n(t) = \int_{-\infty}^{\infty} \dots \int_{-\infty}^{\infty} h_n(\tau_1, \tau_2, \dots, \tau_n) \prod_{i=1}^n x(t-\tau_i) d\tau_i \quad (4.7)$$

Equation (4.4) is the general input-output functional representation of nonlinear systems. The index of the terms,  $n$ , is called the order of the system. This Volterra series representation is useful provided that the system is not driven so hard that the number of terms required for an adequate approximation to  $y(t)$  becomes very large. In practice then, the Volterra series (4.4) is applicable to the small-signal nonlinear case, for which the first few terms of the series usually suffice. The zero-order term —a dc output in the absence of an input —can be neglected in

---

<sup>†</sup> Analyticity of  $H[x]$  implies that all functional derivatives of  $H[x]$  exist.



the analysis as a fixed-bias offset. The first-order term ( $n=1$ ), is the conventional linear response of the system where  $h_1(\tau)$  is the impulse response of the linearized system. The higher-order terms are the system nonlinear responses. Analogous to the linear case, the  $n^{\text{th}}$ -order kernel of Eqn. (4.7),  $h_n(\tau_1, \tau_2, \dots, \tau_n)$ , is called the nonlinear impulse response of order  $n$ . This analogy is extended by calling the  $n$ -dimensional Fourier transform the nonlinear transfer function of order  $n$ :

$$H_n(j\omega_1, j\omega_2, \dots, j\omega_n) = \int_{-\infty}^{\infty} \dots \int_{-\infty}^{\infty} h_n(\tau_1, \tau_2, \dots, \tau_n) \prod_{i=1}^n \exp(-j\omega_i \tau_i) d\tau_i \quad (4.8)$$

The time-domain output,  $y(t)$ , of a mildly nonlinear system, can be found in terms of the low-order transfer functions ( $N$  small) and the spectrum,  $X(j\omega)$ , of the input signal:

$$y(t) = \sum_{n=1}^N \int_{-\infty}^{\infty} \dots \int_{-\infty}^{\infty} H_n(j\omega_1, j\omega_2, \dots, j\omega_n) \prod_{i=1}^n \left(\frac{1}{2\pi}\right) X(j\omega_i) \exp(j\omega_i t) d\omega_i \quad (4.9)$$

The model of an  $n^{\text{th}}$ -order nonlinear system which results from Volterra series analysis is illustrated in Fig. 4.1. The output is written as the sum of paralleled low-order responses from 1 to  $n$ .

A convenient method of computing the nonlinear transfer functions when the system differential equations are known is the "probing" or "harmonic input" method [86], [92]. For a system represented by a Volterra series as in Eqn. (4.4), a harmonic input must result in a harmonic output. Thus, when the input  $x(t)$  is the sum of incommensurable frequencies

$$x(t) = \sum_{i=1}^n \exp(j\omega_i t) \quad (4.10)$$



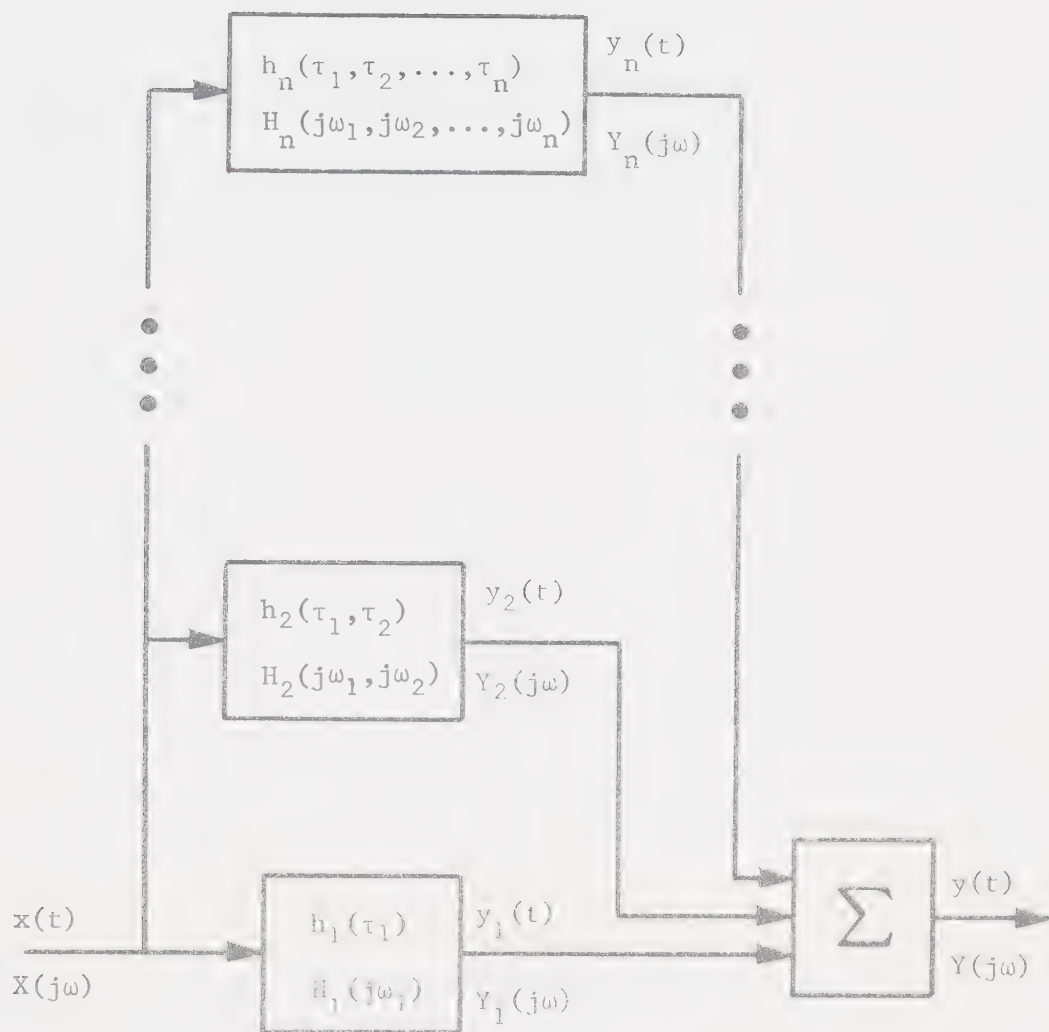


Figure 4.1 Volterra-Wiener model of an  $n^{\text{th}}$ -order nonlinear system [80].



the  $n^{\text{th}}$ -order nonlinear transfer function,  $H_n$ , is given by

$$H_n(j\omega_1, j\omega_2, \dots, j\omega_n) = \left\{ \begin{array}{l} \text{complex coefficient of the} \\ \exp[j(\omega_1 + \omega_2 + \dots + \omega_n)t] \text{ term in the} \\ \text{expansion of } y(t) \end{array} \right\} . \quad (4.11)$$

This procedure is a bootstrap operation in that  $H_1(j\omega_1)$ ,  $H_2(j\omega_1, j\omega_2)$ , ...,  $H_n(j\omega_1, j\omega_2, \dots, j\omega_n)$  are determined in succession with the  $n^{\text{th}}$ -order response based on the  $(n-1)$  lower-order responses. The process can be stopped when the desired order response is obtained.

In summary, the Volterra series can be used to analyse a deterministic, time-invariant, asymptotically stable nonlinear system with memory. This method is most applicable to mild nonlinearities where low-order Volterra kernels can adequately model component and circuit behaviour. It is especially convenient for calculating the response of a nonlinear circuit to an input consisting of a sum of sine waves; e.g., distortion analysis of a nonlinear amplifier via multiple-tone testing. This analysis requires accurate models of the nonlinear devices in the circuit.

### 4.3 Distortion Analysis of a Stable IMPATT Amplifier Using Volterra Series Representation

#### 4.3.1 A Nonlinear Model of a Stable IMPATT Amplifier

Because the magnitudes of the nonlinear terms in the Volterra series are very small for small device nonlinearities, it is difficult to measure them accurately. A better approach is to calculate the Volterra series using a model which accounts for the nonlinear device-circuit interaction. The fundamental device nonlinearities, i.e. the electronic con-





ductance and susceptance, can be measured without too much difficulty as described in Chapter 3, and can be expressed in a form suitable for Volterra series analysis by curve-fitting techniques

A model for a circulator-coupled IMPATT-diode reflection amplifier is shown in Fig. 2.4. The passive two-port network is generally complex for practical amplifiers. Single-stage IMPATT amplifiers, however, are usually narrowband (typically less than 100 MHz). Consequently, over a sufficiently small bandwidth, say the 3-dB passband, the lumped-element model of Fig. 4.2 can be used [3], [12]. It consists of an ideal impedance transformer with turns ratio  $n_1:n_2$ , a parallel  $L_c C_c$  tuning network, and the IMPATT-diode electronic admittance  $Y_e$ . From experimental results, the variation of  $Y_e$  with frequency is very small over the frequency range that the model is valid, and can be neglected. The frequency dependence of the calculated distortion will then be solely due to reactive effects in the circuit. For constant bias current,  $I_{dc}$ , the electronic admittance from Eqn. (2.5) is given by

$$Y_e(V_e) = G_e(V_e) + j\omega C_e(V_e) \quad (4.12)$$

where

$G_e$  = the electronic conductance ( $G_e < 0$ ) at midband

$C_e$  = the equivalent electronic capacitance at midband

and  $V_e$  = the amplitude of the RF voltage at the fundamental frequency  $\omega$  across the diode's active region.

In IMPATT amplifiers with less than octave bandwidth, the circuit  $Q$  is high enough so that the effect of odd-order terms, in the power series expansion of  $G_e(V_e)$  or  $C_e(V_e)$ , on the magnitude  $I_e$  of the RF current at



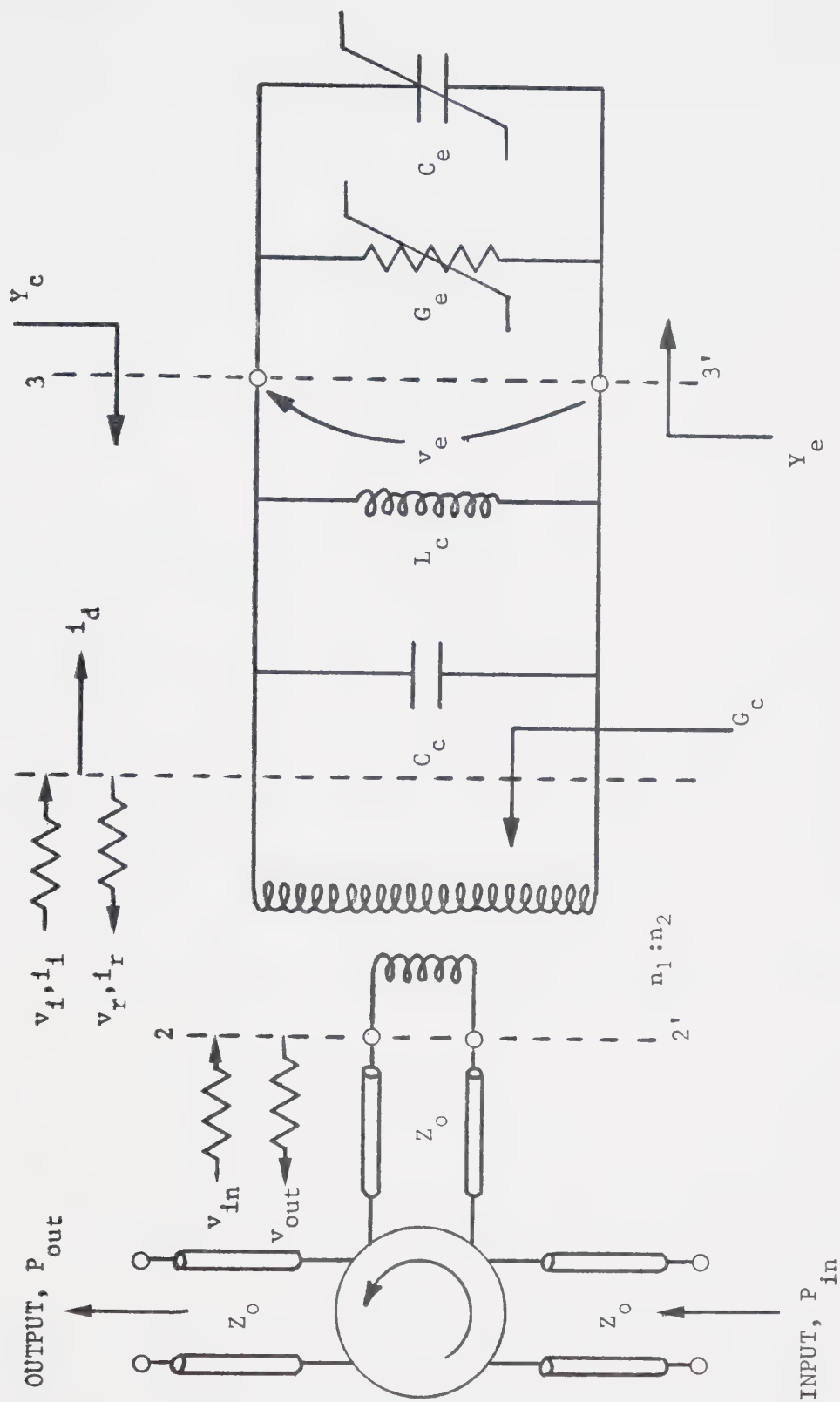


Figure 4.2 Equivalent circuit used for Volterra series distortion analysis of a stable IMPATT reflection amplifier.



the fundamental frequency  $\omega$  is secondary in nature, and the magnitude of the second- and higher-harmonic current is negligible compared to  $I_e$  [3], [67]. The nonlinear characteristics of the IMPATT diode may be expressed by [12], [13]

$$G_e(V_e) = g_0 + \gamma V_e^2 + \sum_{n=2}^{\infty} g_n V_e^{2n} \quad (4.13)$$

$$C_e(V_e) = c_0 + \lambda V_e^2 + \sum_{n=2}^{\infty} c_n V_e^{2n} \quad (4.14)$$

where  $g_0$  ( $g_0 < 0$ ) and  $c_0$  are small-signal values of the diode negative conductance and capacitance, respectively;  $\gamma, \lambda, g_n$  and  $c_n$  are constants. In the region of normal IMPATT amplifier operation, where  $V_e$  is much less than the bias voltage  $V_B$ , the terms for  $n=2$  and higher, in Eqns. (4.13) and (4.14) may be neglected [12]. The constants  $g_0, \gamma, c_0$  and  $\lambda$  can be evaluated by a quadratic polynomial interpolation of the measured large-signal electronic admittance data at the amplifier centre frequency (Fig. 3.15).

The equivalent circuit admittance  $Y_c(\omega)$  seen by the diode is

$$Y_c(\omega) = G_c + j[\omega C_c - (\omega L_c)^{-1}] \quad (4.15)$$

where

$$G_c = (n_1/n_2)^2 Y_0 \quad (4.16)$$

and  $Y_0$ , the characteristic admittance of the waveguide, is assumed to be purely real. Since the amplifier is tuned under small-signal conditions, the external inductance  $L_c$  resonates the effective capacitance ( $C_c + c_0$ )



at the centre frequency  $\omega_0$ .

The equivalent voltage and current components of the incident and reflected waves are denoted by  $v_i$ ,  $i_i$ ,  $v_r$  and  $i_r$  where the subscripts  $i$  and  $r$  refer to incident and reflected waves respectively. The incident and reflected waves are separated into the input and output signals by the circulator. The net current  $i_d$  into the diode and parallel  $L_c C_c$  network, and the voltage  $v_e$  across the diode terminals are given by

$$i_d(t) = i_i(t) - i_r(t) = G_c[v_i(t) - v_r(t)] \quad (4.17)$$

$$v_e(t) = v_i(t) + v_r(t) \quad (4.18)$$

Substituting the expression for  $v_r(t)$  from Eqn. (4.18) into (4.17) we have

$$i_d(t) = G_c[2v_i(t) - v_e(t)] \quad (4.19)$$

Since the generator is assumed to be matched to the circulator, the measured input power is

$$P_{in} = Y_0 |v_{in}|^2 / 2 \quad (4.20)$$

where  $v_{in}(t)$  is the incident voltage wave at reference plane 2-2'. The incident voltage wave,  $v_i(t)$ , referred to the secondary of the lossless impedance transformer is related to  $v_{in}(t)$  by

$$v_{in}(t) = (n_1/n_2)v_i(t) \quad (4.21)$$





Substitution of Eqn. (4.21) into (4.20) and using (4.16) gives

$$V_1 = |v_i(t)| = \left[ \frac{2P_{in}}{Y_0} \left( \frac{n_2}{n_1} \right)^2 \right]^{1/2} = \sqrt{2P_{in}/G_c} \quad (4.22)$$

In the equivalent circuit of Fig. 4.2,  $i_d$  and  $v_e$  are related by the following integro-differential equation:

$$i_d(t) = C_c \frac{dv_e(t)}{dt} + \int_{-\infty}^t \frac{1}{L_c} v_e(t) dt + \frac{d}{dt} [C_e v_e(t)] + G_e v_e(t) \quad (4.23)$$

Substituting Eqns. (4.13), (4.14) and (4.19) into (4.23), and then differentiating we obtain

$$\begin{aligned} 2G_c \frac{dv_i(t)}{dt} = [C_c + c_o + 3\lambda v_e^2(t)] \frac{d^2 v_e(t)}{dt^2} + [G_c + g_o + 3\gamma v_e^2(t)] \frac{dv_e(t)}{dt} \\ + 6\lambda v_e(t) \left[ \frac{dv_e(t)}{dt} \right]^2 + \frac{v_e(t)}{L_c} \quad (4.24) \end{aligned}$$

The IMPATT amplifier is described by the nonlinear differential equation (4.24) in conjunction with Eqn. (4.18).

It is assumed that the nonlinear model can be represented by a Volterra series. A sufficient condition for the existence of a Volterra series for a nonlinear system is that the operation of the system be restricted to a region of asymptotic stability [21]. This includes the IMPATT amplifier under discussion. It is also assumed that the diode nonlinearities are small enough that the first five terms of the Volterra series are sufficient to characterize them. Truncating the infinite series in Eqns. (4.4) to (4.7), the nonlinear output response  $v_r(t)$  is related to



a causal input signal  $v_i(t)$  by

$$v_r(t) = H[v_i(t)] = \sum_{n=1}^5 \int_0^t \cdots \int_0^t h_n(\tau_1, \tau_2, \dots, \tau_n) \prod_{i=1}^n v_i(t-\tau_i) d\tau_i \quad (4.25)$$

where  $h_n(\tau_1, \tau_2, \dots, \tau_n)$  is the  $n^{\text{th}}$ -order Volterra kernel for the nonlinear equivalent circuit. The  $n^{\text{th}}$ -order Fourier transform of  $h_n(\tau_1, \tau_2, \dots, \tau_n)$  is the  $n^{\text{th}}$ -order Volterra transfer function  $H_n(j\omega_1, j\omega_2, \dots, j\omega_n)$ . Similarly, the circuit response  $v_e(t)$  is related to  $v_i(t)$  by

$$v_e(t) = K[v_i(t)] = \sum_{n=1}^5 \int_0^t \cdots \int_0^t k_n(\tau_1, \tau_2, \dots, \tau_n) \prod_{i=1}^n v_i(t-\tau_i) d\tau_i \quad (4.26)$$

where  $K_n(j\omega_1, j\omega_2, \dots, j\omega_n)$  is the  $n^{\text{th}}$ -order Fourier transform of the  $n^{\text{th}}$ -order kernel  $k_n(\tau_1, \tau_2, \dots, \tau_n)$ .

#### 4.3.2 Determination of the IMPATT-Amplifier Volterra Transfer Functions

The Volterra transfer functions for the IMPATT amplifier will be evaluated analytically by the harmonic input method [86], [92].

First let the amplifier input be

$$v_i(t) = \exp(j\omega_1 t) \quad (4.27)$$

where  $\omega_1$  is in the passband of the amplifier. Assume a harmonic response

$$v_e(t) = \sum_{n=1}^{\infty} a_n \exp(jn\omega_1 t) \quad (4.28)$$

Since Eqns. (4.18) and (4.24) must be satisfied for all  $t$  and for any  $\omega$ ,



each harmonic component must also individually satisfy the equations.

Equating the coefficients of the desired term  $\exp(j\omega_1 t)$  on both sides of Eqn. (4.24) after substitution of Eqns. (4.27) and (4.28) we get

$$a_1 = K_1(j\omega_1) = \frac{j2\omega_1 G_c}{L_c^{-1} - (C_c + c_o)\omega_1^2 + j\omega_1(G_c + g_o)} \quad (4.29)$$

Equating the coefficients of  $\exp(j\omega_1 t)$  in Eqn. (4.18) using (4.25)-(4.29) yields

$$H_1(j\omega_1) = K_1(j\omega_1) - 1 \quad (4.30)$$

Thus, for the given circuit, the first-order transfer function  $H_1(j\omega_1)$  is simply the special solution of Eqns. (4.18) and (4.24) when  $\gamma = \lambda = 0$ ; i.e.,  $H_1(j\omega_1)$  is the linear response. Note that the resonant frequency  $\omega_o$  is given by

$$\omega_o = [L_c(C_c + c_o)]^{-1/2} \quad (4.31)$$

and the small-signal gain  $A$  is

$$A = H_1(j\omega_o) = \frac{G_c - g_o}{G_c + g_o} \quad (4.32)$$

as expected from linear circuit analysis. Since  $g_o < 0$  and  $G_c > |g_o|$ , the gain  $A$  is greater than unity.

Proceeding similarly to determine the second-order Volterra transfer function  $H_2(j\omega_1, j\omega_2)$ , let the input be

$$v_1(t) = \exp(j\omega_1 t) + \exp(j\omega_2 t) \quad (4.33)$$



where  $\omega_1$  and  $\omega_2$  are incommensurable frequencies lying in the amplifier passband. Assume a harmonic response

$$v_e(t) = \sum_{m=0}^{\infty} \sum_{n=0}^{\infty} a_{mn} \exp[j(m\omega_1 t + n\omega_2 t)] \quad (4.34)$$

Substituting Eqns. (4.33) and (4.34) into Eqn. (4.24) and employing the principle of harmonic balance together with (4.18) gives the desired coefficients:

$$a_{00} = K_2(0,0) = H_2(0,0) \equiv 0 \quad (4.35)$$

$$a_{10} = K_2(j\omega_1, 0) = K_1(j\omega_1) = H_1(j\omega_1) + 1 \quad (4.36)$$

$$a_{01} = K_2(0, j\omega_2) = K_1(j\omega_2) = H_1(j\omega_2) + 1 \quad (4.37)$$

$$\text{and } a_{11} = K_2(j\omega_1, j\omega_2) = H_2(j\omega_1, j\omega_2) \equiv 0 \quad (4.38)$$

The second-order Volterra transfer function  $H_2(j\omega_1, j\omega_2)$  at the frequency  $\omega_1 + \omega_2$  is identically zero as a consequence of the assumptions leading to Eqns. (4.13) and (4.14).

In the same way, the third-order Volterra transfer function  $H_3(j\omega_1, j\omega_2, j\omega_3)$  at the frequency  $\omega_1 + \omega_2 + \omega_3$  is determined to be

$$a_{111} = K_3(j\omega_1, j\omega_2, j\omega_3) = H_3(j\omega_1, j\omega_2, j\omega_3) \quad (4.39)$$

$$\text{or } H_3(j\omega_1, j\omega_2, j\omega_3) = \frac{6(\omega_1 + \omega_2 + \omega_3)[\lambda(\omega_1 + \omega_2 + \omega_3) - j\gamma] \prod_{i=1}^3 K_1(j\omega_i)}{L_c^{-1} - (C_c + c_o)(\omega_1 + \omega_2 + \omega_3)^2 + j(\omega_1 + \omega_2 + \omega_3)(G_c + g_o)} \quad (4.40)$$





This procedure can be continued indefinitely to find higher-order nonlinear transfer functions in terms of lower-order nonlinear transfer functions as in Eqn. (4.37). Because  $H_2(j\omega_1, j\omega_2)$  is identically zero, all even higher-order transfer functions will also be zero. All odd-order transfer functions will be nonzero. It is assumed, however, that the device nonlinearities are sufficiently small that the first five terms of the Volterra series suffice to characterize them. The fifth-order Volterra transfer function at the frequency  $(\omega_1 + \omega_2 + \omega_3 + \omega_4 + \omega_5)$  is given by

$$\begin{aligned}
 H_5(j\omega_1, j\omega_2, j\omega_3, j\omega_4, j\omega_5) = & \\
 6 \left\{ 2 \lambda \sum_{10}' \omega_1 K_1(j\omega_1) \omega_2 K_1(j\omega_2) H_3(j\omega_3, j\omega_4, j\omega_5) \right. & \\
 + 2 \lambda \sum_5' \left[ \omega_1 K_1(j\omega_1) \sum_4' K_1(j\omega_2) (\omega_3 + \omega_4 + \omega_5) H_3(j\omega_3, j\omega_4, j\omega_5) \right] & \\
 + \lambda \sum_{10}' K_1(j\omega_1) K_1(j\omega_2) (\omega_3 + \omega_4 + \omega_5)^2 H_3(j\omega_3, j\omega_4, j\omega_5) & \\
 + \lambda \sum_5' \left[ \omega_1^2 K_1(j\omega_1) \sum_4' K_1(j\omega_2) H_3(j\omega_3, j\omega_4, j\omega_5) \right] & \\
 - j \gamma \sum_5' \left[ \omega_1 K_1(j\omega_1) \sum_4' K_1(j\omega_2) H_3(j\omega_3, j\omega_4, j\omega_5) \right] & \\
 - j \gamma \sum_{10}' K_1(j\omega_1) K_1(j\omega_2) (\omega_3 + \omega_4 + \omega_5) H_3(j\omega_3, j\omega_4, j\omega_5) \left. \right\} \cdot & \\
 \left\{ L_c^{-1} - (C_c + c_o) (\omega_1 + \omega_2 + \omega_3 + \omega_4 + \omega_5)^2 + j (\omega_1 + \omega_2 + \omega_3 + \omega_4 + \omega_5) (G_c + g_o) \right\}^{-1} & \quad (4.41)
 \end{aligned}$$



where the summation  $\sum_N'$  extends over the  $N$  nonidentical products that can be obtained by permuting the subscripts of the arguments  $\omega_1$ .

$H_n(j\omega_1, j\omega_2, \dots, j\omega_n)$  is symmetric, and "identical" is used in the sense that  $H_2(j\omega_1, j\omega_2)$  is identical with  $H_2(j\omega_2, j\omega_1)$  and  $H_1(j\omega_1) \cdot H_1(j\omega_2)$  is identical with  $H_1(j\omega_2) \cdot H_1(j\omega_1)$ . From Eqn. (4.41), it can be seen how rapidly the high-order transfer functions become very complex:  $H_5$  has 90 terms in the numerator.

#### 4.3.3 Intermodulation Distortion in an IMPATT Amplifier

As discussed in Sec. 2.3, a two-tone test is used here to analyse intermodulation (IM) distortion. Let the input to the IMPATT amplifier consist of two unmodulated signals of equal amplitude at incommensurable frequencies  $\omega_1$  and  $\omega_2$ ; i.e.,

$$v_i(t) = V(\cos \omega_1 t + \cos \omega_2 t) \quad . \quad (4.42)$$

The amplitude  $V$  is related to the input power by Eqn. (4.22) where  $P_{in}$  in this case is the input power per tone.

Nonlinearities in the amplifier will give rise to IM distortion products at frequencies  $\omega_1 \pm \omega_2$ ,  $2\omega_1 \pm \omega_2$ ,  $2\omega_2 \pm \omega_1$ ,  $3\omega_1 \pm 2\omega_2$ , etc.. Since the bandwidth of the amplifier under consideration is much less than an octave, in-band IM products occur at  $2\omega_1 - \omega_2$ ,  $2\omega_2 - \omega_1$ ,  $3\omega_1 - 2\omega_2$ ,  $3\omega_2 - 2\omega_1$ , etc.

Third-order intermodulation  $IM_3$  is defined in Eqn. (2.2). Since the Volterra series representing the nonlinear model includes terms up to the fifth-order, both the third- and fifth-degree Volterra kernels will contribute to the third-order distortion products. For small distortion only these terms need be included, as the higher-order kernels be-



come very small. It is shown in Appendix A that, for small distortion and for input frequencies  $\omega_1 \approx \omega_2$ , the third-order IM product in the response  $v_r(t)$  at frequency  $2\omega_1 - \omega_2$  is

$$\begin{aligned}
 v_{2\omega_1 - \omega_2}(t) = & \frac{3}{4} V^3 |H_3(j\omega_1, j\omega_1, -j\omega_2)| \cos[(2\omega_1 - \omega_2)t + \arg H_3(j\omega_1, j\omega_1, -j\omega_2)] \\
 & + \frac{5}{4} V^5 |H_5(j\omega_1, j\omega_1, -j\omega_2, j\omega_1, -j\omega_1)| \cos[(2\omega_1 - \omega_2)t \\
 & + \arg H_5(j\omega_1, j\omega_1, -j\omega_2, j\omega_1, -j\omega_1)] \\
 & + \frac{15}{8} V^5 |H_5(j\omega_1, j\omega_1, -j\omega_2, j\omega_2, -j\omega_2)| \cos[(2\omega_1 - \omega_2)t \\
 & + \arg H_5(j\omega_1, j\omega_1, -j\omega_2, j\omega_2, -j\omega_2)] \quad . \quad (4.43)
 \end{aligned}$$

Due to the symmetry of  $H_3$  and  $H_5$  in their arguments, the third-order IM product in the response  $v_r(t)$  at frequency  $2\omega_2 - \omega_1$  is the same expression as Eqn. (4.43) with  $\omega_1$  and  $\omega_2$  interchanged. The fundamental signal in  $v_r(t)$  at frequency  $\omega_1$  is given by

$$v_{\omega_1}(t) = V |H_1(j\omega_1)| \cos[\omega_1 t + \arg H_1(j\omega_1)] \quad . \quad (4.44)$$

Substituting the amplitude of  $v_{2\omega_1 - \omega_2}(t)$  from Eqn. (4.43) (noting the phase differences between the Volterra kernels) and the amplitude of  $v_{\omega_1}(t)$  from (4.44) into (2.2) yields the third-order IM distortion in the output of the amplifier at  $2\omega_1 - \omega_2$ :

$$IM_3(dB) = 20 \log \left\{ \frac{V^2}{4 |H_1(j\omega_1)|} \left| 3H_3(j\omega_1, j\omega_1, -j\omega_1) + 5V^2 H_5(j\omega_1, j\omega_1, -j\omega_1, j\omega_1, -j\omega_1) \right| \right\}$$



$$+ \frac{15}{2} V^2 \left| H_5(j\omega_1, j\omega_1, -j\omega_2, j\omega_2, -j\omega_2) \right| \quad (4.45)$$

Similarly the fifth-order intermodulation distortion  $IM_5$  is defined in Eqn. (2.3). Because the Volterra series is truncated at the fifth-degree term, only the fifth-order Volterra kernel will contribute to the fifth-order IM products at  $3\omega_1 - 2\omega_2$  and  $3\omega_2 - 2\omega_1$ . It is shown in Appendix A that, for small distortion and input frequencies  $\omega_1 \approx \omega_2$ , the fifth-order IM product in the output at frequency  $3\omega_1 - 2\omega_2$  is

$$v_{3\omega_1 - 2\omega_2}(t) = \frac{5}{8} V^5 |H_5(j\omega_1, j\omega_1, j\omega_1, -j\omega_2, -j\omega_2)| \cdot \cos [(3\omega_1 - 2\omega_2)t + \arg H_5(j\omega_1, j\omega_1, j\omega_1, -j\omega_2, -j\omega_2)] \quad (4.46)$$

Again, since  $H_5$  is symmetrical in its arguments, the fifth-order product at  $3\omega_2 - 2\omega_1$  is the same expression as Eqn. (4.46), with  $\omega_1$  and  $\omega_2$  interchanged. The amplitude of  $v_{3\omega_1 - 2\omega_2}(t)$  and of  $v_{\omega_1}(t)$ , from Eqns. (4.46) and (4.44), is employed in (2.3) to obtain the fifth-order IM distortion in the amplifier output at  $3\omega_1 - 2\omega_2$ :

$$IM_5(\text{dB}) = 20 \log \left\{ \frac{5V^4 |H_5(j\omega_1, j\omega_1, j\omega_1, -j\omega_2, -j\omega_2)|}{8 |H_1(j\omega_1)|} \right\} \quad (4.47)$$

The Volterra transfer functions  $H_1$ ,  $H_3$  and  $H_5$  are expressed in terms of the parameters of the amplifier nonlinear model. Once the values of these parameters have been determined experimentally, the IM distortion  $IM_3$  and  $IM_5$  can be computed.

For small distortion, a closed-form expression for  $IM_3$  can be derived directly in terms of the device nonlinearities. In this case, the





contribution of the fifth-order term  $H_5$  to  $IM_3$  can be neglected and  $IM_3$  becomes, from (4.45),

$$IM_3 \text{ (dB)} = 20 \log \left\{ \frac{3V^2 |H_3(j\omega_1, j\omega_1, -j\omega_2)|}{4 |H_1(j\omega_1)|} \right\} \quad (4.48)$$

Then, considering operation near the resonant frequency  $\omega_0$  at midband so that  $\omega_1 \approx \omega_2 \approx \omega_0$ , and substituting the small-signal gain  $A$  from Eqn. (4.32) into (4.40), we get

$$H_3(j\omega_1, j\omega_1, -j\omega_2) = \frac{6(\lambda\omega_c - j\gamma)(A+1)^3}{j(G_c + g_o)} \quad (4.49)$$

$$\text{or } |H_3(j\omega_1, j\omega_1, -j\omega_2)| = \frac{6 \left[ (\lambda\omega_0)^2 + \gamma^2 \right]^{1/2} (A+1)^3}{G_c + g_o} \quad (4.50)$$

Substituting Eqns. (4.32) and (4.50) into (4.48) results in

$$IM_3 \text{ (dB)} = 20 \log \left\{ 36 \frac{\left[ (\lambda\omega_0)^2 + \gamma^2 \right]^{1/2} G_c^3 V^2}{(G_c - g_o)(G_c + g_o)^3} \right\} \quad (4.51)$$

Lastly, relating the amplitude  $V$  to the input power  $P_{in}$  per tone from Eqn. (4.22), we obtain the simplified expression

$$IM_3 \text{ (dB)} = 20 \log \left\{ \frac{72 \left[ (\lambda\omega_0)^2 + \gamma^2 \right]^{1/2} G_c^2 P_{in}}{(G_c - g_o)(G_c + g_o)^3} \right\} \quad (4.52)$$

Equation (4.52) relates the third-order distortion  $IM_3$  to the small de-



vice nonlinearities  $\lambda$  and  $\gamma$  directly, as a function of the input power per tone near midband.

#### 4.3.4 Third- and Fifth-Order Intercept Points of an IMPATT Amplifier

The third- and fifth-order intercept points  $P_3$  and  $P_5$  defined in Sec. 2.3.2 can be determined once  $|H_1|$ ,  $IM_3$  and  $IM_5$  have been calculated and plotted on a logarithmic scale. In the case of small distortion a closed-form expression for the third-order intercept point  $P_3$  can be derived as follows.

Using the definitions of  $P_3$  and  $IM_3$  the intercept point occurs at the output power where  $IM_3$  is 0 dB or where, from Eqn. (4.52), the input power per tone is

$$P_{in}(W) = \frac{(G_c - g_o)(G_c + g_o)^3}{72 [(\lambda \omega_o)^2 + \gamma^2]^{1/2} G_c^2} \quad (4.53)$$

Since the output power (in dBm) at the intercept point  $P_3$  is

$$P_3(\text{dBm}) = 10 \log (A^2 \cdot P_{in}(W)) + 30 \quad (4.54)$$

after substituting Eqns. (4.32) and (4.53) we have

$$P_3(\text{dBm}) = 10 \log \left\{ \frac{(G_c - g_o)^3 (G_c + g_o)}{[(\lambda \omega_o)^2 + \gamma^2]^{1/2} G_c^2} \right\} + 11.43 \quad (4.55)$$

Equation (4.55) is a relatively simple expression relating the intercept point to the device nonlinearities.



### 4.3.5 Gain Compression in an IMPATT Amplifier

Gain compression is the nonlinear effect observed in an amplifier when, if the amplitude  $V$  of a single-frequency input signal

$$v_1(t) = V \cos \omega_1 t \quad (4.56)$$

is increased, the amplifier output does not increase linearly with the input but, rather, gradually falls behind. On the other hand, if the gain increases, the nonlinear effect is called gain expansion. Gain compression or gain expansion can be investigated using the Volterra transfer functions [92]. For small device nonlinearities, the terms accounting for this effect are  $H_3(j\omega_1, j\omega_1, -j\omega_1)$  and  $H_5(j\omega_1, j\omega_1, j\omega_1, -j\omega_1, -j\omega_1)$ . The response  $v_r(t)$  at frequency  $\omega_1$  is shown in Appendix B to be

$$\begin{aligned} v_{\omega_1}(t) = & V |H_1(j\omega_1)| \cos [\omega_1 t + \arg H_1(j\omega_1)] \\ & + \frac{3}{4} V^3 |H_3(j\omega_1, j\omega_1, -j\omega_1)| \cos [\omega_1 t + \arg H_3(j\omega_1, j\omega_1, -j\omega_1)] \\ & + \frac{5}{8} V^5 |H_5(j\omega_1, j\omega_1, j\omega_1, -j\omega_1, -j\omega_1)| \cos [\omega_1 t \\ & + \arg H_5(j\omega_1, j\omega_1, j\omega_1, -j\omega_1, -j\omega_1)] \end{aligned} \quad (4.57)$$

The departure from linearity can be examined by considering the compression ratio  $c$  in dB defined by [92]:

$$c(\text{dB}) = 10 \log \left| \frac{\text{Amplitude of output at fundamental frequency}}{\text{Amplitude of linear term in output at fundamental frequency}} \right| \quad (4.58)$$



Substituting the absolute values of Eqns. (4.44) and (4.57) into (4.58) results in

$$c(\text{dB}) = 20 \log \left| 1 + \frac{3V^2 H_3(j\omega_1, j\omega_1, -j\omega_1)}{4 H_1(j\omega_1)} + \frac{5V^4 H_5(j\omega_1, j\omega_1, j\omega_1, -j\omega_1, -j\omega_1)}{8 H_1(j\omega_1)} \right| \quad (4.59)$$

In narrowband circuits such as IMPATT amplifiers, the relative phases of  $H_1$ ,  $H_3$  and  $H_5$  may be highly frequency dependent. Depending on their relative phase, the odd-order products may vectorially add to, or subtract from, the desired signal, thus causing gain expansion or compression respectively.

#### 4.3.6 Computed IMPATT-Amplifier Distortion

The IMPATT-amplifier gain and phase shift were measured across the passband as will be discussed in Chapter 6. The experimental small-signal response ( $P_{\text{in}} = -30 \text{ dBm}$ ) is plotted in Fig. 4.3. At the centre frequency 5.905 GHz, the amplifier has 17.3-dB gain. The 3-dB bandwidth extends from 5.879 to 5.943 GHz. The coefficients of Eqns. (4.13) and (4.14) (neglecting terms of higher degree than the quadratic) were fitted to the electronic admittance data of Fig. 3.15 for RF voltage amplitudes up to 10 V at the centre frequency; the maximum error in the least mean-squares fit was 1.7% for the electronic conductance and 1.3% for the equivalent electronic capacitance. The circuit parameters  $G_c$ ,  $L_c$ ,  $C_c$  were then chosen using Eqns. (4.31) and (4.32) to give the nonlinear model of the amplifier the same small-signal gain at the centre frequency, with the same Q and 3-dB bandwidth as the experimental amplifier. The calculated values for the parameters in the nonlinear equivalent circuit of the IMPATT amplifier are listed in Table 4.1. In Fig. 4.3, the small-signal gain behaviour





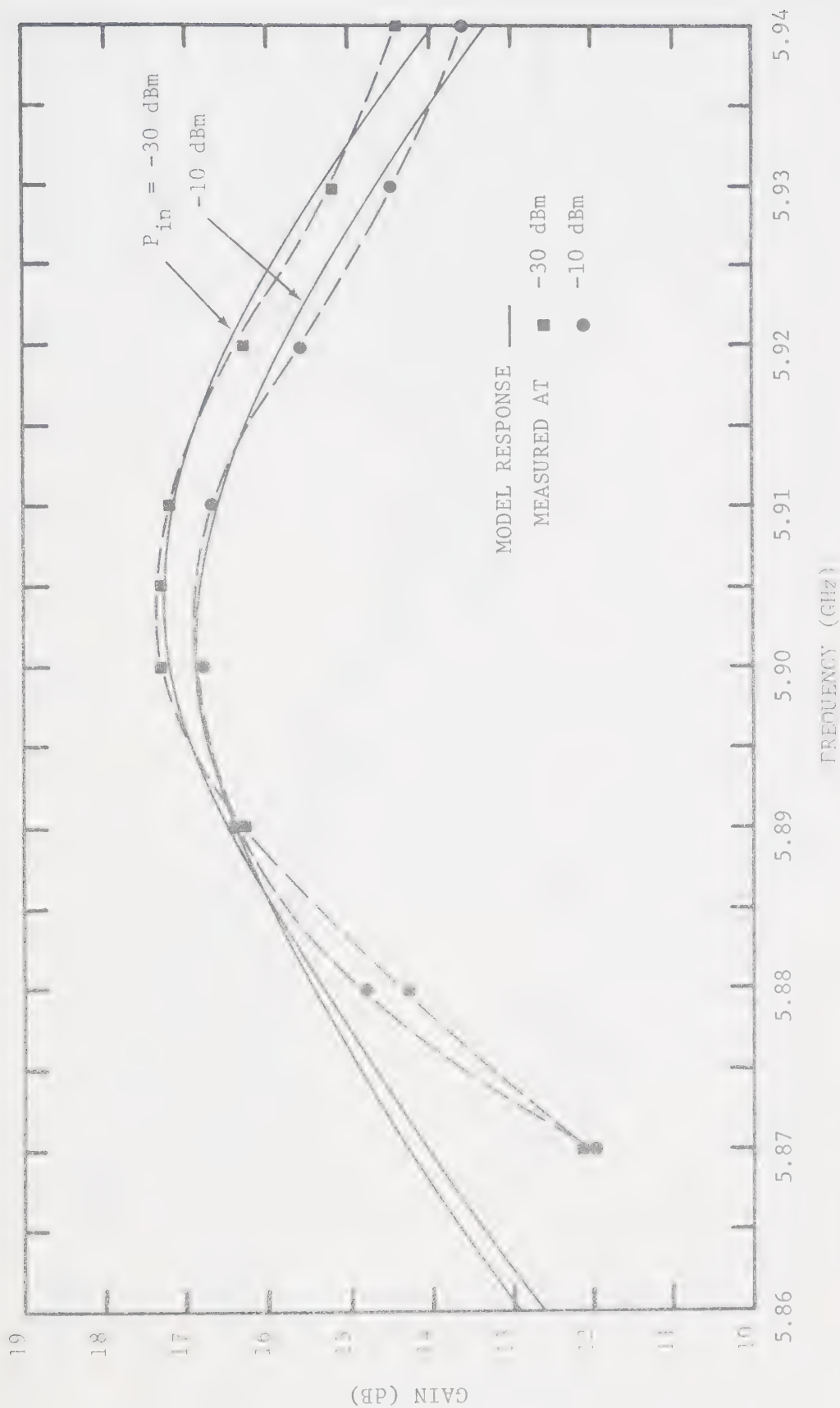


Figure 4.3 Comparison of measured IMPATT-amplifier gain with the gain predicted using the IMPATT-diode amplifier model for Volterra series distortion analysis (at 25-mA dc bias current).



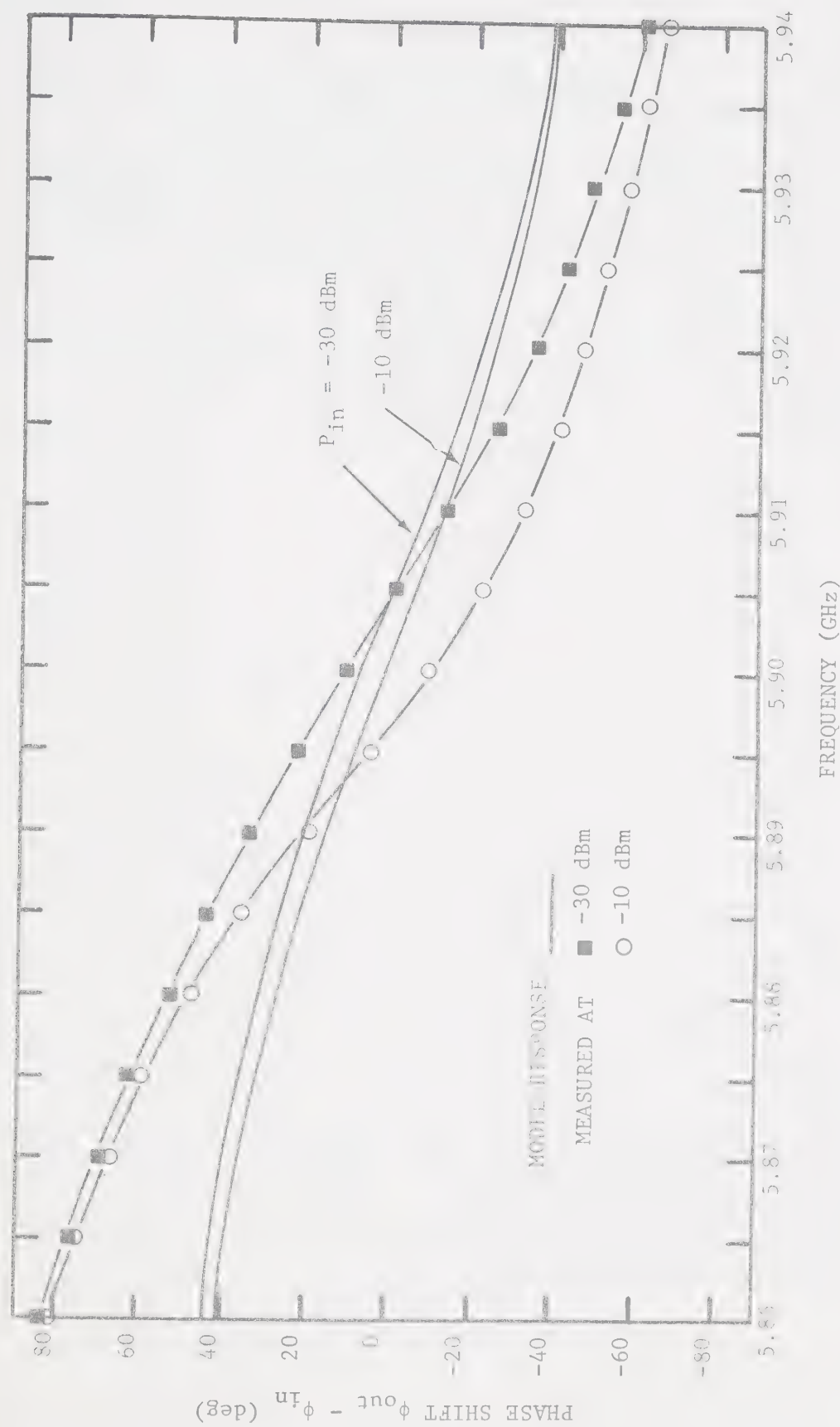


Figure 4.4 Comparison of measured IMPATT-amplifier phase shift with the phase shift predicted using the IMPATT-diode amplifier model for Volterra series distortion analysis (at 25-mA dc bias current).



TABLE 4.1

## IMPATT-AMPLIFIER NONLINEAR MODEL PARAMETERS

PARAMETER	VALUE	DIMENSION
$g_o$	-1.027	mS
$\gamma$	$8.651 \times 10^{-4}$	mS/V <sup>2</sup>
$c_o$	0.1643	pF
$\lambda$	$6.288 \times 10^{-5}$	pF/V <sup>2</sup>
$G_c$	1.351	mS
$L_c$	0.8998	nH
$C_c$	0.6430	pF

of the nonlinear equivalent circuit is seen to approximate the measured response within 0.5 dB over the 3-dB passband. The phase shift of the amplifier model does not follow the measured phase shift as closely in Fig. 4.4; the predicted phase shift does not change fast enough with frequency due to the insufficient reactance slope ( $dX/d\omega$ ) of the single  $L_c(C_c+c_o)$  tuned circuit. However, the measured and predicted phase shift do agree within 20° over the passband. The predicted and measured response differ significantly for input levels larger than -10 dBm, or an RF voltage 5 V across the active diode, where terms higher than the quadratic cannot be neglected in the characterization of the diode's electronic admittance by Eqns. (4.13) and (4.14).

The variation of the IMPATT's conductance parameters,  $g_o$ ,  $\gamma$ , and the IMPATT's capacitance parameters,  $c_o$ ,  $\lambda$ , with frequency is shown in



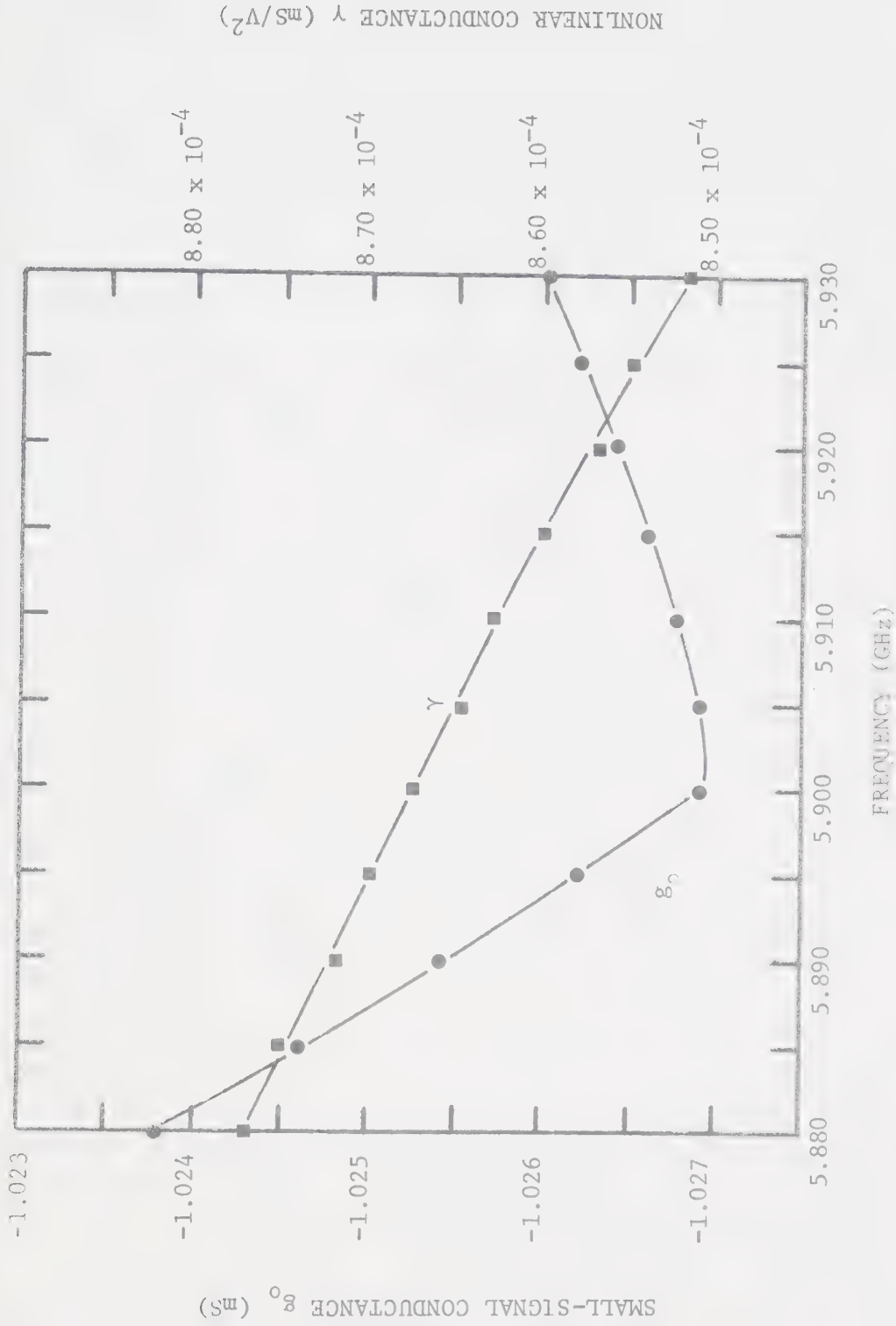


Figure 4.5 Calculated values of small-signal electronic conductance and the nonlinear conductance parameters in the characterization of the IMPATT-diode electronic conductance ( $I_{dc} = 25$  mA) for Volterra series distortion analysis.





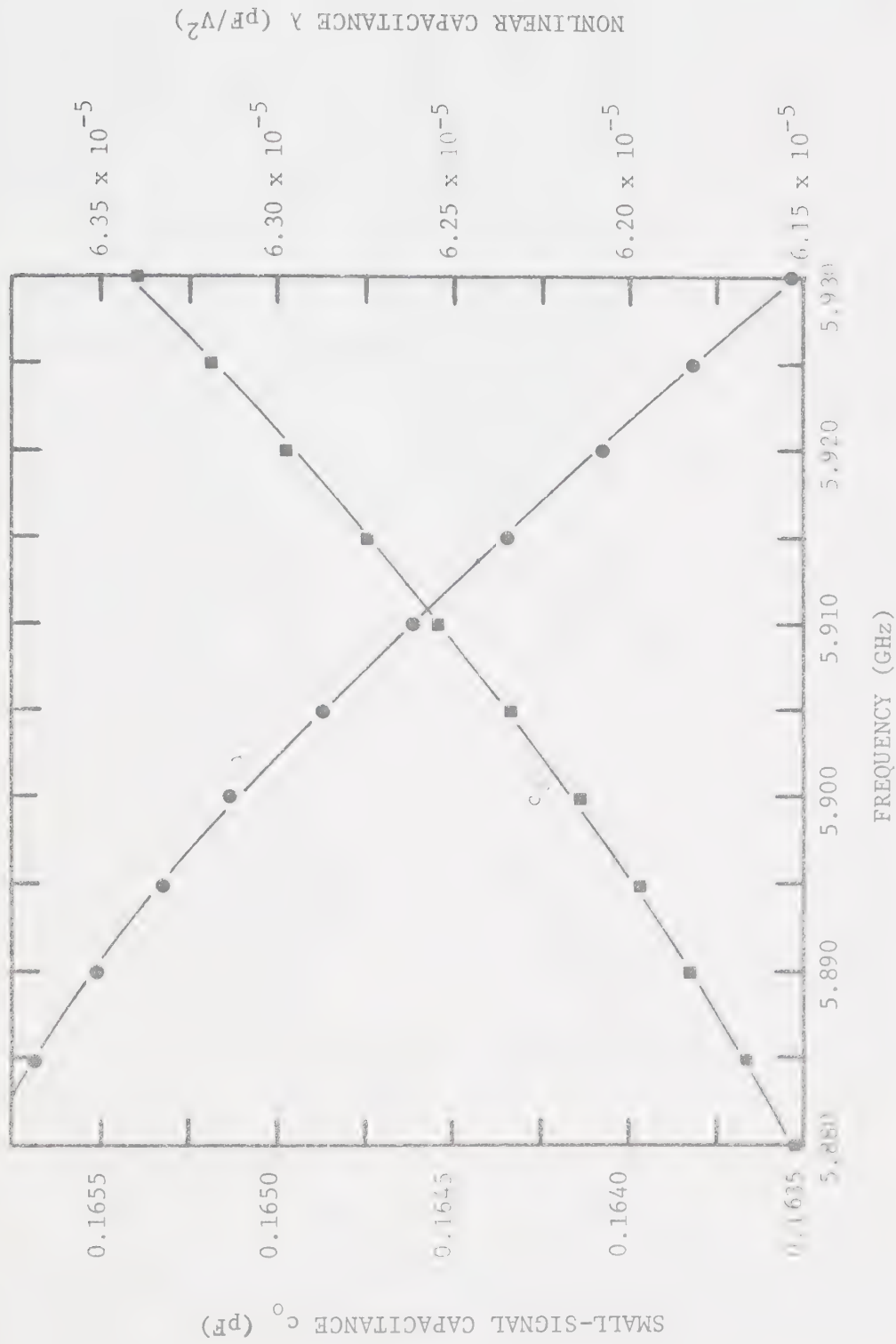


Figure 4.6 Calculated values of small-signal equivalent diode capacitance and the nonlinear diode capacitance parameter in the characterization of the MPATT-diode electronic susceptance ( $I_{dc} = 25$  mA) for Volterra series distortion analysis.



Figs. (4.5) and (4.6), respectively. All of these parameters do not change appreciably from their values at the centre frequency, 5.905 GHz. The effect of such variations on the computed results was found to be negligible. Fixing the model parameters to the values in Table 4.1 is, therefore, a reasonable assumption.

Figures 4.7 to 4.9 show the linear, third- and fifth-order non-linear transfer functions, respectively, for a two-tone input (1-MHz separation) in the passband of the amplifier. The amplitudes of the Volterra transfer functions are maximum at or near the centre frequency. At input signal levels less than -21 dBm, corresponding to a maximum RF voltage 1.8 V across the active diode, the nonlinear model response in Fig. 4.3 deviates only slightly from the linear transfer function. This indicates that seventh- and higher-order responses contribute negligibly and that the fifth-order model is adequate for that range of inputs.

The dependence of two-tone IM distortion on frequency for a constant total output power of -10 dBm is depicted in Figs. 4.10(a) and (b). The value of third-order IM distortion calculated when neglecting the effect of fifth-order products is seen to be maximum at 5.905 GHz or the centre frequency for the small-signal case. At the higher signal level required for -10 dBm output power, where fifth-order effects come into play, the amplifier gain decreases and the resonant frequency shifts to a lower frequency. Since device nonlinearities are coupled most strongly to the external circuit at the resonant frequency,  $IM_3$  decreases and also shifts as plotted in Fig. 4.10(a) when fifth-order distortion is included. This effect was also observed experimentally by Trew *et al.* [32]. The fifth-order IM distortion, Fig. 4.10(b), is 37 dB below  $IM_3$  on average.



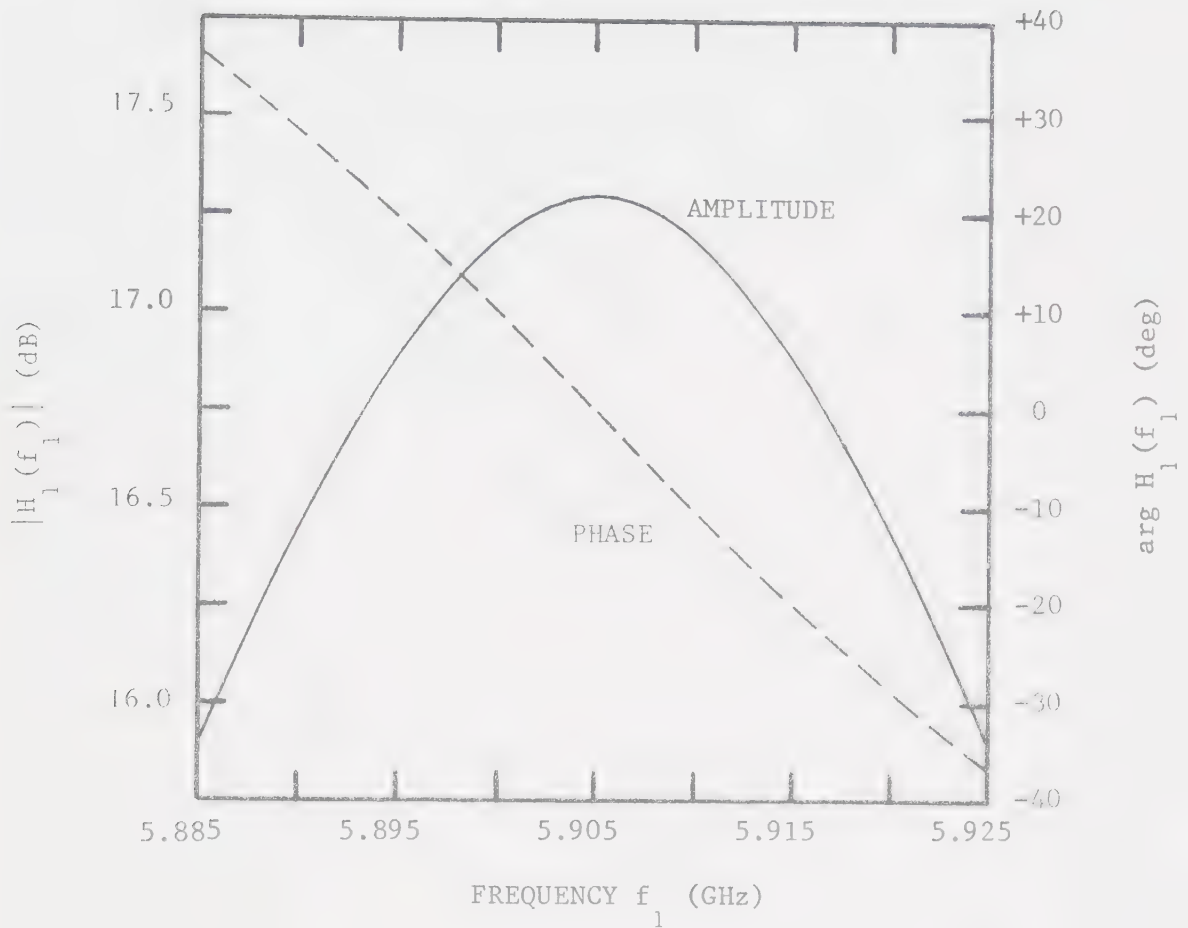


Figure 4.7 Computed linear transfer function, at frequency  $f_1$ , for the experimental IMPATT amplifier ( $I_{dc} = 25$  mA) with a CW input.



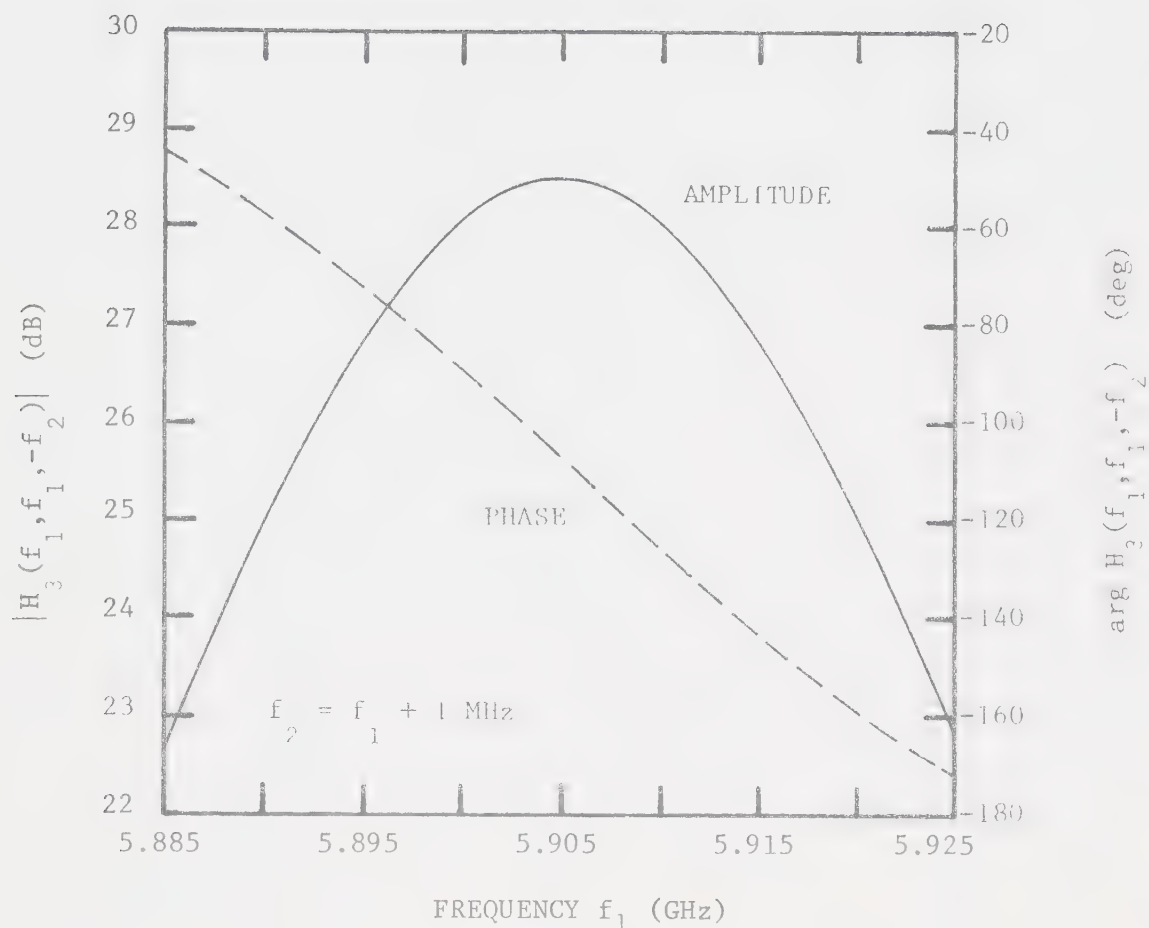


Figure 4.8 Computed third-order nonlinear (Volterra) transfer function, at frequency  $2f_1 - f_2$ , for the experimental IMPATT amplifier ( $I_{dc} = 25 \text{ mA}$ ) with a two-tone input ( $f_2 = f_1 + 1 \text{ MHz}$ ).





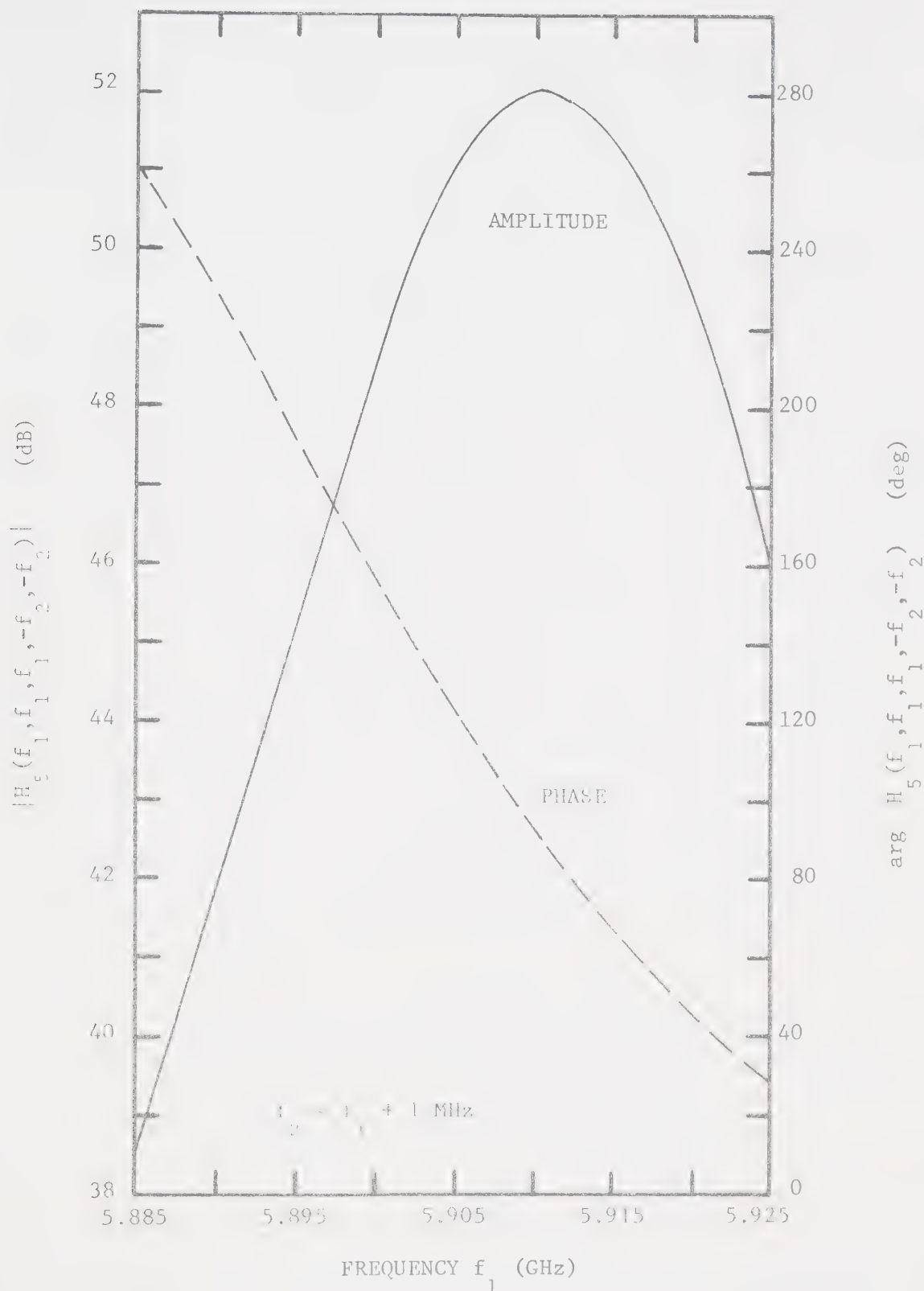


Figure 4.9 Computed fifth-order nonlinear (Volterra) transfer function, at frequency  $3f_1 - 2f_2$ , for the experimental IMPATT amplifier ( $I_{dc} = 25$  mA) with a two-tone input ( $f_2 = f_1 + 1$  MHz).



The results in Fig. 4.10 demonstrate that the magnitude of the IM products is dependent upon both the nonlinear mixing properties of the IMPATT diode and the amplifier passband behaviour. The variation in  $IM_3$  across the passband is 2 dB, whereas  $IM_5$  varies by 8 dB.

Third- and fifth-order IM distortion as a function of input power at the centre frequency 5.905 GHz for a two-tone input with a fixed frequency offset of 1 MHz are plotted in Fig. 4.11.  $IM_3$  is plotted both including and neglecting the effect of fifth-order products. For input levels less than -30 dBm per tone, the fifth-order products contribute negligibly to  $IM_3$ . At an input level of -21 dBm per tone or -18 dBm total power, the value of  $IM_3$  including fifth-order distortion is 3 dB below the value neglecting fifth-order effects. Therefore an input level of -21 dBm per tone is taken as an upper limit on the range of validity of the small-signal nonlinear Volterra series model. For higher input power levels, more terms must be included in the Volterra series to represent the device nonlinearities adequately. The fact that the model breaks down at such a low power level, corresponding to an amplitude of about 1.8 V for the RF voltage across the experimental IMPATT diode, indicates that the diode is quite nonlinear.

The output power at the fundamental ( $f_1$ ), at the third-order distortion product ( $2f_1-f_2$ ), and at the fifth-order distortion product ( $3f_1-2f_2$ ) for a two-tone input under the same conditions as for Fig. 4.11 is plotted in Fig. 4.12. It can be seen that, at -18 dBm total input power, third-order IM distortion is 34 dB below the fundamental and fifth-order IM distortion is 47 dB below the fundamental. The fundamental output power is -3 dBm (0 dBm total) for the same input. At higher power levels the fundamental output power begins to saturate;



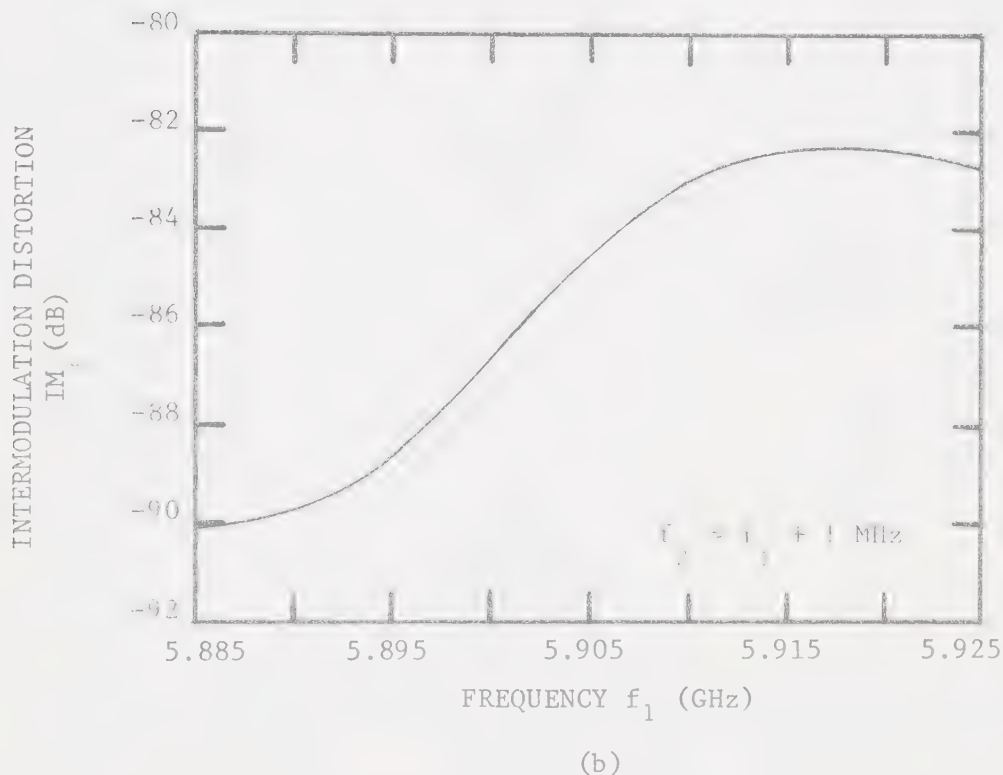
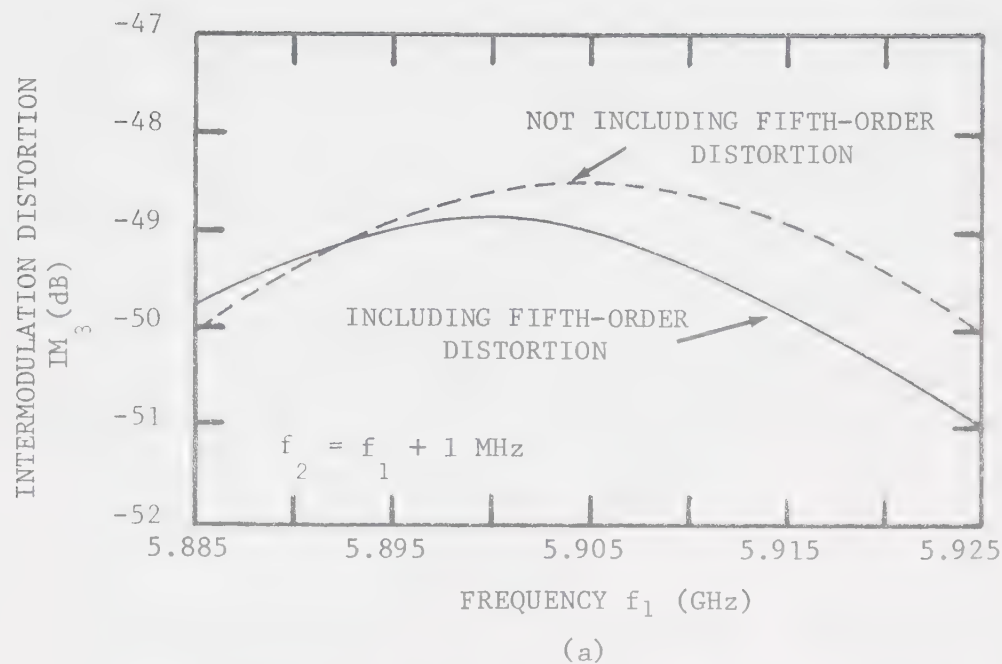


Figure 4.10 Predicted frequency-dependence of IM distortion, using Volterra series analysis, for the experimental IMPATT amplifier ( $I_{dc} = 25 \text{ mA}$ ) with a two-tone input ( $f_2 = f_1 + 1 \text{ MHz}$ ) and constant  $-10\text{-dBm}$  output power. (a) Predicted third-order IM distortion at  $2f_1 - f_2$ . (b) Predicted fifth-order IM distortion at  $3f_1 - 2f_2$ .



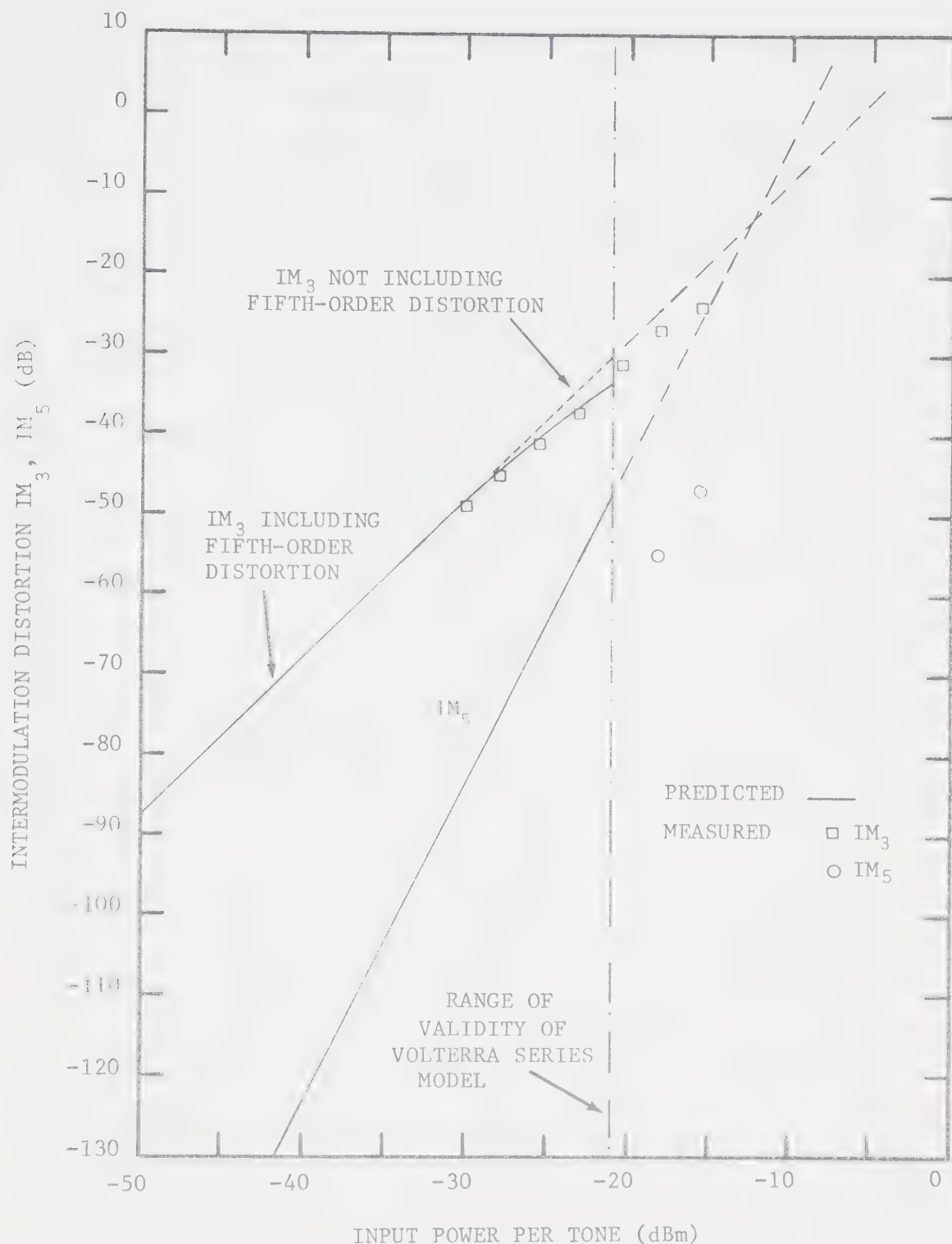


Figure 4.11 Comparison of measured and predicted IM distortion, using Volterra series analysis, for the experimental IMPATT amplifier ( $I_{dc} = 25$  mA) with a two-tone input ( $f_1 = 5.905$  GHz,  $f_2 = 5.906$  GHz) at the centre frequency.





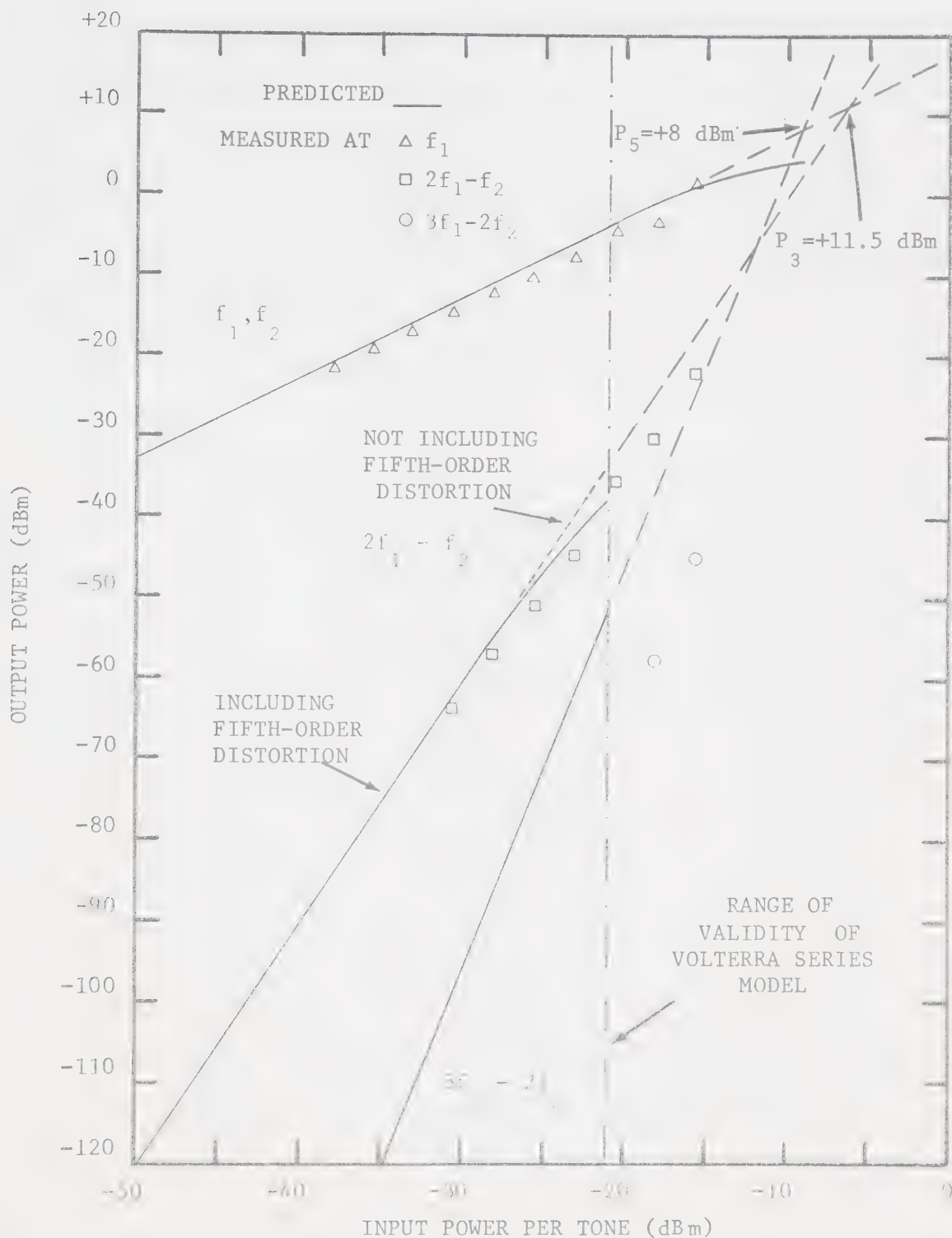


Figure 4.12 Comparison of measured and predicted fundamental output and IM distortion products, using Volterra series analysis, for the experimental IMPATT amplifier ( $I_{dc} = 25 \text{ mA}$ ) with a two-tone input ( $f_1 = 5.905 \text{ GHz}$ ,  $f_2 = 5.906 \text{ GHz}$ ) at the centre frequency.



however, the absolute value cannot be ascertained, since it occurs in the large-signal region. The small-signal results have been extrapolated to obtain the third-order intercept point +11.5 dBm, and fifth-order intercept point, +8 dBm. The proximity of these intercept points is further evidence that both the third- and fifth-order nonlinear responses are important relative to the linear response for input levels greater than -21 dBm per tone. Equation (4.55) also gives  $P_3 = +11.3$  dBm using the values in Table 4.1.

The results in Figs. 4.13 and 4.14 display the frequency dependence of  $IM_3$  and  $IM_5$ , respectively, for constant levels of the two-tone input signal. Third-order IM distortion is maximum at the centre frequency, which shifts to a lower frequency for signal levels outside the small-signal region.  $IM_3$  varies 5 dB over the passband for signal levels less than -28 dBm, and 8 dB for -23 dBm input level per tone.  $IM_5$  is maximum at 5.910 GHz due to the peak in the fifth-order Volterra transfer function at that frequency; the variation is 13 dB over the passband.

Results for the upper IM products  $(2f_2 - f_1)$  and  $(3f_2 - 2f_1)$  differed from those of the lower IM products by less than 1 dB.

Lastly, the amplifier gain compression for various CW inputs is shown as a function of input power level in Fig. 4.15. Amplifier expansion or compression can occur depending on the relative phase of the transfer functions  $H_1$ ,  $H_3$ , and  $H_5$ . The IMPATT amplifier under consideration here generally exhibits compression except at the low end of the passband where expansion occurs. Identical effects have been reported in the literature [31]. Furthermore, the theory predicts that at the frequency 5.895 GHz the relative phases of the Volterra transfer functions are such that both compression and expansion occur as the input level is



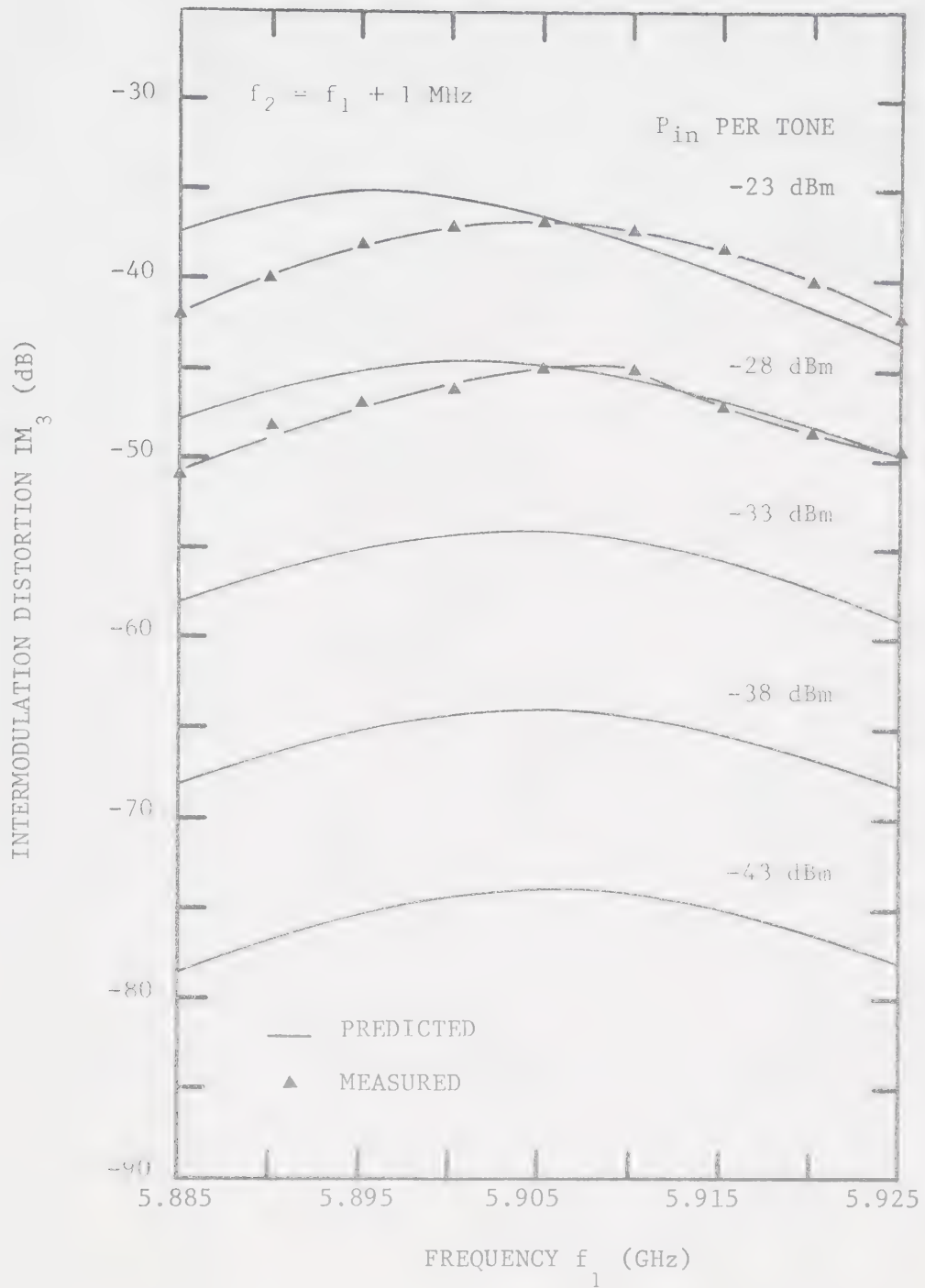


Figure 4.13 Comparison of measured and predicted frequency-dependence of third-order IM distortion at  $2f_1 - f_2$ , using Volterra series analysis, for the experimental IMPATT amplifier ( $I_{dc} = 25$  mA) with a two-tone input ( $f_2 = f_1 + 1$  MHz).



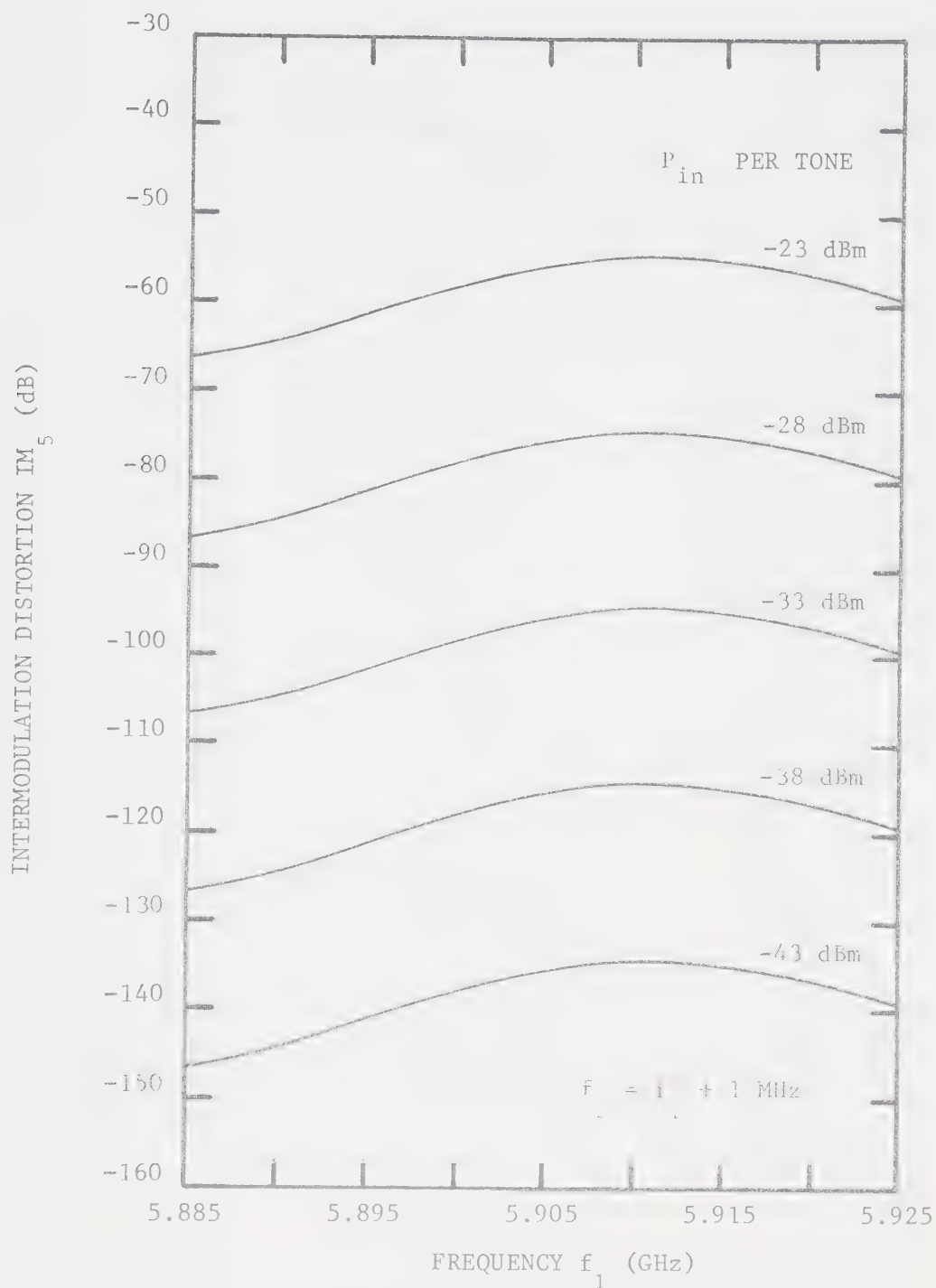


Figure 4.14 Predicted frequency-dependence of fifth-order IM distortion at  $3f_1 - 2f_2$ , using Volterra series analysis, for the experimental IMPATT amplifier ( $I_{dc} = 25 \text{ mA}$ ) with a two-tone input ( $f_2 = f_1 + 1 \text{ MHz}$ ).





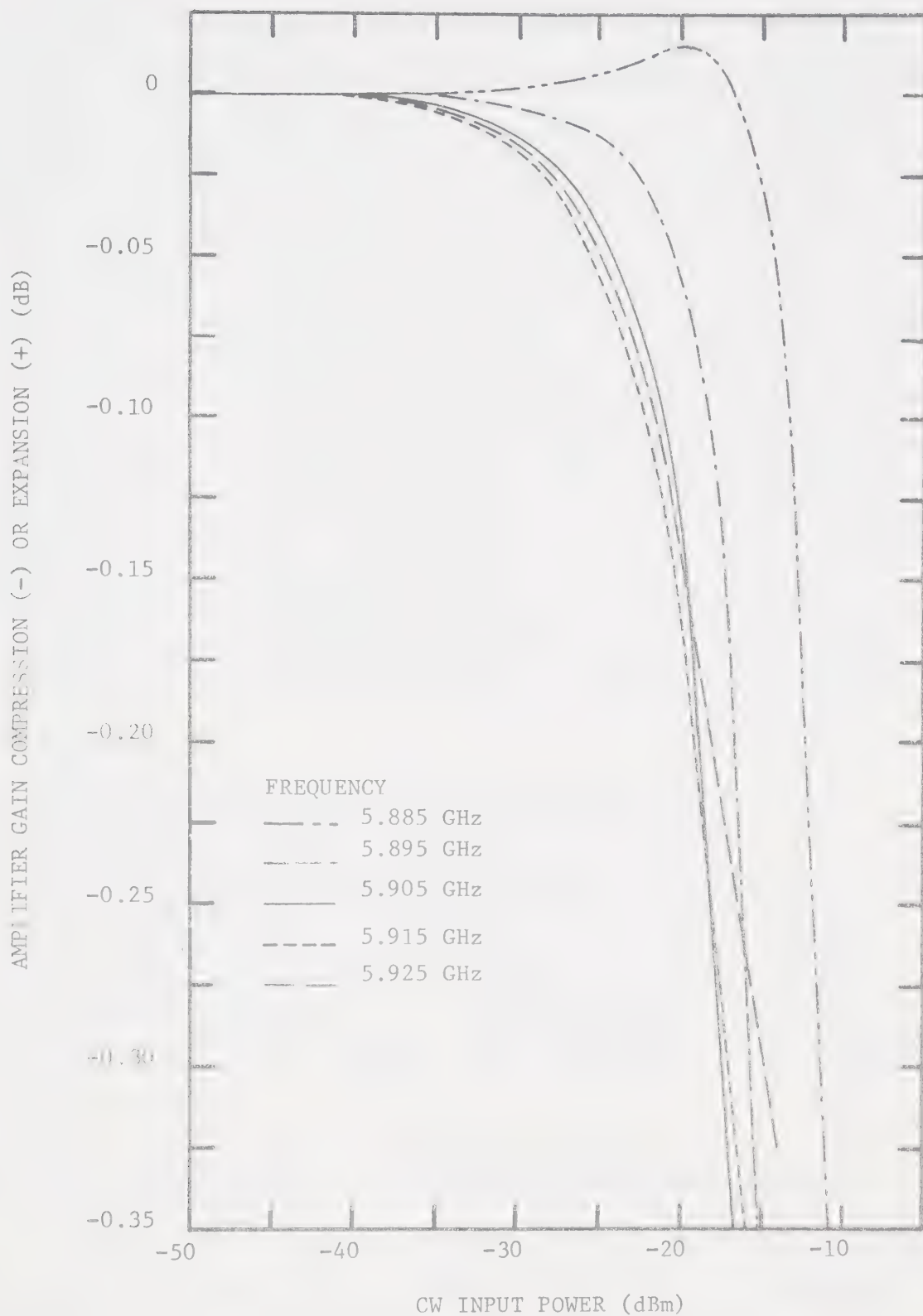


Figure 4.15 Predicted gain compression/expansion, using Volterra series analysis, for the experimental IMPATT amplifier at 25-mA dc bias current.



varied: the amplifier appears to have an extended linear range, whereas the two-tone IM test shows the amplifier to be nonlinear. For this reason, IM distortion measurements are a more dependable indicator of amplifier nonlinearity than compression tests [92]. The output power is dominated by  $H_1$ , with  $H_3$  and  $H_5$  introducing the small compression terms in Eqn. (4.59). Hence the fifth-order Volterra series model is applicable over a wider range for predicting compression than for predicting IM distortion. For compression, input levels up to -15 dBm can be considered in the model. Within this range, the maximum compression occurring in the passband is 1.2 dB, and the maximum expansion is 0.015 dB. Outside this input range, the compression apparently increases without bound because the five-term Volterra series does not suffice to represent the diode nonlinearities.

Experimental verification of these results will be discussed in Chapter 6.

#### 4.4 Extension of Volterra Series Distortion Analysis to a Microwave Feedforward Amplifier

In this section, the effect of feedforward linearization on the distortion produced in the IMPATT amplifier just described is analysed. The analysis, which employs a Volterra series representation of the main power amplifier, is general, however, and can be applied to any practical amplifier.

##### 4.4.1 Basic Nonlinear Model of a Microwave Feedforward Amplifier

An equivalent circuit for the basic feedforward amplifier depicted in Fig. 2.8(b), is shown in Fig. 4.16(a). The input to the feedforward amplifier is the signal  $x(t)$ ; its output is  $y(t)$ . The signal to the error amplifier is  $e(t)$ . Operator notation will be used for analysis. Let the



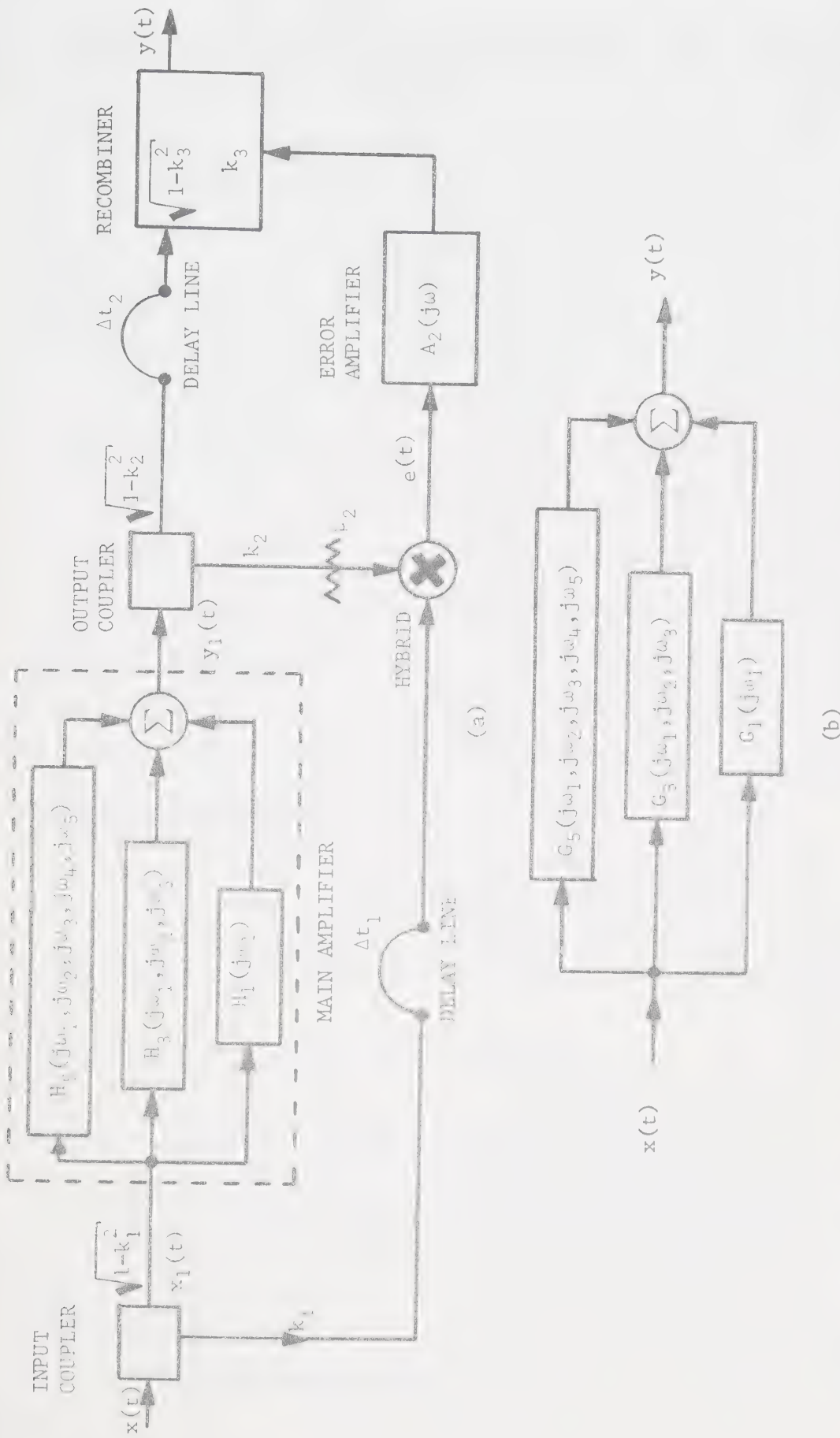


Figure 4.16 Feedforward amplifier representation for the analysis of nonlinear distortion. (a) Feedforward amplifier circuit representation. (b) Overall feedforward system representation.



main power amplifier be denoted by the complex gain operator  $H[ ]$ , and the error amplifier by the complex gain operator  $A_2[ ]$ . The main delay line, having delay  $\Delta t_1$  seconds, is denoted by the time delay operator  $T_1[ ]$ . The error-correction delay line has delay time  $\Delta t_2$  seconds and is denoted by the time delay operator  $T_2[ ]$ . The input, output and recombiner directional couplers have voltage coupling ratios  $k_1$ ,  $k_2$ , and  $k_3$ , respectively. For reasons discussed in Sec. 2.5, the ratios  $k_1$ ,  $k_2$ , and  $k_3$  are generally much less than unity for a feedforward amplifier. Attenuation in the signal arm between the output coupler and the comparator is represented by  $\mu_2$ . Other circuit losses are not represented explicitly. Such losses are easily accounted for by simple modification of the above parameters; however, the notation becomes unwieldy and nothing further is gained from the analysis. The values for  $k_1$ ,  $k_2$ ,  $k_3$  and  $\mu_2$  are chosen from loop-balancing considerations. The gain operator for the overall feedforward amplifier is denoted by  $G[ ]$ . Simple circuit analysis of Fig. 4.11(a) yields the following equations in operator form:

$$e(t) = T_1[k_1 x(t)] - \mu_2 k_2 \left( H \left[ \sqrt{1-k_1^2} x(t) \right] \right) \quad (4.60a)$$

$$y(t) = G[x(t)] = \sqrt{1-k_2^2} T_2 \left[ \sqrt{1-k_1^2} \left( H \left[ \sqrt{1-k_1^2} x(t) \right] \right) \right] \left\{ 1 + k_3 (A_2[e(t)]) \right\} \quad (4.60b)$$

Combining Eqns. (4.60a) and (4.60b) we have

$$G[x(t)] = \sqrt{1-k_2^2} T_2 \left[ \sqrt{1-k_1^2} \left( H \left[ \sqrt{1-k_1^2} x(t) \right] \right) \right] \left\{ 1 + k_3 A_2 \left[ \left( T_1[k_1 x(t)] - \mu_2 k_2 \left( H \left[ \sqrt{1-k_1^2} x(t) \right] \right) \right) \right] \right\} \quad (4.61)$$

Since Eqn. (4.61) must be satisfied for all input signals, this equation can be symbolically expressed by





$$G = \sqrt{1-k_3^2} * T_2 * \sqrt{1-k_2^2} * H * \sqrt{1-k_1^2} +$$

$$k_3 * A_2 * \left[ T_1 * k_1 - \mu_2 * k_2 * H * \sqrt{1-k_1^2} \right] \quad (4.62)$$

where  $*$  denotes the cascade operation.

It is assumed that the main amplifier can be represented by a Volterra series. This assumption is valid for all practical amplifiers which are inherently restricted to a region of asymptotic stability [21]. Furthermore, it is assumed that the amplifier nonlinearities are small enough that only the first five terms of the Volterra series are sufficient to characterize them, as in Fig. 4.16(a). Then, from Eqns. (4.4) to (4.7) the main amplifier output  $y_1(t)$  is related to its input  $x_1(t)$  by

$$y_1(t) = H[x_1(t)] = \sum_{n=1}^5 \int_0^t \dots \int_0^t h_n(\tau_1, \tau_2, \dots, \tau_n) \prod_{i=1}^n x_1(t-\tau_i) d\tau_i \quad (4.63)$$

where  $h_n(\tau_1, \tau_2, \dots, \tau_n)$  is the  $n^{\text{th}}$ -order Volterra kernel for the main amplifier and where

$$x_1(t) = \sqrt{1-k_1^2} x(t) \quad (4.64)$$

The range of integration extends from 0 to present time  $t$  because only causal input functions are considered. The remaining components in the feedforward amplifier are assumed to operate linearly. This is a valid assumption provided that:

- 1) the main amplifier introduces only small distortion; i.e.,



the main amplifier nonlinearities are small.

2) The error-detection loop balance is sufficient that the signal to the error amplifier is essentially the main amplifier distortion signal. The error amplifier then operates in the linear small-signal region. Under the above conditions the feedforward amplifier can also be represented by a five-term Volterra series; i.e.,

$$y(t) = G[x(t)] = \sum_{n=1}^5 \int_0^t \cdots \int_0^t g_n(\tau_1, \tau_2, \dots, \tau_n) \prod_{i=1}^n x(t-\tau_i) d\tau_i \quad (4.65)$$

where  $g_n(\tau_1, \tau_2, \dots, \tau_n)$  is the  $n^{\text{th}}$ -order Volterra kernel for the feedforward amplifier. The overall feedforward system representation is depicted in Fig. 4.16(b). Substituting Eqns. (4.63) and (4.65) into (4.62), we obtain the system equation

$$\begin{aligned} & \sum_{n=1}^5 \int_0^t \cdots \int_0^t g_n(\tau_1, \tau_2, \dots, \tau_n) \prod_{i=1}^n x(t-\tau_i) d\tau_i \\ &= k_1 \int_0^t dx_2(t-\tau_1) \left\{ k_1 x(t-\Delta t_1) + k_2 \left[ \sum_{n=1}^5 \int_0^\sigma \cdots \int_0^\sigma h_n(\tau_1, \tau_2, \dots, \tau_n) \right. \right. \\ & \quad \left. \left. \prod_{i=1}^n \sqrt{1-k_1^2} x(\sigma-\tau_i) d\tau_i \right] \right\} \\ &+ \sqrt{1-k_1^2} \sqrt{1-k_2^2} \left[ \sum_{n=1}^5 \int_0^{t-\Delta t_2} \cdots \int_0^{t-\Delta t_2} h_n(\tau_1, \tau_2, \dots, \tau_n) \prod_{i=1}^n \sqrt{1-k_1^2} x(t-\Delta t_2-\tau_i) d\tau_i \right] \end{aligned} \quad (4.66)$$



#### 4.4.2 Determination of the Feedforward Amplifier Volterra Transfer Functions

Equating the linear terms on both sides of Eqn. (4.66), we get

$$\begin{aligned}
 \int_0^t g_1(\tau_1)x(t-\tau_1)d\tau_1 &= k_1k_3 \int_0^t A_2(t-\sigma)x(\sigma-\Delta t_1)d\sigma \\
 &- \mu_2k_2k_3 \sqrt{1-k_1^2} \int_0^t d\sigma A_2(t-\sigma) \left[ \int_0^\sigma d\tau_1 h_1(\tau_1)x(\sigma-\tau_1) \right] \\
 &+ \sqrt{1-k_1^2} \sqrt{1-k_2^2} \sqrt{1-k_3^2} \int_0^{t-\Delta t_2} h_1(\tau_1)x(t-\Delta t_2-\tau_1)d\tau_1 \quad . \quad (4.67)
 \end{aligned}$$

Taking the Fourier transform of Eqn. (4.67),

$$\begin{aligned}
 G_1(j\omega) &= k_1k_3A_2(j\omega)e^{-j\omega\Delta t_1} \\
 &+ \sqrt{1-k_1^2} H_1(j\omega) \left[ \sqrt{1-k_2^2} \sqrt{1-k_3^2} e^{-j\omega\Delta t_2} - \mu_2k_2k_3A_2(j\omega) \right] \quad . \quad (4.68)
 \end{aligned}$$

$G_1(j\omega)$  is the first-order (linear) Volterra transfer function for the feedforward amplifier.

Considering amplifiers with less than octave bandwidth, such as IMPATT amplifiers, the second-order Volterra transfer function  $H_2(j\omega_1, j\omega_2)$  will produce distortion products  $2\omega_1, 2\omega_2, (\omega_2 \pm \omega_1)$  outside the passband. Similarly, distortion products from any even-order Volterra kernel will lie outside the frequency band of interest. Hence there is no need to calculate the even-order nonlinear transfer functions  $G_2$  and  $G_4$  for the feedforward amplifier.



The third-degree terms on each side of Eqn. (4.66) can be equated to yield

$$\begin{aligned}
 & \int_0^t \int_0^t \int_0^t g_3(\tau_1, \tau_2, \tau_3) x(t-\tau_1) x(t-\tau_2) x(t-\tau_3) d\tau_1 d\tau_2 d\tau_3 \\
 &= -\mu_2 k_2 k_3 [1-k_1^2]^{3/2} \int_0^t d\sigma A_2(t-\sigma) \int_0^\sigma \int_0^\sigma \int_0^\sigma d\tau_1 d\tau_2 d\tau_3 h_3(\tau_1, \tau_2, \tau_3) x(\sigma-\tau_1) \cdot \\
 & \quad x(\sigma-\tau_2) x(\sigma-\tau_3) \\
 &+ [1-k_1^2]^{3/2} \sqrt{1-k_2^2} \sqrt{1-k_3^2} \int_0^{t-\Delta t_2} \int_0^{t-\Delta t_2} \int_0^{t-\Delta t_2} d\tau_1 d\tau_2 d\tau_3 h_3(\tau_1, \tau_2, \tau_3) x(t-\Delta t_2-\tau_1) \\
 & \quad \cdot x(t-\Delta t_2-\tau_2) x(t-\Delta t_2-\tau_3) \quad . \quad (4.69)
 \end{aligned}$$

Taking three-dimensional Fourier transforms of both sides of Eqn. (4.69),

$$\begin{aligned}
 G_3(j\omega_1, j\omega_2, j\omega_3) &= [1-k_1^2]^{3/2} H_3(j\omega_1, j\omega_2, j\omega_3) \left\{ \sqrt{1-k_2^2} \sqrt{1-k_3^2} e^{-j(\omega_1+\omega_2+\omega_3)\Delta t_2} \right. \\
 & \quad \left. -\mu_2 k_2 k_3 A_2 [j(\omega_1+\omega_2+\omega_3)] \right\} \quad . \quad (4.70)
 \end{aligned}$$

In a similar fashion, the fifth-order nonlinear transfer function is determined to be





$$G_5(j\omega_1, j\omega_2, j\omega_3, j\omega_4, j\omega_5) = [1-k_1^2]^{5/2} H_5(j\omega_1, j\omega_2, j\omega_3, j\omega_4, j\omega_5).$$

$$\left\{ \sqrt{1-k_2^2} \sqrt{1-k_3^2} e^{-j(\omega_1+\omega_2+\omega_3+\omega_4+\omega_5)\Delta t_2 - j\mu_2 k_2 k_3 \Delta t_2 [(\omega_1+\omega_2+\omega_3+\omega_4+\omega_5)]} \right\} \quad (4.71)$$

#### 4.4.3 Intermodulation Distortion in a Feedforward Amplifier

The introduction of two or more nonharmonically related signals into the input of the feedforward IMPATT amplifier results in the generation of intermodulation signals in the output of the amplifier. As in Sec. 4.3.3, consider a two-tone input signal

$$x(t) = V(\cos \omega_1 t + \cos \omega_2 t) \quad (4.72)$$

where  $\omega_1$  and  $\omega_2$  are incommensurable frequencies in the passband of the amplifier. For  $\omega_1 \approx \omega_2$  and small distortion, the third-order intermodulation distortion  $IM_{3FF}$  for the feedforward amplifier is the same expression as Eqn. (4.45) with the IMPATT amplifier Volterra kernels  $H_1, H_3, H_5$  replaced by the feedforward amplifier kernels  $G_1, G_3$ , and  $G_5$ ; i.e.,

$$IM_{3FF} (dB) = 20 \log \left\{ \frac{V^2}{4|G_1(j\omega_1)|} \left| G_3(j\omega_1, j\omega_1, -j\omega_1) + V^2 G_5(j\omega_1, j\omega_1, -j\omega_1, j\omega_1, -j\omega_1) \right. \right. \\ \left. \left. + \frac{15}{2} V^2 G_5(j\omega_1, j\omega_1, -j\omega_2, j\omega_2, -j\omega_2) \right| \right\} \quad (4.73)$$

Similarly the fifth-order intermodulation distortion  $IM_{5FF}$  for the feedforward amplifier is



$$\text{IM}_{5\text{FF}}(\text{dB}) = 20 \log \left\{ \frac{5V^4 |G_5(j\omega_1, j\omega_1, j\omega_1, -j\omega_2, -j\omega_2)|}{8 |G_1(j\omega_1)|} \right\} \quad (4.74)$$

The feedforward amplifier third-order intermodulation distortion  $\text{IM}_{3\text{FF}}$  is zero if

$$\left| 3 G_3(j\omega_1, j\omega_1, -j\omega_2) + 5V^2 G_5(j\omega_1, j\omega_1, -j\omega_2, j\omega_1, -j\omega_1) \right. \\ \left. + \frac{15}{2} V^2 G_5(j\omega_1, j\omega_1, -j\omega_2, j\omega_2, -j\omega_2) \right| = 0 \quad (4.75)$$

Substitution of Eqns. (4.70) and (4.71) into (4.75) yields

$$\left| [1-k_1^2]^{3/2} \left[ \sqrt{1-k_2^2} \sqrt{1-k_3^2} e^{-j(2\omega_1-\omega_2)\Delta t_2} - \mu_2 k_2 k_3 A_2 [j(2\omega_1-\omega_2)] \right] \right. \\ \left| 3 H_3(j\omega_1, j\omega_1, -j\omega_2) + 5V^2 H_5(j\omega_1, j\omega_1, -j\omega_2, j\omega_1, -j\omega_1) [1-k_1^2] \right. \\ \left. + \frac{15}{2} V^2 H_5(j\omega_1, j\omega_1, -j\omega_2, j\omega_2, -j\omega_2) [1-k_1^2] \right| = 0 \quad (4.76)$$

Since the main amplifier is generally nonlinear, its intermodulation distortion  $\text{IM}_3$  is nonzero. Also,  $k_1$  cannot be identically unity, for in that case there would be no signal reaching the main amplifier. We can thus conclude from Eqn. (4.76) that

$$\left| \sqrt{1-k_2^2} \sqrt{1-k_3^2} e^{-j(2\omega_1-\omega_2)\Delta t_2} - \mu_2 k_2 k_3 A_2 [j(2\omega_1-\omega_2)] \right| = 0 \quad (4.77)$$



$$\text{or} \quad |A_2 [j(2\omega_1 - \omega_2)]| = \frac{\sqrt{1-k_2^2} \sqrt{1-k_3^2}}{\mu_2 k_2 k_3} \quad (4.78)$$

$$\text{and} \quad \arg A_2 [j(2\omega_1 - \omega_2)] = -(2\omega_1 - \omega_2) \Delta t_2 \quad (4.79)$$

In order that third-order IM products be zero for the feedforward amplifier, the amplitude and phase balances of Eqns. (4.78) and (4.79) respectively must be exact.

Proceeding in an identical manner for the fifth-order IM products, they will be zero if

$$|A_2 [j(3\omega_1 - 2\omega_2)]| = \frac{\sqrt{1-k_2^2} \sqrt{1-k_3^2}}{\mu_2 k_2 k_3} \quad (4.80)$$

$$\text{and} \quad \arg A_2 [j(3\omega_1 - 2\omega_2)] = -(3\omega_1 - 2\omega_2) \Delta t_2 \quad (4.81)$$

Equations (4.78) to (4.81) indicate that the IM distortion performance of the feedforward amplifier is entirely determined by the precision of balance in the error-correction loop as long as the error amplifier  $A_2$  is operating in its linear region.

For amplifiers with two test tones  $\omega_1 \approx \omega_2$  applied,

$$|A| = |A_2(j\omega)| \approx |A_2[j(2\omega_1 - \omega_2)]| \approx |A_2[j(3\omega_1 - 2\omega_2)]| \quad (4.82)$$

$$-\phi_2 = \arg A_2(j\omega_1) \approx \arg A_2[j(2\omega_1 - \omega_2)] \approx \arg A_2[j(3\omega_1 - 2\omega_2)] \quad (4.83)$$



The effect of loop balance on the improvement in IM distortion can be analysed by assuming an amplitude imbalance  $\alpha_2$  and a phase imbalance  $\delta_2$  in the error-correction loop, where

$$\alpha_2 = \frac{|A_2|}{\left[ \sqrt{1-k_2^2} \sqrt{1-k_3^2} \right] \left[ \mu_2 k_2 k_3 \right]^{-1}} \quad (4.84)$$

$$\text{and} \quad \delta_2 = \phi_2 - \omega_1 \Delta t_2 \quad (4.85)$$

Let the Volterra transfer functions for the main amplifier be denoted by  $H_1(j\omega_1)$ ,  $H_3[j(2\omega_1 - \omega_2)]$ , and  $H_5[j(3\omega_1 - 2\omega_2)]$ . Assume, for now, perfect balance of the error-detection loop, i.e.

$$k_1 = \mu_2 k_2 \sqrt{1-k_1^2} |H_1(j\omega_1)| \quad (4.86)$$

$$\arg H_1(j\omega_1) = -\omega_1 \Delta t_1 = -\phi_1 \quad (4.87)$$

This assumption does not affect the generality of the present analysis. Any imbalances which may, in fact, be present cause the error signal to be larger than for the perfectly balanced case. As long as the resulting error signal is small enough for the error amplifier to process it linearly, the same results apply. Substitution of Eqns. (4.84) to (4.87) into (4.68), (4.70), (4.71) and (4.73), in conjunction with the approximation

$$1 - \alpha \exp(-j\delta) = (1 - \alpha \cos \delta) + j \alpha \sin \delta \approx 1 - \alpha + \alpha \delta^2 / 2 + j \alpha \delta + \dots \quad (\text{small } \alpha, \delta) \quad (4.88)$$

results in





$$\begin{aligned}
\text{IM}_{3\text{FF}}(\text{dB}) = & 20 \log \left\{ \frac{(1-k_1^2)V^2}{4|H_1(j\omega_1)|} \left| 3H_3(j\omega_1, j\omega_1, -j\omega_2) \right. \right. \\
& + 5(1-k_1^2)V^2 H_5(j\omega_1, j\omega_1, -j\omega_2, j\omega_1, -j\omega_1) \\
& + \left. \frac{15}{2} (1-k_1^2)V^2 H_5(j\omega_1, j\omega_1, -j\omega_2, j\omega_2, -j\omega_2) \right| \cdot \\
& \left. \left[ (1-\alpha_2)^2 + \alpha_2 \delta_2^2 \right]^{1/2} \right\} . \quad (4.89)
\end{aligned}$$

In the feedforward amplifier the amplitude of each tone at the input of the main amplifier is  $\sqrt{1-k_1^2} V$ , given by Eqns. (4.64) and (4.72). Substituting this amplitude for the amplitude  $V$  in Eqn. (4.45), and comparing the result with Eqn. (4.89) we obtain

$$[\text{IM}_{3\text{FF}} - \text{IM}_3](\text{dB}) = 20 \log \left[ (1-\alpha_2)^2 + \alpha_2 \delta_2^2 \right]^{1/2} . \quad (4.90)$$

Similarly, using Eqns. (4.84) to (4.87), (4.68) and (4.71) in Eqn. (4.74) one can obtain

$$[\text{IM}_{5\text{FF}} - \text{IM}_5](\text{dB}) = 20 \log \left[ (1-\alpha_2)^2 + \alpha_2 \delta_2^2 \right]^{1/2} . \quad (4.91)$$

For small amplitude- and/or phase imbalances, the feedforward amplifier is thus seen to reduce third- and fifth-order IM distortion products in the same ratio.

As regards the third-order intercept point,  $P_3$ , graphical inspection reveals that, for every  $n$ -dB reduction in the third-order IM products of the main amplifier by feedforward correction,  $P_3$  will be extended by  $n/2$  dB.



#### 4.4.4 Computed Distortion in a Feedforward-Corrected Amplifier

Equations (4.90) and (4.91) predict the improvement in IM distortion attainable by feedforward correction of a nonlinear amplifier as a function of amplitude- and phase imbalance in the error-correction loop. Such imbalances are primarily due to error amplifier gain- and phase variations with time and frequency. Figure 4.17 shows the expected improvement in third- and fifth-order IM products for various combinations of amplitude- and phase imbalance in the error-correction loop. Only amplitude imbalance due to gain increase has been considered in the curves of Fig. 4.17. A further set of curves corresponding to gain decrease may be plotted, but the difference between the two sets of curves for amplitude imbalances less than 1 dB are very slight: a 1-dB gain decrease gives a curve approximately equivalent to that for 0.9-dB gain increase. Figure 4.18 displays the contours of constant improvement in  $IM_3$  or  $IM_5$  as a function of gain- and phase variations in the error-correction loop. In Fig. 4.18, both positive and negative amplitude imbalance have been considered; the slight asymmetry of the constant IM improvement contours with respect to gain increase or gain decrease can be seen. From Fig. 4.18, the values of gain- and phase imbalance which can be tolerated for a desired improvement in  $IM_3$  and  $IM_5$  can be determined directly. Several conclusions can be drawn from the curves of Fig. 4.17 and Fig. 4.18. For small gain imbalance ( $\alpha_2 = 0.1$  dB or less), the improvement in  $IM_3$  and in  $IM_5$  is very sensitive to phase imbalance. However, when the gain imbalance is large ( $\alpha_2 \approx 1$  dB), the improvement is rather insensitive to phase imbalance. An improvement in IM distortion of the order of 17 dB is anticipated for a large gain and phase imbalance ( $\alpha_2 = 1$  dB,  $\delta_2 = 5$  degrees). In a practical amplifier, it should not be difficult to achieve at least a 20-dB reduction of the IM products.



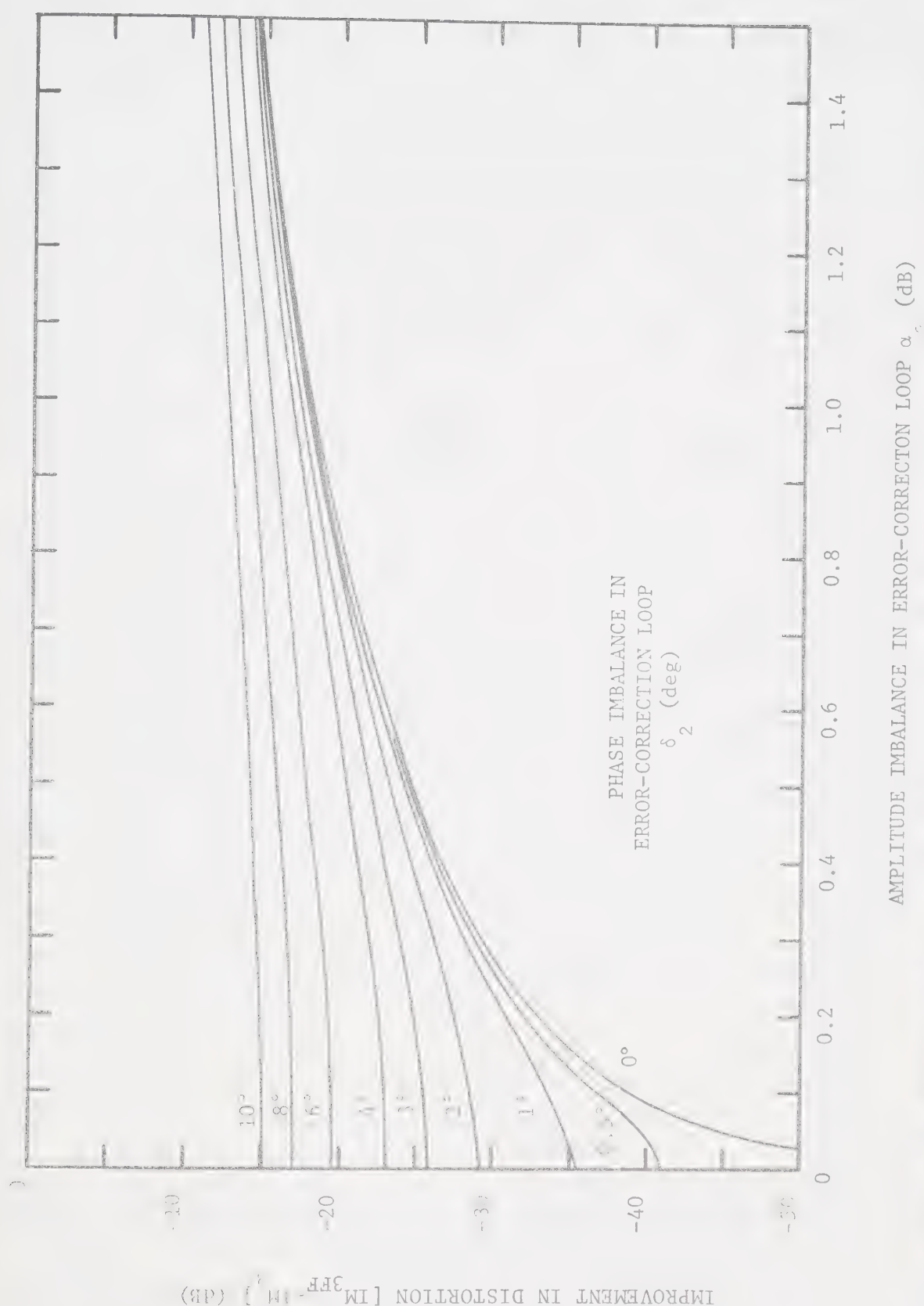


Figure 4.17 Improvement in third- and fifth-order IM distortion,  $IM_3$  and  $IM_5$ , for various values of imbalance in the feedforward amplifier error-correction loop.



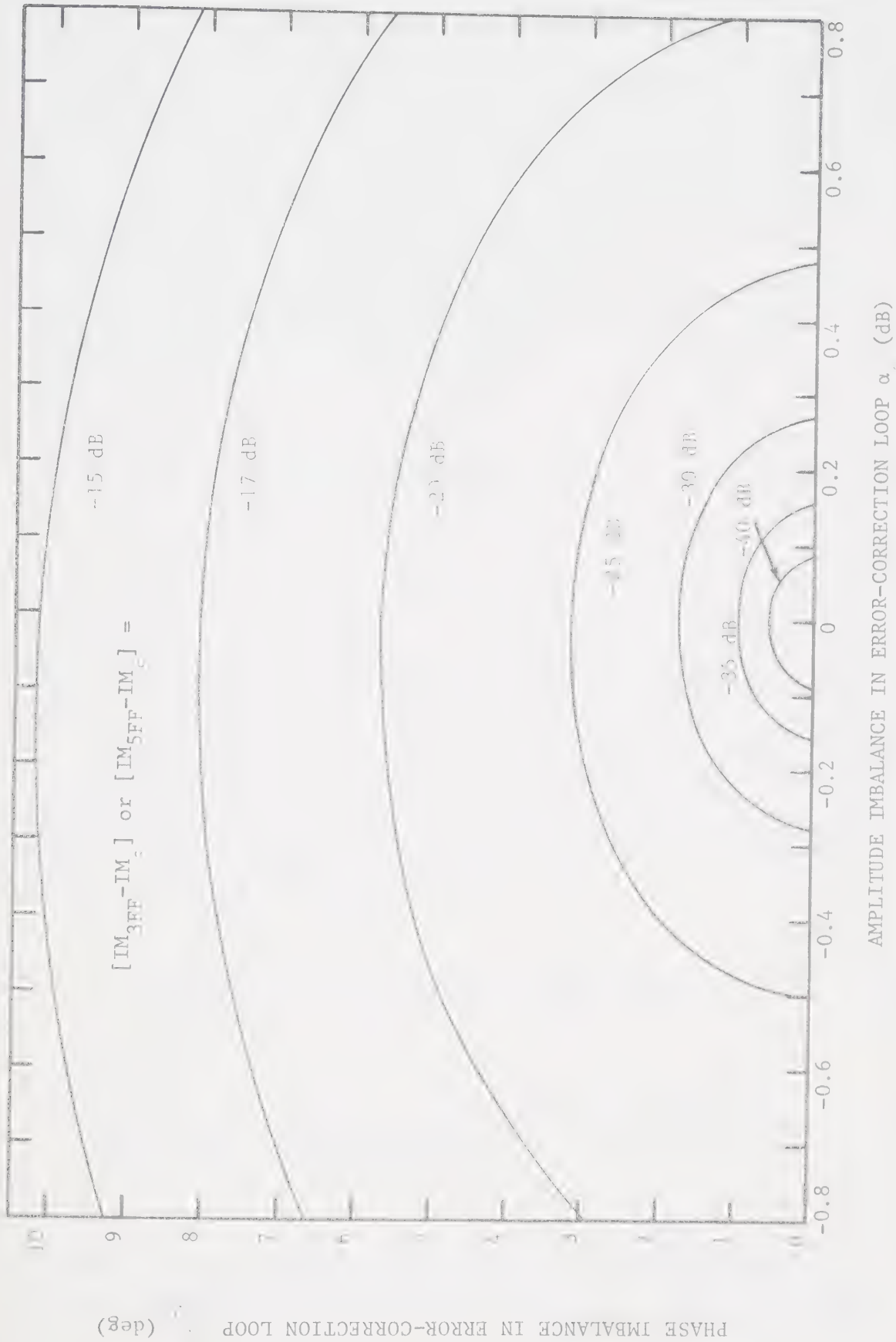


Figure 4.18 Contours of constant improvement in third- and fifth-order IM distortion,  $IM_3$  and  $IM_5$ , for various values of imbalance in the feedforward amplifier error-correction loop.





#### 4.5 Power Considerations in Microwave Feedforward Amplifier Design

It should be emphasized that the expressions (4.90) and (4.91) apply only if the error-detection loop is sufficiently balanced that the amplitude of the error signal is in the small-signal linear region of the error amplifier. The effect of gain- and phase imbalance in the error-detection loop on the error signal can be determined by considering Eqns. (4.86) and (4.87). Consider a gain imbalance  $\alpha_1$  in (4.86) and a phase imbalance  $\delta_1$  in (4.87); i.e.,

$$\alpha_1 = \mu_2 k_2 \sqrt{1-k_1^2} |H_1(j\omega_1)| k_1^{-1} \quad (4.92)$$

$$\delta_1 = \phi_1 - \omega_1 \Delta t_1 \quad (4.93)$$

Then, if the main amplifier introduces small distortion, the error signal obtained under balanced error-detection loop conditions consists solely of undesired distortion products, whereas the error signal for the above imbalance in the error-detection loop is dominated by the desired signal. Analysis of Fig. 4.13(a) gives

$$e(t)/x(t) = k_1 \exp(-j\omega \Delta t_1) [1 - \alpha_1 \exp(-j\delta_1)] \quad (4.94)$$

and

$$y_1(t)/x(t) = \sqrt{1-k_1^2} H_1(j\omega) \quad (4.95)$$

The main amplifier contributes power,  $P_1$ , to the output power,  $P_o$ ; the error-amplifier contributes power,  $P_2$ , to the output power, where



$$P_o = |y(t)|^2 / 2Z_o = P_1 + P_2 \quad (4.96)$$

$$P_1 = (1-k_2^2)(1-k_3^2) |y_1(t)|^2 / 2Z_o \quad (4.97)$$

$$P_2 = k_3^2 |A_2(j\omega)|^2 |e(t)|^2 / 2Z_o \quad (4.98)$$

and  $Z_o$  is the characteristic impedance of the transmission line. From Eqns. (4.96) to (4.98) the relative contribution of  $P_1$  and  $P_2$  to  $P_o$  is

$$\frac{P_2}{P_1} = \frac{k_3^2 |A_2(j\omega)|^2}{(1-k_2^2)(1-k_3^2)} \cdot \frac{|e(t)|^2}{|x(t)|^2} \cdot \frac{|x(t)|^2}{|y_1(t)|^2} \quad (4.99)$$

Assuming the error-correction loop is balanced (i.e.  $\alpha_2=1$ ,  $\delta_2=0$ ), and substituting Eqns. (4.94) and (4.95) into (4.99) yields

$$P_2/P_1 = \left| 1 - \alpha_1 \exp(-j\delta_1) \right|^2 \alpha_1^{-2} \quad (4.100)$$

Using the approximation given in Eqn. (4.88) and expressing the power ratio  $P_2/P_1$  in dB, we obtain

$$[P_2/P_1] \text{ (dB)} = 20 \log \left[ (1-\alpha_1^2) + \alpha_1^2 \delta_1^2 \right]^{1/2} - 20 \log \alpha_1 \quad (4.101)$$

Figure 4.19, based on expression (4.101), shows the relative contribution of the error amplifier power and main amplifier power to the feedforward amplifier output power as a function of amplitude- and phase-imbalance in the error-detection loop. For a constant output power, an increase in main amplifier gain has the opposite effect on the power



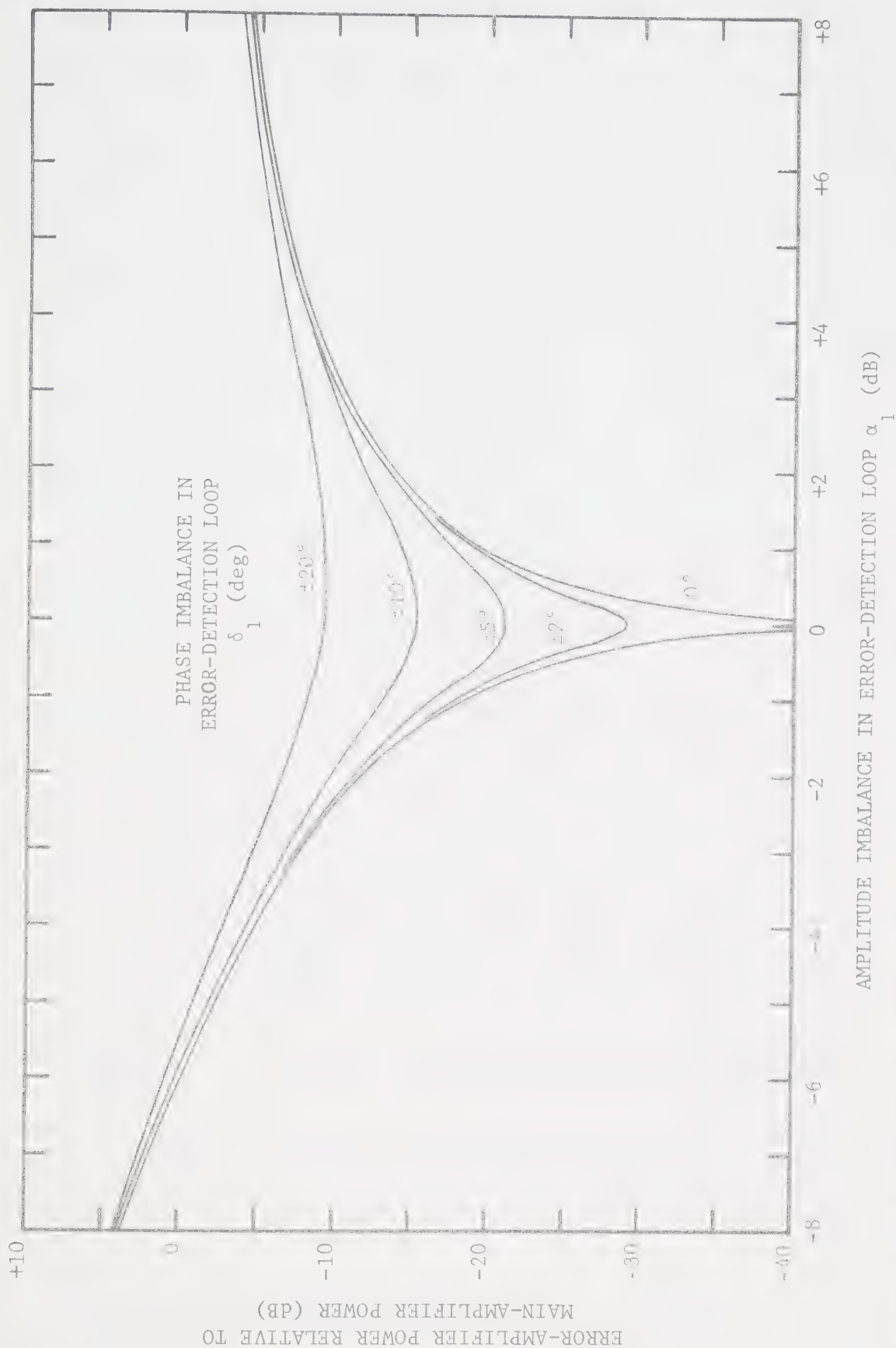


Figure 4.19 Relative contribution of the error-amplifier power and main-amplifier power to the feedforward-amplifier power for various values of imbalance in the feedforward amplifier error-detection loop.



which must be handled by the error amplifier than a decrease in main amplifier gain. If the main amplifier gain decreases by 6 dB to half voltage, the main amplifier and error amplifier (assuming it will operate linearly under these conditions) must provide equal power. Figure 4.19 allows us to specify the requirements for the error amplifier with a knowledge of the gain and phase variations, and distortion products of the main amplifier [57]. For example, if the IMPATT amplifier gain decreases by 3 dB from nominal in the frequency range of interest (the amplifier passband), and its phase varies by  $\pm 10$  degrees, then the error amplifier must deliver -7 dB of the main amplifier power to the output. Since the distortion in the form of IM products is -38 dBm (see Fig. 4.12) for an output power of 0 dBm, the error amplifier power requirements would be dominated by the IMPATT amplifier variations.

#### 4.6 Gain Sensitivity of a Microwave Feedforward Amplifier

Assume that a small gain imbalance  $\alpha_1$  and phase imbalance  $\delta_1$ , given by Eqns. (4.92) and (4.93) respectively, exist in the error-detection loop. Also, assume that a small gain imbalance  $\alpha_2$  and phase imbalance  $\delta_2$ , given by Eqns. (4.84) and (4.85) respectively, exist in the error-correction loop. Substituting these parameters into Eqn. (4.68), we obtain

$$G_1(j\omega)/G'_1(j\omega) = \alpha_1 \exp(-j\delta_1) + \alpha_2 \exp(-j\delta_2) - \alpha_1 \alpha_2 \exp[-j(\delta_1 + \delta_2)] \quad (4.102)$$

where  $G'_1(j\omega)$  is the complex gain when a precise balance exists in both loops, and  $G_1(j\omega)$  is the complex gain when the assumed imbalances are present.

For small phase imbalances; i.e.,  $\delta_1$  and  $\delta_2 \ll 1$ ,





$$\left| \frac{G_1(j\omega)}{G_2(j\omega)} \right| = \alpha_1 + \alpha_2 - \alpha_1 \alpha_2 \quad (4.103)$$

Thus small variations of phase are unimportant as far as their effect on the gain of the feedforward amplifier is concerned. Suppose that the gain of both the main amplifier and error amplifier deviate from the precise balance value by  $p\%$ ; from Eqn. (4.103) we note that the gain of the feedforward amplifier system is changed by only  $0.01p^2\%$ . Moreover, we note that, if there is a precise gain balance in either the error-detection or error-correction loop (i.e.  $\alpha_1$  or  $\alpha_2 = 1$ ), the overall gain remains almost constant for small phase imbalances.

A study of linear gain sensitivity of a feedforward amplifier [94] indicates that the couplers in the feedforward loops are more critical components for linear gain variation than the main or error amplifiers. However, it is also shown that if the nonideal coupling deviations are systematic, the couplers can compensate one another so as to minimize the effects of the variations.

#### 4.7 Summary

Volterra series analysis is a general and useful technique for calculating intermodulation distortion in a nonlinear amplifier with multiple inputs. In practice, however, it is restricted to the representation of mildly driven nonlinearities for which the first terms of the Volterra series suffice. A five-term Volterra series is used to predict third- and fifth-order intermodulation distortion, and intercept points for a narrowband IMPATT amplifier with a two-tone input, and gain compression for a single-tone input. The model applies up to an input level of -21 dBm per tone for IM distortion, and -15 dBm per tone for gain com-



pression. Maximum third-order IM distortion is predicted to be -38 dBm in this region for a fundamental output power of -3 dBm, and intercept point of 11.3 dBm. Maximum fifth-order IM distortion is predicted to be -52 dBm with an intercept point of +8 dBm. Gain compression and expansion in this input range is less than 1.2 dB over the passband of the amplifier. Since the model ceases to be valid at small signal levels relative to the power rating (100 mW) of the diode, it can be concluded that the IMPATT diode is a rather nonlinear device.

Volterra series analysis of the feedforward amplifier predicts the improvement in IM distortion as a function of error-correction loop gain- and phase imbalance. Two important characteristics of the feedforward amplifier are evident: 1) in setting up the feedforward amplifier, the error-detection loop balance determines the error amplifier power while the error-correction loop balance determines the degree of cancellation of distortion products; 2) for the reduction of distortion products to be consistent, close balance of the error-correction loop must be maintained. Hence, the error amplifier gain- and phase variations must either be very small over the frequency range of interest, or else some adaptive loop-balancing technique must be employed [56]. These restrictions can be relaxed for a lower degree of improvement in IM distortion.



## CHAPTER 5

### QUASISTATIONARY NONLINEAR DISTORTION STUDY OF A FEEDFORWARD-CORRECTED IMPATT AMPLIFIER

#### 5.1 Introduction and Overview

A second method of analysing feedforward IMPATT amplifier intermodulation (IM) distortion is developed in this chapter. The IM distortion of the IMPATT amplifier itself is first calculated: the distortion is obtained, together with the fundamental output, as the steady-state frequency-domain solution of the complex nonlinear differential equation describing the equivalent circuit of the amplifier. The effect of the linear feedforward circuitry on IM distortion is then determined by conventional linear circuit analysis.

The method of analysing IMPATT-diode amplifier distortion is applicable to other two-terminal active devices which display negative conductance to the external passive circuitry. Such devices operating at microwave frequencies normally exhibit nonlinear susceptance in addition to nonlinear negative conductance, where the admittance is a nonlinear function of RF voltage amplitude and frequency.

An accurate device model should include both of these elements so that memory effects are accounted for. In the present approach, the nonlinear conductance and the nonlinear susceptance of the active diode are mathematically described by bicubic spline functions which interpolate the active diode admittance in both RF frequency and applied RF voltage level. The passive circuit admittance seen by the active device is also represented by a cubic spline function interpolation in frequency. The data to be interpolated may be in analytic, graphical



or discrete point form. Thus, the method is compatible with experimental measurement of the active diode admittance and passive circuit admittance. These mathematical representations of the active and passive microwave circuits are then related to the differential equations describing the respective terminal voltage-current relationships: a high-order linear differential equation holds true for the passive circuitry while a high-order nonlinear differential equation is assumed for the active diode.

In the steady state, a nonlinear system, which has two or more input signals closely spaced in frequency, generates IM distortion products (centred at the input frequencies) at the output. To determine amplifier IM distortion, a balanced two-tone current signal is injected into the parallel connection of passive and active circuit admittances in the equivalent circuit. The fundamental voltage response, in the zone of the input frequencies, is assumed to be slowly varying in amplitude and phase, compared with the microwave carrier frequency (this is the quasistationarity assumption). The steady-state voltage response is calculated by numerical solution, in the frequency domain, of the complex nonlinear differential equation describing the IMPATT amplifier. The IM distortion products of the IMPATT amplifier can be identified directly since the solution is obtained in the frequency domain.

Most of this chapter is devoted to the presentation of the above technique for evaluating IMPATT amplifier distortion. The method is an extension of a previous, unpublished study on transients in a microwave two-terminal oscillator [95]. To extend said work to amplifier circuits, part of the material of Ref. [95] will first be discussed





in Section 5.2. The nonlinear equivalent circuit of the IMPATT-diode amplifier and the nonlinear differential equation describing the model are developed in Section 5.3. The method for measurement of the equivalent circuit parameters is explained. Also, the numerical technique for calculating IM distortion is developed and computed results are presented. Section 5.4 discusses the improvement in IM distortion which can be obtained by feedforward correction; the feedforward circuit external to the IMPATT amplifier is analysed using linear circuit analysis. The last section is a brief conspectus of results contained in this chapter.

## 5.2 Derivation of Active and Passive Circuit Non-CW Admittance Operators

### 5.2.1 Linear Passive Circuit Non-CW Admittance Operator

The terminal voltage,  $v(t)$ , and terminal current,  $i(t)$ , of a one-port passive circuit are related, in general, by the linear differential equation [95]

$$\sum_{m=0}^M a_m \frac{d^m i(t)}{dt^m} = \sum_{n=0}^N b_n \frac{d^n v(t)}{dt^n} \quad (5.1)$$

where the coefficients  $a_m$  and  $b_n$  are constants. The order of the differential equation is determined by the number of poles and zeros in the passive circuit. Equation (5.1) can be written in operator notation as

$$P[d/dt] \{i(t)\} = Q[d/dt] \{v(t)\} \quad (5.2)$$



where  $P[d/dt]$  and  $Q[d/dt]$  are polynomial differential operators of order  $M$  and  $N$ , respectively.

A single-frequency CW voltage excitation

$$v(t) = V_0 \exp(j\omega_0 t) \quad (5.3)$$

produces the current response

$$i(t) = I_0 \exp(j\omega_0 t) = \exp(j\omega_0 t) Y_c(j\omega_0) V_0 \quad (5.4)$$

in the passive circuit. The actual physical signals are given by  $\text{Re}\{v(t)\}$  and  $\text{Re}\{i(t)\}$ . The term  $Y_c(j\omega_0)$ , called the passive circuit CW admittance, is defined by

$$Y_c(j\omega_0) = \frac{I_0}{V_0} = \frac{Q(j\omega_0)}{P(j\omega_0)} \quad (5.5)$$

This admittance concept can be extended to the case of non-CW excitation by defining an admittance operator [95]. Consider the voltage excitation

$$v(t) = A(t) \exp(j(\bar{\omega}t + \phi(t))) = V(t) \exp(j\bar{\omega}t) \quad (5.6)$$

The signal  $V(t)$  is the complex time-varying voltage amplitude; its magnitude (real) is  $A(t)$ ; its phase (real) is  $\phi(t)$ .

The general current response becomes



$$i(t) = I(t) \exp(j\bar{\omega}t) \quad (5.7)$$

where  $I(t)$  is the complex, time-varying current amplitude.

Differentiating Eqns. (5.6) and (5.7) results in

$$\frac{d^n v(t)}{dt^n} = \exp(j\bar{\omega}t) \cdot [j\bar{\omega} + d/dt]^n \{A(t) \exp(j\phi(t))\} \quad (5.8)$$

and

$$\frac{d^n i(t)}{dt^n} = \exp(j\bar{\omega}t) \cdot [j\bar{\omega} + d/dt]^n \{I(t)\} \quad (5.9)$$

Substituting Eqns. (5.8) and (5.9) into Eqn. (5.1), and utilizing the operator notation of Eqn. (5.2), we obtain

$$P [j\bar{\omega} + d/dt] \{i(t)\} = Q [j\bar{\omega} + d/dt] \{v(t)\} \quad (5.10)$$

Analagous to the CW case, we can define a linear admittance operator  $Y_c[j\omega(t)]$ , for the non-CW case by

$$Y_c[j\omega(t)] = Y_c[j\bar{\omega} + d/dt] = \frac{Q[j\bar{\omega} + d/dt]}{P[j\bar{\omega} + d/dt]} \quad (5.11)$$

The amplitude of the current response is then given by

$$I(t) = Y_c[j\omega(t)] \{A(t) \exp(j\phi(t))\} \quad (5.12)$$



The admittance operator  $Y_c[j\omega(t)]$  operates on the term in the curly brackets { } in this notation. We can also define the frequency operator

$$[\omega(t)] = [\bar{\omega} - j \frac{d}{dt}] \quad (5.13)$$

where  $\omega(t)$  is the instantaneous frequency, and  $\bar{\omega}$  is the quasistationary frequency. The instantaneous frequency of  $v(t)$  is

$$\omega(t) = \frac{d}{dt} (\bar{\omega}t + \phi(t)) = \bar{\omega} + \frac{d\phi}{dt} \quad (5.14)$$

At microwave frequencies, the amplitude  $A(t)$  and phase  $\phi(t)$  are usually slowly varying functions of time (for AM and PM respectively) in comparison with the quasistationary carrier frequency  $\bar{\omega}$ . For  $dA/dt \ll \bar{\omega}A$  and  $d\phi/dt \ll \bar{\omega}$ , the admittance operator can be expanded into a Taylor series about  $\bar{\omega}$ :

$$Y_c[j\omega(t)] = Y_c[j\bar{\omega} + d/dt] = \sum_{n=0}^{\infty} \frac{d^n Y(j\bar{\omega})}{d\bar{\omega}^n} \frac{1}{n!} \left( \frac{d}{dt} \right)^n \quad (5.15)$$

Substituting Eqns. (5.13) and (5.15) into Eqn. (5.12), we have

$$I(t) = \left[ \sum_{n=0}^{\infty} \frac{d^n Y(j\bar{\omega})}{d\bar{\omega}^n} \frac{1}{n!} (j\omega(t) - j\bar{\omega})^n \right] \{A(t) \exp(j\phi(t))\} \quad (5.16)$$

Equation (5.16) is known as the Carson-Fry series [96].





Inspection of Eqn. (5.16) reveals that the operator  $Y_c[j\omega(t)]$  will be composed of terms  $j\omega$ ,  $(j\omega)^2$ ,  $(j\omega)^3$ , etc.. Separating the real and imaginary parts of  $Y_c[j\omega(t)]$  results in

$$Y_c[j\omega(t)] = G[\omega^2(t)] - j\omega(t) S[\omega^2(t)] \quad (5.17)$$

where

$$G[\omega^2(t)] = G[(\bar{\omega} - j \frac{d}{dt})^2] = G[\bar{\omega}^2 - j2\bar{\omega} \frac{d}{dt} - \frac{d^2}{dt^2}] \quad (5.18)$$

and

$$S[\omega^2(t)] = S[(\bar{\omega} - j \frac{d}{dt})^2] = S[\bar{\omega}^2 - j2\bar{\omega} \frac{d}{dt} - \frac{d^2}{dt^2}] \quad (5.19)$$

are conductance and inductive susceptance operators, respectively. For slowly varying amplitude  $A(t)$  and phase  $\phi(t)$ , the second-order term  $d^2/dt^2$  is negligible. Then, expanding Eqns. (5.18) and (5.19) by a Taylor series, we obtain

$$G[\omega^2(t)] = \sum_{n=0}^{\infty} \frac{d^n G(\bar{\omega}^2)}{d(\bar{\omega}^2)^n} \frac{1}{n!} (\omega^2(t) - \bar{\omega}^2)^n \quad (5.20)$$

and

$$S[\omega^2(t)] = \sum_{n=0}^{\infty} \frac{d^n S(\bar{\omega}^2)}{d(\bar{\omega}^2)^n} \frac{1}{n!} (\omega^2(t) - \bar{\omega}^2)^n \quad (5.21)$$

Substitution of these results into Eqn. (5.17) is found to yield the



desired passive circuit non-CW admittance operator [95]:

$$Y_c[j\omega(t)] = \sum_{n=0}^{\infty} \left( \frac{d^n G(\bar{\omega}^2)}{d(\bar{\omega}^2)^n} - j\omega(t) \frac{d^n S(\bar{\omega}^2)}{d(\bar{\omega}^2)^n} \right) \frac{(\omega^2(t) - \bar{\omega}^2)^n}{n!}. \quad (5.22)$$

### 5.2.2 Approximation of the Passive Circuit Linear Admittance Operator by Cubic Spline Interpolation

The expanded Carson-Fry series, Eqn. (5.22), may not be convergent for frequencies far from the quasistationary frequency  $\bar{\omega}$ ; the convergence depends on how slowly  $A(t)$  and  $\phi(t)$  are varying compared to  $\bar{\omega}$ . However, at microwave frequencies, the AM and/or PM modulation is slowly varying compared to the carrier frequency. In this case, the series, Eqn. (5.22) will usually converge [95], and a finite number of terms can approximate the series with sufficient accuracy:

$$Y_c[j\omega(t)] \approx \sum_{n=0}^N \left( \frac{d^n G(\bar{\omega}^2)}{d(\bar{\omega}^2)^n} - j\omega(t) \frac{d^n S(\bar{\omega}^2)}{d(\bar{\omega}^2)^n} \right) \frac{(\omega^2(t) - \bar{\omega}^2)^n}{n!}. \quad (5.23)$$

If  $Y_c[j\omega(t)]$  is given analytically, the derivatives in Eqn. (5.23) are easily found; normally, however, only measured discrete data points are available so that numerical differentiation must be employed. Cubic spline interpolation is an effective technique for numerical differentiation for several reasons [97]:

1) The natural cubic spline interpolating function on the interval  $[a, b]$  exists for all continuous functions in  $[a, b]$ , and is unique.



2) The cubic spline interpolating function,  $f(x)$ , possesses the property of least mean-squared curvature; that is, for all other twice-differentiable interpolating functions  $g(x)$ , the property

$$\int_a^b [f''(x)]^2 dx \leq \int_a^b [g''(x)]^2 dx \quad (5.24)$$

holds. Thus, in the sense of the integral, the cubic spline may be viewed as the smoothest of all possible interpolating functions: it interpolates data points with minimum curvature.

3) The cubic spline is continuous together with its first two derivatives on  $[a, b]$ .

4) The cubic spline has strong convergence properties even for unequal mesh intervals.

5) The cubic spline coefficients in a given mesh interval depend on all data points in the range  $[a, b]$ . Consequently, nonsystematic errors of individual data points on the numerical derivatives are reduced — the derivatives are smoothed.

Let the passive circuit admittance measured at CW frequencies  $\bar{\omega}_1 < \bar{\omega}_2 < \dots < \bar{\omega}_k < \bar{\omega}_{k+1} < \dots < \bar{\omega}_M$  be denoted by

$$Y_{ci}(j\bar{\omega}_i) = G_i(\bar{\omega}_i^2) - j\bar{\omega}_i S_i(\bar{\omega}_i^2); \quad i = 1, 2, \dots, M. \quad (5.25)$$

Equation (5.25) is equivalent to the representation of the circuit admittance operator in Eqn. (5.17) for the CW case ( $d/dt = 0$ ;  $\omega(t) = \bar{\omega}$ ).



Now consider small frequency deviations about the quasistationary frequency  $\bar{\omega}$ . At the instantaneous frequency,  $\omega(t)$ , we wish to approximate the continuous and differentiable functions  $G[\omega^2(t)]$  and  $S[\omega^2(t)]$ , (Eqn. (5.17)), on the interval  $[\bar{\omega}_1^2, \bar{\omega}_M^2]$  in a piecewise fashion, using cubic spline interpolating polynomials over non-overlapping subintervals  $(\bar{\omega}_k^2, \bar{\omega}_{k+1}^2)$ ,  $k = 1, \dots, M - 1$ . A natural cubic spline can be fitted in each of these  $(M - 1)$  frequency intervals. In the  $K^{\text{th}}$ -interval  $(\bar{\omega}_k^2, \bar{\omega}_{k+1}^2)$  the cubic spline functions are [79], [97]: for the conductance,

$$\begin{aligned} G_K(\omega^2) &= \sum_{m=0}^3 \hat{g}_m (\omega^2 - \bar{\omega}_k^2)^m = \sum_{m=0}^3 g_m (\bar{\omega}_k^2) \omega^{2m} \\ &= \sum_{m=0}^3 g_m \omega^{2m} \end{aligned} \quad (5.26)$$

and for the susceptance,

$$\begin{aligned} S_K(\omega^2) &= \sum_{m=0}^3 \hat{s}_m (\omega^2 - \bar{\omega}_k^2)^m = \sum_{m=0}^3 s_m (\bar{\omega}_k^2) \omega^{2m} \\ &= \sum_{m=0}^3 s_m \omega^{2m} \end{aligned} \quad (5.27)$$

The natural cubic spline coefficients  $\hat{g}_m$  and  $\hat{s}_m$  have been rearranged to yield new coefficients,  $g_m$  and  $s_m$ , respectively, which are functions of the CW frequency  $\bar{\omega}_k$ . The new coefficients  $g_m, m=0,1,2,3$





are given by:

$$g_0 = g_0(\bar{\omega}_k^2) = \hat{g}_0 - \hat{g}_1 \bar{\omega}_k^2 + \hat{g}_2 \bar{\omega}_k^4 - \hat{g}_3 \bar{\omega}_k^6 \quad (5.28a)$$

$$g_1 = g_1(\bar{\omega}_k^2) = \hat{g}_1 - 2\hat{g}_2 \bar{\omega}_k^2 + 3\hat{g}_3 \bar{\omega}_k^4 \quad (5.28b)$$

$$g_2 = g_2(\bar{\omega}_k^2) = \hat{g}_2 - 3\hat{g}_3 \bar{\omega}_k^2 \quad (5.28c)$$

$$g_3 = \hat{g}_3 \quad (5.28d)$$

A similar set of relations transforms the normal cubic spline coefficients  $\hat{s}_m$  into the rearranged coefficients  $s_m$ . Combining Eqns. (5.26) and (5.27) as in Eqn. (5.17) we obtain the fitted circuit admittance operator, in the  $K^{\text{th}}$ -interval  $(\bar{\omega}_k, \bar{\omega}_{k+1})$ ,

$$Y_c[j\omega]_K = \sum_{m=0}^3 (g_m - j\omega s_m) \omega^{2m} \quad (5.29)$$

Hence if the frequency intervals are fine enough to reveal all local extrema, the actual admittance function is well approximated by only four terms.

In summary, for a non-CW voltage excitation

$$v(t) = A(t) \exp(j(\bar{\omega}t + \phi(t))) \quad (5.30)$$

where  $A(t)$  and  $\phi(t)$  are slowly varying functions of time in comparison with the carrier frequency  $\bar{\omega}$  (i.e.  $dA/dt \ll \bar{\omega}A$  and



$d\phi/dt < \bar{\omega}$ ), and the instantaneous frequency  $\bar{\omega} + (d\phi/dt)$  lies in the  $K^{\text{th}}$ -frequency interval  $(\bar{\omega}_k, \bar{\omega}_{k+1})$ , the passive circuit current response is

$$i(t) = I(t) \exp(j\bar{\omega}t) \quad . \quad (5.31)$$

The actual physical signals are  $\text{Re}\{v(t)\}$  and  $\text{Im}\{i(t)\}$ . The complex current amplitude  $I(t)$  is given approximately by

$$I(t) = Y_c [j\omega]_K \{A(t) \exp(j\phi(t))\} \quad . \quad (5.32)$$

Using Eqns. (5.13) and (5.29), we can write Eqn. (5.32) in the form

$$I(t) = \left[ \sum_{m=0}^3 (g_m - j\omega s_m) (\bar{\omega} - j d/dt)^{2m} \right]_K \{A(t) \exp(j\phi(t))\}. \quad (5.33)$$

### 5.2.3 Nonlinear Active Circuit Non-CW Admittance Operator

Analysis of a two-terminal active diode is simplified by isolating the nonlinear, relatively frequency-insensitive electronic admittance,  $Y_e$ , of the active region of the device from the admittance of the inactive regions and of the package parasitics. The latter can be included in the linear frequency-sensitive passive circuit admittance,  $Y_c$ , seen by  $Y_e$ .

There are bias components,  $V_B(t)$  and  $I_B(t)$ , superimposed on the active device terminal RF voltage and RF current. Due to rectification and thermal properties, these bias components will be slowly varying functions of time. However, because of large time constants



in the bias circuitry and large thermal time constants for a device mounted into a large heat-sink, changes in the ac bias components are very slow compared with the RF signal variations.

Consider a non-CW, RF voltage excitation given by

$$v(t) = A(t) \exp(j(\bar{\omega}t + \phi(t))) + A(t) \exp(-j(\bar{\omega}t + \phi(t))) \quad (5.34)$$

or

$$v(t) = V(t) \exp(j\bar{\omega}t) + V^*(t) \exp(-j\bar{\omega}t) \quad . \quad (5.35)$$

Both positive and negative exponential signals must be included in analysing nonlinear circuits because both will contribute to the response at each signal through nonlinear effects. The amplitude  $A(t)$  and phase  $\phi(t)$  are both assumed to be slowly varying compared with the quasistationary frequency  $\bar{\omega}$ , and with the response time of the network (i.e.,  $dA/dt \ll \bar{\omega}A$  and  $d\phi/dt \ll \bar{\omega}$ ). This assumption is valid at microwave frequencies. Further, it is assumed that, in the tuned amplifier, the external circuit admittance across the active region of the diode is sufficiently high that this admittance is infinite for all harmonics except the fundamental [3]. This assumption can be made safely for most negative-resistance devices mounted in a tuned circuit with a significant  $Q$ . In fact, the second and other harmonic voltages measured for the experimental 100-mW IMPATT diode were no larger than one percent of the fundamental voltage (there was no detectable harmonic power within 40 dB of the



fundamental) for input levels less than +10 dBm applied to the IMPATT amplifier. Higher-order harmonic current flow is assumed to be unimpeded [3]: the active circuit RF current response to the excitation  $v(t)$  can be written as

$$i(t) = \sum_{\substack{\ell=-L \\ \ell \neq 0}}^{+L} I_{\ell}(t) \exp(j\ell\bar{\omega}t) \quad (5.36)$$

where the bias term ( $\ell=0$ ) has been neglected, and  $I_{\ell}(t)$  is a complex time function. The voltage,  $v(t)$ , and current,  $i(t)$ , can be related, in a simple model [95], by the differential equation

$$i(t) = \sum_{p=0}^P \sum_{q=0}^Q b_{p,q} v^q(t) \frac{d^p v(t)}{dt^p} \quad (5.37)$$

In the above model,  $i(t)$  is a nonlinear function of the voltage  $v(t)$  and its derivatives, but does not depend on the voltage integrals.

Substituting Eqns. (5.35) and (5.36) into Eqn. (5.37), and then differentiating  $v(t)$  as in Eqn. (5.8), we obtain

$$\sum_{\substack{\ell=-L \\ \ell \neq 0}}^{+L} I_{\ell}(t) \exp(j\ell\bar{\omega}t) = \exp(j\bar{\omega}t) \left[ \sum_{p=0}^P \sum_{q=0}^Q b_{p,q} v^q(t) \right. \\ \left. (j\bar{\omega} + d/dt)^p \right] \{V(t)\} + \exp(-j\bar{\omega}t) \left[ \sum_{p=0}^P \sum_{q=0}^Q b_{p,q} v^q(t) \right. \\ \left. (-j\bar{\omega} + d/dt)^p \right] \{V^*(t)\} \quad (5.38)$$





The terms in square brackets [ ] on the right hand side of Eqn. (5.38) operate on the terms in curly brackets { }. After rearranging the right hand side, we find the fundamental complex current amplitude (the current response in the zone of the input frequency) at  $\exp(j\bar{\omega}t)$  to be [95]

$$I_1(t)\exp(j\bar{\omega}t) = \exp(j\bar{\omega}t) \cdot \left[ \sum_{p=0}^P \sum_{n=0}^{\frac{Q-1}{2}} b_{p,0,2n} v^{2n}(t) (j\bar{\omega} + d/dt)^p \{V(t)\} \right. \\ \left. + \exp(-j\bar{\omega}t) \left[ \sum_{p=0}^P \sum_{n=0}^{\frac{Q-1}{2}} b_{p,2,2n} v^{2n}(t) (-j\bar{\omega} + d/dt)^p \{V^*(t)\} \right] \right] \quad (5.39)$$

In the first term on the right hand side of Eqn. (5.39), the middle index 0 in the coefficient  $b_{p,0,2n}$  denotes "take the dc part of the expansion of  $v^{2n}(t)$ ". This term when multiplied by the factor  $\exp(j\bar{\omega}t)$  produces a component at  $\exp(j\bar{\omega}t)$ . Similarly, the index 2 in the coefficient  $b_{p,2,2n}$  in the second term on the right hand side of Eqn. (5.39) denotes "take the second harmonic of the expansion of  $v^{2n}(t)$ ". This term, at  $\exp(j2\bar{\omega}t)$ , when multiplied by the factor  $\exp(-j\bar{\omega}t)$  also produces a component at the fundamental frequency  $\exp(j\bar{\omega}t)$ .

The two terms in square brackets in Eqn. (5.39) together form a nonlinear admittance operator,  $Y_e[j\omega(t), V(t)]$ , for the two-terminal active diode, such that



$$I_1(t) = Y_e[j\omega(t), V(t)] \{V(t)\} \quad (5.40)$$

The complex nonlinear admittance operator describing the active circuit can be simplified greatly for CW excitation,

$$v(t) = A_0 (\exp(j\bar{\omega}t) + \exp(-j\bar{\omega}t)) \quad (5.41)$$

This excitation is also given by Eqn. (5.34) for steady-state CW conditions :  $A(t) = V(t) = A_0$ ,  $\phi(t) = 0$ ,  $\omega = \bar{\omega}$ ,  $d/dt = 0$ . We can substitute these parameters into Eqn. (5.39), and after separating even- from odd-powers  $p$ , we obtain

$$I_1(t) \exp(j\bar{\omega}t) = \exp(j\bar{\omega}t) \cdot \left[ \sum_{m=0}^{\frac{P-1}{2}} \sum_{n=0}^{\frac{Q-1}{2}} \left( b_{2m,2,2n} (j\bar{\omega})^{2m} + b_{2m+1,0,2n} \cdot (+j\bar{\omega})^{2m+1} \right) v^{2n}(t) \right] \{A_0\} \\ + \exp(-j\bar{\omega}t) \cdot \left[ \sum_{m=0}^{\frac{P-1}{2}} \sum_{n=0}^{\frac{Q-1}{2}} \left( b_{2m,2,2n} (-j\bar{\omega})^{2m} + b_{2m+1,2,2n} (-j\bar{\omega})^{2m+1} \right) \cdot v^{2n}(t) \right] \{A_0\} \quad (5.42)$$

Expanding  $v^{2n}(t)$ , retaining the dc component or  $2^{\text{nd}}$ -harmonic component of this expansion according to the middle index of the  $b$  coefficients



(0 and 2, respectively), and also expanding  $(j\bar{\omega})^{2m}$ ,  $(j\bar{\omega})^{2m+1}$ ,  
 $(-j\bar{\omega})^{2m}$ ,  $(-j\bar{\omega})^{2m+1}$  we can prove that

$$I_1 = \left[ \sum_{m=0}^{\frac{P-1}{2}} \sum_{n=0}^{\frac{Q-1}{2}} (-1)^m (A_o)^{2n} (\bar{\omega})^{2m} \left( b_{2m,0,2n} + b_{2m,2,2n} + j\bar{\omega} b_{2m+1,0,2n} - j\bar{\omega} b_{2m+1,2,2n} \right) \right] \{A_o\} \quad (5.43)$$

For simplicity, define a new set of coefficients:

$$d_{2m,2n} = b_{2m,0,2n} + b_{2m,2,2n} \quad (5.44a)$$

$$d_{2m+1,2n} = b_{2m+1,0,2n} - b_{2m+1,2,2n} \quad (5.44b)$$

Then, from Eqns. (5.43) and (5.44),

$$I_1 = \left[ \sum_{m=0}^{\frac{P-1}{2}} \sum_{n=0}^{\frac{Q-1}{2}} (-1)^m (A_o)^{2n} (\bar{\omega})^{2m} \left( d_{2m,2n} + j\bar{\omega} d_{2m+1,2n} \right) \right] \{A_o\} \quad (5.45)$$

Equation (5.45) is the complex amplitude of the current response at the fundamental frequency for a CW voltage excitation given by Eqn. (5.41). By definition, the CW admittance operator for the active region of the device is [95]



$$Y_c[j\bar{\omega}, A_o] = \frac{I}{A_o} = \sum_{m=0}^{\frac{P-1}{2}} \sum_{n=0}^{\frac{Q-1}{2}} (-1)^m \left( d_{2m, 2n} + j\bar{\omega} d_{2m+1, 2n} \right) \bar{\omega}^{2m} A_o^{2n}. \quad (5.46)$$

This electronic admittance operator is seen to be amplitude- and frequency- dependent; that is, it is nonlinear.

#### 5.2.4 Approximation of the Active Circuit Nonlinear Admittance Operator by Bicubic Spline Interpolation

The coefficients in Eqns. (5.44) and (5.45) can be determined by making CW admittance measurements on the active region of the diode. Interpolating these electronic admittance measurements using bicubic spline functions yields an expression of the same form as Eqn. (5.46) defining the CW nonlinear admittance operator. A bicubic spline interpolation is simply a cubic spline interpolation in two dimensions [97]. The existence and uniqueness properties, convergence property, least-squared curvature property, and data-smoothing property of one-dimensional cubic spline interpolation also apply to the two-dimensional case [97].

A bicubic spline function can be fitted through a grid of  $M \times N$  values  $G_{1,1}, G_{1,2}, \dots, G_{M,N}$  of large signal electronic conductance where  $G_{i,j}$  is the value of the electronic conductance measured at CW radian frequency  $\bar{\omega}_i$ , and at large-signal RF voltage amplitude  $V_j$  for  $i = 1, 2 \dots M$  and  $j = 1, 2 \dots, N$ . For instantaneous frequency  $\omega = \bar{\omega}_k + \frac{d\phi(t)}{dt}$ , and instantaneous amplitude  $A$  lying in the  $KL^{th}$ -subrectangle  $(\bar{\omega}_k^2, \bar{\omega}_{k+1}^2) \times (A_L^2, A_{L+1}^2)$ , the non-CW electronic conductance is of the form [79], [97],





$$\begin{aligned}
G_{KL}(\omega, A) &= \sum_{m=0}^3 \sum_{n=0}^3 \hat{g}_{mn} (\omega - \bar{\omega}_k)^{2m-1} (A - A_L)^{2n-1} \\
&= \sum_{m=0}^3 \sum_{n=0}^3 g_{mn} (\bar{\omega}_k, A_L) \omega^{2m} A^{2n} \quad (5.47)
\end{aligned}$$

The natural bicubic spline coefficients  $\hat{g}_{mn}$  have been rearranged to yield a new set of coefficients  $g_{mn}(\bar{\omega}_k, A_L)$  which are functions of  $\bar{\omega}_k$  and  $A_L$ . The new coefficients  $g_{mn}, m, n=0, 1, 2, 3$  are given by:

$$\begin{aligned}
g_{00} &= \hat{g}_{00} - \hat{g}_{10} \bar{\omega}_k^2 + \hat{g}_{20} \bar{\omega}_k^4 - \hat{g}_{30} \bar{\omega}_k^6 - (\hat{g}_{01} - \hat{g}_{11} \bar{\omega}_k^2 + \hat{g}_{21} \bar{\omega}_k^4 - \hat{g}_{31} \bar{\omega}_k^6) A_L^2 \\
&\quad + (\hat{g}_{02} - \hat{g}_{12} \bar{\omega}_k^2 + \hat{g}_{22} \bar{\omega}_k^4 - \hat{g}_{32} \bar{\omega}_k^6) A_L^4 \\
&\quad - (\hat{g}_{03} - \hat{g}_{13} \bar{\omega}_k^2 + \hat{g}_{23} \bar{\omega}_k^4 - \hat{g}_{33} \bar{\omega}_k^6) A_L^6 \quad (5.48a)
\end{aligned}$$

$$\begin{aligned}
g_{10} &= \hat{g}_{10} - 2\hat{g}_{20} \bar{\omega}_k^2 + 3\hat{g}_{30} \bar{\omega}_k^4 - (\hat{g}_{11} - 2\hat{g}_{21} \bar{\omega}_k^2 + 3\hat{g}_{31} \bar{\omega}_k^4) A_L^2 \\
&\quad + (\hat{g}_{12} - 2\hat{g}_{22} \bar{\omega}_k^2 + 3\hat{g}_{32} \bar{\omega}_k^4) A_L^4 - (\hat{g}_{13} - 2\hat{g}_{23} \bar{\omega}_k^2 + 3\hat{g}_{33} \bar{\omega}_k^4) A_L^6 \quad (5.48b)
\end{aligned}$$

$$\begin{aligned}
g_{20} &= \hat{g}_{20} - 3\hat{g}_{30} \bar{\omega}_k^2 - (\hat{g}_{21} - 3\hat{g}_{31} \bar{\omega}_k^2) A_L^2 + (\hat{g}_{22} - 3\hat{g}_{32} \bar{\omega}_k^2) A_L^4 \\
&\quad - (\hat{g}_{23} - 3\hat{g}_{33} \bar{\omega}_k^2) A_L^6 \quad (5.48c)
\end{aligned}$$

$$g_{30} = \hat{g}_{30} - \hat{g}_{31} A_L^2 + \hat{g}_{32} A_L^4 - \hat{g}_{33} A_L^6 \quad (5.48d)$$



$$g_{01} = \hat{g}_{01} - \hat{g}_{11} \bar{\omega}_k^2 + \hat{g}_{21} \bar{\omega}_k^4 - \hat{g}_{31} \bar{\omega}_k^6 - 2(\hat{g}_{02} - \hat{g}_{12} \bar{\omega}_k^2 + \hat{g}_{22} \bar{\omega}_k^4 - \hat{g}_{32} \bar{\omega}_k^6) A_L^2$$

$$+ 3(\hat{g}_{03} - \hat{g}_{13} \bar{\omega}_k^2 + \hat{g}_{23} \bar{\omega}_k^4 - \hat{g}_{33} \bar{\omega}_k^6) A_L^4 \quad (5.48e)$$

$$g_{02} = \hat{g}_{02} - \hat{g}_{12} \bar{\omega}_k^2 + \hat{g}_{22} \bar{\omega}_k^4 - \hat{g}_{32} \bar{\omega}_k^6 - 3(\hat{g}_{03} - \hat{g}_{13} \bar{\omega}_k^2 + \hat{g}_{23} \bar{\omega}_k^4 - \hat{g}_{33} \bar{\omega}_k^6) A_L^2 \quad (5.48f)$$

$$g_{03} = \hat{g}_{03} - \hat{g}_{13} \bar{\omega}_k^2 + \hat{g}_{23} \bar{\omega}_k^4 - \hat{g}_{33} \bar{\omega}_k^6 \quad (5.48g)$$

$$g_{11} = \hat{g}_{11} - 2\hat{g}_{21} \omega_k^2 + 3\hat{g}_{31} \omega_k^4 - 2\hat{g}_{12} A_L^2 + 3\hat{g}_{13} A_L^4 + 4\hat{g}_{22} \omega_k^2 A_L^2$$

$$- 6\hat{g}_{32} \omega_k^4 A_L^2 - 6\hat{g}_{23} \omega_k^2 A_L^4 + 9\hat{g}_{33} \omega_k^4 A_L^4 \quad (5.48h)$$

$$g_{21} = \hat{g}_{21} - 3\hat{g}_{31} \bar{\omega}_k^2 - 2\hat{g}_{22} A_L^2 + 6\hat{g}_{32} \bar{\omega}_k^2 A_L^2 + 3\hat{g}_{23} A_L^4 - 9\hat{g}_{33} \bar{\omega}_k^2 A_L^4 \quad (5.48i)$$

$$g_{31} = \hat{g}_{31} - 2\hat{g}_{32} A_L^2 + 3\hat{g}_{33} A_L^4 \quad (5.48j)$$

$$g_{12} = \hat{g}_{12} - 2\hat{g}_{22} \omega_k^2 + 3\hat{g}_{32} \omega_k^4 - 3\hat{g}_{13} A_L^2 + 6\hat{g}_{23} \omega_k^2 A_L^2 - 9\hat{g}_{33} \omega_k^4 A_L^2 \quad (5.48k)$$

$$g_{13} = \hat{g}_{13} - 2\hat{g}_{23} \bar{\omega}_k^2 + 3\hat{g}_{33} \bar{\omega}_k^4 \quad (5.48l)$$

$$g_{22} = \hat{g}_{22} - 3\hat{g}_{32} \bar{\omega}_k^2 - 3\hat{g}_{23} A_L^2 + 9\hat{g}_{33} \bar{\omega}_k^2 A_L^2 \quad (5.48m)$$

$$g_{32} = \hat{g}_{32} - 3\hat{g}_{33} A_L^2 \quad (5.48n)$$

$$g_{23} = \hat{g}_{23} - 3\hat{g}_{33} \omega_k^2 \quad (5.48o)$$



$$g_{33} = \hat{g}_{33} \quad (5.48p)$$

Similarly, a bicubic spline function can be fitted through a grid of  $M \times N$  values  $C_{1,1}, C_{1,2}, \dots, C_{M,N}$  of large-signal equivalent electronic capacitance<sup>†</sup> where  $C_{i,j}$  is the value of the equivalent electronic capacitance measured at CW radian frequency  $\bar{\omega}_i$ , and at large-signal RF voltage amplitude  $V_j$  for  $i = 1, 2, \dots, M$  and  $j = 1, 2, \dots, N$ .

For instantaneous frequency  $\omega$ , and instantaneous amplitude  $A$  lying in the  $KL^{\text{th}}$ -subrectangle  $(\bar{\omega}_k^2, \bar{\omega}_{k+1}^2) \times (A_L^2, A_{L+1}^2)$ , the non-CW electronic capacitance is [79], [97],

$$\begin{aligned} C_{KL}(\omega, A) &= \sum_{m=0}^3 \sum_{n=0}^3 \hat{c}_{mn} (\bar{\omega}_k^2 - \bar{\omega}_{k+1}^2)^{2m-1} (A - A_L)^{2n-1} \\ &= \sum_{m=0}^3 \sum_{n=0}^3 c_{mn}(\bar{\omega}_k, A_L) \omega^{2m-1} A^{2n-1} \end{aligned} \quad (5.49)$$

The natural bicubic spline coefficients  $\hat{c}_{mn}$  have been rearranged to yield a new set of coefficients  $c_{mn}(\bar{\omega}_k, A_L)$  which are functions of  $\bar{\omega}_k$  and  $A_L$ . The coefficients  $c_{mn}$  are related to the coefficients  $\hat{c}_{mn}$  by equations similar to those in Eqn. (5.48). Equations (5.47) and (5.49) can be combined to obtain the approximate non-CW electronic admittance in the  $KL^{\text{th}}$ -subrectangle:

$$Y_{KL}(j\omega, V) = \sum_{m=0}^3 \sum_{n=0}^3 (g_{mn}(\bar{\omega}_k, A_L) + j\omega c_{mn}(\bar{\omega}_k, A_L)) \omega^{2m-1} A^{2n-1} \quad (5.50)$$

---

<sup>†</sup> The active region of the experimental IMPATT diode displayed a capacitive susceptance above breakdown voltage at the operating frequency.



Inspection reveals that the non-CW approximate electronic admittance given by Eqn. (5.50) is of the same form as the CW admittance operator expressed in Eqn. (5.46); in the CW case (i.e.,  $\omega=\bar{\omega}$ ,  $V=A_0$ ), the coefficients in Eqn. (5.46) for  $P=Q=7$  can be determined from the calculated coefficients in Eqn. (5.50). Equating coefficients for the CW case, with  $P=Q=7$ , we obtain

$$d_{2m,2n} = (-1)^m g_{mn} \quad ; m,n=0,1,2,3 \quad (5.51a)$$

$$d_{2m+1,2n} = (-1)^m c_{mn} \quad ; m,n=0,1,2,3 \quad . \quad (5.51b)$$

To find the  $\underline{b}$  coefficients in Eqn. (5.43) from the known  $\underline{d}$  coefficients we need additional relations : by expanding Eqn. (5.42), for the CW case with  $P=Q=7$ , we find

$$b_{2m,2,2n} = \frac{n}{n+1} b_{2m,0,2n} \quad ; m,n=0,1,2,3 \quad (5.52a)$$

$$b_{2m+1,2,2n} = \frac{n}{n+1} b_{2m+1,0,2n} \quad ; m,n=0,1,2,3 \quad . \quad (5.52b)$$

Using the natural bicubic spline coefficients obtained from measured electronic admittance data, together with Eqns. (5.43), (5.48), (5.51) and (5.52), the CW admittance operator (Eqn. 5.46), for the active region of the diode is determined. Then, since the amplitude  $A(t)$ , phase  $\phi(t)$  and thus the complex amplitude  $V(t)$  of a non-CW excitation, given by Eqn. (5.34) are usually slowly varying compared with the microwave carrier frequency  $\bar{\omega}$ , we can assume that the  $\underline{b}$  coefficients calculated for the CW





case also apply to the non-CW case, Eqns. (5.39) and (5.40). The complex amplitude of the current response at the fundamental frequency  $\exp(j\bar{\omega}t)$  becomes

$$I_1(t) = Y_e[j\omega, V]_{KL} \{V(t)\} \quad (5.53)$$

or

$$I_1(t) = \left[ \sum_{p=0}^7 \left( b_{p,0,0} + b_{p,0,2} V(t)V^*(t) + b_{p,0,4} V^2(t)V^{*2}(t) + b_{p,0,6} V^3(t)V^{*3}(t) \right) (j\bar{\omega} + d/dt)^p \right]_{KL} \{V(t)\} + \left[ \sum_{p=0}^7 \left( b_{p,2,0} + b_{p,2,2} V^2(t) + b_{p,2,4} V^3(t)V^*(t) + b_{p,2,6} V^4(t)V^{*2}(t) \right) (-j\bar{\omega} + d/dt)^p \right]_{KL} \{V^*(t)\} \quad (5.54)$$

for instantaneous frequency  $\omega(t)$ , and instantaneous amplitude  $|V(t)|$  in the  $KL^{th}$ -subrectangle  $(\bar{\omega}_k, \bar{\omega}_{k+1}) \times (A_L, A_{L+1})$ . Equation (5.53) is the operator notation used for the expansion in Eqn. (5.54). If the  $M$  frequencies, and the  $N$  - RF voltage levels used in the large-signal electronic admittance measurements are spaced closely enough to reveal all local extrema, the actual admittance is well-approximated by the fitted bicubic spline functions, and hence the fundamental current response calculated from Eqn. (5.53) should be close to the actual response. Note that different  $b$  coefficients apply to each  $KL^{th}$ -subrectangle,  $k=1,2, \dots, M$



and  $L=1,2, \dots, N$ ; care must be taken to ensure that the instantaneous frequency and amplitude of the response lies in the corresponding  $KL^{\text{th}}$ -subrectangle as the solution progresses.

### 5.3 Numerical Quasistationary Distortion Analysis of an IMPATT Amplifier

#### 5.3.1 Equivalent Circuit of a Stable IMPATT Amplifier

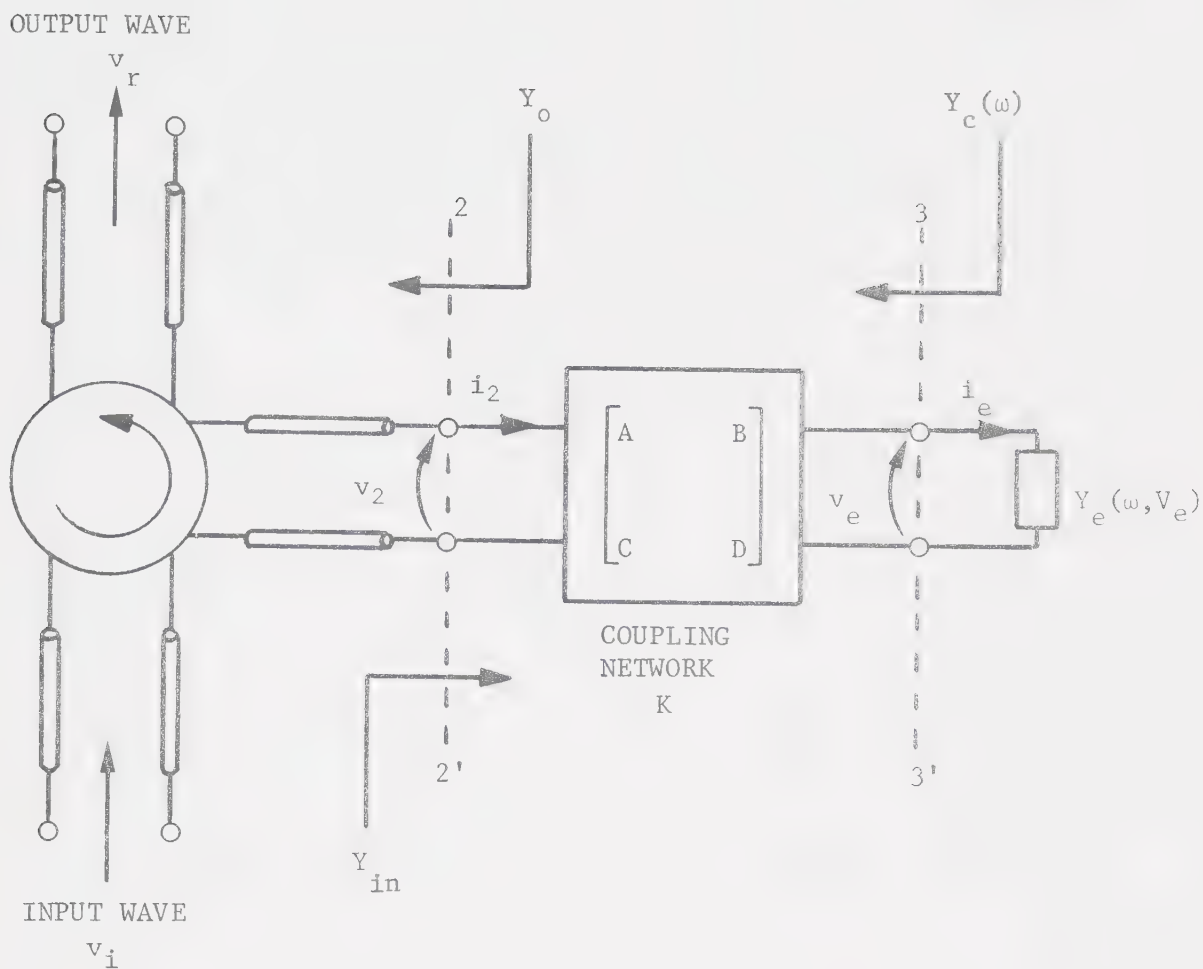
Figure 5.1(a) shows a typical circuit suitable for stable reflection-type amplification using an IMPATT diode. It comprises a circulator to separate the input RF voltage wave  $v_i$  and output RF voltage wave  $v_r$ , a coupling network to establish the desired loading admittance  $Y_c(\omega)$ , and the electronic admittance  $Y_e(\omega, V_e)$  of the diode. The passive circuit admittance  $Y_c(\omega)$  seen by the active region of the diode, includes the inactive regions of the diode and the package parasitics. The coupling network is described by its voltage-current transmission matrix  $K[ABCD]$ , which is a function of the applied radian frequency  $\omega$ . The RF voltage across the diode is denoted by  $v_e$ ; the current through the diode is designated by  $i_e$ . The net current into the coupling network,  $i_2$ , and the voltage across the network terminals,  $v_2$ , are

$$i_2(t) = i_i(t) - i_r(t) \quad (5.55)$$

$$v_2(t) = v_i(t) + v_r(t) = Av_e(t) + B i_e(t) \quad . \quad (5.56)$$

The input and output ports of the amplifier are assumed to be matched to the transmission line characteristic admittance  $Y_0$ . The simple equivalent circuit of Fig. 5.1(b) is used for our analysis of IM distortion. The RF





(a)

(b)

Figure 5.1 (a) IMPATT-diode reflection-type amplifier circuit.  
 (b) Equivalent circuit used for quasistationary distortion analysis of a stable IMPATT amplifier.



current generator  $i_g$  is the Thevenin equivalent current generator for the input wave at the diode.

The measured electronic admittance  $Y_e(\omega, V_e)$ , in Fig. 3.15, for the experimental IMPATT diode is used in the analysis. The passive circuit admittance,  $Y_c(\omega)$ , can also be measured, as will be explained, or can be approximated over a small bandwidth by a  $G_c L_c C_c$  tuned circuit and impedance matching transformer as in Fig. 4.2. Either approach is suitable in the present analysis.

The measurement of  $Y_c(\omega)$  is based on a knowledge of the electronic impedance of the IMPATT diode biased below its breakdown voltage  $V_B$ . The electronic impedance  $Z_e(V)$ , for  $V < V_B$ , is independent of the embedding circuitry. The results in Fig. 3.8 can thus be used here in conjunction with Eqn. (3.12) to determine  $Z_e(V)$ . The input impedance  $Z_{in}(V)$ , seen at reference plane 2-2' in Fig. 5.1(a), when the network is loaded with  $Z_c$  is given by the bilinear transformation:

$$Z_{in}(V) = \frac{A Z_e(V) + B}{C Z_e(V) + D} \quad (5.57)$$

Actually, only three complex parameters are required to characterize the two-port coupling network: division of Eqn. (5.57) by  $Z_o = 1/Y_o$ , and normalization to the factor D results in

$$\tilde{Z}_{in}(V) = \frac{Z_{in}(V)}{Z_o} = \frac{a Z_e(V) + b}{c Z_e(V) + 1} \quad (5.58)$$





where

$$a = A/Z_o D \quad (S) \quad (5.59a)$$

$$b = B/Z_o D \quad (\text{dimensionless}) \quad (5.59b)$$

$$c = C/D \quad (S) \quad (5.59c)$$

are complex constants at fixed frequency  $\omega$ . Since reference planes 2-2' and 3-3' in Fig. 5.1(a) coincide with their corresponding reference planes in the admittance measurement system, Fig. 3.6, the transmission matrix  $K [abc]$  is identical to matrix  $K_2 \begin{bmatrix} a & b & c \\ 2 & 2 & 2 \end{bmatrix}$  representing the coaxial system and parasitics for a particular diode and particular tuning condition. Hence the procedure described in Sections 3.2.2 and 3.2.3 can be followed to extricate the coupling matrix  $K$  for the tuned amplifier at each measurement frequency. The measured admittance,  $Y_c(\omega)$ , seen by the diode when the network is terminated by a matched load  $Z_o$  is then given by the inverse bilinear transformation:

$$Z_c(\omega) = \frac{i}{Y_c(\omega)} = \frac{DZ_o + B}{CZ_o + A} \quad (5.60)$$

or

$$Y_c(\omega) = \frac{a + c}{b + 1} \quad (5.61)$$



In general, the coupling network will be lossy. The relationship between the injected power,  $P_{in}$ , measured at the input port of the amplifier, and the amplitude  $I_g$  of the Thevenin equivalent current source in Fig. 5.1(b) can be found from analysis of the circuit in Fig. 5.1(a). Using Eqns. (5.57) and (5.60), the input admittance of the coupling network is

$$Y_{in} = \frac{C + DY_e}{A + BY_e} \quad (5.62)$$

and the circuit admittance seen by the diode is

$$Y_c = \frac{C + AY_o}{D + BY_o} \quad (5.63)$$

The voltage transmission coefficient at reference plane 2-2' is given by

$$\frac{v_2}{v_i} = \frac{2Y_o}{Y_{in} + Y_o} \quad (5.64)$$

Using  $i_e = Y_e v_e$  in Eqn. (5.56), and substituting the result into Eqn. (5.64) we have

$$v_i = \frac{Y_{in} + Y_o}{2Y_o} (A + BY_e) v_e \quad (5.65)$$

Substituting Eqn. (5.62) into Eqn. (5.65), rearranging the terms, and utilizing Eqn. (5.63) we obtain



$$v_e = \frac{2Y_o}{BY_o + D} \left( \frac{1}{Y_c + Y_e} \right) v_i \quad (5.66)$$

For an input signal  $v_i = V_i \cos \omega t$ ; the injected power at the amplifier input is the maximum available power

$$P_{in} = \frac{1}{2} \operatorname{Re} \{ Y_o V_i^2 \} \quad (5.67)$$

since the input port is matched to the circulator. From Eqn. (5.67), the input voltage amplitude becomes

$$V_i = |v_i| = \sqrt{2P_{in}/G_o} \quad (5.68)$$

where  $G_o = \operatorname{Re} \{ Y_o \}$ . Now considering Fig. 5.1(b) we see that

$$i_g = (Y_c + Y_e) v_e \quad (5.69)$$

Taking the magnitude of Eqn. (5.69), then substituting Eqns. (5.66) and (5.68) we derive

$$I_g = |i_g| = \left| \frac{Y_o}{BY_o + D} \right| \sqrt{8 P_{in}/G_o} \quad (5.70)$$

Without loss of generality, the characteristic admittance  $Y_o$  can be defined to be purely real. Equation (5.70) then becomes

$$I_g = \left| \frac{1}{(b+1)D\sqrt{Z_o}} \right| \sqrt{8 P_{in}} \quad (5.71)$$



where the normalized B coefficient  $b = B/DZ_0$  has been introduced. Since the coupling network, in general, does not contain ferrite devices or active devices, the reciprocity condition

$$A D - B C = Z_0^2 (a-bc) = 1 \quad (5.72)$$

applies. Substituting the result  $D\sqrt{Z_0} = 1/\sqrt{a-bc}$  into Eqn. (5.71), the amplitude of the Thevenin current generator  $i_g = I_g \cos \omega t$  can be written as

$$I_g = \left| \frac{\sqrt{a-bc}}{b+1} \right| \sqrt{8 P_{in}} \quad (5.73)$$

where  $K[abc]$  is known at frequency  $\omega$ .

If a two-tone input  $v_1 = V_1 \cos \omega_1 t + V_2 \cos \omega_2 t$  is applied, the equivalent current generator becomes  $i_g = I_1 \cos \omega_1 t + I_2 \cos \omega_2 t$ , where  $I_1$  and  $I_2$  are each given by Eqn. (5.73), and  $P_{in}$  is the input power at  $\omega_1$  and  $\omega_2$ , respectively.

Instead of measuring  $Y_c(\omega)$ , the circuit admittance can be approximated by a tuned  $G_c L_c C_c$  circuit and impedance transformer as in Fig. 4.2. This simple equivalent circuit is applicable over a limited frequency range of specific interest, say the amplifier 3-dB passband. The circuit admittance is then expressed by Eqn. (4.15). The parameters  $G_c$ ,  $L_c$ ,  $C_c$  are evaluated as outlined in Section 4.3.6. The amplitude  $I_g = \sqrt{8 P_{in} G_c}$  can be determined from Eqn. (5.70) by deriving the following parameters for the lumped-element coupling





$$\text{network : } A = n_1/n_2, B = 0, C = (n_2/n_1) \cdot (j\omega L_c + 1/j\omega C_c), D = n_2/n_1, \\ G_c = (n_1/n_2)^2 G_o.$$

### 5.3.2 Intermodulation Distortion Analysis of an IMPATT Amplifier by Numerical Solution of the Amplifier's Nonlinear Differential Equation

In this analysis we treat intermodulation distortion for the case of an input of two unmodulated signals of equal amplitude at incommensurable frequencies  $\omega_1$  and  $\omega_2$ ,  $\omega_1 \approx \omega_2$ , applied to an IMPATT amplifier. The injected two-tone current signal is

$$i_g(t) = I \cos \omega_1 t + I \cos \omega_2 t. \quad (5.74)$$

Using complex exponential functions Eqn. (5.74) becomes

$$i_g(t) = \frac{I}{2} \left\{ \exp(j\omega_d t) + \exp(-j\omega_d t) \right\} \exp(j\omega_o t) + CC \quad (5.75)$$

where

$$\omega_o = (\omega_1 + \omega_2)/2 \quad (5.76)$$

and

$$\omega_d = (\omega_2 - \omega_1)/2 \quad (5.77)$$

are the carrier frequency and difference frequency, respectively, and where CC represents the complex conjugate terms.

The circuit Q is assumed to be sufficiently high that the



circuit admittance  $Y_c(\omega)$  is infinite for all harmonics except the fundamental. Higher -order harmonic current flow is assumed to be unimpeded, but only the fundamental component of the diode current, i.e. the current in the zone  $\omega_o \pm n\omega_d \approx \omega_o$ , is assumed to affect the voltage of response. Thus, the voltage response for the network of Fig. 5.1(b) is expressed as

$$v_e(t) = A(t) \cos(\omega_o t + \phi(t)) \quad . \quad (5.78)$$

Using complex exponential functions, we can write

$$v_e(t) = \text{Re}\{V(t)\exp(j\omega_o t)\} = \frac{1}{2} V(t)\exp(j\omega_o t) + \text{CC} \quad (5.79)$$

where

$$V(t) = A(t)\exp(j\phi(t)) \quad (5.80)$$

is the complex RF voltage amplitude. Input level varies with the angular frequency  $2\omega_d (= \omega_2 - \omega_1)$ . Hence, the RF voltage amplitude,  $A(t)$ , of the active device changes with the fundamental period  $\pi/\omega_d$ . Delay time exists between the variation of the input level and the RF voltage amplitude. This delay time, causing the arbitrary phase shift  $\phi(t)$  with respect to the driving signal, is usually very small since  $\omega_d$  is normally much less than the operating bandwidth of the amplifier. For  $\omega_d \ll \omega_o$ , the amplitude  $A(t)$  and phase  $\phi(t)$  of  $V(t)$  vary very slowly in comparison with the carrier frequency  $\omega_o$ , and with the response time of the network:  $(dA/dt) \ll \omega_o A(t)$  and



$(d\phi/dt) < \omega_0$ . The principle of quasistationarity —  $V(t)$  is essentially constant during one RF cycle — can thus be employed to calculate  $V(t)$ .

The technique is to write the Kirchhoff nodal equation for the network of Fig. 5.1(b) and obtain the steady-state fundamental voltage response  $V(t)$ . The Kirchhoff equation is simply

$$i_g(t) = \left\{ Y_c(\omega) + Y_e(\omega, V_e) \right\} v_e(t) \quad (5.81)$$

We now approximate the right hand side of Eqn. (5.81) by using the measured non-CW admittance operators derived in the preceding section. Since the effect of the complex conjugate terms in Eqn. (5.79) has already been included in the passive circuit admittance operator, Eqn. (5.33), and in the active circuit admittance operator, Eqn. (5.54), only the components at  $\exp(j\omega_0 t)$  need be operated on to determine the complete response. In operator notation, Eqn. (5.81) becomes

$$\begin{aligned} \frac{I}{2} \exp(j\omega_d t) + \frac{I}{2} \exp(-j\omega_d t) &= \frac{1}{2} Y_c[j\omega]_K \{V(t)\} \\ &+ \frac{1}{2} Y_e[j\omega, V]_{KL} \{V(t)\} \end{aligned} \quad (5.82)$$

with  $\exp(j\omega_0 t)$  understood as a common multiplier. The admittance operators must be chosen so that the frequency  $\omega(\approx \omega_0)$ , and the steady state amplitude  $A(t)$  lie in the correct  $KL^{\text{th}}$ - measurement subrectangle  $(\bar{\omega}_k, \bar{\omega}_{k+1}) \times (A_L, A_{L+1})$ . The factor  $1/2$  appears on the



right hand side of Eqn. (5.82) since we seek the cosine solution expressed in Eqn. (5.79) (compare with Eqn. (5.35)). Substituting Eqns. (5.33) and (5.54) into Eqn. (5.82) gives

$$\begin{aligned}
 I \exp(j\omega_d t) + I \exp(-j\omega_d t) = & \left[ \sum_{m=0}^3 (-1)^m (g_m - j\omega_o s_m) (j\omega_o + d/dt)^{2m} \right]_K \{V(t)\} \\
 & + \left[ \sum_{p=0}^7 \left( b_{p,0,0} + b_{p,0,2} V(t)V^*(t) + b_{p,0,4} V^2(t)V^{*2}(t) + b_{p,0,6} V^3(t)V^{*3}(t) \right) \right. \\
 & \quad \left. \cdot (j\omega_o + d/dt)^p \right]_{KL} \{V(t)\} \\
 & + \left[ \sum_{p=0}^7 \left( b_{p,2,0} + b_{p,2,2} V^2(t) + b_{p,2,4} V^3(t)V^*(t) + b_{p,2,6} V^4(t)V^{*2}(t) \right) \right. \\
 & \quad \left. \cdot (-j\omega_o + d/dt)^p \right]_{KL} \{V^*(t)\}. \quad (5.83)
 \end{aligned}$$

The steady-state nonlinear voltage response of the amplifier to the two-tone input signal will be beat signals at various sum and difference frequencies  $\omega_1 \pm \omega_2$ ,  $2\omega_1 \pm \omega_2$ ,  $2\omega_2 \pm \omega_1$ , etc.. Only the odd-order IM products will lie in the amplifier passband for the case  $\omega_1 \approx \omega_2$ . Let us assume that  $V(t)$  can be expressed as a finite Fourier series of the form

$$V(t) = \sum_{\substack{n=-7 \\ n \text{ odd}}}^{+7} V_n \exp(jn\omega_d t) \quad (5.84)$$

where  $V_n$  is the complex amplitude of the component at  $n\omega_d$ . For small distortion, only odd-order IM products up to and including the seventh-order are considered; higher-order products will be negligible.





Then, the output voltage  $v_e(t) = \text{Re} \{V(t) \exp(j\omega_0 t)\}$  will consist of : 1) the fundamental components  $\omega_1$  and  $\omega_2$ , for  $n = -1$  and  $n = +1$ , respectively; 2) the third-order IM products  $(2\omega_1 - \omega_2)$  and  $(2\omega_2 - \omega_1)$ , for  $n = -3$  and  $n = +3$ , respectively; 3) the fifth-order IM products  $(3\omega_1 - 2\omega_2)$  and  $(3\omega_2 - 2\omega_1)$ , for  $n = -5$  and  $n = +5$ , respectively; 4) the seventh-order IM products  $(4\omega_1 - 3\omega_2)$  and  $(4\omega_2 - 3\omega_1)$ , for  $n = -7$  and  $n = +7$ , respectively. The assumed basic frequency solution, Eqn. (5.84), is in a form that can be operated on conveniently in Eqn. (5.83).

The factor  $(j\omega_0 + d/dt)^P$  in Eqn. (5.83) can be expanded using the differential operator  $D = d/dt$  to give

$$(j\omega_0 + D)_1^0 = 1 \quad (5.85a)$$

$$(j\omega_0 + D)_1^1 = j\omega_0 + D \quad (5.86b)$$

$$(j\omega_0 + D)_1^2 = (D^2 - \omega_0^2) + j 2\omega_0 D \quad (5.85c)$$

$$(j\omega_0 + D)_1^3 = (D^3 - 3\omega_0^2 D) + j(3\omega_0 D^2 - \omega_0^3) \quad (5.85d)$$

$$(j\omega_0 + D)_1^4 = (D^4 - 6\omega_0^2 D^2 + \omega_0^4) + j(4\omega_0 D^3 - 4\omega_0^3 D) \quad (5.85e)$$

$$(j\omega_0 + D)_1^5 = (D^5 - 10\omega_0^2 D^3 + 5\omega_0^4 D) + j(5\omega_0 D^4 - 10\omega_0^3 D^2 + \omega_0^5) \quad (5.85f)$$

$$(j\omega_0 + D)_1^6 = (D^6 - 15\omega_0^2 D^4 + 15\omega_0^4 D^2 - \omega_0^6) + j(6\omega_0 D^5 - 20\omega_0^3 D^3 + 6\omega_0^5 D) \quad (5.85g)$$



$$\begin{aligned}
 (j\omega_o + D)^7 = & (D^7 - 21\omega_o^2 D^5 + 35\omega_o^4 D^3 - 7\omega_o^6 D) \\
 & + j(7\omega_o^6 D^6 - 35\omega_o^3 D^4 - 21\omega_o^5 D^2 - \omega_o^7) \quad . \quad (5.85h)
 \end{aligned}$$

Similarly, one can derive

$$(-j\omega_o + D)^P = (j\omega_o + D)^{P*} \quad . \quad (5.86)$$

We will only include the constant terms, and the terms in  $D$  and  $D^2$ , in the analysis since the response  $V(t)$  is slowly varying.

Substituting Eqns. (5.84) - (5.86) into Eqn. (5.83) and performing the differentiations results in

$$\begin{aligned}
 I \exp(j\omega_d t) + I \exp(-j\omega_d t) = & \sum_{m=0}^3 (-1)^m (g_m - j\omega_o s_m) \left[ X_{2m}(t) + jY_{2m}(t) \right] \\
 & + \sum_{p=0}^7 \left\{ X_p(t) [b_{p,0,0} + U_p(t)] + X_p^*(t) [b_{p,2,0} + W_p(t)] \right\} \\
 & + j \sum_{p=0}^7 \left\{ Y_p(t) [b_{p,0,0} + U_p(t)] - Y_p^*(t) [b_{p,2,0} + W_p(t)] \right\} \quad (5.87)
 \end{aligned}$$

where

$$X_o(t) = V(t) = \sum V_n \exp(jn\omega_d t) \quad (5.88a)$$

$$X_1(t) = \dot{V}(t) = j \sum n\omega_d V_n \exp(jn\omega_d t) \quad (5.88b)$$

$$X_2(t) = \ddot{V}(t) - \omega_o^2 V(t) = - \sum (n^2 \omega_d^2 + \omega_o^2) V_n \exp(jn\omega_d t) \quad (5.88c)$$



$$X_3(t) = -3\omega_o^2 \dot{V}(t) = -j \sum 3\omega_o^2 n \omega_d V_n \exp(jn\omega_d t) \quad (5.88d)$$

$$X_4(t) = -6\omega_o^2 \ddot{V}(t) + \omega_o^2 V(t) = \sum (6\omega_o^2 n^2 \omega_d^2 + \omega_o^2) V_n \exp(jn\omega_d t) \quad (5.88e)$$

$$X_5(t) = 5\omega_o^4 \dot{V}(t) = j \sum 5\omega_o^4 n \omega_d V_n \exp(jn\omega_d t) \quad (5.88f)$$

$$X_6(t) = 15\omega_o^4 \ddot{V}(t) - \omega_o^6 V(t) = - \sum (15\omega_o^4 n^2 \omega_d^2 + \omega_o^6) V_n \exp(jn\omega_d t) \quad (5.88g)$$

$$X_7(t) = -7\omega_o^6 \dot{V}(t) = -j \sum 7\omega_o^6 n \omega_d V_n \exp(jn\omega_d t) \quad (5.88h)$$

$$Y_o(t) = 0 \quad (5.89a)$$

$$Y_1(t) = \omega_o V(t) = \sum \omega_o V_n \exp(jn\omega_d t) \quad (5.89b)$$

$$Y_2(t) = 2\omega_o \dot{V}(t) = j \sum 2\omega_o n \omega_d V_n \exp(jn\omega_d t) \quad (5.89c)$$

$$Y_3(t) = 3\omega_o \ddot{V}(t) - \omega_o^3 V(t) = - \sum (3\omega_o^2 n^2 \omega_d^2 + \omega_o^3) V_n \exp(jn\omega_d t) \quad (5.89d)$$

$$Y_4(t) = -4\omega_o^3 \dot{V}(t) = -j \sum 4\omega_o^3 n \omega_d V_n \exp(jn\omega_d t) \quad (5.89e)$$

$$Y_5(t) = -10\omega_o^3 \ddot{V}(t) + \omega_o^5 V(t) = \sum (10\omega_o^3 n^2 \omega_d^2 + \omega_o^5) V_n \exp(jn\omega_d t) \quad (5.89f)$$

$$Y_6(t) = 6\omega_o^5 \dot{V}(t) = j \sum 6\omega_o^5 n \omega_d V_n \exp(jn\omega_d t) \quad (5.89g)$$

$$Y_7(t) = 21\omega_o^5 \ddot{V}(t) - \omega_o^7 V(t) = - \sum (21\omega_o^5 n^2 \omega_d^2 + \omega_o^7) V_n \exp(jn\omega_d t) \quad (5.89h)$$



$$U_p(t) = b_{p,0,2} V(t) V^*(t) + b_{p,0,4} V^2(t) V^{*2}(t) + b_{p,0,6} V^3(t) V^{*3}(t) \quad (5.90)$$

$$W_p(t) = b_{p,2,2} V^2(t) + b_{p,2,4} V^3(t) V^*(t) + b_{p,2,6} V^4(t) V^{*2}(t) \quad (5.91)$$

and where all summations in Eqns. (5.88) and (5.89) are from  $n=-7$  to  $n=+7$  with  $n$  odd. Equation (5.87) can then be rearranged into the form

$$\begin{aligned} & \sum_{m=0}^3 (-1)^m (g_m - j\omega_o s_m) [X_{2m}(t) + jY_{2m}(t)] + \sum_{p=0}^7 [X_p(t) b_{p,0,0} + jY_p(t) b_{p,0,0}] \\ &= I \exp(j\omega_d t) + I \exp(-j\omega_d t) - \sum_{p=0}^7 [X_p(t) U_p(t) + X_p^*(t) W_p(t)] \\ & \quad - j \sum_{p=0}^7 [Y_p(t) U_p(t) - Y_p^*(t) W_p(t)] \end{aligned} \quad (5.92)$$

where  $b_{p,2,0} = 0$  from Eqn. (5.52).

A numerical iteration procedure is used to calculate the complex coefficients  $V_n$  in Eqn. (5.84) satisfying Eqn. (5.92). Inspection of Eqn. (5.92) reveals that the left hand side contains only linear terms, while the summation terms on the right hand side include all the nonlinear terms which arise from Eqns. (5.90) and (5.91). In the iteration procedure the linearized equation

$$\begin{aligned} & \sum_{m=0}^3 (-1)^m (g_m - j\omega_o s_m) [X_{2m}(t) + jY_{2m}(t)] + \sum_{p=0}^7 [X_p(t) b_{p,0,0} + jY_p(t) b_{p,0,0}] \\ &= I \exp(j\omega_d t) + I \exp(-j\omega_d t) \end{aligned} \quad (5.93)$$





is first solved to obtain an initial estimate of the solution.

Substitution of Eqns. (5.84) and (5.88)-(5.91) into Eqn. (5.93) gives

$$\sum_{\substack{n=-7 \\ n \text{ odd}}}^{+7} \beta_n V_n \exp(jn\omega_d t) = I \exp(j\omega_d t) + I \exp(-j\omega_d t) \quad (5.94)$$

where

$$\begin{aligned} \beta_n = & g_0 + g_1 (\omega_o^2 + 2\omega_o n\omega_d + n^2 \omega_d^2) + g_2 (\omega_o^4 + 4\omega_o^3 n\omega_d + 6\omega_o^2 n^2 \omega_d^2) \\ & + g_3 (\omega_o^6 + 6\omega_o^5 n\omega_d + 15\omega_o^4 n^2 \omega_d^2) \\ & + b_{p,0,0} (1 - \omega_o^6 - 6\omega_o^5 n\omega_d - 15\omega_o^4 n^2 \omega_d^2 + 4\omega_o^3 n\omega_d^3 + 6\omega_o^2 n^2 \omega_d^2 - 2\omega_o n\omega_d^3 - n^2 \omega_d^2) \\ & - j \left[ s_o \omega_o + s_1 (\omega_o^3 + 2\omega_o^2 n\omega_d + \omega_o n^2 \omega_d^2) + s_2 (\omega_o^5 + 4\omega_o^4 n\omega_d + 6\omega_o^3 n^2 \omega_d^2) \right. \\ & \left. + s_3 (\omega_o^7 + 6\omega_o^6 n\omega_d + 15\omega_o^5 n^2 \omega_d^2) \right. \\ & \left. + b_{p,0,0} (\omega_o^7 + 7\omega_o^6 n\omega_d + 21\omega_o^5 n^2 \omega_d^2 - \omega_o^5 - 5\omega_o^4 n\omega_d - 10\omega_o^3 n^2 \omega_d^2 \right. \\ & \left. + \omega_o^3 + 3\omega_o^2 n\omega_d - \omega_o - n\omega_d) \right] \end{aligned} \quad (5.95)$$

Since Eqn. (5.94) must be true for any time  $t$ , we can use the principle of harmonic balance: an  $n^{\text{th}}$ -order approximate solution is obtained if  $n$  harmonics of the basic frequency are adjusted to satisfy all terms at their respective frequencies.



The initial solution is

$$V_1 = I/\beta_1 \quad (5.96a)$$

$$V_{-1} = I/\beta_{-1} \quad (5.96b)$$

$$V_n = 0 ; n = -7, -5, -3, +3, +5, +7 \quad . \quad (5.96c)$$

These initial values are substituted into the right hand side of the nonlinear Eqn. (5.92) to give

$$\sum_{\substack{n=-7 \\ n \text{ odd}}}^{+7} \beta_n V_n \exp(jn\omega_d t) = I \exp(j\omega_d t) + I \exp(-j\omega_d t) - \sum_{\substack{n=-7 \\ n \text{ odd}}}^{+7} \gamma_n \exp(jn\omega_d t) \quad (5.97)$$

where the complex coefficients  $\gamma_n$  are functions of the current estimate  $V_n$  obtained by the indicated multiplications of the exponential series. Equation (5.97) can then be solved to obtain the next estimate to the solution  $V_n$ , and so on:

$$V_1 = (I - \gamma_1)/\beta_1 \quad (5.98a)$$

$$V_{-1} = (I - \gamma_{-1})/\beta_{-1} \quad (5.98b)$$

$$V_n = -\gamma_n/\beta_n ; n = -7, -5, -3, +3, +5, +7 \quad . \quad (5.98c)$$

The errors in the initial estimate of the solution are decreased or



relaxed as the iteration procedure continues. The solution will converge for small distortion for which the nonlinear coefficients  $\gamma_n$  are much smaller than the linear coefficients  $\beta_n$ . Care must be taken to ensure that the frequencies  $\omega_o \pm 7\omega_d$  and the steady-state RF voltage amplitude  $|V(t)|$  lie in the  $KL^{th}$  solution grid  $(\bar{\omega}_K, \bar{\omega}_{K+1}) \times (A_L, A_{L+1})$  where the admittance operators apply.

The IM distortion products  $IM_3$  and  $IM_5$ , are calculated using Eqns. (2.2) and (2.3), respectively;  $IM_7$  is calculated similarly. The output voltage for the model using the measured  $Y_c(\omega)$ , Fig. 5.1(a), is given by

$$v_r(t) = v_2(t) - v_i(t) \quad . \quad (5.99)$$

If the amplifier has sufficient gain, in the order of 20 dB, then  $v_r(t) \gg v_i(t)$ , and

$$v_r(t) \approx v_2(t) \quad . \quad (5.100)$$

Since the definition of IM distortion in Eqns. (2.2) and (2.3) is the ratio of distortion power to fundamental power at the output port, and since the distortion products and fundamental frequencies  $\omega_1 \approx \omega_2$  will undergo approximately the same attenuation through network K, then  $IM_3$ ,  $IM_5$  and  $IM_7$  will be the same ratio at the active region of the diode, Fig. 5.1(b), as at the output port. The  $n^{th}$ - order IM distortion can be written as

$$IM_n \text{ (dB)} \approx 20 \log |V_n/V_1| \quad (5.101)$$



where  $n > 0$  gives the upper IM products and  $n < 0$  gives the lower IM products. To determine actual distortion power at the output, the losses of network K must be taken into consideration.

Intermodulation distortion calculated using the  $G_c L_c C_c$  tuned-circuit model, Fig. 4.2, can be treated more directly. In this case, the output voltage is expressed as

$$v_r(t) = v_e(t) - v_i(t) \quad (5.102)$$

where any circuit losses are implicitly present in the selection of  $G_c$ ; i.e., the model's parameters are chosen to match the predicted gain at the output port with the gain measured at the same port. The amplitude of the fundamental component of the voltage response  $v_r(t)$  is  $|V_{-1} - V_i|$  for  $\omega_1$  and  $|V_1 - V_i|$  for  $\omega_2$ , where  $V_i$  is given by  $\sqrt{2 P_{in} / G_c}$ . The distortion products in  $v_r(t)$  are exactly those in  $v_e(t)$ . Hence, the  $n^{th}$ - order IM distortion is

$$IM_n(\text{dB}) = 20 \log |V_n / (V_1 - V_i)| \quad (5.103)$$

where  $n > 0$  gives the upper IM products and  $n < 0$  gives the lower IM products. For amplifiers with sufficient gain, the approximation in Eqn. (5.101) can be used. The power at the fundamental frequency is

$$P_{\omega_1} = 10 \log \{ |V_1 - V_i|^2 G_c / 2 \} \quad (5.104)$$





The power at the distortion products can be calculated by means of Eqns. (5.103) and (5.104).

### 5.3.3 Computed IMPATT-Amplifier Distortion

Large numbers are generated in Eqn. (5.97) at microwave frequencies because of the terms  $\omega_o^7$ ,  $\omega_o^2 V(t)$  etc.. To avoid floating-point overflow problems in solving Eqn. (5.97), the equation was first normalized:  $\omega_o$  was replaced by  $\omega_o / (2\pi \times 10^{10}) = f_o \times 10^{-10}$ ;  $V_n$  was replaced by  $V_n / 10$ ;  $I$  was replaced by  $I / 10$ . The passive- and active circuit CW admittance data was scaled to these normalized variables. The cubic spline coefficients for the passive circuit admittance operator, and bicubic spline coefficients for the active circuit admittance operator were determined by curve fitting this scaled data. The iteration procedure for solving Eqn. (5.97) was stopped when successive estimates of  $V_n$  for  $n = \pm 1, \pm 3, \pm 5, \pm 7$  differed by less than about  $|V_1| \times 10^{-6}$ .

Intermodulation distortion was computed for both the measured circuit admittance  $Y_c(\omega)$ , shown in Fig. 5.2, and for the  $G_c L_c C_c$  tuned-circuit model.

The measured circuit admittance is estimated to involve an error of 10-20%. This error estimate is the same as for the electronic admittance, because the same procedure was followed in both measurements to determine the two-port networks  $K_1$  and  $K_2$  defined in Fig. 3.6. In the circulator-coupled amplifier configuration, it is assumed that a matched load is presented at reference plane 2-2'; Eqn. (5.61) can then be used to calculate  $Y_c(\omega)$ . This assumption introduces little error since the VSWR of the waveguide circulator is less than 1.16 over the amplifier bandwidth. The



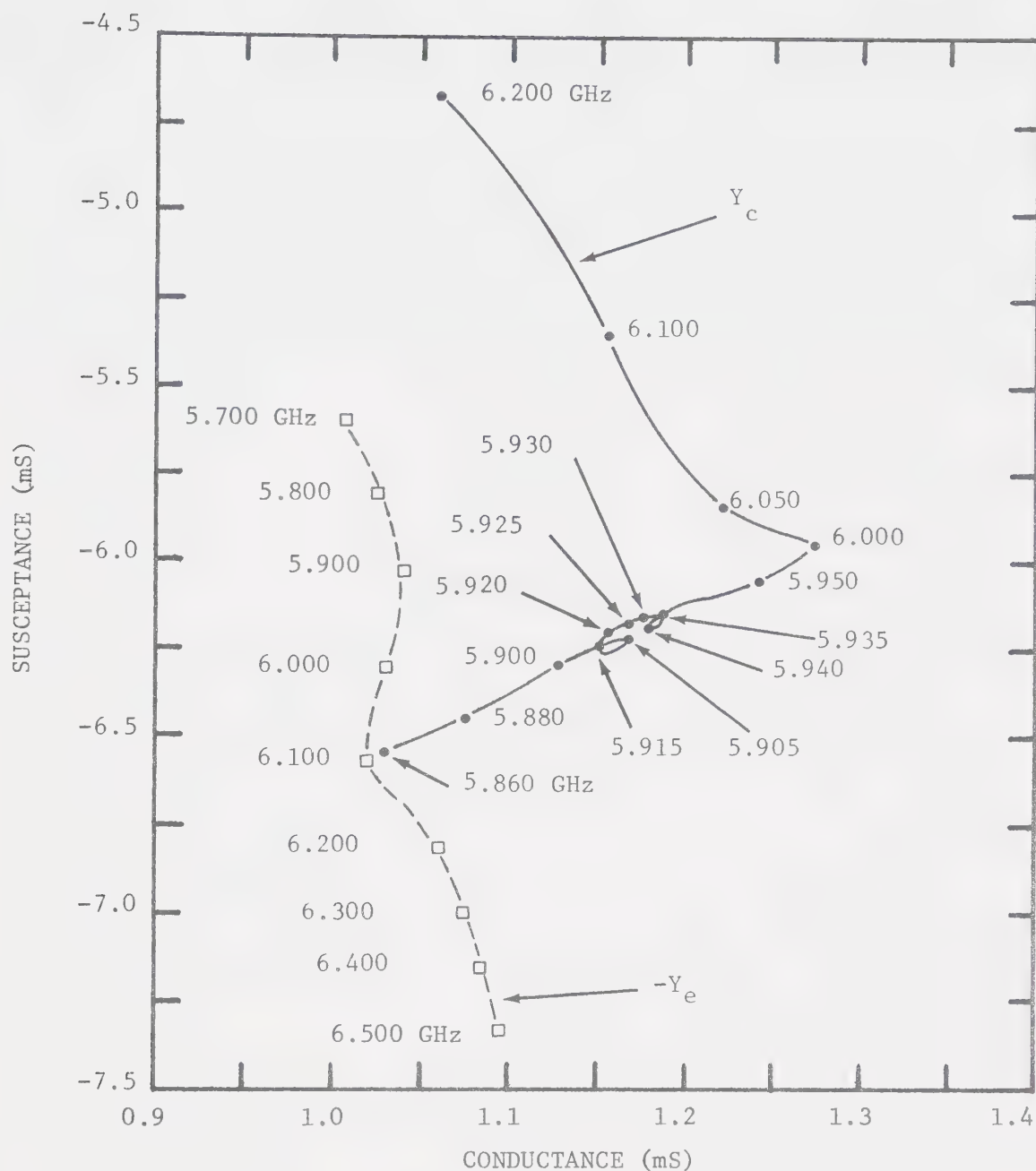


Figure 5.2 Measured circuit admittance presented to the active region of the IMPATT diode in the experimental IMPATT amplifier. The measured small-signal electronic admittance (negative) of the IMPATT diode ( $I_{dc} = 25$  mA) is also shown.



measured circuit admittance is the admittance seen by the active region of the IMPATT diode. Amplifier gain, calculated using Eqn. (2.6), is the gain predicted at the terminals of the IMPATT-diode electronic admittance. This gain can be transformed to the output port, where the gain was measured, through a knowledge of the transmission parameters of lossy two-port network K in Fig. 5.1(a). The measured and predicted small-signal gain response at the output port are compared in Fig. 5.3. It can be seen that: 1) the predicted gain peaks at 19.8 dB whereas the measured gain peaks at 17.3 dB (14% difference); 2) the predicted centre frequency is 5.930 GHz, while the actual centre frequency occurs at 5.905 GHz (0.4% difference); and 3) the predicted 3-dB bandwidth is 24 MHz as compared to the actual bandwidth of 64 MHz (63% difference). These discrepancies appear, at first, to warrant a higher error estimate for the measurement of  $Y_c(\omega)$ . However, a 4% increase in  $G_c(\omega)$ , to decrease the maximum gain, and a 4% decrease in  $B_c(\omega)$ , to lower the centre frequency, has a much larger effect on the predicted gain, as illustrated in Fig. 5.3: the difference in gain is reduced to 3%; the difference in centre frequency is reduced to 0.2%; and the difference in 3-dB bandwidth is reduced to 3%. The 10-20% error estimate for  $Y_c(\omega)$  is therefore reasonable.

Figure 5.3 also shows double the insertion loss of network K (calculation of gain at the output involves incident- and reflected signal transmission through network K). The power gain at the output port is about 3.8-dB less than the power gain at the active region of the diode. The 1.9-dB insertion loss of network K is



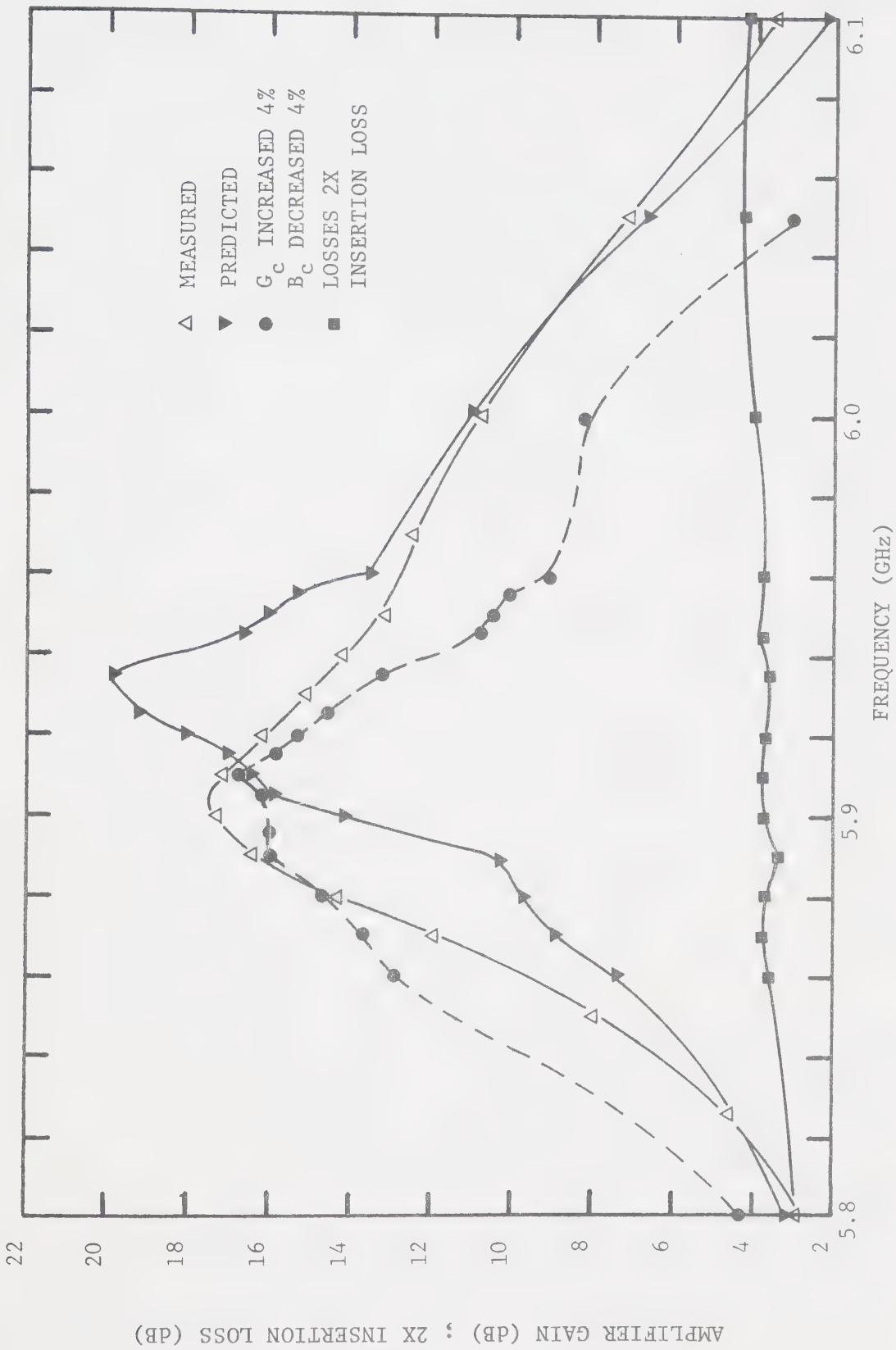


Figure 5.3 Comparison of measured IMPATT-amplifier small-signal gain with the gain predicted using the measured circuit- and electronic admittance ( $I_{dc} = 25$  mA). The effect of a 4% increase and a 4% decrease in the measured circuit conductance and susceptance, respectively, on the predicted gain is shown. The calculated insertion loss X2 of the coupling network K is also plotted.





attributable collectively to the waveguide-to-coaxial transition (0.3 dB), several coaxial adapters (0.4 dB), the bias tee (0.2 dB), cavity losses, small impedance-transformer mismatches and package parasitics (1 dB).

The tuned amplifier is an undercoupled double-tuned circuit because the measured gain curve shows only a single peak which is lower than the maximum gain which could be achieved experimentally through double-tuning. The two resonances near the centre frequency are observed in the measured  $Y_c(\omega)$  locus. Nevertheless, these resonance loops can be approximated by a cubic spline interpolation of  $G_c(\omega)$  and  $B_c(\omega)$ , which are single-valued continuous functions of  $\omega$ .

The computed two-tone ( $f_2 = f_1 + 1$  MHz) IM distortion for the model using the measured circuit admittance is shown in Figs. 5.4 and 5.5. The predicted third-order IM distortion is about 10 dB higher than the measured IM distortion because the model's gain is higher than the actual gain. The calculated IM distortion is maximum at 5.920 GHz in comparison with 5.905 GHz for the measured distortion. Again, this discrepancy is due to the small error in the measurement of  $Y_c(\omega)$  and  $Y_e(\omega, V_{RF})$ .

The gain and phase response of the  $G_c L_c C_c$  tuned-circuit model are plotted in Figs. 5.6 and 5.7, respectively. The values of  $G_c$ ,  $L_c$  and  $C_c$  were obtained by fitting the gain expressed in Eqn. (2.6), where  $Y_c(\omega)$  is given by Eqn. (4.15) and  $Y_e(\omega)$  is the measured small-signal electronic admittance, to the measured small-signal gain curve. The circuit parameter values are:



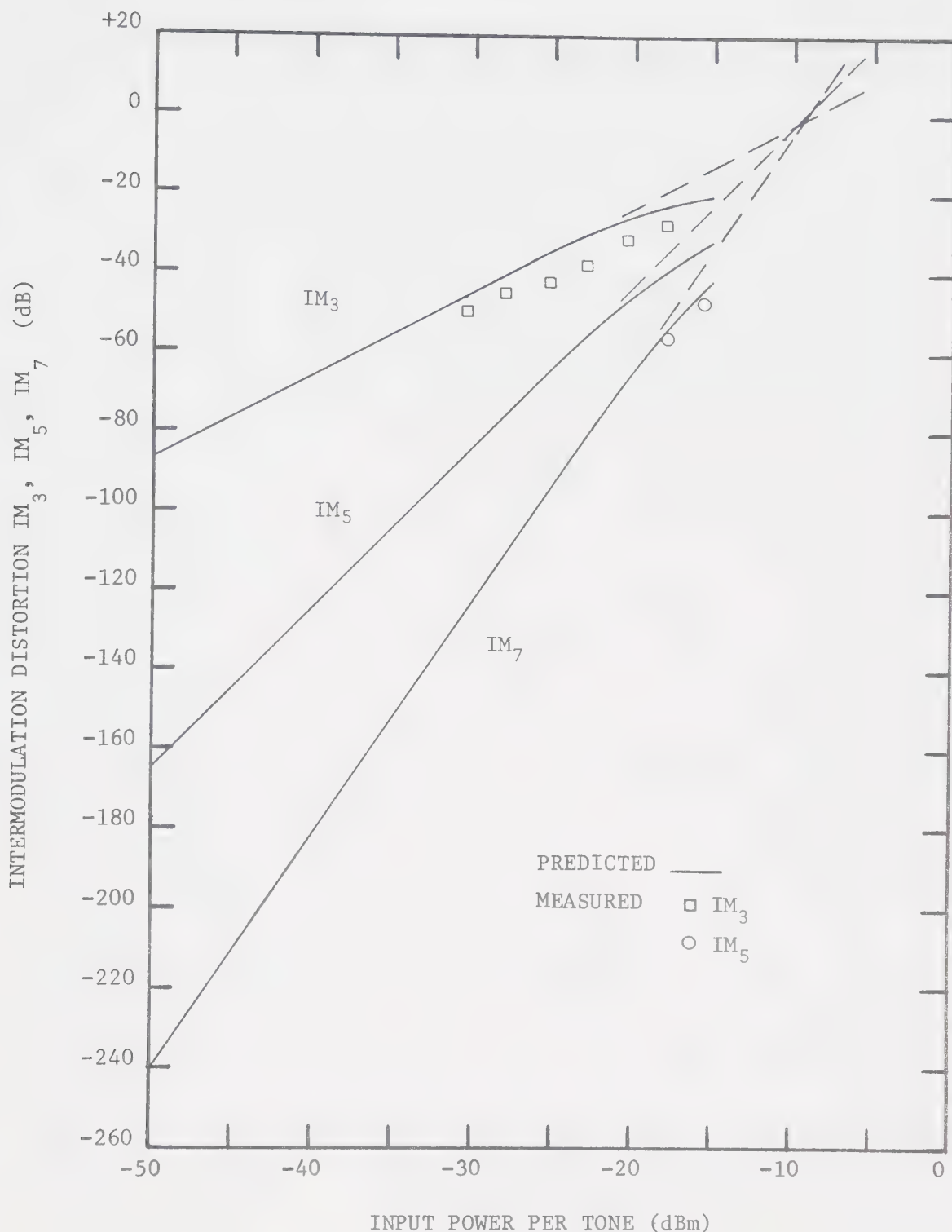


Figure 5.4 Comparison of measured and predicted IM distortion, using quasistationary distortion analysis for the experimental IMPATT amplifier ( $I_{dc} = 25$  mA) with a two-tone input ( $f_1 = 5.905$  GHz,  $f_2 = 5.906$  GHz) at the centre frequency. The measured circuit admittance is used in the analysis.



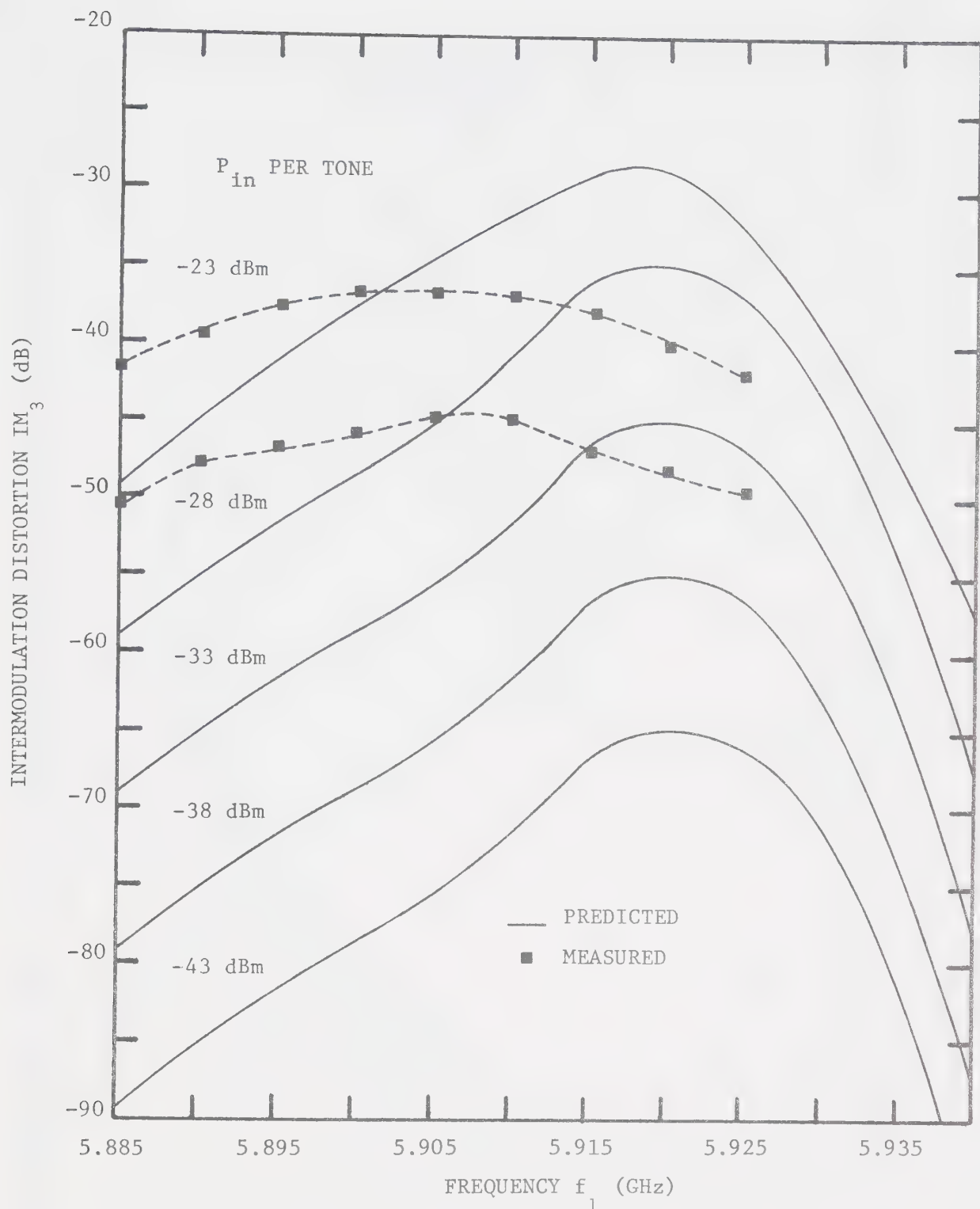


Figure 5.5 Comparison of measured and predicted frequency-dependence of third-order IM distortion at  $2f_1 - f_2$ , using quasistationary distortion analysis, for the experimental IMPATT amplifier ( $I_{dc} = 25$  mA) with a two-tone input ( $f_2 = f_1 + 1$  MHz). The measured circuit admittance is used in the analysis.



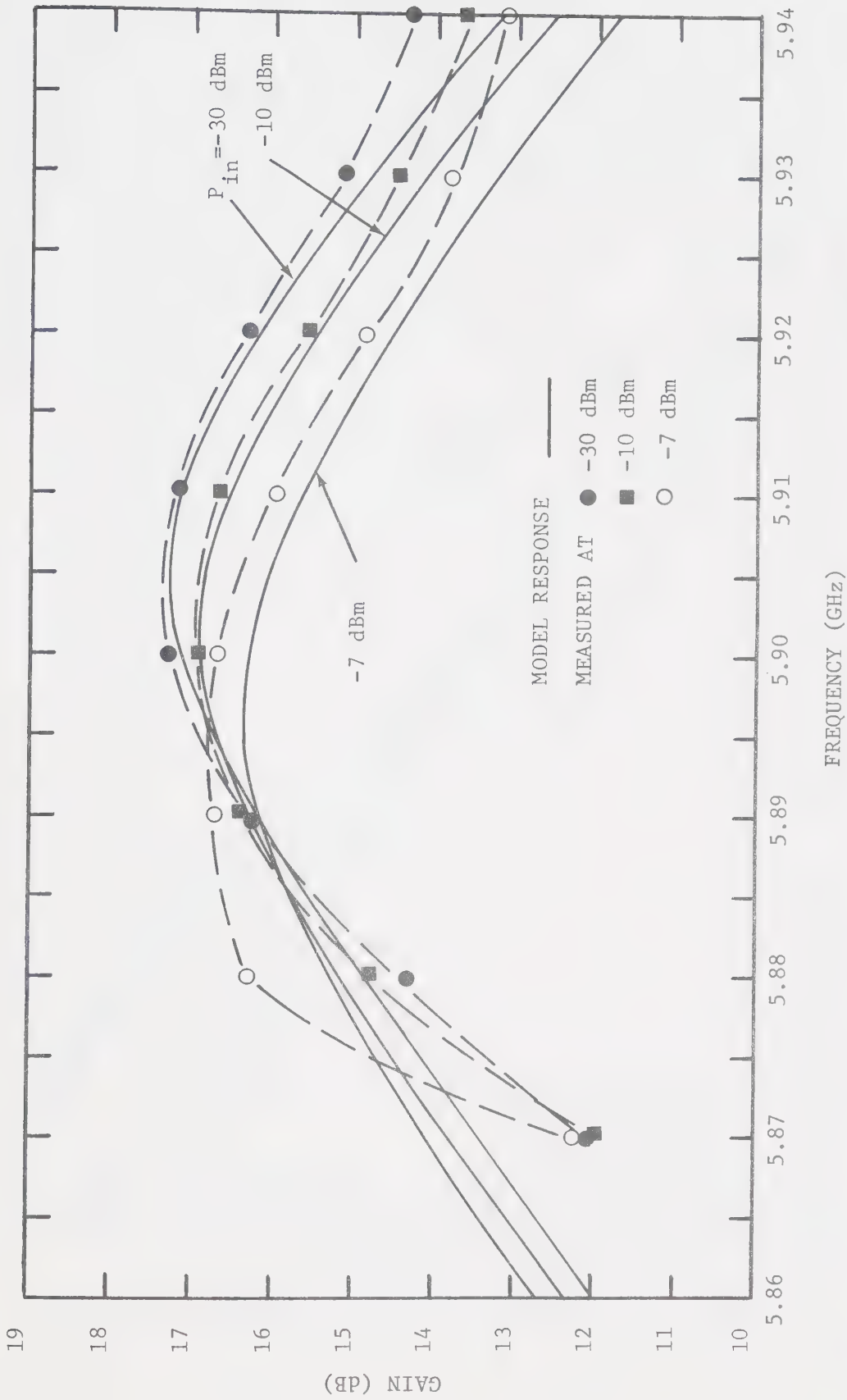


Figure 5.6 Comparison of measured IMPATT-amplifier gain with the gain predicted using the IMPATT-diode amplifier tuned-circuit model for quasistationary distortion analysis (at 25-mA dc bias current).





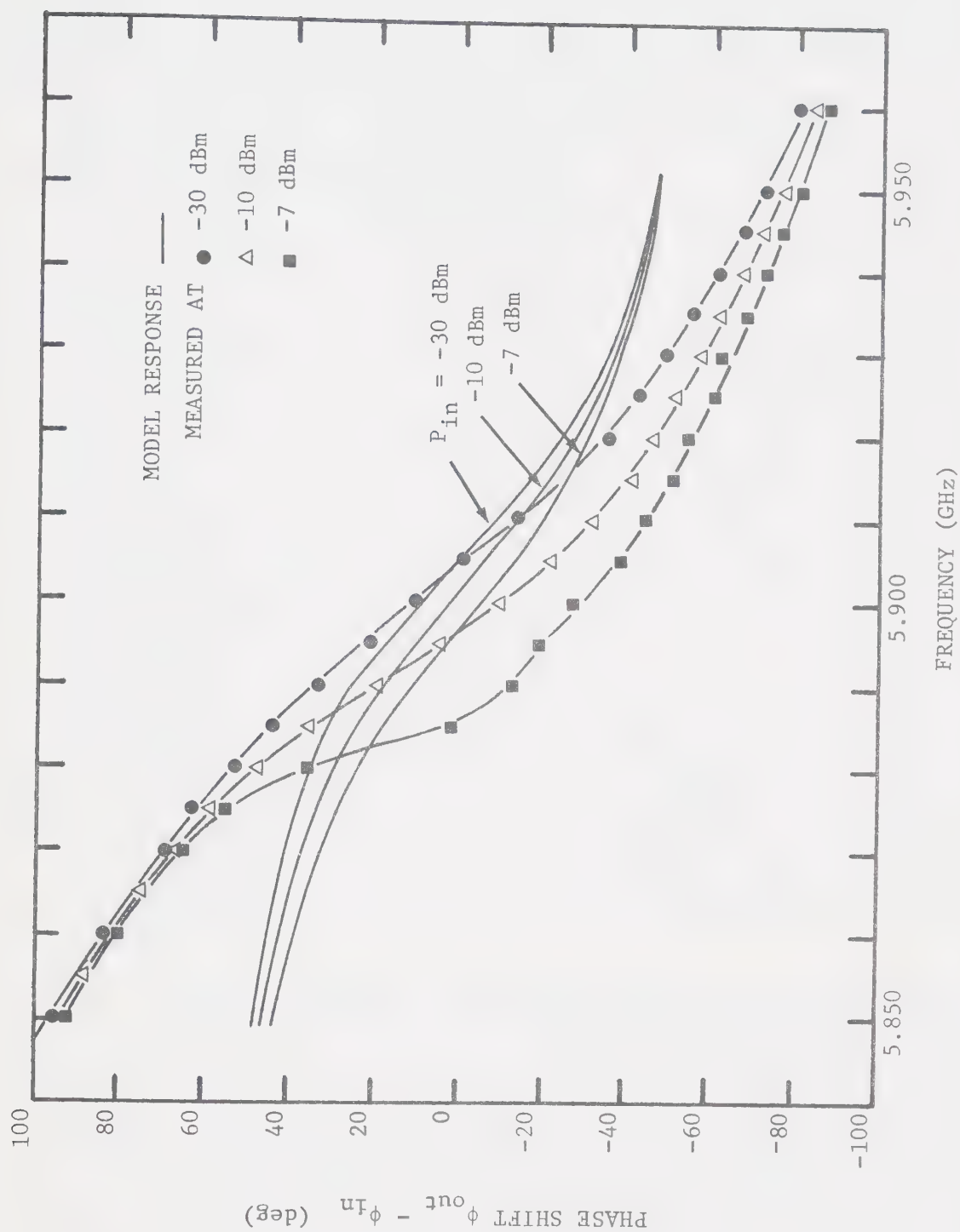


Figure 5.7 Comparison of measured IMPATT-amplifier phase shift with the phase shift predicted using the IMPATT-diode amplifier tuned-circuit model for quasistationary distortion analysis (at 25-mAdc bias circuit).



$G_c = 1.371 \text{ mS}$ ,  $L_c = 0.8876 \text{ nH}$ , and  $C_c = 0.6557 \text{ pF}$ . The measured and predicted gain response agree quite closely for input levels up to  $-10 \text{ dBm}$ . The phase responses do not agree as closely, since the undercoupled double-tuned circuit is approximated by a single-tuned circuit; however, the phase difference is less than  $20^\circ$  over the amplifier bandwidth.

The two-tone IM distortion computed using the  $G_c L_c C_c$  model is plotted in Figs. 5.8 to 5.11. Predicted gain compression is shown in Fig. 5.12. Intermodulation distortion calculated by means of Eqn. (5.103) was found to be less than 2 dB higher than that calculated using the approximate relationship in Eqn. (5.101). Upper IM distortion differed from the plotted lower IM distortion by less than 2 dB. The results in Figs. 5.8 to 5.12 show the same behaviour as a function of frequency and input level as the results of the Volterra series distortion analysis. Consequently, the discussion in Sec. 4.3.6 also applies here. In fact, the same third-order intercept point ( $11.5 \text{ dBm}$ ) is obtained by the two methods. A more detailed comparison of the results of these two different methods with experimental measurements appears in Chapter 6.

This quasistationary nonlinear distortion study is applicable up to input levels of  $-13 \text{ dBm}$  per tone, at which the model's gain response begins to deviate appreciably from the measured gain response. At  $-13\text{-dBm}$  input level, the computing time also becomes excessive due to the slower convergence of the iteration procedure. At an input level of  $-43 \text{ dBm}$  per tone, only 3 iterations were needed; while at  $-13$



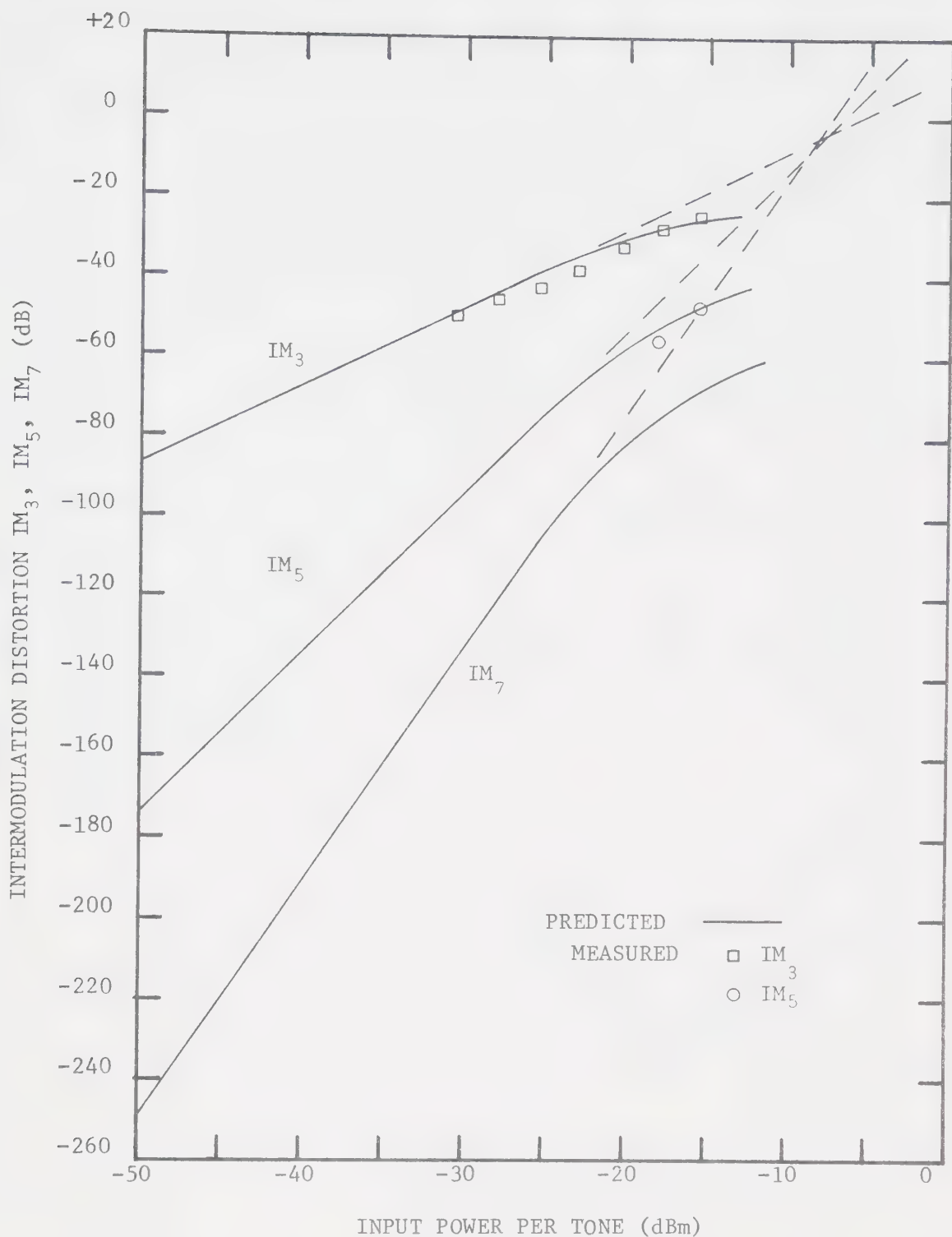


Figure 5.8 Comparison of measured and predicted IM distortion, using quasistationary distortion analysis of the amplifier tuned-circuit model, for the experimental IMPATT amplifier ( $I_{dc}=25$  mA) with a two-tone input ( $f_1=5.905$  GHz,  $f_2=5.906$  GHz) at the centre frequency.



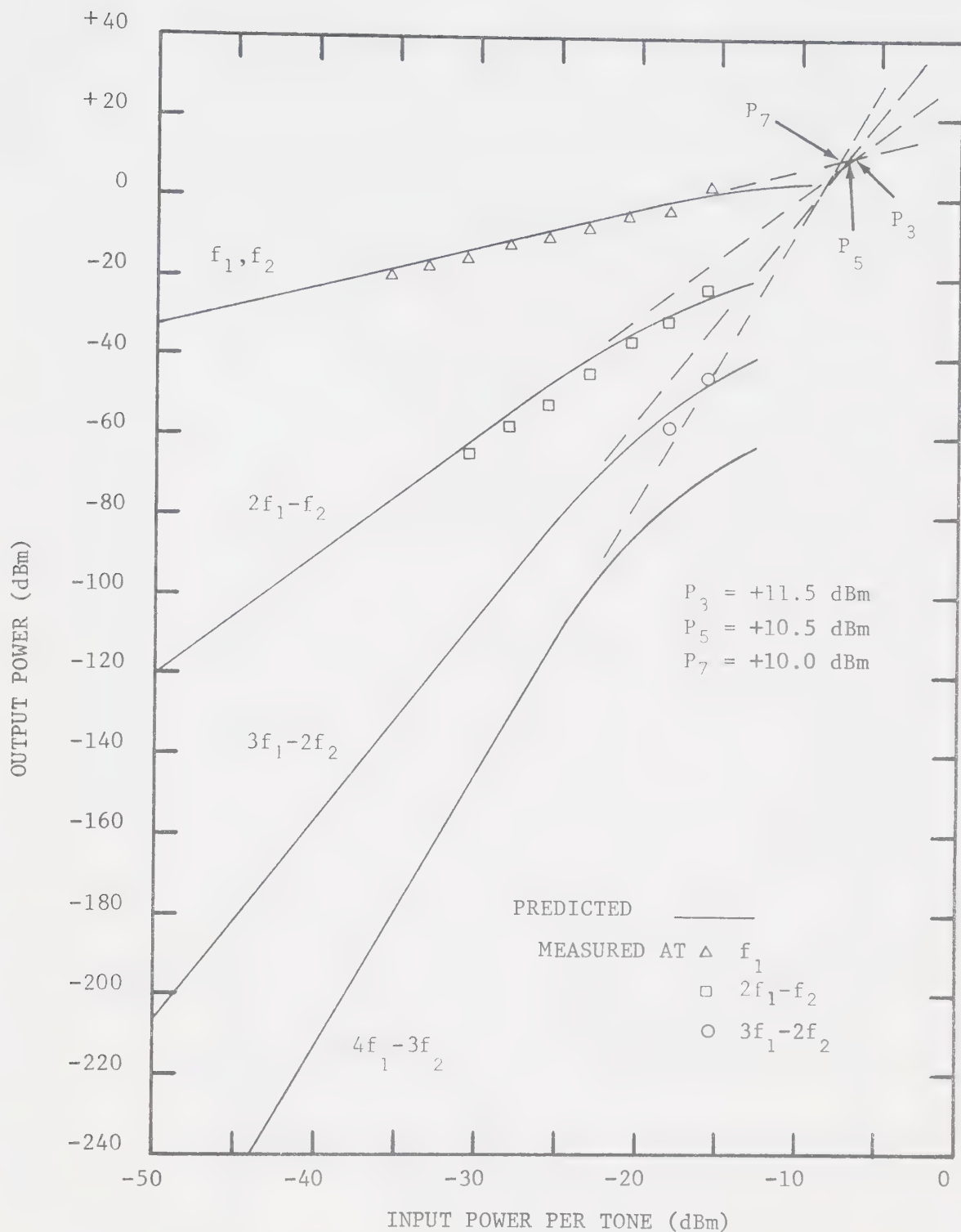


Figure 5.9 Comparison of measured and predicted fundamental output power and IM distortion products, using quasistationary distortion analysis of the amplifier tuned-circuit model, for the experimental IMPATT amplifier ( $I_{dc}=25$  mA) with a two-tone input ( $f_1=5.905$  GHz,  $f_2=5.906$  GHz) at the centre frequency.





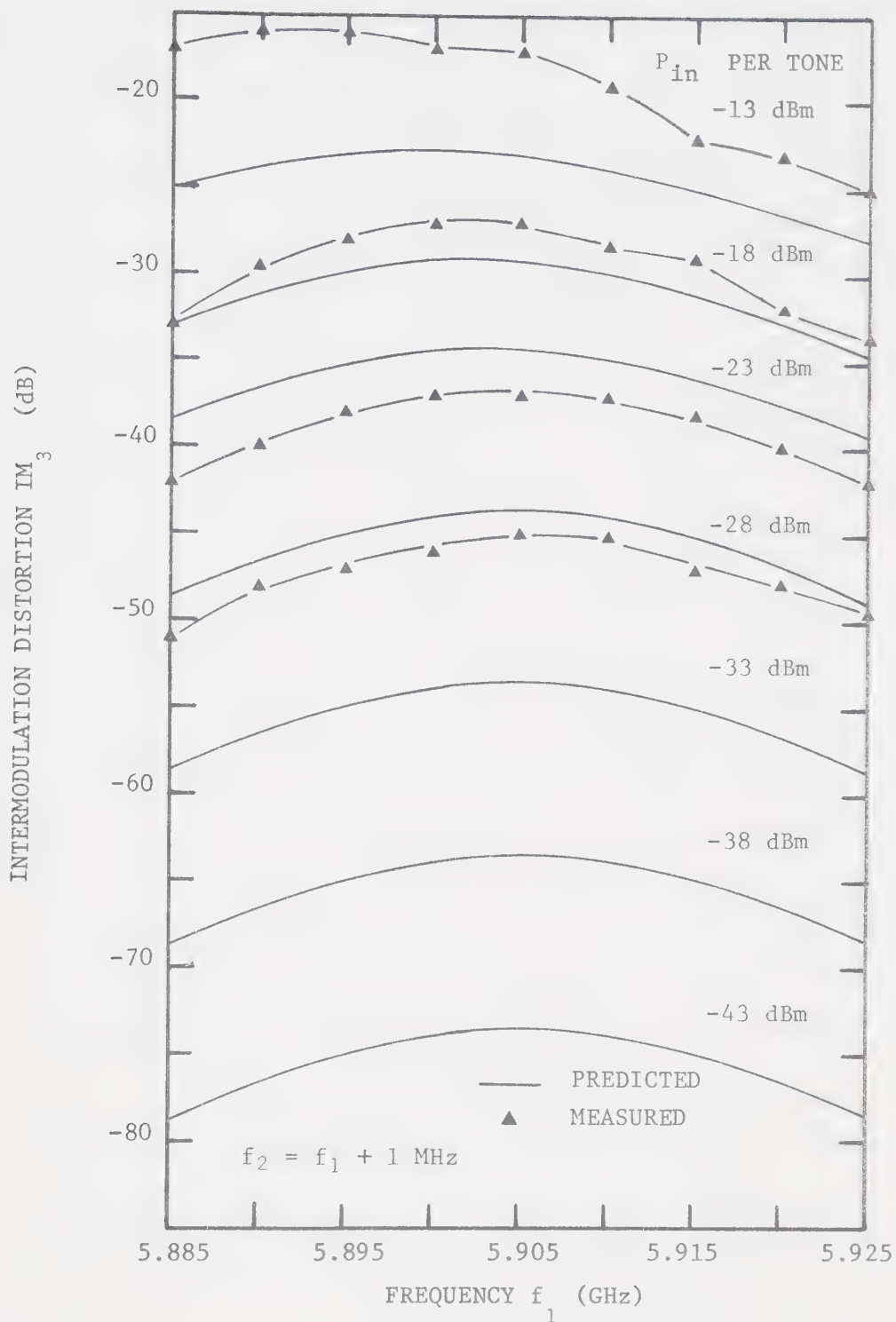


Figure 5.10 Comparison of measured and predicted frequency-dependence of third-order IM distortion at  $2f_1 - f_2$ , using quasistationary distortion analysis of the amplifier tuned-circuit model, for the experimental IMPATT amplifier ( $I_{dc} = 25 \text{ mA}$ ) with a two-tone input ( $f_2 = f_1 + 1 \text{ MHz}$ ).



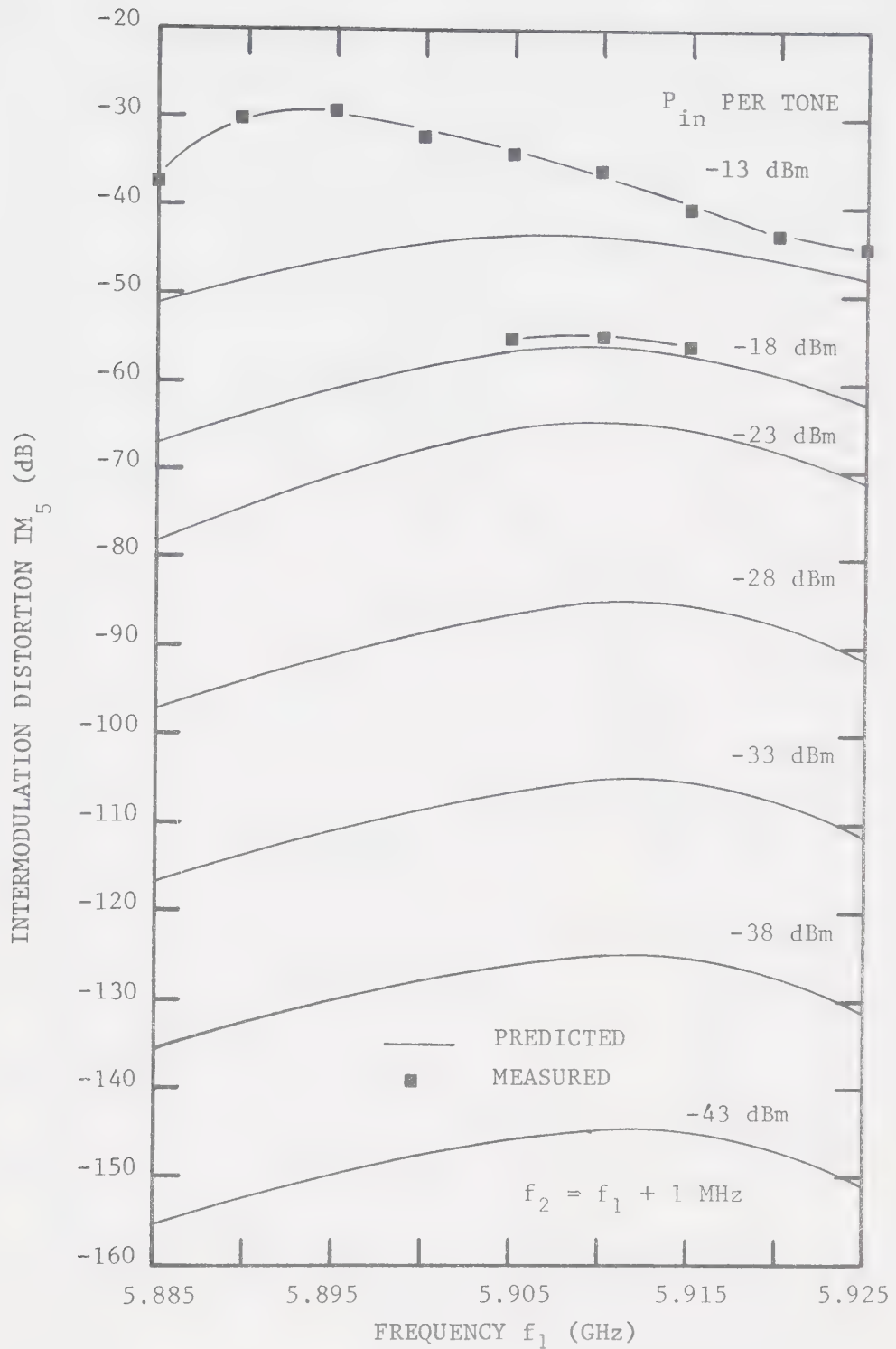


Figure 5.11 Comparison of measured and predicted frequency-dependence of fifth-order IM distortion at  $3f_1 - 2f_2$ , using quasistationary distortion analysis of the amplifier tuned-circuit model, for the experimental IMPATT amplifier ( $I_{dc} = 25 \text{ mA}$ ) with a two-tone input ( $f_2 = f_1 + 1 \text{ MHz}$ ).



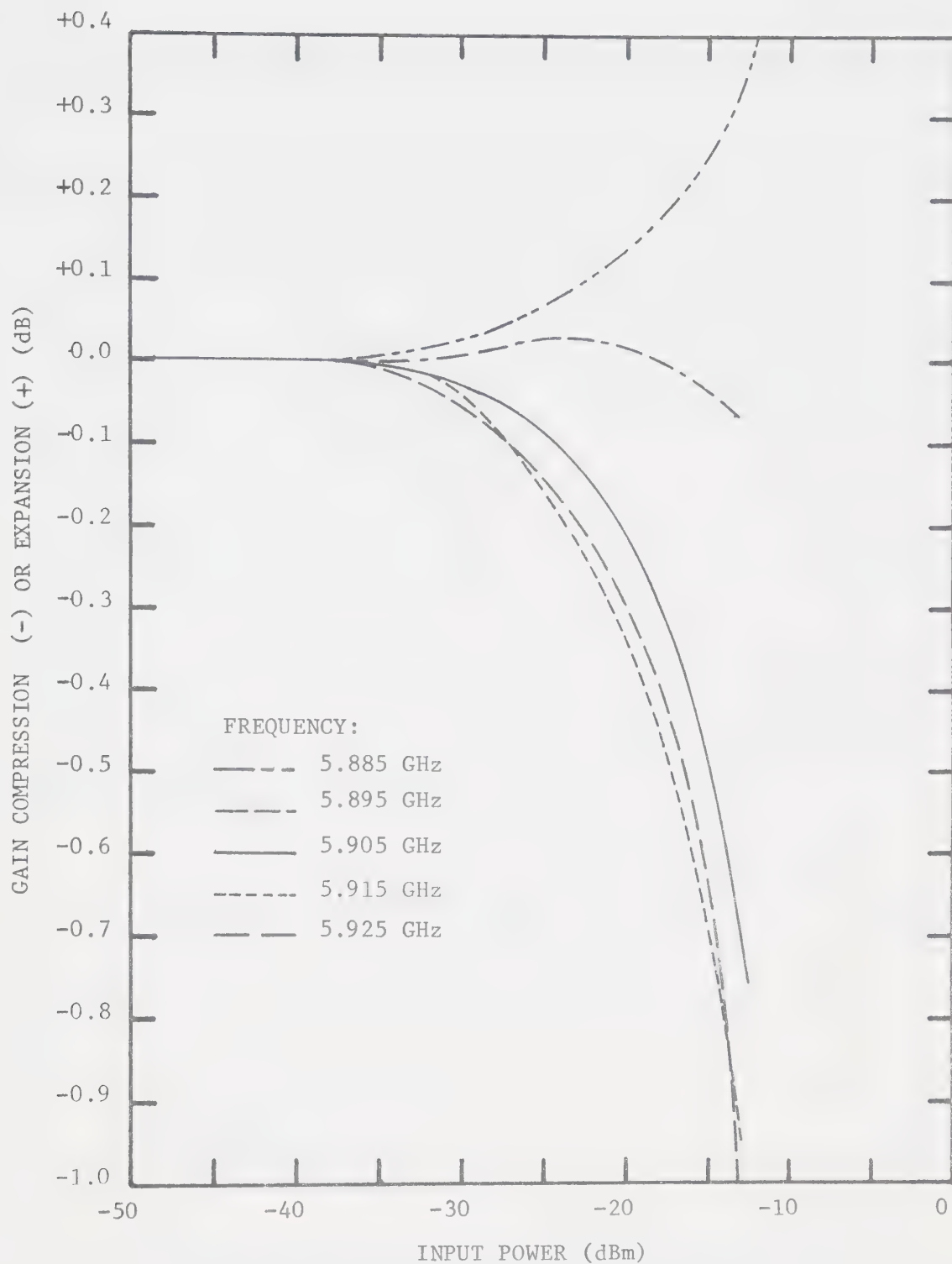


Figure 5.12 Predicted gain compression/expansion, using quasistationary distortion analysis of the amplifier tuned-circuit model, for the experimental IMPATT amplifier at 25-mA dc bias current.



dBm per tone, 40 iterations were usually required to reach the solution of Eqn. (5.97).

#### 5.4 Reduction of IMPATT-Amplifier Distortion by Feedforward Correction

Consider the equivalent circuit of the feedforward-corrected amplifier shown in Fig. 4.11. A simple analysis of the reduction of IMPATT-amplifier distortion in the feedforward system can be undertaken by assuming all the circuitry external to the nonlinear IMPATT amplifier to be linear. Let the input signal be

$$x(t) = V_1 \cos \omega_1 t + V_2 \cos \omega_2 t \quad (5.105)$$

where  $\omega_1$  and  $\omega_2$  are incommensurable frequencies in the passband of the IMPATT amplifier, and  $\omega_1 \approx \omega_2$ . Let the IMPATT-amplifier produce distortion  $\sqrt{1-k_1^2} v_d(t)$ ; its output is then

$$y_1(t) = |H| x_1(t-t_{d_1}) + \sqrt{1-k_1^2} v_d(t) \quad (5.106)$$

where

$$x_1(t) = \sqrt{1-k_1^2} x(t), \quad (5.107)$$

$|H|$  is the IMPATT-amplifier gain, and  $t_{d_1}$  is its group delay at frequency  $\omega_1$ . Assume that the error-detection loop is balanced so that the error signal  $e(t)$  consists only of the distortion produced by the IMPATT amplifier; i.e.,





$$e(t) = -\mu_2 k_2 \sqrt{1-k_1^2} v_d(t) \quad . \quad (5.108)$$

If the error amplifier is operating in its small-signal linear region it contributes negligible distortion. Thus, the feedforward amplifier output signal is

$$y(t) = \sqrt{1-k_2^2} \sqrt{1-k_3^2} y_1(t-\Delta t_2) + k_3 |A_2| e(t-t_{d_2}) \quad (5.109)$$

where  $|A_2|$  is the error amplifier gain, and  $t_{d_2}$  is the group delay of the error amplifier at frequency  $\omega_1$ . Substituting Eqns. (5.106)-(5.108) into (5.109) yields

$$y(t) = \sqrt{1-k_1^2} \sqrt{1-k_2^2} \sqrt{1-k_3^2} [ |H| x(t-\Delta t_2 - t_{d_1}) + v_d(t-\Delta t_2) ] \\ - \mu_2 k_2 k_3 \sqrt{1-k_1^2} |A_2| v_d(t-t_{d_2}) \quad . \quad (5.110)$$

Precise balance of the error-correction loop exists when

$$|A_2| = \frac{\sqrt{1-k_2^2} \sqrt{1-k_3^2}}{\mu_2 k_2 k_3} \quad . \quad (5.111)$$

and

$$t_{d_2} = \Delta t_2 \quad . \quad (5.112)$$

Consider a small amplitude imbalance,



$$\alpha_2 = \frac{|A_2|}{[1-k_2^2]^{\frac{1}{2}}[1-k_3^2]^{\frac{1}{2}}[\mu_{22}k_{23}]^{-1}} \quad (5.113)$$

and a small phase imbalance

$$\delta_2 = t_{d2} - \Delta t_2 \quad . \quad (5.114)$$

We can write Eqn. (5.110) in the form

$$y(t) = \sqrt{1-k_1^2} \sqrt{1-k_2^2} \sqrt{1-k_3^2} [ |H| x(t-\Delta t_2 - t_{d1}) + v_d(t-\Delta t_2) - \alpha_2 v_d(t-\Delta t_2 - \delta_2) ] \quad . \quad (5.115)$$

If  $v_d(t)$  is third-order IM distortion, i.e.,

$$v_d(t) = V_3 \cos((3\omega_2 - 2\omega_1)t) \quad (5.116)$$

where  $3\omega_2 - 2\omega_1 \approx \omega_1$ , then the magnitude of distortion in the output, from vector analysis of Eqn. (5.115), is

$$y_d(t) = \sqrt{1-k_1^2} \sqrt{1-k_2^2} \sqrt{1-k_3^2} V_3 [1 + \alpha_2^2 - 2\alpha_2 \cos \delta_2]^{\frac{1}{2}} \quad . \quad (5.117)$$

Using Eqns. (5.115) and (5.117) in (2.2), the third-order distortion for the feedforward-corrected amplifier at frequency  $\omega_1$  is



$$IM_{3FF}(dB) = 20 \log \left\{ \frac{V_3 [1 + \alpha_2^2 - 2\alpha_2 \cos \delta_2]^{\frac{1}{2}}}{|H| V_1} \right\} \quad (5.118)$$

The third-order distortion for the uncorrected IMPATT amplifier, from Eqns. (5.106), (5.107) and (5.116) is

$$IM_3 (dB) = 20 \log \left\{ \frac{V_3}{|H| V_1} \right\} \quad (5.119)$$

Combining Eqns. (5.118) and (5.119), the improvement in IM distortion is given by

$$[IM_{3FF} - IM_3](dB) = 20 \log [1 + \alpha_2^2 - 2\alpha_2 \cos \delta_2]^{\frac{1}{2}} \quad (5.120)$$

For small amplitude- and phase imbalances, Eqn. (5.120) can be approximated by

$$[IM_{3FF} - IM_3](dB) = 20 \log [(1 - \alpha_2^2) + \alpha_2^2 \delta_2^2]^{\frac{1}{2}} \quad (5.121)$$

which is the same result as Eqn. (4.90) derived from a more rigorous Volterra series analysis, and plotted in Figs. 4.17 and 4.18.

## 5.5 Summary

A technique for the prediction of two-tone IM distortion in a two-terminal negative-resistance reflection amplifier is developed. The technique is based on the analysis of a nonlinear amplifier model comprising admittance operators which represent the nonlinear active



diode admittance and the linear passive circuit admittance. These operators are fitted to the model by cubic-spline approximation of the respective experimentally-determined admittances. For an equal-level two-tone input, the admittance operators operate on the corresponding quasistationary input signal; i.e. the two-tone input can be considered as an RF carrier signal with LF-AM modulation superimposed. After these operations are carried out, the result is a nonlinear differential equation which approximately describes the response of the reflection amplifier to a two-tone input. The equation can be solved iteratively, directly in the frequency domain, for the steady-state amplitudes of the nonlinear distortion products.

This method was applied to a stable IMPATT-diode amplifier. The predicted third-order IM distortion agrees quite closely (within 3 dB) with the distortion predicted using Volterra series analysis (Chapter 4) in the range of validity of the Volterra series model (-23 dBm per tone maximum). This technique is slow-running, however, compared to the Volterra series approach because of the number of multiplications of complex exponential series necessary for reasonable accuracy in the iteration procedure.

The reduction in nonlinear distortion by feedforward-correction is calculated using simple network analysis of the linear feedforward circuitry external to the main (IMPATT) amplifier. The resulting expression is identical to the expression derived using Volterra series analysis.





## CHAPTER 6

### EXPERIMENTAL STUDY OF IMPATT-AMPLIFIER DISTORTION AND OF FEEDFORWARD-CORRECTED DISTORTION

#### 6.1 Scope of the Experimental Study

This chapter describes an experimental study of IMPATT-amplifier distortion and of the reduction of this distortion by feedforward correction. An experimental 6-GHz feedforward amplifier was designed and constructed in a waveguide transmission medium; the main amplifier is a coaxial stable IMPATT amplifier; the error amplifier is a low-noise TWT amplifier.

The experimental investigation includes the following measurements.

- 1) The gain response, phase response, and gain compression of the experimental IMPATT amplifier are measured as a function of both frequency and input power.
- 2) The intermodulation (IM) distortion of the IMPATT amplifier alone (i.e., with the feedforward circuit switched "off") is measured as a function of both frequency and input power. Spectrum signature data is measured for a two-tone test signal to obtain the IM distortion.
- 3) The two-tone IM distortion of the IMPATT amplifier with feedforward-correction applied (i.e., with the feedforward circuit switched "on") is measured as a function of both frequency and input power.
- 4) The two-tone IM distortion of the IMPATT amplifier with feedforward correction applied is measured as a function of small gain- and/or phase imbalances in the error-correction loop.
- 5) The gain sensitivity of the feedforward-corrected IMPATT amplifier is measured.

The experimental data is compared with the predicted IM distortion



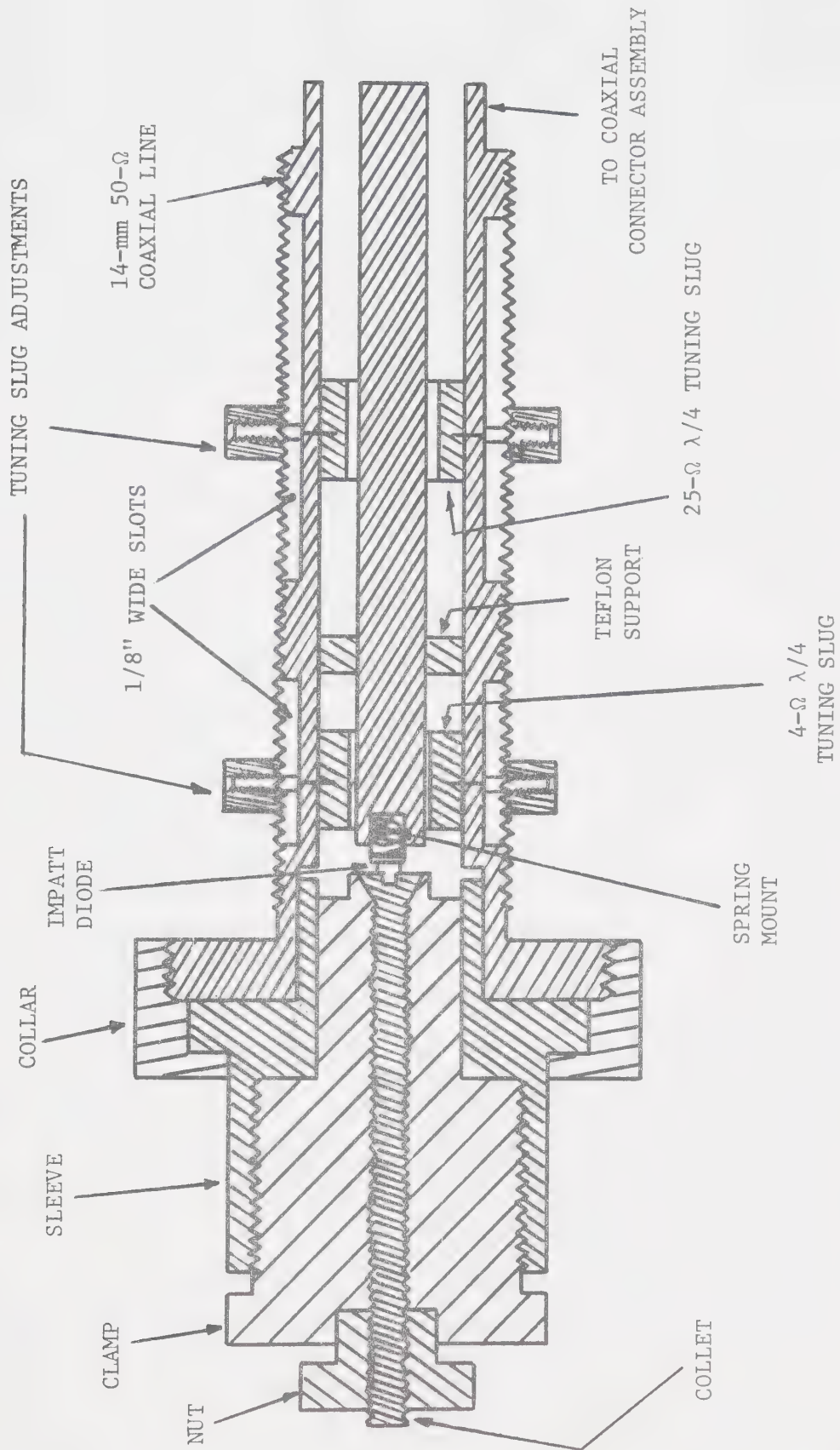
to validate the two nonlinear models for the IMPATT amplifier and the feedforward-corrected amplifier, and to verify the two theoretical IM distortion analysis techniques: 1) the Volterra series approach; 2) the numerical quasistationary analysis based on nonlinear admittance operators. Gain compression is also measured to provide further validation of the above theoretical analyses.

The design of the experimental IMPATT amplifier is discussed in Sec. 6.2. The experimental feedforward-corrected IMPATT amplifier is described in Sec. 6.3. Section 6.4 includes the experimental test bench and the two-tone method of IM distortion measurement. The experimental distortion results are presented in Secs. 6.5 and 6.6 and compared with the theoretical results predicted in Chapters 4 and 5.

## 6.2 The Experimental Stable IMPATT Amplifier

The diode mount, impedance-transforming elements and tuning resonators are realized in precision 14-mm coaxial air line as illustrated in Fig. 6.1. The diode resonator is a short length of series transmission line which acts as a lumped inductance to tune out the diode- and package capacitive susceptance at the centre frequency 5.905 GHz. The tuning resonator, another series section of line, has the same centre frequency in principle, but a different reactance slope with frequency in order to increase the amplifier bandwidth. The experimental IMPATT diode is a 100-mW Silicon diode, type HP 5082-0431, in an S-4 package (pill with one prong). The diode is biased at 117 Vdc and 25 mAdc via a bias tee. The IMPATT amplifier is tuned to provide 17.3-dB small-signal gain at centre frequency 5.905 GHz with a 3-dB bandwidth of 64 MHz, using two coaxial tuning slugs. Two slugs are used in the experimental amplifier since the value of peak gain and its frequency can then be varied somewhat independently in con-





SCALE: 4mm/in.

Figure 6.1 Cross section of J-band coaxial double-slug-tuned IMPATT amplifier circuit.



trast with a single-tuned amplifier. The slug closest to the diode is 1.250 cm long ( $\lambda_g/4$  at 6 GHz) with an inner diameter of 0.66 cm, corresponding to a characteristic impedance of about  $4\ \Omega$ ; the second slug is also 1.250 cm long with an inner diameter of 0.937 cm, corresponding to a characteristic impedance of about  $25\ \Omega$ . The closest face of the first slug is located 0.14 cm from the diode flange, while the equivalent dimension for the second slug is 3.32 cm. A Teflon support for the coaxial centre conductor is 0.43 cm or  $0.085\ \lambda_g$  thick at the centre frequency; it also has some impedance-transforming effect. A four-port waveguide circulator is used to separate the incident- and reflected signals at port 2 of the circulator; isolation of the IMPATT-amplifier output (port 3) from the input (port 1) is achieved by match-terminating port 4.

Under the above tuning conditions, curves of gain versus CW frequency were measured at input power levels of -30, -20, -10, -7, -3 and 0 dBm. No spurious oscillations were observed over this input range. Gain was measured relative to a 0-dB reference obtained by replacing the amplifier assembly with a waveguide short-circuit at reference plane 2-2' in Fig. 3.6 (i.e., at port 2 of the waveguide circulator). All the theoretical results for IMPATT-amplifier performance in Chapters 4 and 5 are referred to this reference plane. Figure 6.2 displays the measured gain behaviour of the IMPATT amplifier, with an experimental error of  $\pm 0.1$  dB. Absence of gain ripple in the small-signal response, together with the fact that the amplifier was not tuned for maximum experimental gain, indicates that the double-tuned circuit is undercoupled. As the input level increases, the resonant frequency is lowered, the gain decreases, and the 3-dB bandwidth widens although the gain response becomes more asymmetrical. Values for the parameters in the tuned  $G_c L_c C_c$  circuit model of the IMPATT amplifier,





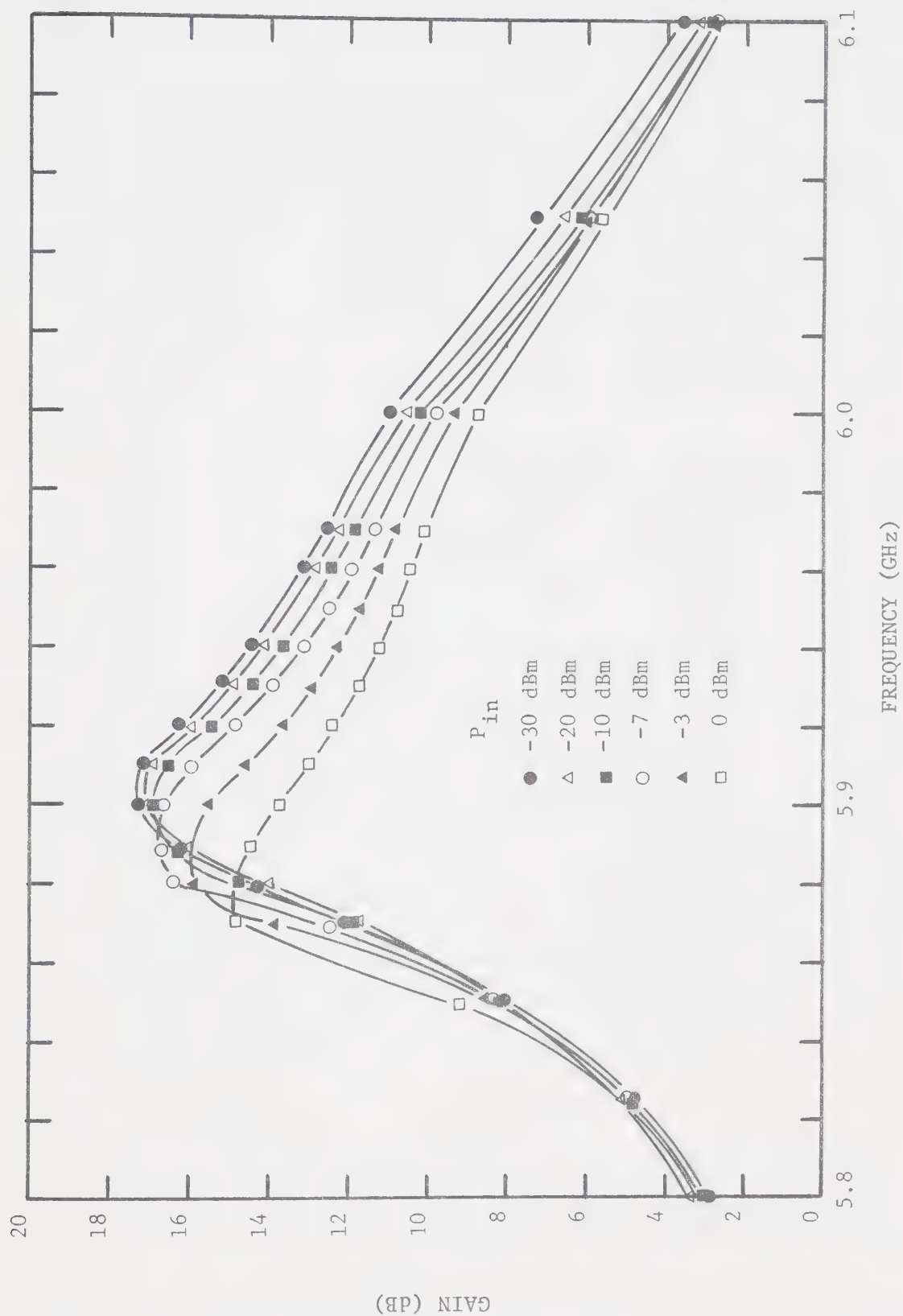


Figure 6.2 Measured gain behaviour of the experimental IMPATT amplifier at constant 25-mA dc bias current.



Fig. 4.2, were derived by matching the model's gain with the measured gain. A comparison of these responses appears in Fig. 4.3, for the Volterra series approach to predicting IMPATT-amplifier distortion, and in Fig. 5.6, for the quasistationary approach. Agreement of the predicted and measured gain over the amplifier bandwidth is seen to be good in both cases, at input levels up to  $-10$  dBm. The gain predicted using the measured circuit admittance, Fig. 5.2, does not compare as favourably with the measured gain in Fig. 5.3, because of the 10-20% error in the measurement of the circuit admittance and the electronic admittance of the IMPATT diode.

Figure 6.3 presents information about the saturation and dynamic-range properties of the IMPATT amplifier at several different frequencies in the amplifier passband. Gain expansion over a limited input range at frequencies below the centre frequency is clearly evident; gain compression at frequencies above the centre frequency is also observed. The input level at which departure occurs from small-signal operation, and hence gain compression or expansion, is highly dependent on frequency. This is due to the narrowband nature of the experimental IMPATT amplifier. Gain compression or expansion is shown distinctly in Fig. 6.4. The estimated error for this measurement is  $\pm 0.2$  dB. An interesting feature shown by these curves is the gain linearization that can be obtained by operating below the small-signal resonant frequency of the IMPATT amplifier. The input levels for 1-dB compression are listed in Fig. 6.4. This gain linearization is achieved by a partial compensation of the gain reduction, under large-signal operation, for the gain expansion due to lowering of the resonant frequency.

The phase shift of the IMPATT amplifier was measured by balancing



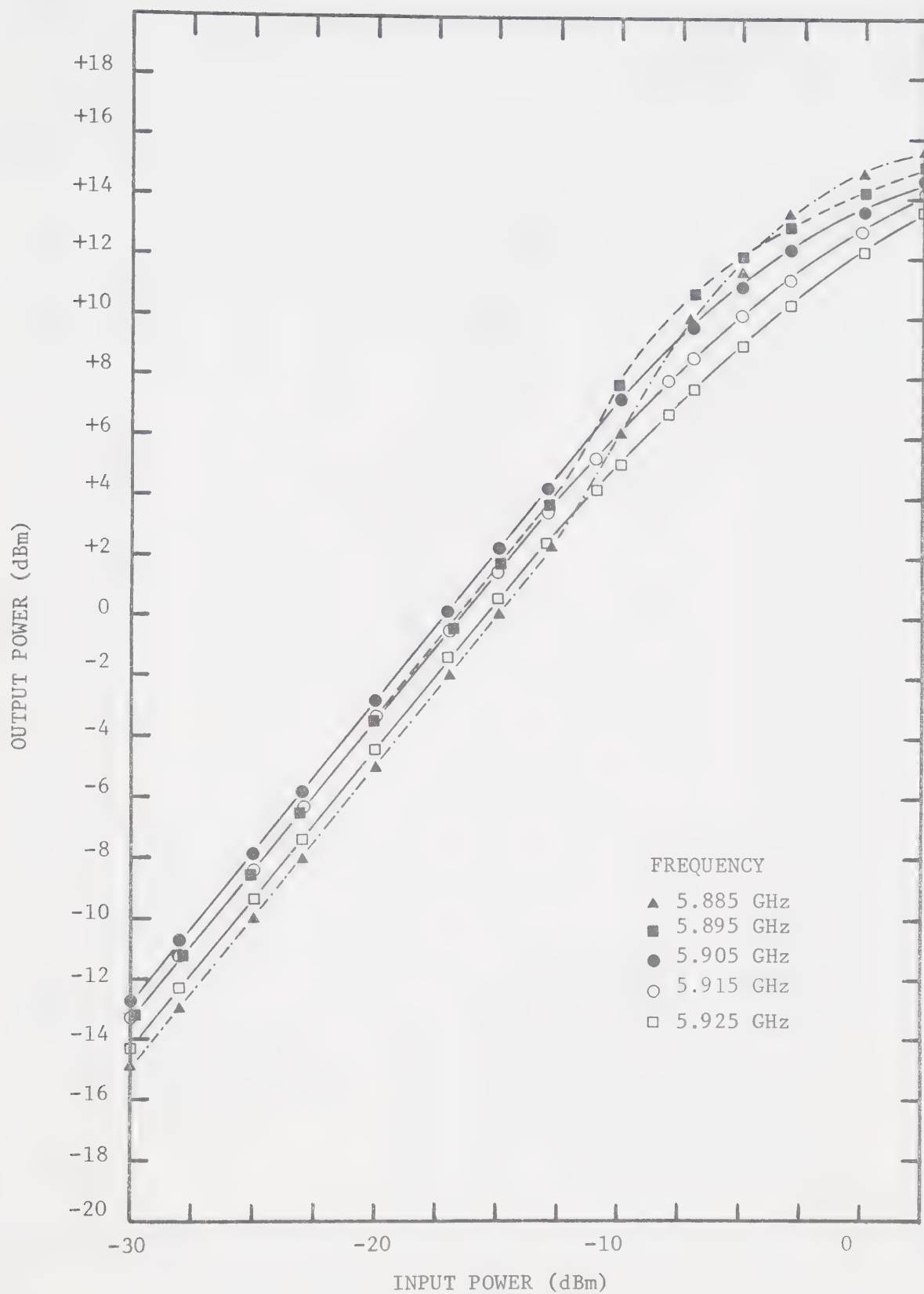


Figure 6.3 Measured saturation characteristics of the experimental IMPATT amplifier at constant 25-mA dc bias current.



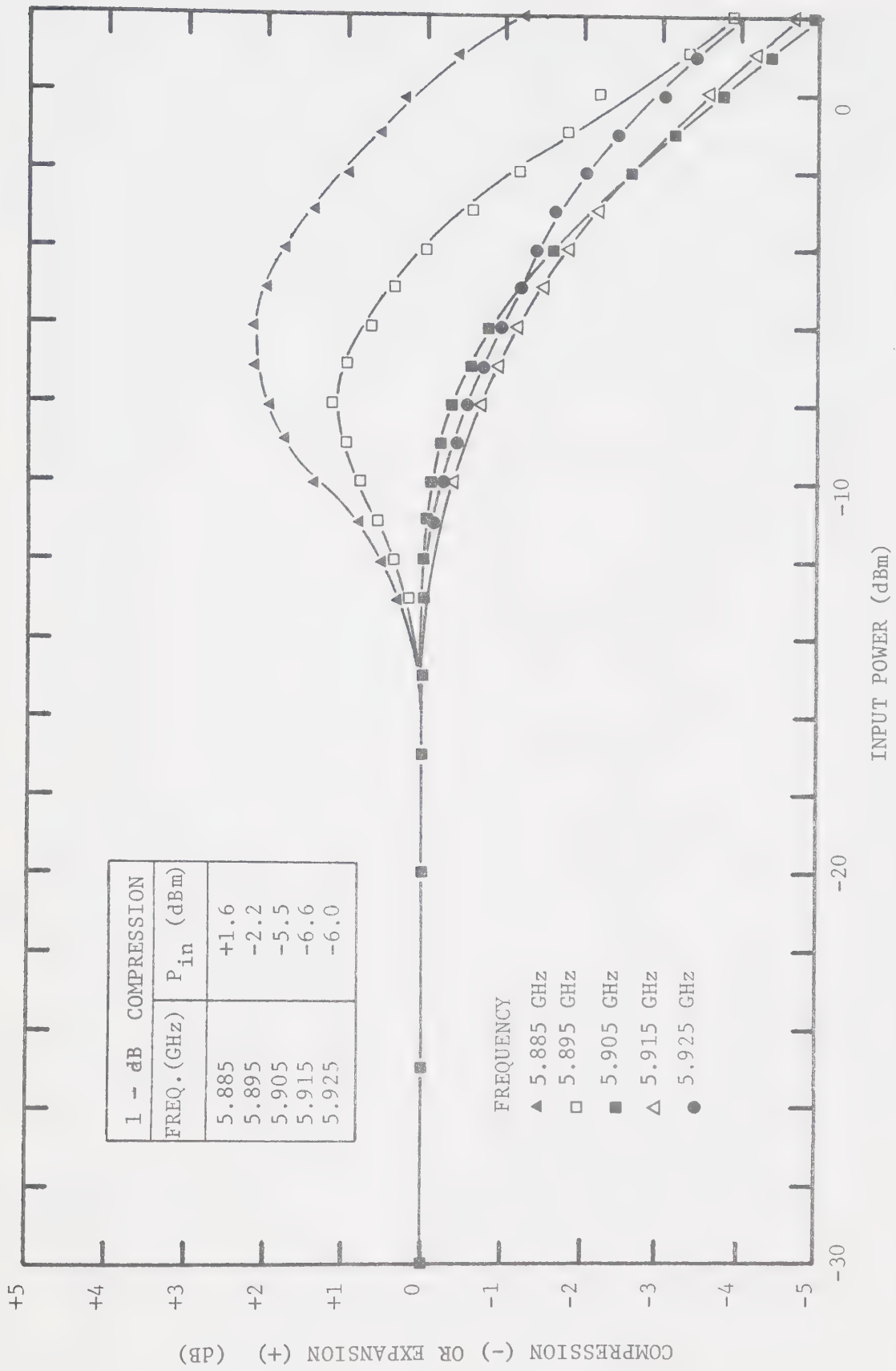


Figure 6.4 Measured gain compression of the experimental IMPATT amplifier at constant 25-mA dc bias current.





the amplifier output against an attenuated and phase-shifted version of the amplifier input, in a waveguide bridge circuit utilizing a hybrid tee as the signal-combining element. The bridge is calibrated by balancing it with a waveguide short-circuit connected at port 2 of the amplifier circulator. The amplifier phase shift is then the excess phase shift, introduced by a precision phase-shifter, necessary to achieve a bridge null when the amplifier is connected at port 2 of the circulator. The measured phase shift is compared with the phase shift of the  $G_c L C_c$  tuned-circuit model in Fig. 4.4 for the Volterra series method to predict IM distortion, and in Fig. 5.7 for the quasistationary distortion analysis. As mentioned previously, the deviation in the predicted and measured phase shift, is a consequence of approximating the undercoupled double-tuned amplifier circuit by a single-tuned circuit. In addition there is an experimental error of  $\pm 5^\circ$  associated with the phase shift measurement.

The group delay of the IMPATT amplifier was determined using the principle stated by Nyquist and Brand [98]. Essentially, the delay variations of the network under test are converted into variations in the phase shift of an LF sinusoidal modulation signal. The conventional method consists of first amplitude-modulating a CW signal, transmitting it through the test device, and then measuring the phase shift of the envelope. The group delay of the test device at the CW frequency is directly proportional to the envelope phase shift [99]. The group delay of the IMPATT amplifier is  $10 \text{ ns} \pm 1 \text{ ns}$  at the centre frequency.

### 6.3 The Experimental Feedforward-Corrected IMPATT Amplifier

The experimental IMPATT-amplifier with feedforward-correction applied is shown in the schematic diagram of Fig. 6.5. All the feedforward



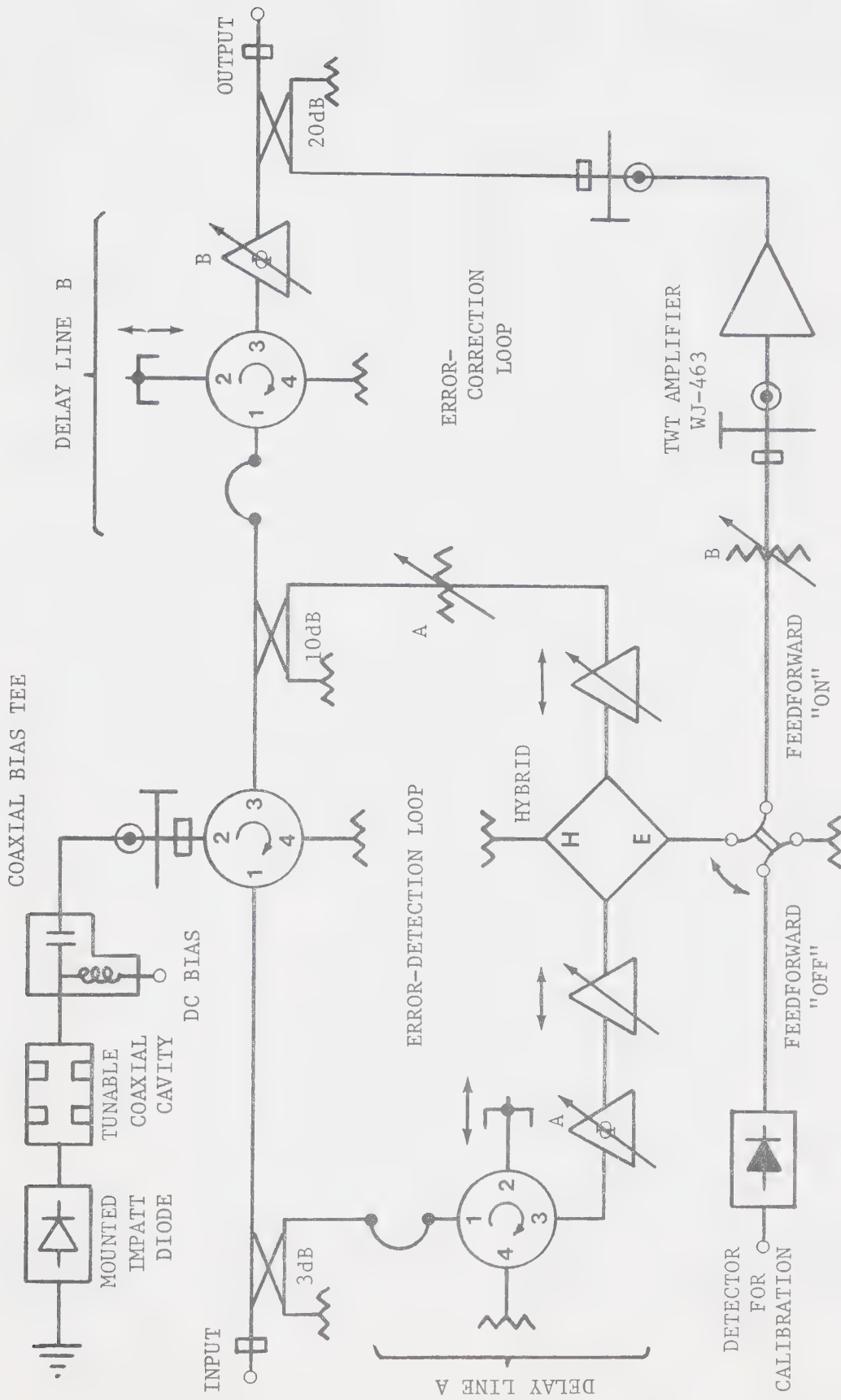


Figure 6.5 The experimental feedforward-corrected IMPATT amplifier.



network components are realized in WR-137 waveguide because of the wide choice of components which were available. Notes on the choice of components are listed.

1) A low-noise (10-dB NF maximum) TWT, type Watkins-Johnson WJ-463, is used as the error amplifier. It has 43-dB gain for small signals (less than -30 dBm) and 1-dB compression occurs at an input power of -34 dBm. The error-detection loop has to be balanced sufficiently such that error signals are in this order of magnitude; the error amplifier then adds negligible distortion to the amplified error signal. Also, because the TWT is broadband (4 to 8 GHz), operation over the narrow band of applied signals is nearly linear. The TWT group delay was measured as approximately  $15 \text{ ns} \pm 1 \text{ ns}$  at 5.905 GHz.

2) The required delay lines are 20-30 ns long, allowing for additional waveguide circuitry. High attenuation loss (about 1 dB/m at 6 GHz) prohibited the use of 50- $\Omega$  coaxial cable; therefore, WR-137 waveguide, having attenuation loss less than 0.1 dB/m, was chosen for the delay lines. The physical length of the delay lines (group delay 4.8 ns/m at 6 GHz) is adjusted by means of a variable short-circuit connected at port 2 of a circulator; the signal enters port 1 and leaves port 3 with adjustable delay. Precision phase shifters are used to make fine adjustments to delay-line electrical length.

3) A 3-dB directional coupler is used as the input signal divider.

4) A hybrid tee is used as the signal-comparator, with the error signal appearing at the E-plane arm. Slide-screw tuners are used to reduce the VSWR at the input ports of the hybrid tee from 1.29 to 1.10 over a 100-MHz bandwidth at 5.905 GHz.

5) Precision attenuators are used for balancing the amplitudes of the signals in both the error-detection loop and the error-correction





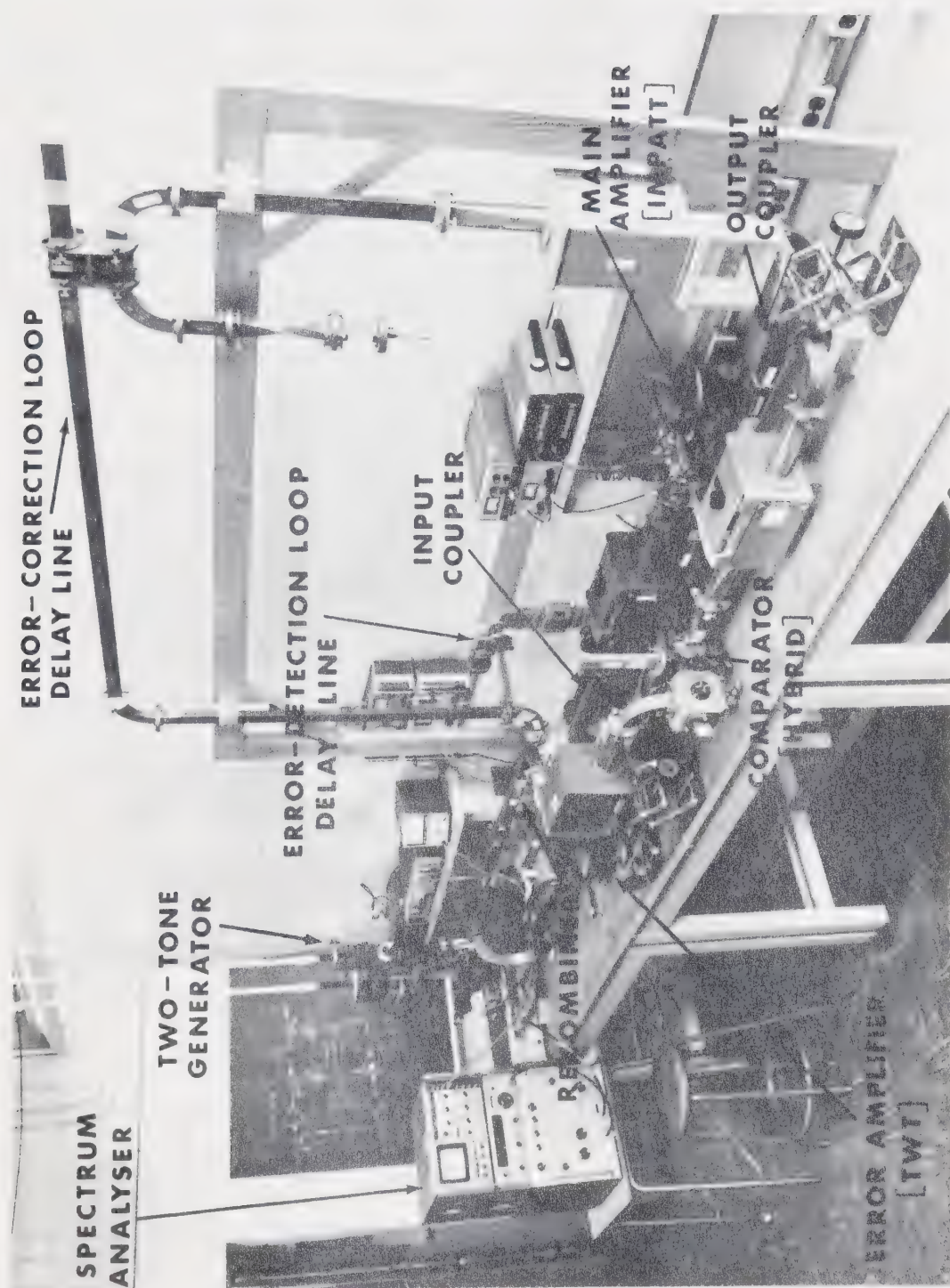


FIGURE 6.6 Photographic view of the experimental feedforward-corrected IMPATT amplifier and two-tone distortion test equipment.





loop.

6) The amplified error signal and delayed distorted main signal are recombined in a 20-dB directional coupler.

A photograph of the assembled feedforward system appears in Fig. 6.6; the chief components are identified.

Calibration of the microwave feedforward amplifier was performed first in the error-detection loop and then in the error-correction loop. With feedforward correction switched "off", see Fig. 6.5, a small AM-modulated 5.905-GHz calibrating signal was applied at the input of the feedforward amplifier. Attenuator A, and phase-shifter A were adjusted for minimum (ideally zero) signal at the calibration port, thus balancing the error-detection loop. Next, the feedforward correction was switched "on", the IMPATT-amplifier assembly was disconnected at port 2 of the waveguide circulator and the calibrating signal was applied there. Balance of the error-correction loop was achieved by adjusting phase shifter B, and attenuator B for minimum (ideally zero) signal at the output port of the feedforward amplifier.

The quality of the interferometric null in the error-detection loop and in the error-correction loop across the IMPATT-amplifier passband is shown in Fig. 6.7. A best null figure of  $40 \text{ dB} \pm 1 \text{ dB}$  is obtained at the centre frequency. The null figure decreases to 6 dB for the error-detection loop at the edge of the passband, and to 8 dB for the error-correction loop at the edge of the passband. This substantial degradation of the loop balance is a consequence of the narrowband tuned-circuit behaviour of the IMPATT amplifier, and in particular, the rapid phase shift through the resonant frequency.



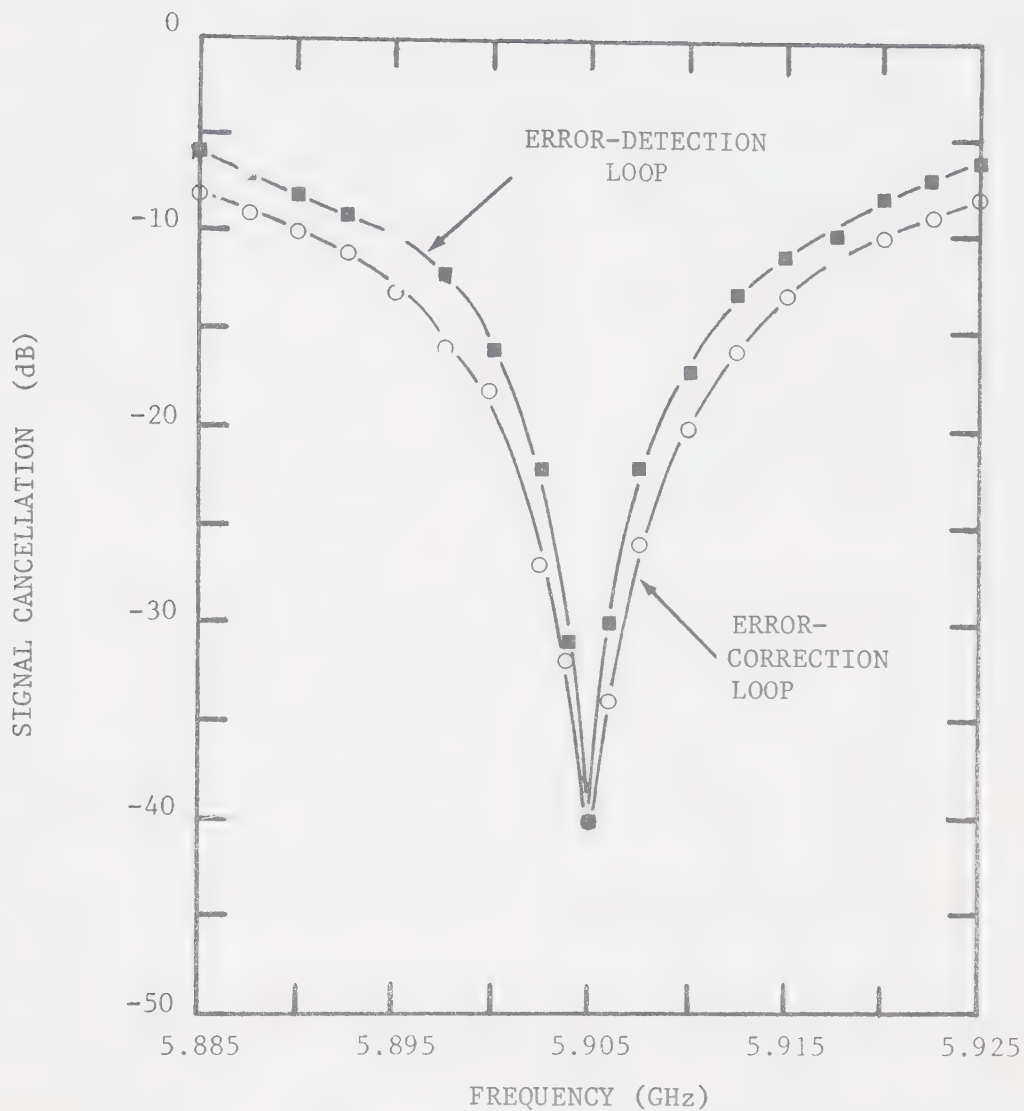


Figure 6.7 Measured variation in the quality of the error-detection loop balance and error-correction loop balance in the experimental feedforward-corrected IMPATT amplifier.



#### 6.4 The Experimental IM Distortion Test Bench and Procedures

A test signal consisting of two equal-level tones, having a very stable 1-MHz frequency difference, was required for the IM distortion measurements. At microwave frequencies, it is difficult to achieve such a relatively constant small frequency difference between two independent RF signal generators, since their frequency stability is usually of the same magnitude or larger. For example, the frequency stability of the HP 618C J-band signal generator (klystron type) is:  $\pm 0.006\%/^{\circ}\text{C}$  change in ambient temperature (this is equivalent to  $\pm 360 \text{ KHz}/^{\circ}\text{C}$  at 6 GHz);  $\pm 0.02\%$  change (i.e.,  $\pm 1.2 \text{ MHz}$  change at 6 GHz) for line voltage variation of  $\pm 10\%$ . In order to have a fixed frequency difference between the outputs of two separate RF signal generators, the outputs must track one another.

The microwave two-tone generator shown schematically in Fig. 6.8 operates on the principle of a frequency-locked loop [100]. The frequency,  $f_2$ , of the varactor-tuned Gunn-effect slave oscillator (Varian VSC-9019S4 with frequency stability  $\pm 200 \text{ KHz}/^{\circ}\text{C}$ ) depends on the frequency,  $f_1$ , of the stable klystron (HP 618C) master oscillator. These two RF signals are combined in a hybrid tee: one output from the hybrid is used to control the frequency difference ( $f_2 - f_1$ ) and the other output is the usable two-tone test signal. The two sources are initially adjusted so that  $f_1$  is the desired test frequency and ( $f_2 - f_1$ ) lies within the capture range of the frequency-locked loop. The frequency comparator circuit of Fig. 6.9, modified slightly from [100], compares the mixer output voltage at frequency ( $f_2 - f_1$ ) with the 1-MHz output voltage of an extremely stable ( $\pm 5 \times 10^{-5} \text{ Hz}/^{\circ}\text{C}$ ) Quartz-crystal oscillator (HP 105A) and generates a dc voltage proportional to the error signal comprising the frequency- and/or



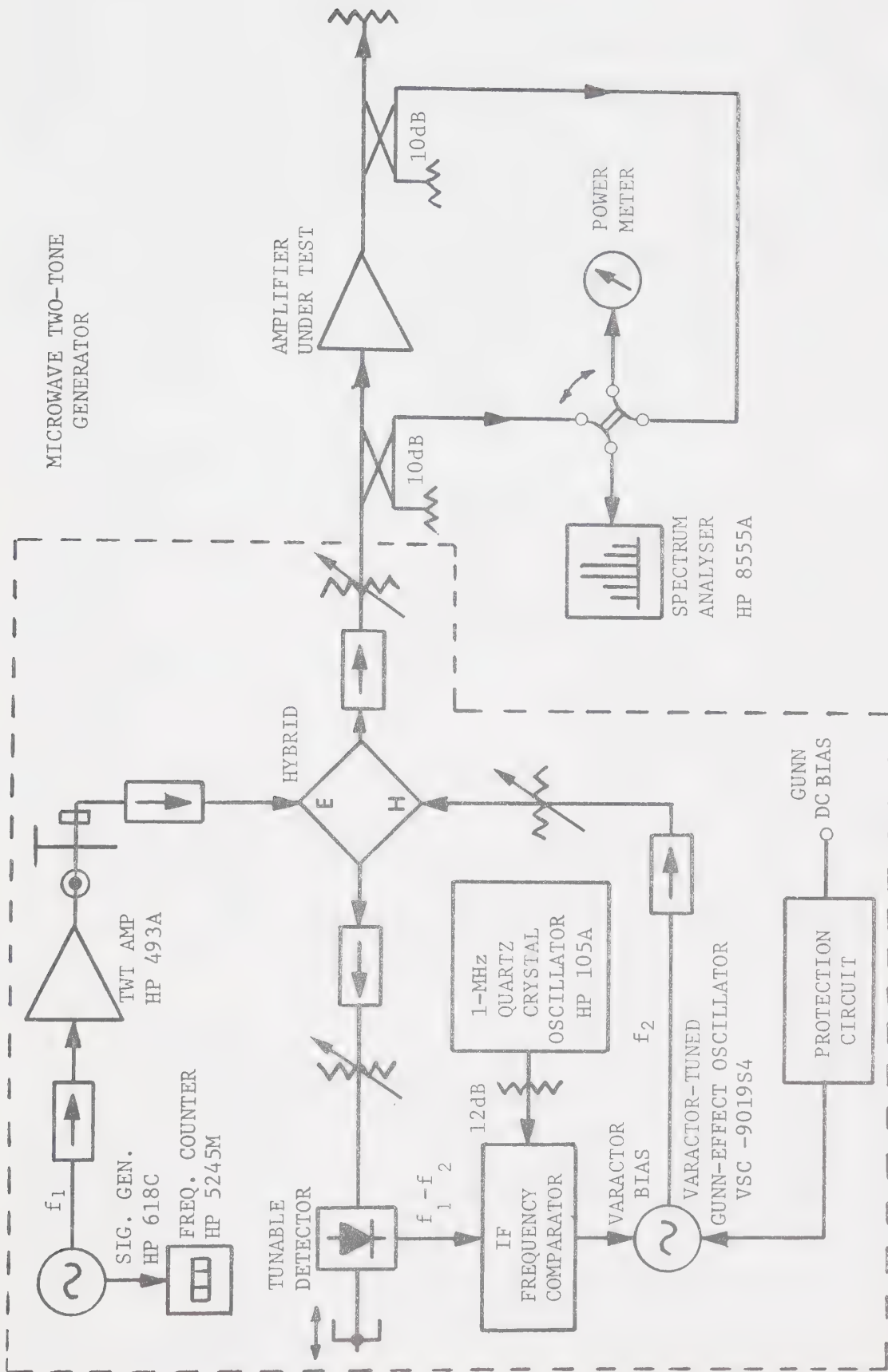


Figure 6.8 The experimental two-tone IM distortion test bench.





phase difference. The derived dc voltage is applied to the varactor-tuned oscillator so that the error signal tends to zero ( $\pm 20$  MHz electronic tuning is attainable for  $\pm 20$  Vdc change about the varactor +20 Vdc offset voltage). In this locked condition, the output frequencies  $f_1$  and  $f_2$  will have a frequency separation with a fixed frequency/phase relationship relative to the 1-MHz reference signal. The two-tone generator remained locked with a 1-MHz frequency difference for variations in the master oscillator ( $f_1$ ) of  $\pm 5$  MHz. A maximum signal output of 4.5 dBm per tone was obtained; this level was adjusted by means of a precision attenuator.

In the experimental IM distortion test set, shown in Fig. 6.3, the waveguide switch is used to select either the input- or output test signal for display on the spectrum analyser (HP 8555A); the other signal's level is monitored on the power meter. The IM products were positively identified on the spectrum analyser by reducing the input test-signal power level and observing the decrease in IM product level: third-order IM products decrease 3 dB for every 1-dB reduction in input level; fifth-order IM products decrease 5 dB for every 1-dB reduction in input level.

For single-tone gain compression tests the stable klystron source was used.

The above tests were performed on the stable IMPATT amplifier alone, and on the IMPATT amplifier with feedforward correction applied. Feedforward correction was switched "on" and "off" via the waveguide switch at the output of the hybrid tee in the feedforward amplifier, Fig. 6.5. Signal power levels for the IMPATT amplifier alone were measured relative to a 0-dB reference obtained by replacing the amplifier assembly with a waveguide short-circuit at port 2 of the IMPATT-amplifier circulator.







## 6.5 Experimental IMPATT-Amplifier Distortion Results and Comparison with Theory

The measured third-order IM distortion for the IMPATT amplifier is compared in Figs. 4.11 and 4.13 with the distortion predicted using Volterra series analysis. It is also compared in Figs. 5.8 and 5.10 with the distortion calculated using quasistationary distortion analysis of the tuned-circuit amplifier model. Within an expected measurement error of  $\pm 2$  dB, the theoretical results are in good agreement with experimental values, as shown to better advantage in Fig. 6.10. At small-signal levels, both theories predict the same distortion within 1 dB. The absence of measured data at input levels less than -30 dBm per tone, indicates its unresolvability on the spectrum analyser and represents IM distortion more than 60 dB below the carrier. There is less than 3 dB difference between the measured distortion and the distortion predicted using the Volterra series approach for input levels up to -23 dBm per tone. The quasistationary method is applicable at higher input levels: theory and experiment agree within 3 dB up to drive levels of -18 dBm per tone, and within 8 dB at -13 dBm per tone. The agreement is generally better at the upper edge of the passband than at the low edge of the passband. This difference may be attributable to a stronger low-frequency dominance mechanism outside the small-signal region than either theory predicts. Also, the quasistationary analysis ceases to make reasonably accurate distortion predictions at levels higher than -15 dBm per tone because the larger RF voltage (4.5 V compared with 1.4 V at -23 dBm per tone) developed across the IMPATT diode demands a larger solution grid for the iteration procedure. The fitted bicubic spline coefficients approximate the measured admittance in this grid with less accuracy than in a smaller solution grid because fewer data points can be used.



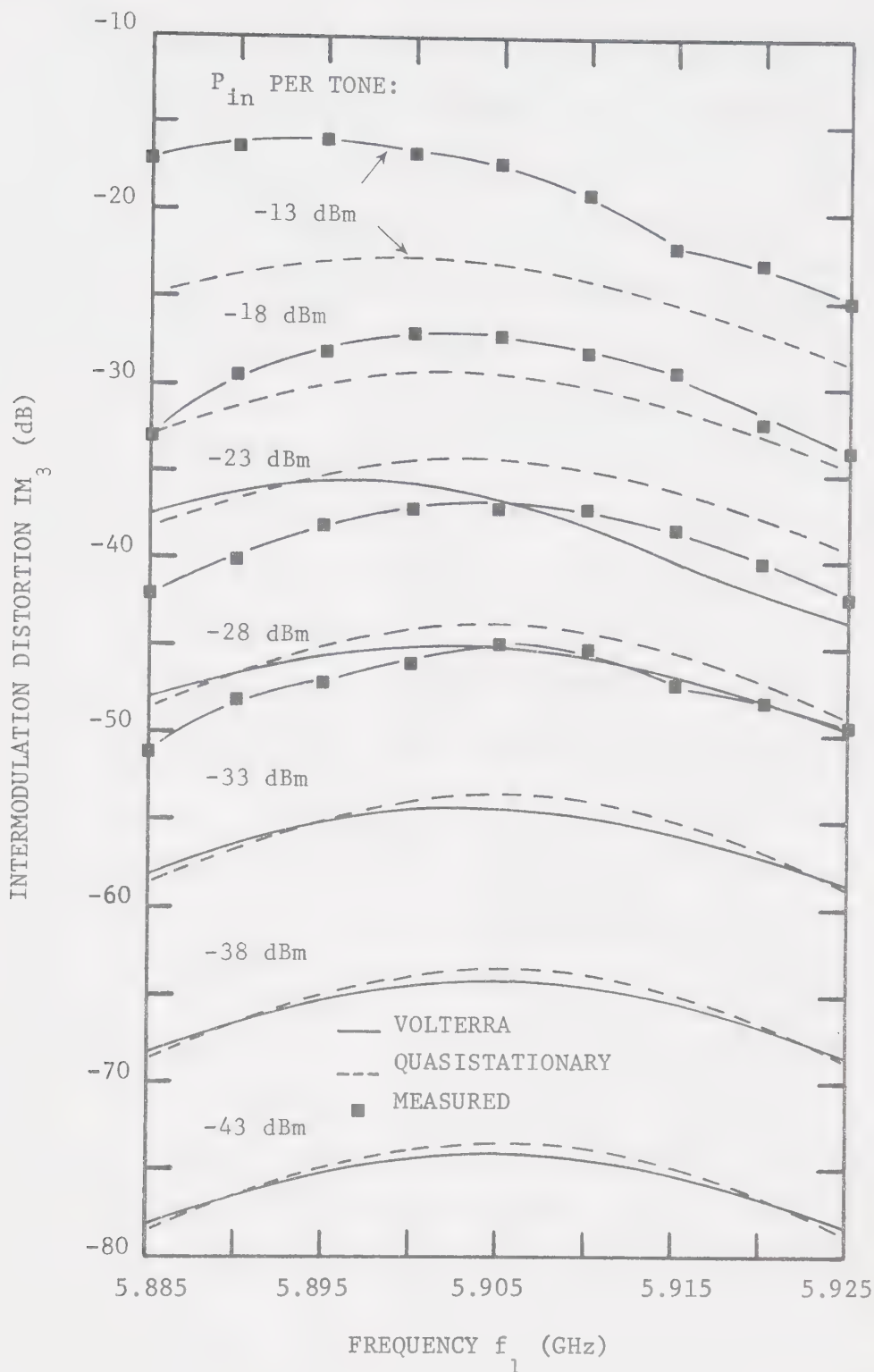


Figure 6.10 Comparison of measured third-order IM distortion at  $2f_1 - f_2$ , for the experimental IMPATT amplifier ( $I_{dc} = 25$  mA) with a two-tone input ( $f_2 = f_1 + 1$  MHz), with the theoretical values calculated using 1) the Volterra series analysis; 2) the quasistationary distortion analysis.





Measured fifth-order distortion is plotted together with the theoretical results in Fig. 6.11. Experimental data could only be resolved at input levels above -18 dBm per tone. The Volterra series analysis is not applicable at that level for reasons discussed in Sec. 4.3.6. Quasistationary distortion analysis of the tuned-circuit amplifier model predicts  $IM_5$  within 2 dB of the experimental results for an input of -18 dBm per tone; i.e., there is good agreement within the expected measurement error of  $\pm 2$  dB. This agreement becomes poorer at -13 dBm input per tone. The rather sudden increase in measured fifth-order distortion at input powers above -18 dBm per tone indicates that nonlinear phenomena of higher order than fifth become significant at that level. Such high-order nonlinear behaviour is not characterized adequately by the amplifier nonlinear model. Volterra series analysis predicts fifth-order distortion 10 dB above the values computed using the quasistationary distortion analysis at small-signal levels. This discrepancy occurs because the Volterra series representation of the IMPATT amplifier is based upon a simple second-order power series approximation of the electronic conductance and equivalent electronic capacitance. Even though the diode nonlinearities each have just a single second-order term, the Volterra series expansion has an infinite number of terms. The fifth- and higher-order terms in the resulting Volterra series, however, will not represent fifth-order effects as accurately as if the nonlinearities were described by a fourth-order power series. The limited available experimental data necessitates the use of a more sensitive microwave receiver for verification of the theoretical analyses conclusively at small-signal levels where the analyses apply.

Figures 4.12 and 5.9 compare the measured fundamental output



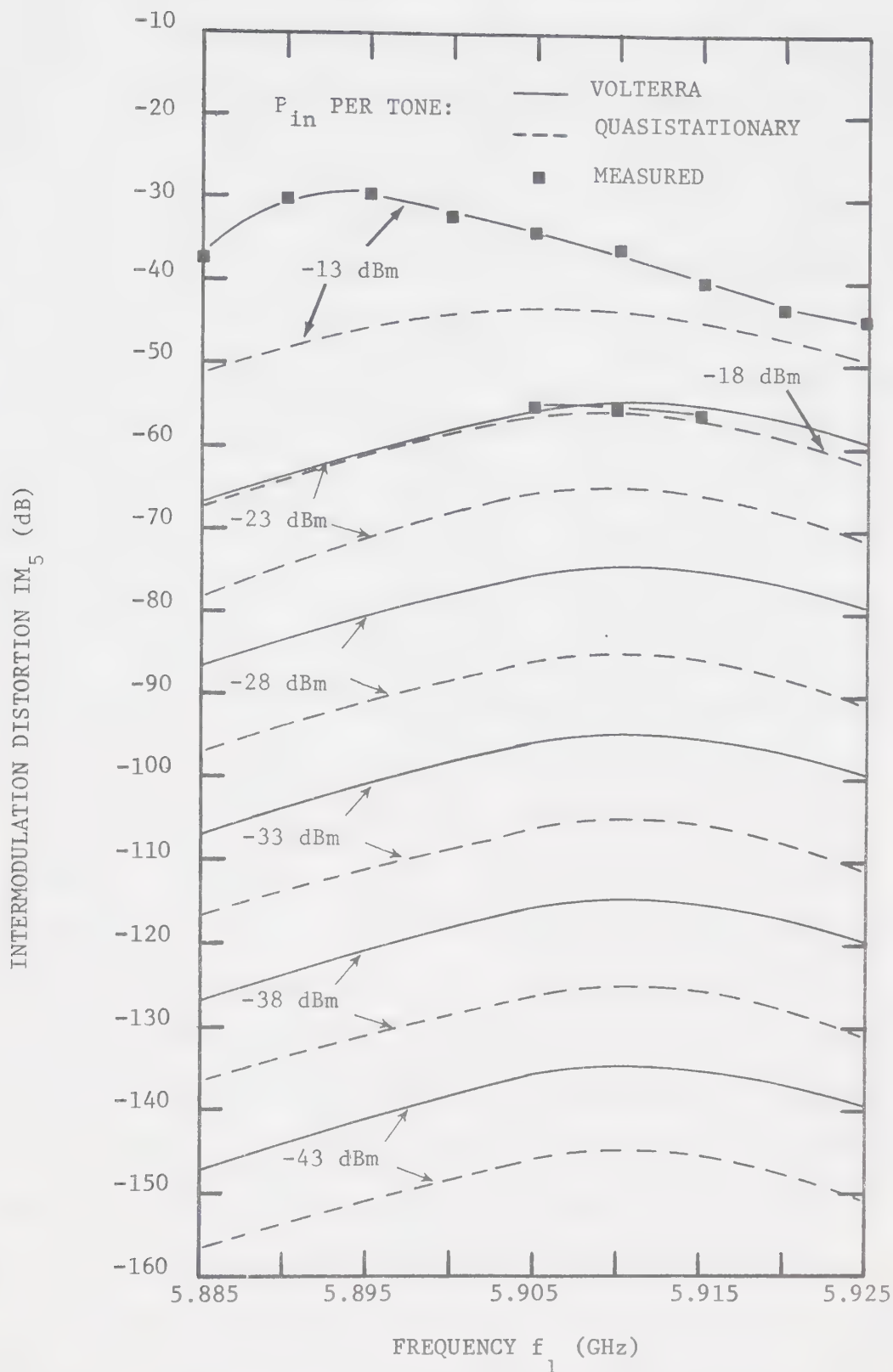


Figure 6.11 Comparison of measured fifth-order IM distortion at  $3f_1 - 2f_2$ , for the experimental IMPATT amplifier ( $I_{dc} = 25$  mA) with a two-tone input, ( $f_2 = f_1 + 1$  MHz), with the theoretical values calculated using 1) the Volterra series analysis; 2) the quasistationary distortion analysis.



power and distortion products, near the centre frequency, with the theoretical results of Volterra series analysis and quasistationary distortion analysis, respectively. The values compare well, within a measurement error of  $\pm 1$  dB, at the fundamental frequency and at the third-order product  $2f_1 - f_2$ . However, the error between theory and measurement increases markedly at the fifth-order product  $3f_1 - 2f_2$ . Both theories predict a third-order intercept point  $P_3 \approx 11.5$  dBm referenced to the output drive signal. The Volterra series analysis gives a fifth-order intercept  $P_5 \approx 8$  dBm, whereas the quasistationary analysis yields  $P_5 \approx 10.5$  dBm. These values agree quite closely with the measured values:  $P_3 \approx 12$  dBm,  $P_5 \approx 11$  dBm. The proximity of the fifth-order intercept point to the third-order intercept point is evidence that fifth- and higher-order nonlinear effects become increasingly important as the output power approaches nearer to the 1-dB compression point ( $\sim +3$  dBm) and the saturation level.

The curves of Fig. 6.4 show the measured gain compression, with an estimated measurement error of  $\pm 0.3$  dB, as a function of input power and frequency. The measured compression cannot be compared quantitatively with the predicted compression, Figs. 4.15 and 5.12, since the predicted values are of the same magnitude as the expected measurement error. However, the theories show good qualitative agreement with experimental data. It is of interest that both the Volterra series analysis and the quasistationary distortion analysis predict gain expansion over a range of input levels below the centre frequency as confirmed by measurement.

There is a large difference in the cost per distortion solution using the two theoretical analyses. The program as written for the Amdahl 470 computer can be executed at approximately \$0.07 per solution at each frequency of interest using the Volterra series approach; the cost is



about \$40 to obtain the solution using quasistationary distortion analysis.

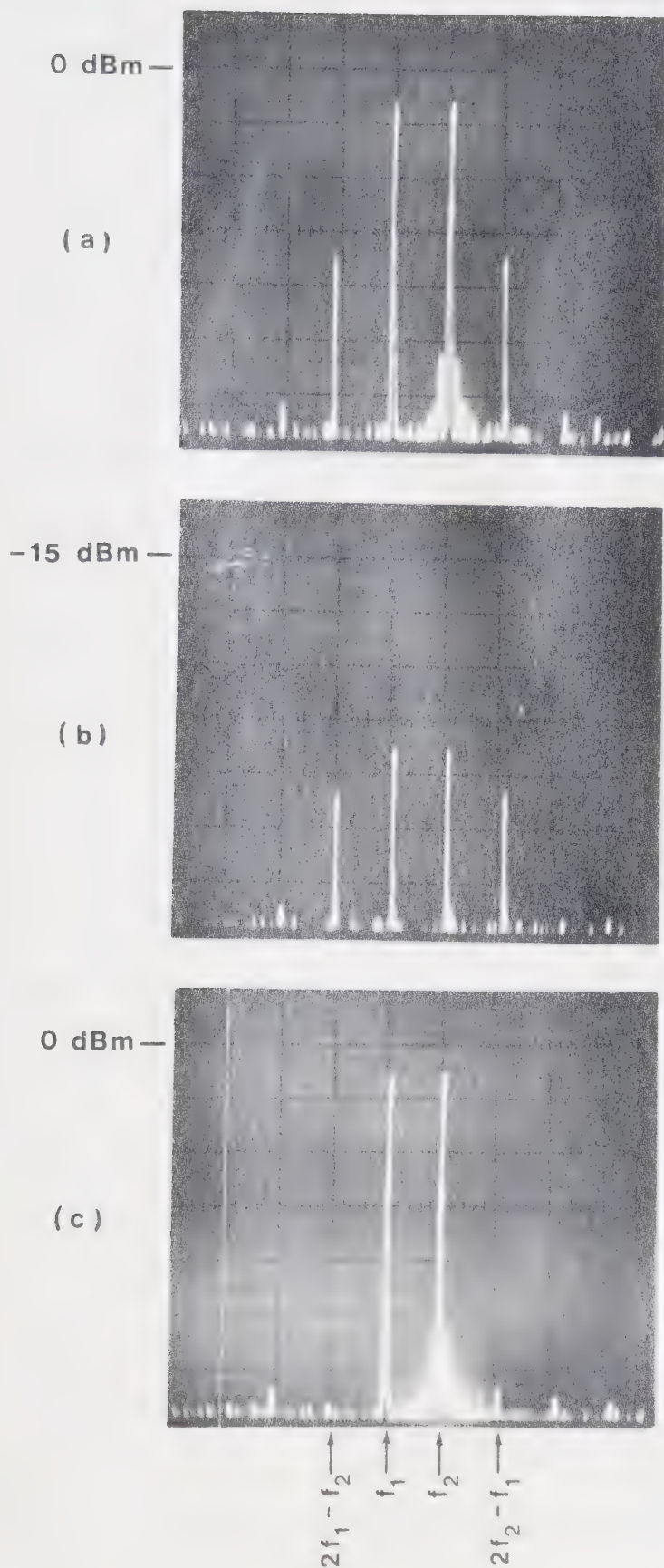
#### 6.6 Experimental Distortion Results for the Feedforward-Corrected IMPATT Amplifier and Comparison with Theory.

The reduction of the IM distortion of the IMPATT amplifier by feedforward correction is a function of the precision of balance in both the error-detection loop and the error-correction loop. With only small imbalance in the error-detection loop, which occurs for operation near the centre frequency, the distortion reduction depends predominantly on the error-correction loop balance. The measured interferometric null in the error-detection loop was  $40 \text{ dB} \pm 2 \text{ dB}$  at the centre frequency, or  $34 \text{ dB} \pm 2 \text{ dB}$  over a 1-MHz bandwidth as evident in Fig. 6.7. This error sensor null was sufficient to avoid observable distortion in the TWT (WJ 463) error amplifier at feedforward amplifier input levels less than 0 dBm. The corresponding error injection null in the error-correction loop was also  $40 \text{ dB} \pm 2 \text{ dB}$ . This figure suggests, ideally, a 40-dB distortion correction capability at the centre frequency.

Figure 6.12(a) illustrates the feedforward amplifier uncorrected output (i.e., with the error-correction loop disabled) for an input signal consisting of two tones at 5.9045 GHz and 5.9055 GHz with equal -13.8-dBm amplitudes (equivalent to -18 dBm per tone at the IMPATT amplifier input). Visible in the photograph are: 1) the input signals at  $-6 \text{ dBm} \pm 1 \text{ dBm}$  ( $-3 \text{ dBm} \pm 1 \text{ dBm}$  at the IMPATT amplifier output). The low-level noise at  $f_2$  is FM noise of the HP 618C signal generator; 2) third-order distortion products 5.9035 GHz and 5.9065 GHz having  $-34 \text{ dBm} \pm 1 \text{ dBm}$  amplitude ( $-31 \text{ dBm} \pm 1 \text{ dBm}$  referenced to the IMPATT amplifier output); 3) fifth-order distortion products at 5.9025 GHz and 5.9075 GHz with  $-62 \text{ dBm} \pm 1 \text{ dBm}$  levels ( $-59 \text{ dBm} \pm 1 \text{ dBm}$  referenced to the IMPATT amplifier output).







Spectrum photographs of the IM products of the experimental feedforward amplifier with an equal-level ( $-13.8$  dBm) two-tone input at the centre frequency ( $f_1 = 5.9045$  GHz,  $f_2 = 5.9055$  GHz) [vertical scale  $10$  dB/cm; horizontal scale  $1$  MHz/cm].

(a) The output of the feedforward amplifier without feedforward correction.

(b) The input to the error amplifier when the error-detection loop is balanced at  $5.905$  GHz.

(c) The output of the feedforward amplifier with feedforward correction applied.



The degree of balance in the error-detection loop is shown in the spectrogram of Fig. 6.12(b). The amplitudes of the carrier frequencies have been reduced by  $44 \text{ dB} \pm 2 \text{ dB}$  when compared with Fig. 6.12(a). The distortion products have been reduced by the 24-dB loss from the IMPATT amplifier output to the error amplifier input in Fig. 6.5. The total input power to the error amplifier was  $-46 \text{ dBm}$  which is in the linear operating range of the error amplifier.

The output spectrum for the feedforward amplifier with feedforward correction applied is shown in Fig. 6.12(c) which indicates that a  $31\text{-dB} \pm 2 \text{ dB}$  reduction in IM distortion was achieved. This result agrees with the measured 34-dB interferometer null over 1-MHz bandwidth in the error-correction loop. The output power of the feedforward system was measured at the two input frequencies to be  $-6 \text{ dBm} \pm 1 \text{ dBm}$ , indicating a loss of 3 dB in power level from the main amplifier output. This loss is due to the insertion loss of ports 2-3 in the IMPATT-amplifier circulator (0.6 dB), and the insertion loss of: the output coupler; the delay line (1.7 dB including 1.2-dB losses in the delay line circulator); the variable phase shifter; the recombiner. The overall gain of the feedforward amplifier was  $8 \text{ dB} \pm 1 \text{ dB}$ , compared with  $15 \text{ dB} \pm 1 \text{ dB}$  for the IMPATT amplifier at  $-15 \text{ dBm}$  total input power. The remaining 4 dB loss in feedforward amplifier gain is mainly due to the 3-dB input coupler and insertion loss of ports 1-2 of the amplifier circulator.

According to the theoretical results of Fig. 4.18, 31-dB improvement in IM distortion is obtained for  $-0.3 \text{ dB} < 0 < 0.3 \text{ dB}$  amplitude imbalance and/or less than  $1.8^\circ$  phase imbalance in the error-correction loop. Unfortunately it is difficult to discern at such small levels a quantitative evaluation of the relative contribution of gain and phase in failing to



achieve a more perfect balance. When an additional 1-dB gain imbalance was introduced into the error-correction loop, Fig. 6.13(a) shows that the IM products were reduced by 21 dB when compared with Fig. 6.12(a). In Fig. 4.18 it is clear that 21-dB reduction is obtained at  $0.7^\circ$  phase imbalance together with 0.8-dB amplitude imbalance; if the original gain imbalance was -0.2 dB these results are compatible. Similarly, Fig. 6.13(b) depicts that the IM products were reduced by 26 dB when a additional  $2^\circ$  phase imbalance was introduced into the error-correction loop; if the original phase imbalance was  $0.7^\circ$  and the original gain imbalance was -0.2 dB, then this result is compatible with Fig. 4.18. Finally, the effect of both an additional 1-dB gain imbalance and a  $2^\circ$  phase imbalance on the degree of distortion correction is shown in Fig. 6.13(c). Here, the distortion was reduced by 20 dB when compared with Fig. 6.12(a). In Fig. 4.18, a hypothetical  $2.7^\circ$  phase imbalance and 0.8-dB amplitude imbalance provides 19-dB reduction of IM distortion in the feedforward system. Hence the experimental measurements are consistent with theory if, for the measured maximum 31-dB reduction of IM distortion, the gain imbalance and phase imbalance in the error-correction loop were -0.2 dB and  $0.7^\circ$ , respectively.

Another set of spectrograms for a -13.8 dBm per tone input at 5.9005 GHz and 5.9015 GHz appears in Fig. 6.14. Comparing Figs. 6.14(a) and (c) we see that the IMPATT-amplifier IM distortion has been reduced by 11 dB, which is considerably below the 22-dB reduction figure predicted at 5.901 GHz in Fig. 6.7. Only an 18-dB error sensor null occurs at this frequency because of the  $11^\circ$  difference between the IMPATT-amplifier phase shift at 5.901 GHz and at 5.905 GHz, where the loops were balanced. This rather low error sensor null results in -33-dBm total input power to the error amplifier at 5.901 GHz, as seen in Fig. 6.14(b). Since the error





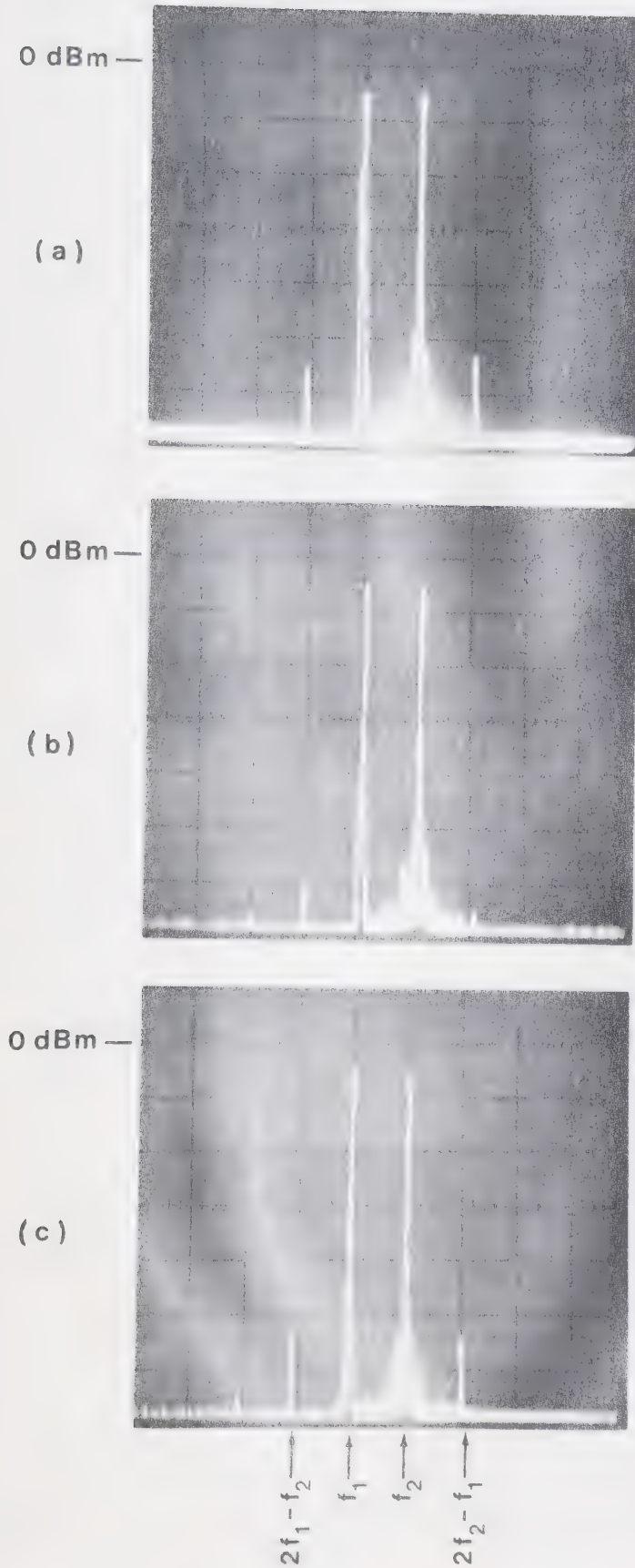


Figure 6.13

Spectrum photographs of the output of the feedforward amplifier with an equal-level ( $-13.8$  dBm) two-tone input at the centre frequency ( $f_1 = 5.9045$  GHz,  $f_2 = 5.9055$  GHz) [vertical scale 10 dB/cm; horizontal scale 1 MHz/cm].

- (a) The feedforward-corrected output for 1-dB amplitude imbalance in the error-correction loop.
- (b) The feedforward-corrected output for  $2^\circ$  phase imbalance in the error-correction loop.
- (c) The feedforward-corrected output for both 1-dB amplitude imbalance and  $2^\circ$  phase imbalance in the error-correction loop.





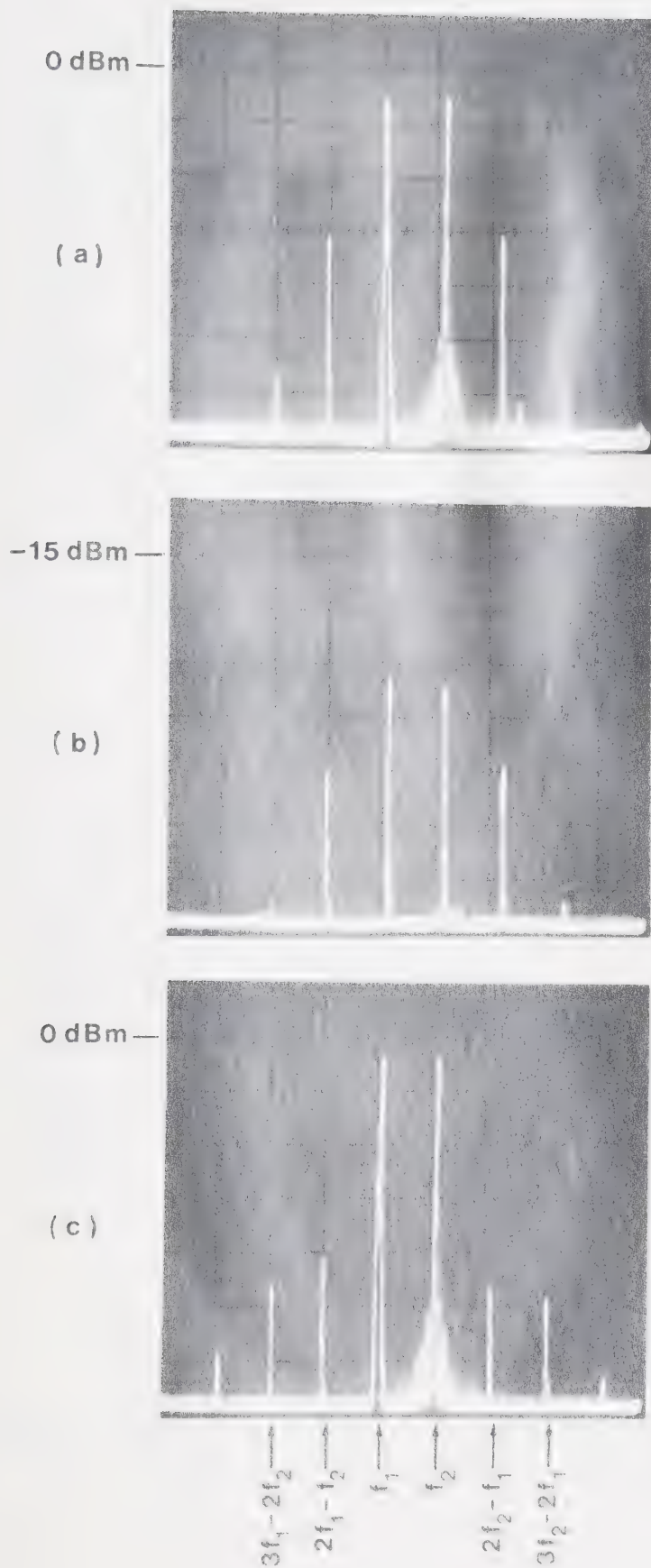


Figure 5.1

Spectrum photographs of the IM products of the experimental feedforward amplifier with an equal-level (-13.8 dBm) two-tone input at 5.901 GHz ( $f_1 = 5.9005$  GHz,  $f_2 = 5.9015$  GHz) [vertical scale 10 dB/cm; horizontal scale 1 MHz/cm].

(a) The output of the feedforward amplifier without feedforward correction.

(b) The input to the error amplifier when the error-detection loop is balanced at 5.905 GHz.

(c) The output of the feedforward amplifier with feedforward correction applied.



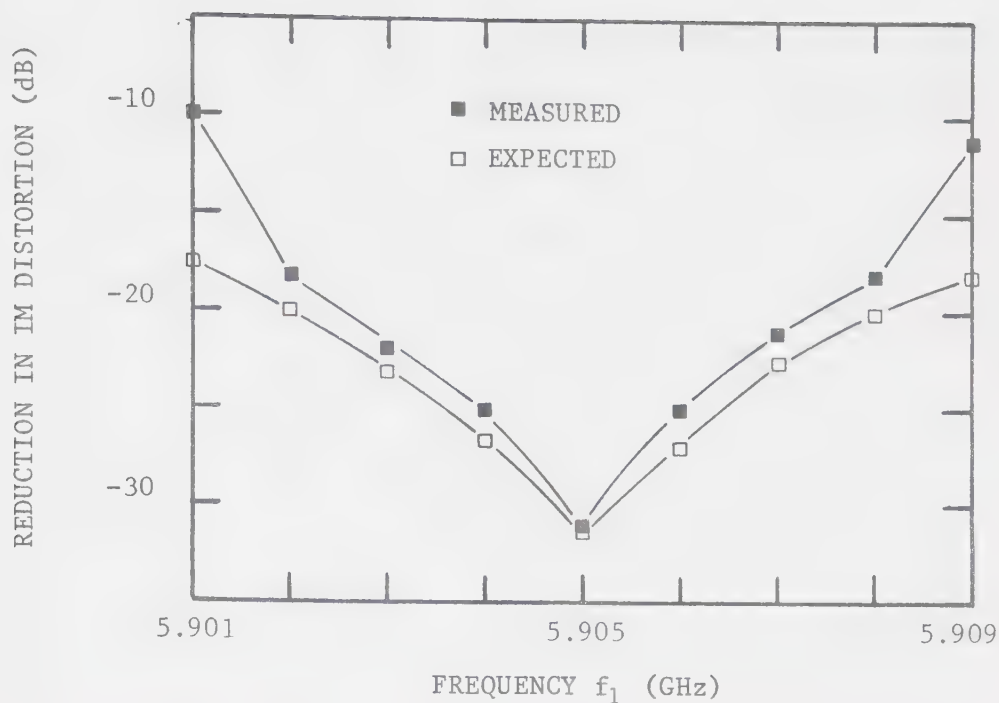


Figure 6.15 Comparison of measured reduction of IMPATT-amplifier third-order IM distortion by means of feedforward correction with the expected improvement values as a function of frequency.

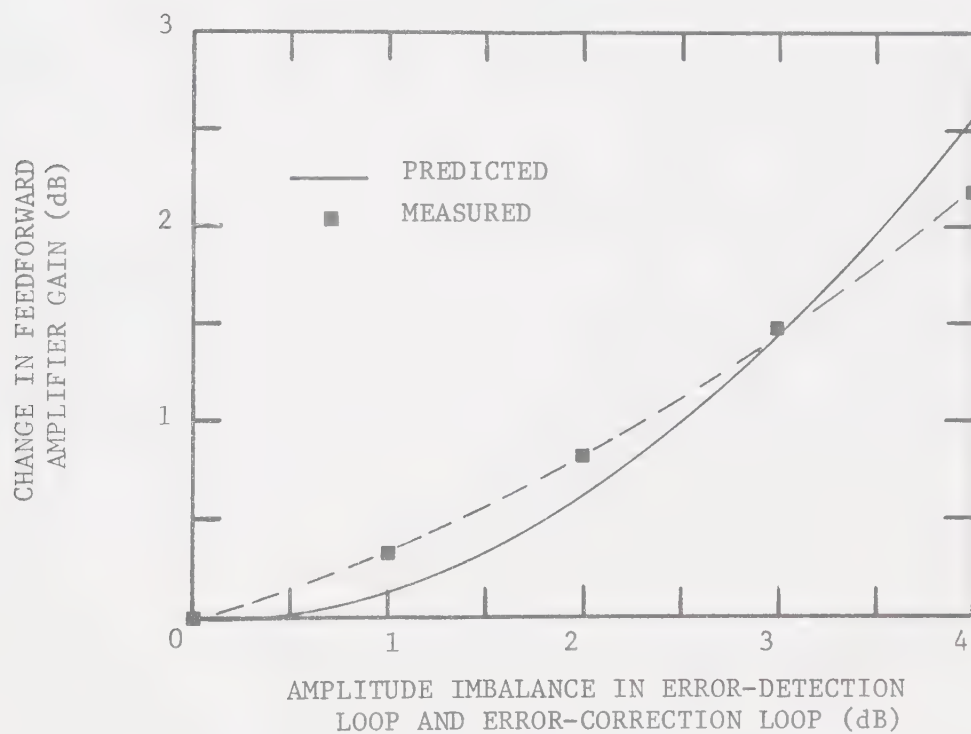


Figure 6.16 Comparison of measured feedforward-amplifier gain sensitivity with the predicted gain sensitivity.



amplifier 1-dB compression point occurs at -31-dBm input power, the error amplifier was operating in its nonlinear region and introducing its own IM distortion to the feedforward amplifier.

Measured reduction of distortion in the feedforward amplifier is plotted as a function of frequency in Fig. 6.15 together with the improvement expected on the basis of the measured error-injection null. Over the 5.902 - 5.908 GHz range, the distortion was reduced by more than 18 dB and the reduction differs from the error-injection null by less than 2 dB. Outside this range the distortion reduction sharply decreased due to the error amplifier being overdriven. This narrowband operation of the feedforward-corrected IMPATT amplifier is a consequence of the IMPATT-amplifier resonant-circuit characteristics.

Lastly the gain sensitivity of the feedforward amplifier for a CW input at the centre frequency was measured as a function of amplitude imbalance in the error-correction loop and error-detection loop by varying the insertion loss of attenuator A in Fig. 6.5. The results, displayed in Fig. 6.16, show favourable agreement with theory; namely, that the gain of the feedforward amplifier is changed by only  $.01p^2\%$  for a  $p\%$  change in amplitude imbalance. The difference between the curves is due to an imperfect initial balance in each of the interference loops.



## CHAPTER 7

### CONCLUSION

#### 7.1 Recapitulation of Theoretical and Experimental Results with Concluding Remarks

IMPATT diodes are widely used, at present, in microwave oscillators and amplifiers due to these inherent advantages: low cost; high reliability; small power supply requirement; and medium-power capability at high microwave frequencies. However, IMPATT-diode amplifiers typically exhibit a relatively high level of intermodulation (IM) distortion which has restricted their application to FM and PCM communications systems [41]. This IM distortion must be reduced if the IMPATT amplifier is to be used in microwave SSB-AM communications systems. In SSB-AM systems, channel spectrum width is utilized more efficiently than in FM systems but IM distortion level is a critical factor. Feedforward linearization is an effective technique for reducing IM distortion of a microwave amplifier to tolerable levels: the distortion is cancelled by adding the inverse phase distortion.

In this thesis, theoretical and experimental investigations of IM distortion in a feedforward-corrected IMPATT amplifier have been presented. A recapitulation of the major theoretical and experimental results reveals that all the objectives, stated in Sec. 1.2, have been fulfilled.

1) To characterize the nonlinear behaviour of an IMPATT diode as a function of frequency and RF voltage, a technique for the measurement of large-signal IMPATT electronic admittance has been developed. The method features: i) measurement of the electronic admittance without removal of the diode from the microwave circuitry; ii) use of a





network analyser for ease and flexibility in changing measurement frequency, and rapidity in data logging; iii) computer-aided data reduction for accuracy enhancement. The electronic admittance of an IMPATT diode (HP 5082-0431) was measured within an estimated error of 20% in the frequency range 5.7 - 6.5 GHz, for RF voltage amplitudes up to 20 V across the active region of the diode at constant 25-mA dc bias current. The experimental diode was successfully modelled by this measured nonlinear electronic admittance.

2) An experimental feedforward amplifier has been constructed mainly in a waveguide transmission medium, using a stable coaxial double-tuned IMPATT-diode amplifier (with the experimentally measured diode) as the main amplifier and a low-noise, low-power, 40-dB gain TWT as the error amplifier. The IMPATT amplifier was tuned at 25-mA dc bias current for 17.3-dB small-signal gain at the centre frequency, 5.905 GHz, with a 3-dB bandwidth of 64 MHz. The phase shift introduced by the IMPATT amplifier was approximately  $+60^\circ$  at the low end of the passband and  $-60^\circ$  at the high end of the passband.

3) A mathematical model for the IMPATT amplifier itself, and for the complete feedforward-corrected IMPATT amplifier, has been developed. This model is based on the Volterra series representation of the amplifier's input/output characteristics. The Volterra series incorporates the capability of the conventional power series representation of nonlinear devices without memory to predict amplitude dependence of nonlinear effects, together with the capability to predict the frequency dependence of nonlinear effects in devices with memory. Hence, either the Volterra series representation in the time-domain, or the Volterra transform representation in the frequency-domain, is a useful



approach to the analysis and understanding of microwave circuits in which memory effects are definitely not negligible. The Volterra series is an infinite series in which the labour of computing the  $n^{\text{th}}$ -term increases rapidly as the order  $n$  increases. Fortunately, in the study of nonlinear devices and systems it is often possible to neglect terms in the Volterra series of higher order than the fourth or fifth; if not the analysis must be confined to mild nonlinear operation for which only the low-order terms are needed to characterize the input/output behaviour. When the first few nonlinear Volterra transfer functions are known, items of interest regarding the output can be obtained by substituting the values in general formulae derived from the Volterra series representation. Of special interest here are the output IM distortion for an equal-level two-tone input and gain compression for a single-tone input.

The nonlinear Volterra transfer functions up to fifth-order for the IMPATT amplifier were derived from an equivalent circuit of the amplifier. In this equivalent circuit, the IMPATT-diode nonlinearities are represented by a separate quadratic power series approximation of the measured diode electronic conductance and equivalent electronic capacitance which is included to account for memory effects. The passive circuit admittance presented to the active region of the diode is represented by a  $G_C L_C C_C$  tuned circuit. The parameter values were experimentally determined from single-tone measurements.

The gain- and phase response of the equivalent circuit were in good agreement with the measured amplifier performance for input powers up to -10 dBm. In particular, as the input power increased: the amplifier gain decreased; the resonant frequency shifted downwards; the gain



curve became increasingly asymmetrical; and the group delay at the centre frequency increased.

The Volterra transfer functions were used to calculate third- and fifth-order IM distortion for the experimental IMPATT amplifier with a two-tone input. Predicted third-order IM distortion agreed with the measured distortion within 3 dB up to input levels of -23 dBm per tone over the passband. However, the predicted fifth-order distortion only agreed to within 10 dB with the measured distortion, due to the inadequacy of the quadratic power series representation of the diode's nonlinear admittance for predicting fifth-order effects. The measured value of third-order IM distortion for an input at the centre frequency was  $-22 \text{ dBm} \pm 1 \text{ dBm}$  for  $0 \text{ dBm} \pm 1 \text{ dBm}$  output at each fundamental tone; the measured fifth-order IM distortion was  $-45 \text{ dBm} \pm 1 \text{ dBm}$  for the same output power. These values indicate that the IM distortion was predominantly third-order distortion and hence the total distortion was predicted very well by the Volterra series analysis for input levels up to -21 dBm per tone. Beyond this range, more terms must be included in the Volterra series to describe the nonlinear behaviour of the IMPATT amplifier. In addition, to predict fifth-order distortion accurately, the diode's nonlinear electronic conductance and susceptance should each be represented by a fourth-order power series which greatly complicates the analysis. Gain compression was also predicted using the Volterra transfer functions and showed good qualitative agreement with measured values; quantitative agreement could not be verified because the measurement error ( $\pm 0.3 \text{ dB}$ ) was larger than the magnitude of the predicted values.

The nonlinear Volterra transfer functions up to fifth-order



were derived for the general microwave feedforward amplifier. The following major results have been obtained from a distortion analysis of the feedforward amplifier by means of these nonlinear transfer functions.

i) The degree of balance in the error-detection loop determines the power which must be handled by the error amplifier. As long as the power rating of the error amplifier is not a factor in the feedforward amplifier design, good cancellation of the information-bearing signal in the first loop is not required. However, if the power capability of the error amplifier is sacrificed for a lower noise figure (the noise figure of the overall amplifier is basically that of the error amplifier) then very good cancellation of the input signal in the first loop is required so that the error amplifier does not saturate and thereby increase the overall IM distortion. When the error amplifier is driven into its nonlinear region the results can be disastrous. For example, suppose the error signal grows by 3 dB in response to a 1-dB input power change to the main amplifier. If the error amplifier is in its nonlinear region due to a poor error-sensor null in the error-detection loop, its output has a component growing at 3 dB for each dB in, or 9 dB from input to output of the feedforward amplifier. For SSB-AM systems, where we are seeking good amplifier linearity even to high peak powers, this effect is substantial. Hence the error amplifier must operate in its linear region to obtain the desired distortion reduction.

Another observation regarding the error-detection loop





balance can be made for application of the feedforward amplifier in communications systems. Any imbalance in the error-detection loop produces a feedthrough of the input signal which shows as an echo on the feedforward amplifier output if a mismatched delay exists in either the error-detection loop or error-correction loop. Although this is not a non-linear problem, it may be serious, e.g. for telephone repeaters, where very good linear response (gain flatness and linear delay over the channel bandwidth) is also a priority.

ii) If the error amplifier is operating in its linear region, the distortion reduction capability of the feedforward amplifier is entirely dependent on the degree of gain- and/or phase balance in the error-correction loop. Moreover, the distortion reduction is independent of the actual values of the uncompensated distortion. An expression, Eqn. (4.90), has been derived for the relationship between amplifier distortion suppression and the degree of gain- and phase imbalance in the error-correction loop. Contours of constant improvement in IM distortion as a function of gain- and phase variations in the error-correction loop have been presented in Fig. 4.18. These contours directly determine the values of gain- and phase imbalance which can be tolerated for a given desired improvement in IM distortion. An improvement of the order of 17 dB is anticipated for a large gain and phase imbalance (1 dB and  $6^\circ$ , respectively).

iii) The sensitivity of feedforward amplifier gain to small gain fluctuations  $\epsilon_m$  and  $\epsilon_e$  of the main- and error amplifiers,



respectively, from the precise balance values is given by  $(1 - \epsilon_m \epsilon_e)$  for small phase imbalances. Hence the overall gain sensitivity is reduced by  $\epsilon_m \epsilon_e$ ; e.g., if both the main- and error amplifier deviate from the precise balance value by  $p\%$ , or if the amplitude imbalance in both loops is  $p\%$ , the gain of the feedforward amplifier is changed by only  $0.01p^2\%$ . Furthermore, if there is a precise amplitude balance in either the error-detection loop or error-correction loop (i.e.,  $\epsilon_m = 0$  or  $\epsilon_e = 0$ ), the overall gain remains almost constant for small phase imbalances.

In particular application to the experimental IMPATT amplifier the measured feedforward amplifier behaviour compared well with the predicted behaviour near the amplifier centre frequency. Intermodulation distortion products were reduced by: 30 dB at the centre frequency; 18 dB over a 6-MHz bandwidth; and 10 dB over an 8-MHz bandwidth. However, outside this frequency range the imbalance in the error-detection loop degraded rapidly because of the resonant-circuit characteristics of the IMPATT-amplifier, chiefly the large change in phase shift through the resonant frequency. The rather large imbalance in the error-detection loop outside the 8-MHz bandwidth caused the error amplifier to saturate and to contribute its own distortion to the feedforward amplifier output. The resonant character of an IMPATT amplifier leads to narrowband performance of a feedforward-corrected IMPATT amplifier. Some method of adaptive phase control, such as a bandpass filter with basically the same group delay characteristic as the IMPATT amplifier, is required to obtain a higher degree of interference in the error-detection loop across the band.



4) A second mathematical model of the feedforward-corrected IMPATT amplifier has been developed. This model provides a very satisfactory basis for quasistationary IM distortion analysis of the IMPATT amplifier (with a two-tone input) over a wider range of input power levels than the Volterra formulation. However, the method is not as general as the Volterra series approach, since only specific information, viz two-tone IM distortion and gain compression, can be obtained in the analysis. The amplifier model consists of a parallel combination of the measured electronic admittance and passive circuit admittance, with an equivalent current generator for the input signal. The circuit admittance can be measured as described in Sec. 5.3.1 (within an experimental error of 20%), or approximated by a tuned  $G_C L_C C_C$  circuit. The admittance data can be in discrete form, tabular form, graphical form, or expressed as a function of voltage amplitude and frequency. The unique smoothness property of the cubic spline function (bicubic spline function in two dimensions), i.e. it is the smoothest interpolating function through a set of data points, makes this function useful for approximating the derivatives in the nonlinear differential equation describing the amplifier's equivalent circuit. A cubic spline function of frequency is used to describe the passive circuit admittance; a bicubic spline function of RF voltage amplitude and frequency is used to describe the IMPATT electronic admittance. The resulting nonlinear differential equation was solved, in the frequency domain, for the IM distortion produced for a two-tone input, using the quasistationarity assumption. If the frequency separation of the two input signals is small (in the order of 1 MHz) relative to the absolute RF frequencies, this assumption (i.e., that the amplitude



and phase variations of the carrier frequency are much slower than the response time of the network) is generally valid. The calculated third-order IM distortion for the IMPATT amplifier was in close agreement with the measured values at input levels up to -18 dBm per tone, and was also in very good agreement with values predicted via Volterra series analysis. Predicted fifth-order distortion agreed favourably with the measured values. Gain compression calculated from the fundamental output power agreed qualitatively with the measured compression although the values were too small for quantitative comparison. In regards to efficiency, the quasistationary analysis costs about 600 times the cost of the Volterra series analysis for a distortion solution at a single frequency and several input power levels in the range -43 dBm to -18 dBm per tone.

Feedforward amplifier performance has also been analysed from linear equations describing the interferometer behaviour of the error-detection loop and error-correction loop in the time-domain. The results of this analysis are identical to those calculated by means of the Volterra series method.

5) In general, good agreement of the predicted IM distortion for the IMPATT amplifier, and for the feedforward-corrected IMPATT amplifier, with the measured distortion has been obtained. Thus, the nonlinear IMPATT-diode amplifier models, IM distortion analysis methods, software implementation, and measurement methods and techniques have all been validated.

## 7.2 Recommendations for Further Research

Both the Volterra transform method in the frequency domain and the interferometer approach in the time-domain have been shown to be suitable for IM distortion analysis of the feedforward amplifier. It





appears that the Volterra transform representation of nonlinear devices and systems does not enable us to do anything that cannot be done otherwise. However, other direct approaches for solving distortion problems in such systems often lead to a morass of algebra, e.g. the quasistationary approach developed here, or computational difficulties, e.g. integration routines may not be sensitive enough for calculating low-level distortion by integration of the nonlinear differential equation. The Volterra transform approach has the virtue that many such problems can be treated in an orderly fashion by first computing the Volterra transfer functions and then substituting them in the appropriate general formulae.

Outside the scope of this thesis, the Volterra transform method has already been used to predict amplitude crossmodulation distortion (AM-to-AM conversion) and phase crossmodulation distortion (AM-to-PM conversion) in both a stable IMPATT amplifier, and in the feedforward-corrected IMPATT amplifier [101]. In [101] it is shown that the phase imbalance in the error-correction loop may lead to improvements in the crossmodulation distortion substantially different from the corresponding improvement in the intermodulation distortion. Moreover, it is shown that by appropriate adjustment of the phase imbalance, large reductions (over 30 dB) in crossmodulation distortion of the feedforward amplifier can be achieved while maintaining over 20 dB reduction in IM distortion. The author feels that these theoretical results should be verified by thorough experimental investigation. It is also suggested that the Volterra transform technique be used to predict IM distortion in the IMPATT-amplifier and in the feedforward-corrected IMPATT amplifier for a random bandlimited Gaussian noise input. Such a random noise input



should be considered since it well represents frequency-multiplexed speech in a communications channel. The results of this analysis should be verified by noise-power-ratio distortion testing of the amplifier.

For practical application, it is recommended that an attempt be made to broadband the feedforward-corrected IMPATT amplifier. Possible techniques are: 1) Fabrication of the amplifier in microwave integrated circuit (MIC) form using an IMPATT amplifier as the main amplifier because of its relatively high output power, and a Gunn-effect amplifier as the error amplifier because of its low-noise characteristics. A common heat sink would allow the components to track one another and thus the necessary loop balance could be sustained; 2) Use of bandpass filters to compensate the group-delay characteristics of the main- and error-amplifiers. These could be the interdigital type for an MIC feedforward amplifier. Alternatively, a feedforward-corrected FET amplifier might avoid the narrow bandwidth problem since resonant circuits are not needed. Such an inexpensive microwave solid-state feedforward amplifier could be considered for use in future SSB-AM communications systems where the dominant limitations have been amplifier non-linearity and dynamic range.



## REFERENCES

- [1] F. Ivanek, "Single-Sideband Amplitude Modulation in Microwave Transmission Systems", *Microwave Journal*, vol. 15, pp. 27-36, April 1972.
- [2] R.G. Medhurst, J.H. Roberts and W.R. Walsh, "Distortion of SSB Transmission due to AM/PM Conversion", *IEEE Trans. Comm. Systems*, vol. CS-12, pp. 166-176, June 1964.
- [3] M.E. Hines, "Negative Resistance Diode Power Amplification", *IEEE Trans. Electron Devices*, vol. ED-17, pp. 1-8, Jan. 1970.
- [4] H.S. Black, "Translating Systems", U.S. Patent No. 1686792, (filed Feb. 3, 1925), 1928.
- [5] R.K. Jurgen, "Feedforward Correction: A Late-Blooming Design", *IEEE Spectrum*, vol. 9, pp. 41-43, April 1972.
- [6] C.C. Hsieh and S.P. Chan, "A Feedforward S-Band MIC Amplifier System", *Proc. IEEE Int. Solid-State Circuits Conf.* (Philadelphia, 1975), Paper THAM 9.1, pp. 90-91, Feb. 1975.
- [7] Ibid., *IEEE J. Solid-State Circuits*, vol. SC-11, pp. 271-278, April 1976.
- [8] H. Sobol and F. Sterzer, "Microwave Power Sources", *IEEE Spectrum*, vol. 9, pp. 20-33, April 1972.
- [9] B. Anderson, "M/W Solid-State Device Market", *Microwave Journal*, vol. 19, pp. 14-16, Feb. 1976.
- [10] H.C. Bowers, "IMPATT Diodes Start Competing as Microwave System Amplifiers", *Electronics*, vol. 45, pp. 82-88, Aug. 28, 1972.
- [11] B. Van der Pol, "The Nonlinear Theory of Electric Oscillations", *Proc. IRE*, vol. 22, pp. 1051-1085, Sept. 1934.
- [12] H.J. Kuno, "Analysis of Nonlinear Characteristics and Transient Response of IMPATT Amplifiers", *IEEE Trans. Microwave Theory and Tech.*, vol. MTT-21, pp. 694-702, Nov. 1973.
- [13] T. Berceci, "Nonlinear Effects in IMPATT Diode Amplifiers", *Proc. Fifth European Microwave Conference* (Hamburg, 1975), pp. 705-709, 1975.
- [14] G.L. Heiter, "Characterization of Nonlinearities in Microwave Devices and Systems", *IEEE Trans. Microwave Theory and Tech.*, vol. MTT-21, pp. 797-805, Dec. 1973.
- [15] L. Gustafsson, G.H.B. Hanson, and K.I. Lundstrom, "On the Use of Describing Functions in the Study of Nonlinear Active Microwave Circuits", *IEEE Trans. Microwave Theory and Tech.*, vol. MTT-20, pp. 402-409, June 1972.



- [16] V. Volterra, *Theory of Functionals and of Integral and Integro Differential Equations*. New York: Dover, 1959.
- [17] Panel Session "Nonlinearities in Microwave Devices and Systems", *Digest 1973 IEEE G-MTT Int. Microwave Symp.* (Boulder, Colorado, June 4-6, 1973, pp. 111-114, June 1973.
- [18] J.P. Laico, H.L. McDowell and C.R. Moster, "A Medium Power Travelling-Wave Tube for 6000 Mc Radio Relay", *Bell System Tech. J.*, vol. 35, pp. 1285-1346, Nov. 1956.
- [19] Technical Staff of Bell Telephone Labs., *Transmission Systems for Communications*. Winston Salem: Bell Telephone Laboratories Inc., 1970.
- [20] J. Putz, "Non-Linear Behaviour of Travelling-Wave Amplifiers", *Proc. Fifth International Congress on Microwave Tubes* (Paris, Sept. 14-18, 1964), pp. 56-61, 1964.
- [21] R.G. Meyer, M.J. Shensa and R. Eschenbach, "Cross Modulation and Intermodulation in Amplifiers at High Frequencies", *IEEE J. Solid-State Circuits*, vol. SC-7, pp. 16-23, Feb. 1972.
- [22] W.T. Read, "A Proposed High-Frequency Negative Resistance Device", *Bell System Tech. J.*, vol. 37, pp. 401-446, 1958.
- [23] M. Gilden and M.E. Hines, "Electronic Tuning Effects in the Read Microwave Avalanche Diode", *IEEE Trans. Electron Devices*, vol. ED-13, pp. 169-175, Jan. 1966.
- [24] T. Misawa, "Negative Resistance in P-N Junction Under Avalanche Breakdown Conditions, Part 1 and 2", *IEEE Trans. Electron Devices*, vol. ED-13, pp. 137-151, Jan. 1966.
- [25] G.I. Haddad *et al.*, "Basic Principles and Properties of Avalanche Transit Time Devices", *IEEE Trans. Microwave Theory and Tech.*, vol. MTT-18, pp. 752-772, Nov. 1970.
- [26] *Hewlett Packard Application Note 935*, "Microwave Power Generation and Amplification Using IMPATT Diodes".
- [27] D.L. Scharfetter and H.K. Gummel, "Large-Signal Analysis of Silicon Read-Diode Oscillator", *IEEE Trans. Electron Devices*, vol. ED-16, pp. 64-77, Jan. 1969.
- [28] W.J. Evans and G.I. Haddad, "A Large-Signal Analysis of IMPATT Diodes", *IEEE Trans. Electron Devices*, vol. ED-15, pp. 708-717, Oct. 1968.
- [29] P.T. Greiling and G.I. Haddad, "Large-Signal Equivalent Circuits of Avalanche Transit-Time Devices", *IEEE Trans. Microwave Theory and Tech.*, vol. MTT-18, pp. 842-853, Nov. 1970.





- [30] W.E. Schroeder and G.I. Haddad, "Nonlinear Properties of IMPATT Devices", *Proc. IEEE*, vol. 61, pp. 153-181, Feb. 1973.
- [31] R.W. Laton and G.I. Haddad, "Characteristics of IMPATT Diode Reflection Amplifiers", *IEEE Trans. Microwave Theory and Tech.*, vol. MTT-21, pp. 668-680, Nov. 1973.
- [32] R.J. Trew, N.A. Masnari and G.I. Haddad, "Intermodulation Characteristics of X-Band IMPATT Amplifiers", *IEEE Trans. Microwave Theory and Tech.*, vol. MTT-20, pp. 805-812, Dec. 1972.
- [33] W.E. Schroeder and G.I. Haddad, "Effect of Harmonic and Subharmonic Signals on Avalanche Diode Oscillator Performance", *IEEE Trans. Microwave Theory and Tech.*, vol. MTT-18, pp. 327-331, June 1970.
- [34] E.F. Scherer, "Large-Signal Operation of Avalanche Diode Amplifiers", *IEEE Trans. Microwave Theory and Tech.*, vol. MTT-18, pp. 922-932, Nov. 1970.
- [35] M.E. Hines, "Large-Signal Noise, Frequency Conversion, and Parametric Instabilities in IMPATT Diode Networks", *Proc. IEEE*, vol. 60, pp. 1534-1548, Dec. 1972.
- [36] P. Lubell, W. Denniston, and R. Hertz, "Linearizing Amplifiers for Multisignal Use", *Microwaves*, vol. 13, pp. 46-50, April 1974.
- [37] K.A. Simons, "The Decibel Relationships Between Amplifier Distortion Products", *Proc. IEEE*, vol. 58, pp. 1071-1086, July 1970.
- [38] K. Yamasuchi, "Equalization of Intermodulation due to TWT Amplification", *Trans. Joint Conv. of the Four Elec. Inst. of Japan*, No. 1599, 1965.
- [39] S. Owaku and D. Kuwagaki, "Common Amplification of Many Signals by a Travelling Wave Tube Amplifier", *J. Inst. Electron. Commun. Eng. Jap.*, vol. 51-B, pp. 193-200, 1968.
- [40] O. Shimbo, "Effect of Intermodulation, AM-PM Conversion and Additive Noise in Multicarrier TWT Systems", *Proc. IEEE*, vol. 59, pp. 230-238, Feb. 1971.
- [41] H. Komizo *et al.*, "Improvement of Nonlinear Distortion in an IMPATT Stable Amplifier", *IEEE Trans. Microwave Theory and Tech.*, vol. MTT-21, pp. 721-728, Nov. 1973.
- [42] H.W. Bode, *Network Analysis and Feedback Amplifier Design*. Princeton: Van Nostrand, 1945, p. 481.
- [43] R.C. Dorf, *Modern Control Systems*. Don Mills, Ont.: Addison-Wesley, 1967, p. 73.
- [44] C.J. Van Loon, "Improvement in Radio Receivers", *Philips Tech. Rev.*, vol. 1, pp. 264-269, Sept. 1936.



- [45] B.D.H. Tellegen, "Inverse Feedback", *Philips Tech. Rev.*, vol. 2, pp. 289-294, Oct. 1937.
- [46] H.A. Rosen and A.T. Owens, "Power Amplifier Linearity Studies for SSB Transmissions", *IEEE Trans. Communication Systems*, vol. CS-12, pp. 150-159, June 1964.
- [47] E. Bava, G.P. Bava and G. Zito, "Negative Feedback Improves TWT Linearity", *Proc. 1967 Cornell Conf. on High Frequency Generation and Amplification* (Ithaca, New York, Aug. 29-31, 1967), pp. 228-242, 1967.
- [48] D. Leypold, H. Leysieffer and H.K. Grunow, "Development Problems of Radio Relay Systems Using Single-Sideband Modulation", *Nachrichtentechnische Zeitschrift*, vol. 8, pp. 68-74, 1965.
- [49] Tech. Staff of Bell Telephone Labs., "Amplifier Correction System Demonstrated at Bell Labs.", *Bell Labs. Record*, vol. 50, p. 95, March 1972.
- [50] "Feedforward Error Control", *Wireless World*, vol. 78, p. 232, May 1972.
- [51] H. Seidel, "Feedforward Technology", *Proc. 1973 Int. Symposium on Circuit Theory* (Toronto, Canada), pp. 13-14, 1973.
- [52] Z. van Zelst, "Stabilised Amplifiers", *Philips Tech. Rev.*, vol. 9, pp. 25-32, 1947.
- [53] J.J. Golembeski *et al.*, "A Class of Minimum Sensitivity Amplifiers", *IEEE Trans. Circuit Theory*, vol. CT-14, pp. 69-74, March 1967.
- [54] H. Seidel, H.R. Beurrier and A.N. Friedman, "Error-Controlled High Power Linear Amplifiers at VHF", *Bell System Tech. J.*, vol. 47, pp. 651-722, May-June 1968.
- [55] H. Seidel, "A Feedforward Experiment Applied to an L-4 Carrier System Amplifier", *IEEE Trans. Comm. Tech.*, vol. COM-19, pp. 320-325, June 1971.
- [56] *Ibid.*, "A Microwave Feedforward Experiment", *Bell System Tech. J.*, vol. 50, pp. 2879-2916, Nov. 1971.
- [57] T.J. Bennett and R.F. Clements, "Feedforward - An Alternative Approach to Amplifier Linearization", *The Radio and Electronics Engineer*, vol. 44, pp. 257-262, May 1974.
- [58] P.M. Bakken, "Feedforward Linearized Travelling Wave Tube Satellite Transponder", *Proc. of EASCON '74 Conf.* (Wash. D.C., Oct. 7-9, 1974), 1974.
- [59] K.B. Klassen, R.J. Dekok and J.C.L. van Peppen, "Signal-Error-



- Feedforward-Controlled Amplifiers", *Electronics Letters*, vol. 11, pp. 250-251, June 12, 1975.
- [60] R.G. Meyer, R. Eschenbach, and W.M. Edgerley, "A Wide-Band Feed-forward Amplifier", *IEEE J. Solid-State Circuits*, vol. SC-9, pp. 422-428, Dec. 1974.
  - [61] J.L. Blue, "Approximate Large-Signal Analysis of IMPATT Oscillators", *Bell System Tech. J.*, vol. 48, pp. 383-396, Feb. 1969.
  - [62] M. Matsumura, "Large-Signal Analysis of Read Diodes", *Japan J. Appl. Phys.*, vol. 8, pp. 218-226, Feb. 1969.
  - [63] W.J. Getsinger, "The Packaged and Mounted Diode as a Microwave Circuit ", *IEEE Trans. Microwave Theory and Tech.*, vol. MTT-14, pp. 58-69, Feb. 1966.
  - [64] B.B. van Iperen and H. Tjassens, "Novel Accurate Methods for Measuring Small- and Large-Signal Impedances of IMPATT Diodes", *Philips Res. Repts.*, vol. 27, pp. 38-75, 1972.
  - [65] Ibid., "An Accurate Bridge Method for Impedance Measurements of IMPATT Diodes", *Microwave Journal*, vol. 15, pp. 29-33, Nov. 1972.
  - [66] C.N. Dunn and J.E. Dalley, "Computer-Aided Small-Signal Characterization of IMPATT Diodes", *IEEE Trans. Microwave Theory and Tech.*, vol. MTT-17, pp. 691-695, Sept. 1969.
  - [67] D.R. Decker, C.N. Dunn and R.L. Frank, "Large-Signal Silicon and Germanium Avalanche Diode Characteristics", *IEEE Trans. Microwave Theory and Tech.*, vol. MTT-18, pp. 872-876, Nov. 1970.
  - [68] J.W. Gewartowski and J.E. Morris, "Active IMPATT Diode Parameters Obtained by Computer Reduction of Experimental Data", *IEEE Trans. Microwave Theory and Tech.*, vol. MTT-18, pp. 157-161, March 1970.
  - [69] T. Isobe and T. Nakamura, "Admittance Measurement of IMPATT Diode at X-Band", *IEEE Trans. Microwave Theory and Tech.*, vol. MTT-18, pp. 993-995, Nov. 1970.
  - [70] D.H. Steinbrecher and D.F. Peterson, "Small-Signal Model with Frequency-Independent Elements for the Avalanche Region of a Microwave Negative-Resistance Diode", *IEEE Trans. Electron Devices*, vol. ED-17, pp. 883-891, Oct. 1970.
  - [71] Y. Ito *et al.*, "K-Band High-Power Single-Tuned IMPATT Oscillator Stabilized by Hybrid-Coupled Cavities", *IEEE Trans. Microwave Theory and Tech.*, vol. MTT-20, pp. 799-805, Dec. 1972.
  - [72] R.A. Hackborn, "An Automatic Network Analyser System", *Microwave Journal*, vol. 11, pp. 45-52, May 1968.
  - [73] G.L. Matthaei, L. Young and E.M.T. Jones, *Microwave Filters*,



*Impedance Matching Networks and Coupling Structures*.  
New York: McGraw-Hill, 1964, pp. 26-28.

- [74] E.F. Bolinder, "General Method of Analysing Bilateral, Two-Port Networks from Three Arbitrary Impedance Measurements", *Ericsson Technics*, vol. 14, No. 1, pp. 3-37, 1958.
- [75] S.M. Sze, *Physics of Semiconductor Devices*. Toronto: Wiley, 1969, pp. 42-43.
- [76] *Principles of Microwave Circuits*, C.G. Montgomery, R.H. Dicke, and E.M. Purcell, ed., New York: Dover, 1965, p. 75.
- [77] R.W. Anderson, "S-Parameter Techniques for Faster, More Accurate Network Design", *Hewlett-Packard Journal*, vol. 18, pp. 11-24, Feb. 1967.
- [78] R. Fletcher and M.J.D. Powell, "A Rapidly Convergent Descent Method for Minimization", *Computer J.*, vol. 6, pp. 163-168, June 1963.
- [79] T.N.E. Greville, *Mathematical Methods for Digital Computers*, vol. 2. New York: Wiley, 1967, Chapter 8.
- [80] N. Wiener, "Reponse of Nonlinear Device to Noise", *M.I.T. Radiation Lab.*, Rep. V-165, April 6, 1942.
- [81] M.B. Brilliant "Theory of the Analysis of Nonlinear Systems", *M.I.T. Res. Lab. Electron.*, Tech. Rep. 345, 1958.
- [82] D.A. George, "Continuous Nonlinear Systems", *M.I.T. Res. Lab. Electron.*, Tech. Rep. 355, July 1959.
- [83] G.D. Zames, "Nonlinear Operators for System Analysis", *M.I.T. Res. Lab. Electron.*, Tech. Rep. 370, Aug. 1960.
- [84] D.A. Chesler, "Nonlinear Systems with Gaussian Inputs", *M.I.T. Res. Lab. Electron.*, Tech. Rep. 366, Feb. 1960.
- [85] R.B. Parante, "Functional Analysis of Systems Characterized by Nonlinear Differential Equations", *M.I.T. Res. Lab. Electron.*, Tech. Rep. 444, July 1966.
- [86] E. Bedrosian and S.O. Rice, "The Output Properties of Volterra Systems (Nonlinear Systems with Memory) Driven by Harmonic and Gaussian Inputs", *Proc. IEEE*, vol. 59, pp. 1688-1707, Dec. 1971.
- [87] S. Narayanan, "Transistor Distortion Analysis Using Volterra Series Representation", *Bell System Tech. J.*, vol. 46, pp. 991-1024, May-June 1967.
- [88] Ibid., "Intermodulation Distortion of Cascaded Amplifiers", *IEEE J. Solid-State Circuits*, vol. SC-4, pp. 97-106, June 1969.





- [89] Ibid., "Application of Volterra Series to Intermodulation Distortion Analysis of Transistor Feedback Amplifiers", *IEEE Trans. Circuit Theory*, vol. CT-17, pp. 518-527, Nov. 1970.
- [90] H.C. Poon, "Modeling of Bipolar Transistor Using Integral Charge Control Model with Application to Third-Order Distortion Studies", *IEEE Trans. Electron Devices*, vol. ED-19, pp. 719-731, June 1972.
- [91] Y.L. Kuo and J.D. Witkowski, *Computer-Aided Distortion Analysis of Bipolar Transistor Circuits*. North Andover, Mass.: Bell Telephone Labs. Inc., 1972.
- [92] J.J. Bussgang, L. Ehrman and J.W. Graham, "Analysis of Nonlinear Systems with Multiple Inputs", *Proc. IEEE*, vol. 62, pp. 1088-1119, Aug. 1974.
- [93] A. Prochazka and R. Neumann, "High Frequency Distortion Analysis of a Semiconductor Diode for CATV Applications", *IEEE Trans. Consumer Electronics*, vol. CE-21, pp. 120-130, May 1975.
- [94] Y. Cho, "Sensitivity Analysis of Feedforward Amplifier", *Conf. Rec. of IEEE Int. Conf. on Communications*, pp. 3C1-3C5, June 1974.
- [95] J. Nigrin, N. Mansour and W.A.G. Voss, "Nonlinear Dynamic Study on Active Microwave Circuits", to be published.
- [96] F.L.H.M. Stumpers, "Distortion of Frequency Modulated Signals in Electrical Networks", *Communication News (Philips)*, vol. 9, pp. 82-92, April 1948.
- [97] J.H. Ahlberg, E.N. Nelson, J.L. Walsh, *The Theory of Splines and Their Applications*. New York: Academic Press, 1967.
- [98] H. Nyquist and S. Brand, "Measurement of Phase Distortion", *Bell System Tech. J.*, vol. 9, pp. 522-549, July 1930.
- [99] *Hewlett Packard Application Note 77-4*, "Swept-Frequency Group Delay Measurements".
- [100] C.W. Ip, "Design of a Microwave Two-Tone Signal Generator for Intermodulation Distortion Measurements", *M. Eng. Report*, Dept. of Elect. Eng., University of Alberta, unpublished, 1976.
- [101] A. Javed, P.A. Goud, B.A. Syrett, "Analysis of a Microwave Feed-forward Amplifier Using Volterra Series Representation", accepted for publication in *IEEE Trans. Comm.*



## APPENDIX A

### INTERMODULATION DISTORTION IN TERMS OF VOLTERRA TRANSFER FUNCTIONS

It is assumed that the nonlinear amplifier in question can be represented by the Volterra series given in Eqn. (4.4). A sufficient condition for the existence of the Volterra series is that the operation of the system be restricted to a region of asymptotic stability [21]. This includes the practical amplifiers under investigation here. Without loss of generality, assume the  $n^{\text{th}}$ -order kernel,  $h_n$ , to be a symmetric function of its arguments (a symmetric kernel can be obtained by permuting the  $n$  arguments in all  $n!$  ways, and taking the representative symmetric kernel to be  $1/n!$  times the sum of the resulting kernels) [86]. Then, the Fourier transform,  $H_n$ , from Eqn. (4.8), is also a symmetrical function of its arguments. Also assume that  $H_n$  is continuous in its arguments. This is true for the amplifier under consideration here, and should be true for all practical amplifiers [21].

Consider the application of a two-tone input,  $x(t)$ , as given by

$$x(t) = V(\cos \omega_1 t + \cos \omega_2 t) \quad . \quad (A1)$$

The input can be rewritten as

$$x(t) = \frac{V}{2} [\exp(j\omega_1 t) + \exp(j\omega_2 t) + \text{CC}] \quad (A2)$$

where CC represents the complex conjugate terms. For small distortion and frequencies  $\omega_1 \approx \omega_2$ , the third and fifth terms in Eqn. (4.4) are the major contributors to the third-order IM product. Even-order terms will produce distortion products outside the passband of the amplifier if it has less than octave bandwidth. Substituting Eqn. (A2) into (4.4),



carrying out the integration and using the Fourier transform notation, we obtain the steady-state response at frequency  $2\omega_1 - \omega_2$ :

$$y_{2\omega_1 - \omega_2}(t) = \frac{V^3}{8} \left\{ \left[ \sum_3' H_3(j\omega_1, j\omega_1, -j\omega_2) \right] \exp(j(2\omega_1 - \omega_2)t) + CC \right\} \\ + \frac{V^5}{32} \left\{ \left[ \sum_{20}' H_5(j\omega_1, j\omega_1, -j\omega_2, j\omega_1, -j\omega_1) + \right. \right. \\ \left. \left. \sum_{30}' H_5(j\omega_1, j\omega_1, -j\omega_2, j\omega_2, -j\omega_2) \right] \exp(j(2\omega_1 - \omega_2)t) + CC \right\} \quad (A3)$$

where

$$H_n^*(j\omega_1, j\omega_2, \dots, j\omega_n) = H(-j\omega_1, -j\omega_2, \dots, -j\omega_n) \quad (A4)$$

and  $\sum_N'$  denotes the  $N$  nonidentical terms obtained by permuting the arguments of the kernels. The number of terms,  $N$ , can be calculated from the number of permutations of  $n$  arguments, where  $p$  arguments are of one type,  $q$  arguments are of another type, and the remaining, if any,  $(n-p-q)$  arguments are distinct. The number  $N$  is given by  $N = n!/p!q!$ ; e.g., in the first term of Eqn. (A3),  $N = 3!/2!1! = 3$ .

Since  $H_3$  and  $H_5$  are symmetrical in their arguments,

$$y_{2\omega_1 - \omega_2}(t) = \left[ \frac{3V^3}{8} H_3(j\omega_1, j\omega_1, -j\omega_2) + \frac{5V^5}{8} H_5(j\omega_1, j\omega_1, -j\omega_2, j\omega_1, -j\omega_1) \right. \\ \left. + \frac{15V^5}{16} H_5(j\omega_1, j\omega_1, -j\omega_2, j\omega_2, -j\omega_2) \right] \cdot \exp(j(2\omega_1 - \omega_2)t) + CC \quad (A5)$$

now as  $\omega_1 \rightarrow \omega_2$ ,  $y_{2\omega_1 - \omega_2}(t)$  approaches in the limit,



$$\begin{aligned}
y_{2\omega_1 - \omega_2}(t) = & \frac{3V^3}{4} |H_3(j\omega_1, j\omega_1, -j\omega_2)| \cos[(2\omega_1 - \omega_2)t + \arg H_3(j\omega_1, j\omega_1, -j\omega_2)] \\
& + \frac{5V^5}{4} |H_5(j\omega_1, j\omega_1, -j\omega_2, j\omega_1, -j\omega_1)| \cos[(2\omega_1 - \omega_2)t \\
& \quad + \arg H_5(j\omega_1, j\omega_1, -j\omega_2, j\omega_1, -j\omega_1)] \\
& + \frac{15V^5}{8} |H_5(j\omega_1, j\omega_1, -j\omega_2, j\omega_2, -j\omega_2)| \cos[(2\omega_1 - \omega_2)t \\
& \quad + \arg H_5(j\omega_1, j\omega_1, -j\omega_2, j\omega_2, -j\omega_2)] \quad . \quad (A6)
\end{aligned}$$

Equation (A6) expresses the amplitude of the third-order IM product in the response of a nonlinear amplifier.

Similarly, for small distortion and frequencies  $\omega_1 \approx \omega_2$ , the fifth term in Eqn. (4.4) is the major contributor to the fifth-order IM product. Performing the integration with the two-tone input of Eqn. (A2) inserted into Eqn. (4.4) yields the steady-state response at frequency  $3\omega_1 - 2\omega_2$ :

$$y_{3\omega_1 - 2\omega_2}(t) = \frac{V^5}{32} \left\{ \left[ \sum_{10} H_5(j\omega_1, j\omega_1, j\omega_1, -j\omega_2, -j\omega_2) \right] \exp(j(3\omega_1 - 2\omega_2)t) + CC \right\} . \quad (A7)$$

Since  $H_5$  is symmetrical in its arguments,

$$y_{3\omega_1 - 2\omega_2}(t) = \frac{5V^5}{16} H_5(j\omega_1, j\omega_1, j\omega_1, -j\omega_2, -j\omega_2) \exp(j(3\omega_1 - 2\omega_2)t) + CC. \quad (A8)$$

now, as  $\omega_1 \rightarrow \omega_2$ ,  $y_{3\omega_1 - 2\omega_2}(t)$  approaches in the limit,





$$y_{3\omega_1 - 2\omega_2}(t) = \frac{5V^5}{8} |H_5(j\omega_1, j\omega_1, j\omega_1, -j\omega_2, -j\omega_2)| \cos[(3\omega_1 - 2\omega_2)t + \arg H_5(j\omega_1, j\omega_1, j\omega_1, -j\omega_2, -j\omega_2)] \quad . \quad (A9)$$

Equation (A9) expresses the amplitude of the fifth-order IM product in the response of a nonlinear amplifier.



## APPENDIX B

### GAIN COMPRESSION IN TERMS OF VOLTERRA TRANSFER FUNCTIONS

It is assumed, as in Appendix A, that the nonlinear amplifier in question can be represented by the Volterra series given in Eqn. (4.4). It is also assumed that: 1) the Volterra kernels and the Volterra transforms are symmetric functions of their respective arguments; 2) the Volterra transforms are continuous functions of their arguments.

Consider the application of a CW input,  $x(t)$ , as given by

$$x(t) = V \cos \omega_1 t = \frac{V}{2} [\exp(j\omega_1 t) + CC] \quad (B1)$$

where CC denotes the complex conjugate terms. If the amplifier is only driven mildly into the nonlinear region of operation, the third and fifth terms in Eqn. (4.4) are the major contributors to amplifier gain compression. The even-order terms in Eqn. (4.4) produce harmonics of the input signal and will not contribute to the output at the fundamental frequency. Substituting Eqn. (B1) into (4.4) and then integrating gives the following result for the amplifier output at frequency  $\omega_1$ :

$$\begin{aligned} y_{\omega_1}(t) = & \frac{V}{2} [H_1(j\omega_1) \exp(j\omega_1 t) + CC] \\ & + \frac{V^3}{8} \left\{ \left[ \sum_3' H_3(j\omega_1, j\omega_1, -j\omega_1) \right] \exp(j\omega_1 t) + CC \right\} \\ & + \frac{V^5}{32} \left\{ \left[ \sum_{10}' H_5(j\omega_1, j\omega_1, j\omega_1, -j\omega_1, -j\omega_1) \right] \exp(j\omega_1 t) + CC \right\} . \end{aligned} \quad (B2)$$



Since  $H_3$  and  $H_5$  are symmetrical in their arguments,

$$y_{\omega_1}(t) = \left[ \frac{V}{2} H_1(j\omega_1) + \frac{3}{8} V^3 H_3(j\omega_1, j\omega_1, -j\omega_1) + \frac{5}{16} V^5 H_5(j\omega_1, j\omega_1, j\omega_1, -j\omega_1, -j\omega_1) \right] \cdot \exp(j\omega_1 t) + CC \quad (B3)$$

The amplifier output at the fundamental frequency  $\omega_1$ , is thus

$$\begin{aligned} y_{\omega_1}(t) = & V |H_1(j\omega_1)| \cos[\omega_1 t + \arg H_1(j\omega_1)] \\ & + \frac{3}{4} V^3 |H_3(j\omega_1, j\omega_1, -j\omega_1)| \cos[\omega_1 t + \arg H_3(j\omega_1, j\omega_1, -j\omega_1)] \\ & + \frac{5}{8} V^5 |H_5(j\omega_1, j\omega_1, j\omega_1, -j\omega_1, -j\omega_1)| \cos[\omega_1 t \\ & + \arg H_5(j\omega_1, j\omega_1, j\omega_1, -j\omega_1, -j\omega_1)] \quad (B4) \end{aligned}$$

The first term in Eqn. (B4) represents the linear amplifier output; the other two terms are the amplifier gain compression terms.

















**B30167**